CLASSICAL DYNAMICS OF TRIATOMIC SYSTEMS

I. Dynamics of Energized Harmonic Molecules
II. Dynamics of Energized Anharmonic Molecules
III. The H + DX Reactions

Thesis by

Christopher Alan Parr

In Partial Fulfillment of the Requirements

For the Degree of

Doctor of Philosophy

California Institute of Technology

Pasadena, California

1969

(Submitted September 5, 1968)

ACKNOWLEDGMENTS

It is a pleasure and an honor to acknowledge the patient guidance of my research advisor, Dr. Aron Kuppermann. His suggestion of and discussions about these thesis topics merit my heartfelt gratitude. May he forgive my penchant for practical jokes at his expense.

The efforts of Dr. R. N. Porter, who made many of the preliminary calculations for Parts I and II, are gratefully acknowledged.

Many thanks are due to the noble Kuppermann group theoreticians, Don Truhlar, whose withering commentary rarely failed to enlighten, Dr. Merle Riley, whose dedication to matters quantum mechanical, weakened my classical bias (for which I am everlastingly grateful), and Dr. Dave Cartwright, whose grasp on chemical physical concepts was uncannily tenacious.

The group's experimentalists are gratefully acknowledged for nurturing a respect for chemical pragmatism. Lonne Lane is especially thanked for six memorable years of camaraderie. Drs. Mike White and Oakley Crawford, Jim Rice, Drs. Avigdor Persky and Don Davis, and many others are all to be highly commended for patience with the naiveté of this "hypothetical" chemist.

The staffs of the chemistry departments of both the University of Illinois and Caltech are roundly appreciated for lubricating my graduate career in dozens of ways. And the financial support of NASA and NSF for traineeships and the above-mentioned departments for assistantships is most gratefully acknowledged.

Finally, and most importantly, I am ever so grateful to my

wife, Necia, whose four-and-a-half years of absolutely indispensable snuggle made my graduate years as pleasant as I anticipate the rest of our life together will be.

ABSTRACTS

Part I. Dynamics of Energized Harmonic Molecules

The classical equations of motion of some bent triatomic harmonic molecular models are integrated numerically to investigate the assumptions underlying contemporary theories of unimolecular reaction rates. The small vibration and weak coupling approximations are shown to be inadequate for energies near dissociation, but reaction frequencies, based upon a modification of the former approximation, are seen to be in good agreement with the model's actual reaction frequencies. The effects of rotation upon intramolecular energy exchange are shown to be non-negligible. The effects of bond anharmonicity were not included in this paper.

Part II. Dynamics of Energized Anharmonic Molecules

The classical equations of motion of two anharmonic bent triatomic molecular models are integrated numerically. It is found that at dissociative energies, the intramolecular energy transfer rate is the frequency with which any two bonds compress. The normal mode description of the motion is observed to be entirely inadequate. Molecular lifetimes are shown to be unstable to small perturbations in the initial conditions for the molecular trajectory. This instability may imply gross differences in the classical and quantal lifetimes of energized molecules.

Part III. The H + DX Reactions

A Sato surface, free of spurious wells, is proposed for the reaction H + DBr. The abstraction fraction, the ratio of abstraction to total reaction rate, is shown to have similar large temperature dependence from activated complex theory that is found from classical trajectory results. The latter yield broad product energy distributions and reaction cross sections which peak (at ~ 1 eV relative energies) at 3 and 13 a_o^2 for abstraction and exchange, respectively.

TABLE OF CONTENTS

Part I. Dynamics of Energized Harmonic Molecules

DYNAMICS OF ENERGIZED HARMONIC MOLECULES

1. Introduction

Theories of thermal unimolecular decomposition or isomerization rates of molecules (1-6) make heavy use of harmonic models. Harmonic oscillators are attractive for their relative mathematical tractability in both classical and quantum mechanics. In either formulation, harmonicity lends itself to separation (7) of the total Hamiltonian into a sum of normal mode Hamiltonians in the limit of vibrations of vanishingly small amplitude. The resultant normal mode energies, which, in this case, are constants of the motion, allow dynamical attacks on the problem of decomposition rates in energized molecules.

For non-linear molecules, even if their bonds are perfectly harmonic, the normal mode energies are constants of the (classical or quantum mechanical) motion only in the limit of infinitesimal displacements of the atoms from their equilibrium configuration. One of Slater's theories (8) assumes, among other things, that the normal mode energies are rigorous constants of the motion even for large displacements. This is the small vibration approximation (hereinafter designated as SVA) to the nuclear motion of molecules. This paper examines the applicability of this approximation in some classical harmonic molecular models when their energies approach those necessary for reaction. In Slater's treatment (8), reaction occurs when some critical co-ordinate (or co-ordinates (9)) is stretched or compressed to a critical value. The reaction rate becomes, in part, a measure

of the frequency with which the critical co-ordinate attains its critical value. We wish to test the sensitivity of this frequency to the failure of the SVA. We will also test the perturbing effect of rotation, which is neglected in Slater's treatment of the model's vibrations.

The Rice-Ramsberger-Kassel-Marcus (RRKM) theory (2, 6) of unimolecular decomposition considers molecules to be sets of harmonic oscillators coupled together in such a way as to allow energy to flow freely between them but not so furiously that the oscillator energies fail to sum to the total vibration energy (10). Since the terms in the Hamiltonian which couple these oscillators will contribute to the energy of the system, one assumption in RRKM theory is that these terms are small enough to be ignored in summing contributions to the model's total energy and large enough to allow facile scrambling of the energy among the oscillators. The validity of this assumption is tested in this paper. The RRKM oscillators have never been defined (11) more closely than as "harmonic degrees of freedom." The term "oscillator" might apply to the interatomic bonds or the normal modes, and both of these interpretations are examined here.

Since harmonic springs cannot be broken, these models are fated never to dissociate in the sense that, at some time, restoring forces become and remain arbitrarily small. We expect the anharmonicity, which allows actual molecules to decompose, will render the normal mode description a poor one (12-15). Thus, aside from any question of activation/deactivation mechanisms, the theories will disagree with experiment in both the artificial choice of potential and the approximate way they solve the dynamic

problem for this potential. Direct comparison of these theories with experiment is an inadequate test of the validity of the dynamic treatment. A better comparison, for this problem, is to do a rigorous and an approximate calculation with the same assumed harmonic potential. Discrepancies between these results may provide information about the magnitude and direction of errors made in applying these approximations to real molecules.

The simplest system of interest in unimolecular decomposition studies is the triatomic molecule. As the equations of motion of three-body systems in general cannot be solved analytically in either classical or quantal formulations, they must be solved numerically. An accurate quantum mechanical solution is not necessary for verification of the constancy of dynamical functions. For conservative systems, the correspondence principle insures that a dynamical function is a quantum mechanical constant of the motion, simultaneously knowable with the Hamiltonian, if and only if it is a classical constant of the motion as well (16). Thus classical nuclear trajectory calculations suffice to test the constancy of normal mode energies assumed in Slater's theory and the constancy of total oscillator energy required for RRKM theory.

In the present paper, we analyze the high energy dynamics of two harmonic models to test the assumptions of the unimolecular theories mentioned above. The first model is a fairly artifical one called M_3 and consisting of three point particles of equal mass connected pairwise by three identical, massless, harmonic springs. In their equilibrium configuration, the mass points are located on the vertices of an equilateral triangle. Since the

equations of motion of this and other models were solved in dimensionless form (see Section 3.2.) there exist infinitely many sets of model parameters which correspond to the dimensionless parameters used. We shall discuss M_3 in terms of only one such set, wherein the masses all correspond to O^{16}, the spring force constants and equilibrium lengths all correspond to the O_2 molecule (17), and the dissociation energy, $2D_o$, is taken to be twice that of molecular oxygen.

The second model is a more realistic one for nitrosyl chloride, wherein the experimental structure (18), central (pairwise) force constants (19), and dissociation energy (20) are employed. In a subsequent paper (15), we shall examine the dynamic behavior of anharmonic versions of these two models.

Some studies were made of the low energy dynamics of harmonic H_2O, HOD, D_2S, H_2Se, NO_2, SO_2, F_2O and ClNO (18). The model and molecular parameters of the pertinent triatoms studied are given in Table I.

Table I. Model and Molecular Parameters

MODEL	r_1^{eq}	r_3^{eq}	Angle	r_2^{eq}	k_1	k_3	k_2	ω_s	ω_a	ω_b
					(millidynes/Angstrom)			(wavenumbers cm^{-1})		
H_2O	0.957Å	0.957Å	104.5°	1.514Å	8.45 (8.49)	8.45 (8.49)	1.78 (1.93)	4376 (3832)	3934 (3943)	1380 (1648)
HOD		same				same		4175 (2824)	2993 (3890)	1211 (1440)
M_3	1.207Å (1.278)	1.207Å (1.278)	60° (117°)	1.207Å (1.591)	11.77	11.77	11.77	1931 (1110)	1370 (1042)	1370 (702)
$ClNO^{18}$	1.139Å	1.975Å	114°	2.650Å	13.97	1.92	0.98	592 (592)	1750 (1799)	329 (329)
FOO	1.575Å	1.217Å	109.5°	2.290	1.43	10.47	2.29	1520 (1500)	586 (699)	376 (384)

2. Previous Trajectory Calculation Studies of Unimolecular Reactions

Thiele and Wilson (12) used classical mechanical trajectory calculations to comment upon the impropriety of the application of the SVA to the in-line vibrations of linear anharmonic molecules. The in-line vibrations of linear harmonic molecules follow rigorously the same vibration equations (see Section 4. 1.) for all vibration amplitudes. However, when Thiele and Wilson introduced chemically interesting energies into an anharmonic model for CO_2, the rigorous solution of the equations of motion gave normal mode co-ordinates which were aperiodic functions of time. Although the normal mode energies were not given in the paper, they must surely have reflected this failure of the SVA. Similar anharmonicity effects for non-linear molecules will be reported in a separate paper.

Kuppermann and Porter (21) reported preliminary trajectory calculation results of the research to be described in this paper.

In the first of his trajectory calculation papers, Bunker (13) briefly investigated the kinetics of three classical harmonic molecular models, two of linear N_2O and one of bent O_3. He found that the normal mode co-ordinates appeared to be almost periodic functions of time. His harmonic models apparently had metrically decomposable (22) phase spaces. Large numbers of initial conditions, which gave the molecules sufficient energy to "dissociate," failed to produce dissociation, as the energy did not accumulate in the reaction co-ordinate within about 50

symmetric stretch periods over which the trajectories were observed. The metric decomposability persisted under rotation (14) as well.

It developed (13, 14) that Slater's frequency factor (23), $\bar{\nu}$, was in good agreement with k_∞, the high pressure limit of the rate constant obtained from the trajectory calculations. This implies to us that Slater's treatment correctly calculates the distribution of model lifetimes as they become arbitrarily short. Hence the SVA to the model's trajectory does not diverge immediately from the true trajectory. Although they do diverge eventually, the SVA would still be a useful approach <u>if</u> it reproduced the reaction frequencies of the harmonic model. One of the motivations of the present work is to verify whether or not this is the case.

3. The Classical Mechanical Equations of Motion

3.1. Harmonic Triatomic Model

Let m_i and $\underset{\sim}{X}_i$ $(i = 1, 2, 3)$ be the masses and the Cartesian position vectors of the nuclei of a triatomic molecule in a center-of-mass system of reference. The $\underset{\sim}{X}_i$ are then related by the expression

$$\sum_{i=1}^{3} m_i \underset{\sim}{X}_i = 0 . \qquad (3.1.-1)$$

We take $\underset{\sim}{X}_1$ and $\underset{\sim}{X}_3$ to be the independent co-ordinates. The corresponding conjugate momenta are

$$\begin{aligned} \underset{\sim}{P}_1 &= m_1 (1 + m_1/m_2) \dot{\underset{\sim}{X}}_1 + m_1 m_3 \dot{\underset{\sim}{X}}_3/m_2 \\ \underset{\sim}{P}_3 &= m_1 m_3 \dot{\underset{\sim}{X}}_1/m_2 + m_3 (1 + m_3/m_2) \dot{\underset{\sim}{X}}_3 . \end{aligned} \qquad (3.1.-2)$$

The Hamiltonian for this system is

$$\mathcal{H} = T + V \qquad (3.1.-3)$$

where

$$2T = [(m_2 + m_3) \underset{\sim}{P}_1 \cdot \underset{\sim}{P}_1/m_1 - \underset{\sim}{P}_1 \cdot \underset{\sim}{P}_3 + (m_1+m_2) \underset{\sim}{P}_3 \cdot \underset{\sim}{P}_3/m_3]/M \qquad (3.1.-4)$$

and

$$V = V(r_1, r_2, r_3) \ . \qquad (3.1.-5)$$

Here $M = \sum_{i=1}^{3} m_i$ and r_i is the internuclear distance opposite nucleus i. Hamilton's equations of motion for this system are

$$\dot{\underset{\sim}{X}}_i = \partial \mathcal{H} / \partial \underset{\sim}{P}_i \qquad (24) \qquad (3.1.-6)$$

and

$$\dot{\underset{\sim}{P}}_i = - \partial \mathcal{H} / \partial \underset{\sim}{X}_i \ . \qquad (3.1.-7)$$

Performing the partial differentiation in equation (3.1.-6) is equivalent to inverting equations (3.1.-2) and furnishes

$$\dot{\underset{\sim}{X}}_1 = [(m_2 + m_3)\underset{\sim}{P}_1/m_1 - \underset{\sim}{P}_3] / M \qquad (3.1.-8)$$

and

$$\dot{\underset{\sim}{X}}_3 = [(m_1 + m_2)\underset{\sim}{P}_3/m_3 - \underset{\sim}{P}_1]/M \ .$$

Since the expression for the kinetic energy, T, in equation (3.1.-4) is independent of $\underset{\sim}{X}_i$, equation (3.1.-7) becomes

$$\dot{\underset{\sim}{P}}_i = -\partial V / \partial \underset{\sim}{X}_i = - \sum_{j=1}^{3} (\partial V / \partial r_j)(\partial r_j / \partial \underset{\sim}{X}_i) \ . \qquad (3.1.-9)$$

The $\partial r_j/\partial \underset{\sim}{X}_i$ follow from the expressions for the r_j in terms of the independent co-ordinates, viz.,

$$r_1 = |m_1 \underset{\sim}{X}_1 + (m_2 + m_3)\underset{\sim}{X}_3|/m_2$$

$$r_2 = |\underset{\sim}{X}_1 - \underset{\sim}{X}_3| \qquad (25) \qquad (3.1.-10)$$

$$r_3 = |(m_1 + m_2)\underset{\sim}{X}_1 + m_3 \underset{\sim}{X}_3|/m_2 .$$

Differentiation of equations (3.1.-10)with respect to $\underset{\sim}{X}_1$ and $\underset{\sim}{X}_3$ yields

$$\partial r_1/\partial \underset{\sim}{X}_1 = m_1 \underset{\sim}{\gamma}_1/m_2$$

$$\partial r_2/\partial \underset{\sim}{X}_1 = \underset{\sim}{\gamma}_2$$

$$\partial r_3/\partial \underset{\sim}{X}_1 = (1 + m_1/m_2)\underset{\sim}{\gamma}_3 \qquad (3.1.-11)$$

$$\partial r_1/\partial \underset{\sim}{X}_3 = (1 + m_3/m_2)\underset{\sim}{\gamma}_1$$

$$\partial r_2/\partial \underset{\sim}{X}_3 = -\underset{\sim}{\gamma}_2$$

$$\partial r_3/\partial \underset{\sim}{X}_3 = m_3 \underset{\sim}{\gamma}_3/m_2$$

where

$$\underset{\sim}{\gamma}_1 = [m_1 \underset{\sim}{X}_1/m_2 + (1 + m_3/m_2)\underset{\sim}{X}_3]/r_1$$

$$\underset{\sim}{\gamma}_2 = (\underset{\sim}{X}_1 - \underset{\sim}{X}_3)/r_2 \qquad (3.1.-12)$$

and

$$\underset{\sim}{\gamma}_3 = [(1 + m_1/m_2)\underset{\sim}{X}_1 + m_3\underset{\sim}{X}_3/m_2]/r_3$$

The complete specifications of Hamilton's equations (3.1.-6) and (3.1.-9) requires only a choice of the potential, which, in this work, will be taken to be

$$V = \sum_{i=1}^{3} V_i \qquad (3.1.-13)$$

where

$$2V_i = k_i(r_i - r_i^{eq})^2 \ . \qquad (3.1.-14)$$

The k_i are internuclear harmonic force constants and the r_i^{eq} are the equilibrium internuclear distances in the molecule.

3.2. Dimensionless Equations of Motion

The twelve first order coupled differential equations of motion symbolized by (3.1.-6) and (3.1.-7) were reduced to dimensionless form for solution by the numerical integration procedure outlined in Section 5.1. One advantage of using dimensionless formulae is that every trajectory produced is associated with an infinite set of molecular models.

Let the units of any quantity, q, be given by q*. We may define the dimensionless quantity $\bar{q}$ by

$$\bar{q} = q/q^* \quad . \qquad (3.2.-1)$$

The conversion of equations (3.1.-9) to dimensionless form yields

$$d\bar{\underset{\sim}{P}}_i/d\bar{t} = - a\, \partial\bar{V}/\partial\bar{\underset{\sim}{X}}_i \qquad (3.2.-2)$$

where a is a dimensionless parameter given by

$$a = V^* t^*/X^* P^* \quad , \qquad (3.2.-3)$$

and will be called the dimensionality factor for equations (3.2.-2) . Similarly, the dimensionality factor for the dimensionless form of equations (3.1.-8) is

$$b = P^* t^*/m^* X^* \quad . \qquad (3.2.-4)$$

The expression for angular momentum is

$$\underset{\sim}{L} = \sum_{i=1}^{3} m_i(\underset{\sim}{X}_i \times \dot{\underset{\sim}{X}}_i) \quad . \qquad (3.2.-5)$$

With the aid of equations (3.1.-1) and (3.1.-8) , it can easily be shown that

$$\underset{\sim}{L} = \underset{\sim}{X}_1 \times \underset{\sim}{P}_1 + \underset{\sim}{X}_3 \times \underset{\sim}{P}_3 \quad . \qquad (3.2.-6)$$

The dimensionality factor for the dimensionless form of the last equation is

$$c = X^* P^*/L^* \ . \qquad (3.2.-7)$$

Clearly, any molecular model, which differs from the ones discussed below by a change in its parametric units such that the values of a, b, and c are preserved, will exhibit the same trajectory in the configuration space of the dimensionless coordinates as do the models discussed, so long as the same dimensionless initial conditions are used. We have taken our units, q*, from the parameters of the oxygen atom and molecule (17). Let the Morse function for O_2 be (26)

$$V_{O_2} = D_{O_2}\left\{1 - \exp[-\beta_{O_2}(r - r_{O_2}^{eq})]\right\}^2 \qquad (3.2.-8)$$

where

$$D_{O_2} = 119.43 \text{ kcal/mole} \quad \text{and} \quad \beta_{O_2} = 2.663 \ \text{Å}^{-1}.$$

We used the following arbitrary choices for the dimensionality factors: a = 1/64, b = 1/16, and c = 1. One set of q*s which give these values to the dimensionality factors and which was used in our calculations is

$$m^* = m_O = 2.656 \times 10^{-23} \text{ gms} = 16 \text{ awu}$$

$$X^* = 16/\beta_{O_2} = 6.008 \ \text{Å}$$

$$V^* = 4D_{O_2} = 477.72 \text{ kcal/mole}$$

$$P^* = 4(m_O D_{O_2})^{1/2} = 5.937 \times 10^{-17} \text{ gm cm/sec}$$

$$t^* = (m_O/D_{O_2})^{1/2}/4\beta_{O_2}$$

$$= 1.6795 \times 10^{-15} \text{ sec}$$

and

$$L^* = 64(m_O D_{O_2})^{1/2}/\beta_{O_2}$$

$$= 5.707 \times 10^{-23} \text{ gm cm}^2/\text{sec}$$

We feel it to be much more instructive to quote results for a single member of the set of models which satisfy the chosen values of a, b, and c. In the remainder of the article, familiar units will be employed as they apply to the chosen member of the set. It should be borne in mind that the dynamical results given below are therefore more general than the accompanying discussions imply.

4. The Small Vibration Approximation (SVA)

4.1. Assumptions in the SVA

It is necessary that we discuss these assumptions in some detail in order to understand the nature of the errors introduced when we apply it to large vibrations. Let us use the M_3 molecular model, described in the Introduction, to demonstrate how the SVA equations are derived. In M_3, all the masses are the same and will be denoted by m without a subscript. Similarly, all the force constants and equilibrium internuclear distances will be denoted by k and r^{eq} respectively. With these parameters, the equations of motion (3.1.-8) and (3.1.-9) for this model become

$$\underset{\sim}{\dot{P}}_1 = (2\underset{\sim}{P}_1 - \underset{\sim}{P}_3)/3m \qquad (4.1.-1)$$

$$\underset{\sim}{\dot{P}}_3 = (2\underset{\sim}{P}_3 - \underset{\sim}{P}_1)/3m \qquad (4.1.-2)$$

$$\underset{\sim}{\dot{P}}_1 = -k[(r_1 - r^{eq})\underset{\sim}{r}_1/r_1 + (r_2 - r^{eq})\underset{\sim}{r}_2/r_2 + 2(r_3 - r^{eq})\underset{\sim}{r}_3/r_3] \qquad (4.1.-3)$$

$$\dot{P}_3 = -k[2(r_1 - r^{eq})\underset{\sim}{r}_1/r_1 - (r_2 - r^{eq})\underset{\sim}{r}_2/r_2 + (r_3 - r^{eq})\underset{\sim}{r}_3/r_3] . \qquad (4.1.-4)$$

The internuclear vectors, $\underset{\sim}{r}_i$, are

$$\underset{\sim}{r}_1 = \underset{\sim}{X}_1 + 2\underset{\sim}{X}_3$$

$$\underset{\sim}{r}_2 = \underset{\sim}{X}_1 - \underset{\sim}{X}_3 \qquad (4.1.-5)$$

$$\underset{\sim}{r}_3 = 2\underset{\sim}{X}_1 + \underset{\sim}{X}_3$$

and the corresponding distances, r_i, are

$$r_i = |\underset{\sim}{r}_i| = (\underset{\sim}{r}_i \cdot \underset{\sim}{r}_i)^{1/2} \quad . \qquad (4.1.-6)$$

Due to the presence of the r_i in equations (4.1.-3) and (4.1.-4), which are non-linear in the X_i, equations (4.1.-1) through (4.1.-4) cannot be solved analytically.

If we define a "displacement vector," $\underset{\sim\sim}{\Delta X}_i$, such that

$$\underset{\sim}{X}_i = \underset{\sim\sim}{\Delta X}_i + \underset{\sim}{X}_i^{eq} , \qquad (4.1.-7)$$

and substitute all $\underset{\sim}{X}_i$ in equations (4.1.-1) through (4.1.-4) by the rhs of (4.1.-7), the resulting equations are still not soluble analytically. However, if we make the basic assumption of the SVA, namely that all $\underset{\sim\sim}{\Delta X}_i / r^{eq}$ are so small that we may ignore terms of order $(\Delta X_i / r^{eq})^2$ or higher, which arise in expansions of functions of ΔX_i, the problem reduces to a linear one.

At time t = 0, let the molecular plane be coincident with the X - Y plane in our center-of-mass reference system. If we force the nuclei to stay in this plane (by having the initial values of the Z component of their velocities vanish) we may omit the equations involving the Z components of $\underset{\sim}{X}_i$ and $\underset{\sim}{P}_i$. In that event, we may define the column vectors

$$\mathbb{X} = \begin{pmatrix} \Delta X_1 \\ \Delta Y_1 \\ \Delta X_3 \\ \Delta Y_3 \end{pmatrix} \qquad (4.1.-8)$$

$$\mathbb{P} = \begin{pmatrix} P_{1_X} \\ P_{1_Y} \\ P_{3_X} \\ P_{3_Y} \end{pmatrix} \qquad (4.1.-9)$$

in terms of which the SVA form of the equations of motion (4.1.-1) through (4.1.-4) becomes

$$\dot{\mathbb{X}} = /\!\mathbb{A}\ \mathbb{P}/3m \qquad (4.1.-10)$$

$$\dot{\mathbb{P}} = -k\,\mathbb{B}\ /r^{eq\,2}\ . \qquad (4.1.-11)$$

The fourth order square symmetric matrices $/\!\mathbb{A}$ and $\mathbb{B}$ are easily seen to be given by

$$/\!\mathbb{A} = \begin{pmatrix} 2 & 0 & -1 & 0 \\ 0 & 2 & 0 & -1 \\ -1 & 0 & 2 & 0 \\ 0 & -1 & 0 & 2 \end{pmatrix} \qquad (4.1.-12)$$

and $\mathbb{B} = (b_{ij})$ i, j = 1, 2, 3, 4 where the b_{ij} are functions of the $\underset{\sim i}{X}^{eq}$ components given in Appendix 1. By making convenient choices for the $\underset{\sim i}{X}^{eq}$, $\mathbb{B}$ simplifies appreciably, without loss of generality. Let the initial equilibrium positions for the nuclei of M_3 be such that nucleus 2 lies on the positive Y axis and nuclei 1 and 3 are symmetric with respect to this axis as indicated in Figure 1. In this case

$$X_1^{eq} = -X_3^{eq} = e = r^{eq}/2$$

and

$$Y_1^{eq} = Y_3^{eq} = -d = -\sqrt{3}\, r^{eq}/6 \ . \qquad (4.1.-13)$$

With this choice for the equilibrium configuration, $\mathbb{B}$ becomes

$$\mathbb{B} = \begin{pmatrix} 9e^2 & -9ed & 0 & 0 \\ -9ed & 45d^2 & 0 & 36d^2 \\ 0 & 0 & 9e^2 & 9ed \\ 0 & 36d^2 & 9ed & 45d^2 \end{pmatrix} \qquad (4.1.-14)$$

Substituting equation (4.1.-11) into (4.1.-10), one obtains

$$\ddot{\mathbb{X}} = -k\mathbb{C}\mathbb{X}/m \ , \qquad (4.1.-15)$$

where

$$\mathbb{C} = \mathbb{A}\,\mathbb{B}/3r^{eq\,2} \qquad (4.1.-16)$$

FIG. 1. Equilibrium configuration of M_3.

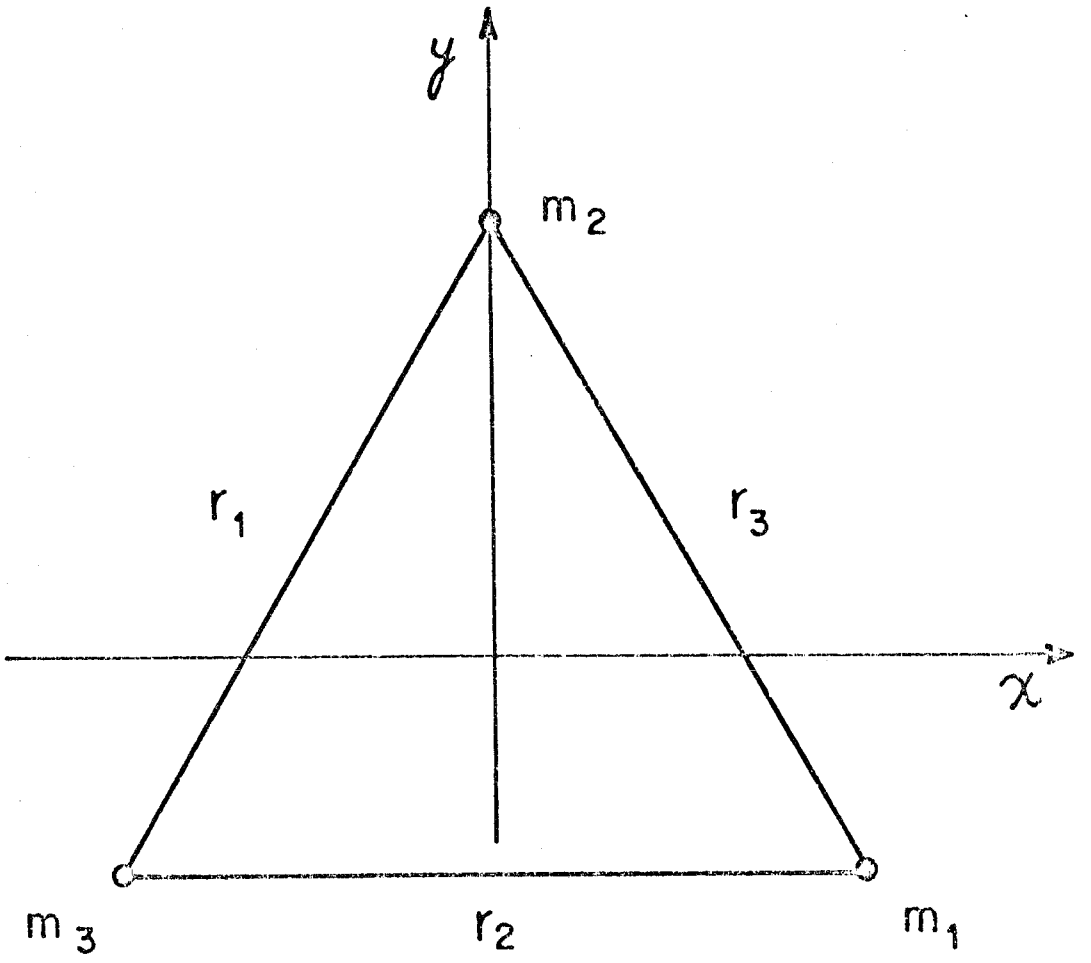
y
m 2
r 1
r 3
x
m 3
r 2
m 1

$$\mathbb{C} = \frac{3}{r^{eq\ 2}} \begin{pmatrix} 2e^2 & -2ed & -e^2 & -ed \\ -2ed & 6d^2 & -ed & 3d^2 \\ -e^2 & ed & 2e^2 & 2ed \\ ed & 3d^2 & 2ed & 6d^2 \end{pmatrix} \qquad (4.1.-17)$$

Equation (4.1.-15) is a form of the SVA equations of motion equivalent to equations (4.1.-10,11).

A consequence of the small vibration approximation is that when it is applied to large vibrations, it violates conservation of angular momentum. Indeed, let the row vectors of $\mathbb{C}$ be defined by

$$\mathbb{C}_i = (C_{i1} \quad C_{i2} \quad C_{i3} \quad C_{i4}) \qquad (4.1.-18)$$

$$\text{for } i = 1,\ 2,\ 3,\ 4\ .$$

It can be seen from (4.1.-17) that

$$3d\,\mathbb{C}_1 + e\,\mathbb{C}_3 + 3d\,\mathbb{C}_3 - e\,\mathbb{C}_4 = 0\ . \qquad (4.1.-19)$$

The rows of $\mathbb{C}$ are not linearly independent. Thus for any given $\divideontimes$, there exists a linear dependence among the components of $\ddot{\divideontimes}$ obtained through equation (4.1.-15), viz.,

$$3d\Delta\ddot{X}_1 + e\Delta\ddot{Y}_1 + 3d\Delta\ddot{X}_3 - e\Delta\ddot{Y}_3 = 0\ . \qquad (4.1.-20)$$

Integrating equation (4.1.-20)once with respect to time, there results

$$-(2Y_1^{eq} + Y_3^{eq})\Delta\dot{X}_1 + (2X_1^{eq} + X_3^{eq})\Delta\dot{Y}_1 - (Y_1^{eq} + 2Y_3^{eq})\Delta\dot{X}_3$$

$$+ (X_1^{eq} + 2X_3^{eq})\Delta\dot{Y}_3 = \alpha \qquad (4.1.-21)$$

where α is an integration constant determined by the initial conditions of a given trajectory.

On the other hand, for the planar motion being considered, the only non-vanishing component of the angular momentum (3.2.-5) of M_3 is the $\hat{Z}$ one, and it is given by

$$L_Z = 2(X_1\dot{Y}_1 - Y_1\dot{X}_1) + 2(X_3\dot{Y}_3 - Y_3\dot{X}_3) + (X_1\dot{Y}_3 - Y_1\dot{X}_3)$$

$$+ (X_3\dot{Y}_1 - Y_3\dot{X}_1) \; . \qquad (4.1.-22)$$

Substitution of equations (4.1.-7) into (4.1.-22) gives

$$L_Z = [-(2Y_1^{eq} + Y_3^{eq})\Delta\dot{X}_1 + (2X_1^{eq} + X_3^{eq})\Delta\dot{Y}_1 - (Y_1^{eq} + 2Y_1^{eq})\Delta\dot{X}_3$$

$$+ (X_1^{eq} + 2X_3^{eq})\Delta\dot{Y}_3] + [-(2\Delta Y_1 + \Delta Y_3)\Delta\dot{X}_1 + (2\Delta X_1 + \Delta X_3)\Delta\dot{Y}_1$$

$$- (\Delta Y_1 + 2\Delta Y_3)\Delta\dot{X}_3 + (\Delta X_1 + 2\Delta X_3)\Delta\dot{Y}_3] \; . \qquad (4.1.-23)$$

Substitution of (4. 1. -21) into (4. 1. -23) yields

$$L_Z = \alpha + [-(2\Delta Y_1 + \Delta Y_3)\Delta\dot{X}_1 + (2\Delta X_1 + \Delta X_3)\Delta\dot{Y}_1$$

$$- (\Delta Y_1 + 2\Delta Y_3)\Delta\dot{X}_3 + (\Delta X_1 + 2\Delta X_3)\Delta\dot{Y}_3] . \quad (4. 1. -24)$$

For vanishingly small ΔX_1, ΔY_1, ΔX_3, ΔY_3, the bracket in the equation above vanishes and $\alpha = L_Z$. However, for non-vanishing Δ's, that bracket is non-zero and time dependent, even if we use, in its evaluation, the Δ's obtained from solving the SVA equations of motion. If we call α the SVA angular momentum, equation (4. 1. -21) says that α, rather than L_Z given by equation (4. 1. -23) is a constant of the motion.

As a result of (4. 1. -21), we can reduce the number of independent component equations implied in (4. 1. -15) from four to three. Indeed, taking initial conditions for which the first integration constant $\alpha = 0$ (i.e., no SVA angular momentum) and the second integration constant is zero (27), the integrated form of equation (4. 1. -21) becomes

$$-(2Y_1^{eq} + Y_3^{eq})\Delta X_1(0) + (2X_1^{eq} + X_3^{eq})\Delta Y_1(0) - (Y_1^{eq} + 2Y_3^{eq})\Delta X_3(0)$$

$$+ (X_1^{eq} + 2X_3^{eq})\Delta Y_3(0) = 0. \quad (4. 1. -25)$$

If we substitute equations (4. 1. -13) into the integrated form of equation (4. 1. -21), we get that at all times

$$\Delta Y_3 = \sqrt{3}\ \Delta X_1 + \Delta Y_1 + \sqrt{3}\ \Delta X_3 . \quad (4. 1. -26)$$

Therefore, eliminating the equation for ΔY_3 and defining $\mathbb{X}'$ as

$$\mathbb{X}' = \begin{pmatrix} \Delta X_1 \\ \Delta Y_1 \\ \Delta X_3 \end{pmatrix} \qquad (4.1.-27)$$

we obtain

$$\ddot{\mathbb{X}}' = -k\mathbb{D}\mathbb{X}'/m \qquad (4.1.-28)$$

where

$$\mathbb{D} = \begin{pmatrix} 3/4 & -3\sqrt{3}/4 & -3/2 \\ \sqrt{3}/4 & 9/4 & \sqrt{3}/2 \\ 3/4 & 3\sqrt{3}/4 & 3 \end{pmatrix} \qquad (4.1.-29)$$

The problem is summed up in equations (4.1.-28) and (4.1.-26). We have merely to uncouple these linear differential equations to solve the problem in the SVA.

4.2. Normal Mode Co-ordinates and Energies for M_3

We choose a mass weighted displacement vector, $\mathbb{q} = \sqrt{m}\,\mathbb{X}'$ for convenience in describing the energies below. We must then solve

$$\ddot{\mathbb{q}} = - k \, \mathbb{D} \, \mathbb{q} / m \ . \qquad (4.2.-1)$$

This system of equations can be separated into three independent ones by an adequately chosen linear transformation from the variables q_i to the variables $Q_i (i = 1, 2, 3)$. Such a transformation

$$\mathbb{Q} = \mathbb{N}^{-1} \mathbb{q} \qquad (4.2.-2)$$

must diagonalize $\mathbb{D}$, reducing equation (4.2.-1) to

$$\ddot{\mathbb{Q}} = -k(\mathbb{N}^{-1} \mathbb{D} \, \mathbb{N}) \mathbb{Q}/m = -k \, \mathbb{\Lambda} \mathbb{Q}/m. \qquad (4.2.-3)$$

The matrices $\mathbb{N}$ and $\mathbb{\Lambda}$ can be obtained by the usual matrix diagonalization methods (28), and the final results are

$$\mathbb{N} = \begin{pmatrix} 1/2 & 0 & \sqrt{3}/3 \\ -\sqrt{3}/6 & \sqrt{3}/3 & 0 \\ -1/2 & -1/2 & -\sqrt{3}/6 \end{pmatrix} \qquad (4.2.-4)$$

and $(\mathbb{\Lambda})_{ij} = \lambda_i \, \delta_{ij}$ where $\lambda_1 = 3$ and $\lambda_2 = \lambda_3 = 3/2$. These results separate equation (4.2.-3) into

$$\ddot{Q}_1 = -3k \, Q_1/m$$

$$\ddot{Q}_2 = -3k \, Q_2/2m \qquad (4.2.-5)$$

and

$$\ddot{Q}_3 = -3k \, Q_3/2m \ .$$

Because $\lambda_2 = \lambda_3$, the second and third normal mode eigenvectors are degenerate. Any linear combination of Q_2 and Q_3 results in an acceptable normal mode. The pair of Q_2 and Q_3 which come from the matrix, equation (4.2.-4) , were not chosen with any special symmetry considerations in mind. Some linear combination of Q_2 and Q_3 will result in a new pair Q_2' and Q_3', which have C_{2v} (bend) and asymmetric stretch symmetries. These primed normal mode co-ordinates will be discussed in Section 4.3.2. Equations (4.2.-5) are readily integrated to give

$$Q_i = A_i \cos 2\pi(\nu_i t + \delta_i) \qquad (4.2.-6)$$

where

$$\nu_i = (\lambda_i k/m)^{1/2}/2\pi$$

and A_i and δ_i are integration constants to be determined by the molecule's initial conditions.

Multiplication of $\ddot{Q}_i = -k\lambda_i Q_i/m$ by $\dot{Q}_i$ followed by a single integration results in

$$2\epsilon_i = \dot{Q}_i^2 + k\lambda_i Q_i/m \qquad (4.2.-7)$$

where the ϵ_i are integration constants and therefore constants of the motion. They may be related to the A_i through application of equation (4.2.-6) and its first derivative to equation (4.2.-7) . There results

$$A_i = (2m\epsilon_i/k\lambda_i)^{1/2} \quad . \qquad (4.2.-8)$$

From the relations given, it can be shown (see Appendix 1) that the kinetic energy

$$2T = \sum_{i=1}^{3} \dot{Q}_i^2 \qquad (4.2.-9)$$

and the potential energy

$$2V = k \sum_{i=1}^{3} \lambda_i Q_i^2 \ . \qquad (4.2.-10)$$

Thus the total energy of the system, in the SVA, is the sum of the constant normal mode energies

$$E = \sum_{i=1}^{3} \epsilon_i \ . \qquad (4.2.-11)$$

When the complete Hamiltonian equations of motion, (3.1.-8,9) , for harmonic triatomic molecules are integrated numerically (see Section 5.1.) from initial conditions consistent with the SVA, i.e., very small normal mode amplitudes, A_i, from very small normal mode energies, ϵ_i, the resulting displacement co-ordinates approximately obey the relation (4.1.-26) . For example, when M_3 is one-third of 0.01 D_O in each of its normal modes, equation (4.1.-26) gives Y_3 s which are slightly different from those obtained from the trajectories. These former,

SVA to Y_3 s can be used to define a configuration for the molecule. The bond lengths in this SVA configuration differ from those in the actual configuration by only about 0.4%. Furthermore, the normal mode co-ordinates and velocities, Q_i and $\dot{Q}_i$, resulting from the trajectory calculated $\underset{\sim\sim}{\Delta X}_i$ yield normal mode energies, ϵ_i, which are constants of the motion. However, when the molecular energies approach those necessary for reaction, the solution of the actual equations of motion give $\underset{\sim\sim}{\Delta X}_i$ which produce normal mode energies which are no longer even approximately constant in time. For example, when the initial normal mode energies (see Section 5.2.1.) in M_3 are each one-third D_{O_2} (totalling one-half the dissociation energy for M_3), the trajectory calculation gives normal mode energies which show large fluctuations, peaking, for one mode, at over 20 D_{O_2} ! In addition, their sum deviates from the initial energy by as much as 33 D_{O_2}. It should be noted that this does <u>not</u> mean that conservation of total energy is violated. The numerical integration of the equations of motion conserves that energy to about 5 digits (see Section 5.1.4.). The large fluctuations in the total normal mode energy imply that the total energy becomes a small difference between large normal mode energies and large normal mode interaction energies. Therefore, the concept of normal mode energies looses its utility under these conditions.

In this high energy example, the SVA configuration of the molecule, taken from the Y_3 approximated by equation (4.1.-26), has bond lengths which differ by more than 5% from those in the actual configuration.

This complete failure of the SVA stems, in part, from the fact that the small vibration angular momentum does not remain constant for the large displacements of the nuclei resulting from the high energy vibrations. Part of the fluctuation of the ϵ_i with time can be eliminated by choosing a system of molecular (or body-fixed) axes which actually rotate or oscillate with respect to the laboratory-fixed axes. The molecular axes may be chosen in such a way as to reduce the length of the displacement vectors measured in the body-fixed system. Several different ways of doing this have been devised. One such system (29) uses the molecule's instantaneous principal axes of inertia. Another is the Eckart (30) system, which will be discussed in the next section.

4.3. Normal Mode Analysis for the General Bent Harmonic Triatomic Molecule

4.3.1. Eckart Rotating Axes

Let us consider a general non-linear harmonic triatomic molecule consisting of three mass points pairwise interconnected by three massless harmonic springs. As seen in Section 4.2. that, partly as a consequence of the incorrectly assumed constancy of the approximate SVA angular momentum, the constancy of the normal mode energies breaks down, when the vibration amplitudes of the symmetric M_3 molecule are not vanishingly small. This breakdown is independent of the triangular symmetry of M_3 and should occur for any non-linear molecule. Eckart (30) has defined a system of reference which rotates with the molecule, so as to minimize the values of the displacement co-ordinates, components of the $\underset{\sim}{\Delta X}_i$. This system is useful not only when the molecule is actually rotating but also when its angular momentum is zero. In this case, Eckart's axes follow the apparent rocking of the molecule which results from large vibration amplitudes.

The equation defining the Eckart axes is (31b)

$$\sum_{i=1}^{3} m_i \left(\underset{\sim}{x}_i^{eq} \times \underset{\sim}{x}_i\right) = 0 \qquad (4.3.1.-1)$$

where $\underset{\sim}{x}_i$ is the position vector of nucleus i in the Eckart (rotating/center-of-mass) system. It should be noted that $\underset{\sim}{x}_i$ and $\underset{\sim}{X}_i$ are geometrically the <u>same</u> vector (connecting the center-of-mass with

nucleus i). The different notation indicates that when we represent them in column matrix form, the elements of $\underset{\sim}{X}_i$ are its components in the laboratory system whereas those of $\underset{\sim}{x}_i$ are the Eckart ones. The equilibrium position vectors, $\underset{\sim}{x}_i^{eq}$, in the Eckart system have the same components as did the $\underset{\sim}{X}_i^{eq}$ (of Section 3.1.) in the laboratory system. Therefore $\underset{\sim}{x}_i^{eq}$ and $\underset{\sim}{X}_i^{eq}$ represent vectors which are geometrically <u>different</u>, and although the $\underset{\sim}{x}_i^{eq}$ are independent of time (meaning that the corresponding equilibrium position are fixed in the Eckart system), they move with the Eckart axes with respect to the laboratory ones. With the other molecules to be discussed in this paper, as with M_3, the $\underset{\sim}{x}_i^{eq}$ will be completely defined by requiring that $z_1^{eq} = z_3^{eq} = 0$ and that $\underset{\sim}{x}_1^{eq} - \underset{\sim}{x}_3^{eq} = \underset{\sim}{r}_2^{eq}$ be parallel to and in the same sense as the $\underset{\sim}{x}$ unit vector.

The transformation from $\underset{\sim}{X}_i$ to $\underset{\sim}{x}_i$ is achieved by a rotation matrix, U, such that

$$\underset{\sim}{x}_i = U \underset{\sim}{X}_i \ . \qquad (4.3.1.-2)$$

U is obtained by substituting this equation into (4.3.1.-1) and requiring the resultant expression to be valid for all $\underset{\sim}{X}_i$ at all times. The elements of this three by three matrix involve the three Euler angles (31c) θ, φ, and ψ, which relate the (center-of-mass) laboratory axes to the instantaneous Eckart axes. Using the conventions of Wilson, Decius, and Cross (31a), hereinafter referred to as WDC, we have

$$U = U_\psi U_\theta U_\varphi \qquad (4.3.1.-3)$$

where

$$U_{\psi} = \begin{pmatrix} \cos\psi & \sin\psi & 0 \\ -\sin\psi & \cos\psi & 0 \\ 0 & 0 & 1 \end{pmatrix}$$

$$U_{\theta} = \begin{pmatrix} \cos\theta & 0 & -\sin\theta \\ 0 & 1 & 0 \\ \sin\theta & 0 & \cos\theta \end{pmatrix}$$

and

$$U_{\varphi} = \begin{pmatrix} \cos\varphi & \sin\varphi & 0 \\ -\sin\varphi & \cos\varphi & 0 \\ 0 & 0 & 1 \end{pmatrix} .$$

For a planar molecule, we make the Eckart $\hat{z}$ axis be perpendicular to the instantaneous plane of the molecule. Then the θ and φ Euler angles are simply the spherical polar angles of $\hat{z}$ in the laboratory XYZ system. The unit vector, $\hat{z}$, is given by

$$\hat{z} = \frac{X_3 \times X_1}{|X_3 \times X_1|} = \sin\theta\cos\varphi\,\hat{X} + \sin\theta\sin\varphi\,\hat{Y} + \cos\theta\,\hat{Z} \qquad (4.3.1.-4)$$

from which θ and φ and therefore U_{θ} and U_{φ} are uniquely determined in terms of the laboratory co-ordinates of the nuclei. The remaining Euler angle, ψ, can be obtained from the Eckart condition (4.3.1.-1) . Let us define

$$\underset{\sim}{X}_i'' = \cup_\theta \cup_\varphi \underset{\sim}{X}_i \ . \qquad (4.3.1.-5)$$

As can easily be verified, the $\underset{\sim}{X}_i''$ vectors lie in the plane of the molecule, as do the $\underset{\sim}{x}_i$ and the $\underset{\sim}{X}_i$. From (4.3.1.-2) , (4.3.1.-3) and (4.3.1.-5) we have

$$\underset{\sim}{x}_i = \cup_\psi \underset{\sim}{X}_i'' \qquad (4.3.1.-6)$$

and therefore

$$x_i = X_i'' \cos\psi + Y_i'' \sin\psi$$

$$y_i = -X_i'' \sin\psi + Y_i'' \cos\psi \qquad (4.3.1.-7)$$

and

$$z_i = Z_i'' = 0 \ .$$

Substitution of (4.3.1.-7) into (4.3.1.-1) yields

$$\psi = \arctan(n/d) \qquad (4.3.1.-8)$$

where

$$n = \sum_{i=1}^{3} m_i (x_i^{eq} Y_i'' - y_i^{eq} X_i'') \qquad (4.3.1.-9)$$

and

$$d = \sum_{i=1}^{3} m_i (x_i^{eq} X_i'' + y_i^{eq} Y_i'') \ . \qquad (4.3.1.-10)$$

Thus, given the instantaneous center-of-mass laboratory co-ordinates of the nuclei of the molecule, $\underset{\sim}{X}_i$, and the co-ordinates of its equilibrium configuration, $\underset{\sim}{x}_i^{eq}$, all the Euler angles for the Eckart axes are specified up to an additive π in ψ.

The choice between $0 \leq \psi < \pi$ and $\pi \leq \psi < 2\pi$ can be made as follows. Rotation of $\underset{\sim}{x}_i$ by π about $\hat{\underset{\sim}{z}}$ gives $-\underset{\sim}{x}_i$ since $\underset{\sim}{x}_i$ has no $\hat{\underset{\sim}{z}}$ component. Then

$$\sum_{i=1}^{3} m_i \left[\underset{\sim}{x}_i^{eq} \times (-\underset{\sim}{x}_i)\right] = 0$$

if and only if equation (4.3.1.-1) holds. However, the displacement vectors

$$\underset{\sim\sim}{\Delta x}_i = \underset{\sim}{x}_i - \underset{\sim}{x}_i^{eq} \qquad (4.3.1.-11)$$

will be very sensitive to which of the two values satisfying (4.3.1.-1) we choose. We could do it in such a way that these $\underset{\sim\sim}{\Delta x}_i$ are as small as possible. For convenience, we have chosen between the two values of ψ by taking the one which maximizes $\underset{\sim}{x}_1 \cdot \underset{\sim}{x}_1^{eq} + \underset{\sim}{x}_3 \cdot \underset{\sim}{x}_3^{eq}$, thereby insuring that the $\underset{\sim}{x}_i$ lie near and not opposed to the $\underset{\sim}{x}_i^{eq}$.

4.3.2. Normal Mode Co-ordinate Transformation

For the triatomic molecules considered, a normal mode analysis was made according to the powerful G F method (31d). The results of this treatment follow below. Let Q be the three by one column vector whose elements are Q_1, Q_2, and Q_3, the normal mode co-ordinates in the Eckart system. (As usual, the kinetic and potential energies of the molecule in this system are sums of square terms in the $\dot{Q}_i$ and Q_i respectively. The vector is given by

$$Q = L^{-1} M \Delta X = (LN')^{-1} \Delta X .$$

Similarly

$$\dot{Q} = (LN')^{-1} \Delta \dot{X} . \qquad (4.3.2.-1)$$

Here, ΔX is the three by one column vector whose elements are Δx_1, Δy_1, Δx_3. Δy_3 is determined from them by the Eckart condition (4.3.1.-1) . Clearly, the elements of $\Delta \dot{X}$ are $\Delta \dot{x}_1$, $\Delta \dot{y}_1$, and $\Delta \dot{x}_3$. The $\Delta \dot{y}_3$ comes from the first derivative of equation (4.3.1.-1) . The L and M are three by three matrices defined in terms of the force constants, masses, and equilibrium configuration of the molecule. Associated to the L matrix there is a three by three diagonal Λ matrix, whose diagonal elements are λ_1, λ_2, and λ_3, related to the normal mode frequencies according to

$$\lambda_i = 4\pi^2 \nu_i^2 . \qquad (4.3.2.-2)$$

The procedure we follow for determining the normal mode co-ordinates is as follows. Once the molecular parameters are chosen, we determine $\mathbb{L}$, $\mathbb{M}$, and $/\!/\!\Lambda$ as described in Appendix 2. We then solve the equations of motion for chosen initial conditions by the numerical procedures described in Section 5. 2. and determine the laboratory vectors $\mathcal{X}$ and $\dot{\mathcal{X}}$ as a function of time. Substitution of this result for $\mathcal{X}$ into (4. 3. 1. -2) and (4. 3. 1. -11) furnishes the Eckart displacement vector $\Delta\mathcal{X}$ as a function of time, according to (4. 3. 1. -1) . The $\Delta\dot{\mathcal{X}}$ follow from the differentiation of equations (4. 3. 1. -6) . The required $\dot{X}_i''$ and $\dot{\psi}$ expressions will be derived in Section 5. 3. below.

When the λ_i are not all different, a certain ambiguity arises in the definition of the corresponding Q_i. We have seen that for M_3, for example, $\lambda_2 = \lambda_3$ (Section 4. 2.). If we use the Q_2 and Q_3 defined by equations (4. 2. -2) and (A1-9) , except that we replace the lab. displacement vectors by the corresponding Eckart ones, any linear combination of Q_2 and Q_3 furnish new normal mode co-ordinates of the same frequency. To lift this arbitrariness in this case, it is customary to choose Q_2 and Q_3 so as to make them correspond to motions with certain symmetries. For example, in the M_3 case, just mentioned, one can impose the condition that Q_2 correspond to a (C_{2v}) symmetric bend and Q_3 correspond to an asymmetric stretch. The procedure for obtaining the corresponding $\mathbb{L}$ is given in Appendix 2. With this choice, equations (4. 2. -2) and (A1-9) get replaced by

$$\mathcal{Q} = (\mathbb{N}')^{-1}\,\Delta\mathcal{X} \qquad (4.3.2.-3)$$

where

$$(\mathbb{N}')^{-1} = \sqrt{m}\begin{pmatrix} -1 & -\sqrt{3} & -2 \\ -2 & -\sqrt{3} & -1 \\ -\sqrt{3} & 0 & \sqrt{3} \end{pmatrix} \quad . \qquad (4.3.2.-4)$$

These are the normal mode co-ordinates of M_3 used in most of the M_3 calculations, to be discussed in Section 7. It should be noted that the last two rows of $(\mathbb{N}')^{-1}$ are linear combinations of the corresponding ones of $\mathbb{N}^{-1}$ given in equation (A1-9).

5. Molecular Energies

5.1. Normal Mode Energies

The normal mode energies, mentioned in Section 4.2., are the ϵ_i given by

$$2\epsilon_i = \dot{Q}_i^2 + \lambda_i Q_i^2 \quad (i=1,2,3) . \qquad (5.1.-1)$$

In the SVA, the ϵ_i are constants of the motion and sum to the total Eckart vibration energy (see Section 5.3.)

$$\sum_{i=1}^{3} \epsilon_i \xrightarrow[\text{lim SVA}]{} T_v + V . \qquad (5.1.-2)$$

As rotation of the molecule is expected to be coupled with the internal vibrations, Slater's assumption of constancy of the ϵ_i is expected to fail for <u>two</u> reasons: the presence of high amplitude vibrations and of vibration-rotation coupling. Both these effects will be considered in subsequent sections.

5.2. Bond Energies

The RRKM treatment requires that the sum of oscillator energies be constant in time. If the oscillators are taken to be normal modes, this amounts to assuming that $\sum_{i=1}^{3} \epsilon_i$ is a good constant of the motion. The RRKM oscillators are often associated with the molecule's bonds. Some intuitive definition of bond energy

would be useful to test the RRKM assumption for this choice of oscillators.

Let us define the energy of bond i as

$$E_i = T_{B_i} + V_i \qquad (5.2.-1)$$

where the V_i are given in equation (3.1.-14) and T_{B_i} is the kinetic energy of bond i given by

$$2T_{B_i} = \mu_i | (\dot{\underset{\sim}{x}}_k - \dot{\underset{\sim}{x}}_j) \cdot \underset{\sim}{\rho}_i |^2 \qquad (5.2.-2)$$

where i, j, k is a cyclic permutation of 1, 2, 3, $\underset{\sim}{\rho}_i$ is a unit vector along the bond i between atoms k and j, and μ_i is the reduced mass of this bond:

$$\mu_i = m_j m_k / (m_j + m_k) \ . \qquad (5.2.-3)$$

It should be noticed that $(\dot{\underset{\sim}{x}}_k - \dot{\underset{\sim}{x}}_j) \cdot \underset{\sim}{\rho}_i$ is simply the component of the Eckart velocity of atom k with respect to atom j along the bond i connecting these two atoms. The expression is equal to the speed with which the length of this bond changes. We call it the bond velocity.

Equation (5.2.-2) gives the same T_{B_i} when the vectors in it are measured in either the center-of-mass laboratory or the Eckart rotating reference frame. Indeed, the relation between the corresponding velocities is

$$\dot{\underset{\sim}{X}}_i = \dot{\underset{\sim}{x}}_i - \underset{\sim}{\omega} \times \underset{\sim}{x}_i \qquad (5.2.-4)$$

where $\underset{\sim}{\omega}$ is the instantaneous angular velocity of the Eckart axes with respect to the laboratory ones. Therefore,

$$\dot{\underset{\sim}{X}}_j - \dot{\underset{\sim}{X}}_k = \dot{\underset{\sim}{x}}_j - \dot{\underset{\sim}{x}}_k - r_i \, (\underset{\sim}{\omega} \times \underset{\sim}{\rho}_i) \; . \qquad (5.2.-5)$$

The bond velocity in terms of the laboratory nuclei velocities is

$$(\dot{\underset{\sim}{X}}_j - \dot{\underset{\sim}{X}}_k) \cdot \underset{\sim}{\rho}_i = (\dot{\underset{\sim}{x}}_j - \dot{\underset{\sim}{x}}_k) \cdot \underset{\sim}{\rho}_i - r_i \, (\underset{\sim}{\omega} \times \underset{\sim}{\rho}_i) \cdot \underset{\sim}{\rho}_i$$

$$= (\dot{\underset{\sim}{x}}_j - \dot{\underset{\sim}{x}}_k) \cdot \underset{\sim}{\rho}_i \qquad (5.2.-6)$$

and the independence of T_{B_i} on the system of reference is an immediate consequence of this expression and equation (5.2.-2) .

The terms V_i in equation (5.2.-1) are the pairwise potentials of the problem, defined by equation (3.1.-14) . At all times, their sum is the total potential energy of the molecule. Unfortunately, the bond kinetic energies do not necessarily sum to the molecule's total vibrational kinetic energy, T_v (see Section 5.3.). A decomposition of the atomic velocities resulting from various normal mode kinetic energies in M_3 shows that $T_B = \sum_{i=1}^{3} T_{B_i}$ will differ with T_v by +50%, +41%, -40%, and +13%, when the normal modes excited are Q_1, Q_2, Q_3, and when all three modes have equal excitation energy, respectively. In this calculation, the molecule was assumed to be at its equilibrium configuration, i.e.,

all the normal mode energy was kinetic. With this assumption, the percentages given above are independent of total energy, which means that the % error in the T_B will not go to zero in the limit of small vibration amplitudes. Consequently, it is expected that the sum of the bond energies, E_i, will differ from that of the normal mode energies, ϵ_i, as well as from the total vibrational energy, $E_v = T_v + V$ (see Section 5.3.). Whether ΣE_i or $\Sigma \epsilon_i$ are better approximate constants of the motion can be determined only from an exact solution to the dynamic problem. This was done in this paper, and the results are described in Section 7.1.

Improvements might be made in the definition of the T_{B_i} so as to bring their sum into closer agreement with T_v. For example, one might weight the quantities $\dot{\underset{\sim}{x}}_i \cdot \underset{\sim}{\rho}_j$ and $\dot{\underset{\sim}{x}}_i \cdot \underset{\sim}{\rho}_k$ by the factors, f_i, defined by

$$f_i^2 \left[\mu_j (\dot{\underset{\sim}{x}}_i \cdot \underset{\sim}{\rho}_j)^2 + \mu_k (\dot{\underset{\sim}{x}}_i \cdot \underset{\sim}{\rho}_k)^2\right] = m_i \dot{\underset{\sim}{x}}_i^2 \qquad (5.2.-7)$$

in an attempt to decompose the Eckart energy $\frac{1}{2} m_i \dot{\underset{\sim}{x}}_i^2$ into the energies of the two bonds involving atom i. Such a decomposition should result in T_{B_i} sums closer to the T_v than did those of the previous definition, but it would do so at the expense of violating the spirit of the RRKM oscillators. If we are trying to associate them with the molecule's bonds, we do not want to use a non-local definition like (5.2.-7), wherein the energy in bond i lying between nuclei j and k is dependent on velocity vector of nucleus i.

In neither of the above definitions do the component velocities along adjacent bonds always add up to the velocity of the common atom. This is a result of the perpendicular projections in equations (5.2.-2) and (5.2.-7) . Only when these adjacent bonds meet at right angles will perpendicular projections yield components which sum to the original vector. An alternative atomic velocity decomposition, using projections parallel to bond i when calculating components along adjacent bond j, will make the component velocities sum correctly. This velocity analysis must be carried out in the Eckart system to avoid rotational "contamination" in the bond energies. Though this parallel projection scheme makes the bond component velocities sum to the atomic velocities, it still does not necessarily sum the bond energies to the total vibration energy, E_v. This bond energy definition is also non-local, as it makes i'th bond energy dependent on i'th nucleus position.

Hereafter in this paper, "bond energy" will be taken with reference to equation (5.2.-2) .

5.3. Eckart Energies

The total kinetic energy of the molecule can be expressed in terms of the co-ordinates and velocities of the nuclei with respect to the Eckart axes and the angular velocity of these axes with respect to the laboratory system (31e). This expression is

$$T = T_v + T_r + T_{vr} \qquad (5.3.-1)$$

where T_v, T_r, and T_{vr} are the kinetic energies of vibration, rotation, and vibration-rotation interaction (i.e., Coriolis energy) respectively, given by

$$2T_v = \sum_{i=1}^{3} m_i \dot{\underset{\sim}{x}}_i \cdot \dot{\underset{\sim}{x}}_i \qquad (5.3.-2)$$

$$2T_r = \sum_{i=1}^{3} m_i (\underset{\sim}{\omega} \times \underset{\sim}{x}_i) \cdot (\underset{\sim}{\omega} \times \underset{\sim}{x}_i) \qquad (5.3.-3)$$

and

$$T_{vr} = \underset{\sim}{\omega} \cdot \sum_{i=1}^{3} (\Delta \underset{\sim}{x}_i \times \dot{\underset{\sim}{x}}_i) \, . \qquad (5.3.-4)$$

The vector $\underset{\sim}{\omega}$ is the angular velocity vector of the rotating Eckart axes with respect to the laboratory ones. It can be expressed as

$$\underset{\sim}{\omega} = \omega_x \hat{\underset{\sim}{x}} + \omega_y \hat{\underset{\sim}{y}} + \omega_z \hat{\underset{\sim}{z}} \qquad (5.3.-5)$$

where the $\hat{\underset{\sim}{x}}$, $\hat{\underset{\sim}{y}}$, and $\hat{\underset{\sim}{z}}$ are the unit vectors of the Eckart system, and the corresponding components ω_x, ω_y, and ω_z of $\underset{\sim}{\omega}$ are given by (31e)

$$\begin{aligned} \omega_x &= \dot{\theta} \sin\psi - \dot{\varphi} \sin\theta \cos\psi \\ \omega_y &= \dot{\theta} \cos\psi + \dot{\varphi} \sin\theta \sin\psi \\ \omega_z &= \dot{\varphi} \cos\theta + \dot{\psi} \, . \end{aligned} \qquad (5.3.-6)$$

The expressions for θ, φ, and ψ in terms of the instantaneous laboratory co-ordinates of the nuclei are given in equations (4.3.1.-4) and (4.3.1.-8) . Differentiation of these equations leads to the following expressions for $\dot{\theta}$, $\dot{\varphi}$, and $\dot{\psi}$:

$$\begin{aligned}\hat{\underset{\sim}{Z}} = &(-\dot{\theta}\cos\theta\cos\varphi + \dot{\varphi}\sin\theta\sin\varphi)\,\hat{\underset{\sim}{X}} \\ &+ (\dot{\theta}\cos\theta\sin\varphi + \dot{\varphi}\sin\theta\cos\varphi)\,\hat{\underset{\sim}{Y}} \\ &- \dot{\theta}\sin\theta\,\hat{\underset{\sim}{Z}}\end{aligned} \qquad (5.3.-7)$$

and

$$\dot{\psi} = \frac{d\dot{n} - n\dot{d}}{d^2}\cos^2\psi \qquad (5.3.-8)$$

where

$\dot{n}$ and $\dot{d}$ refer to time derivatives of equations (4.3.1.-9) and (4.3.1.-10). The components of the $\underset{\sim}{X}_i''$, appearing in those equations, are given by (4.3.1.-5)

$$\begin{aligned}X_i'' &= X_i\cos\theta\cos\varphi + Y_i\cos\theta\sin\varphi - Z_i\sin\theta \\ Y_i'' &= -X_i\sin\varphi + Y_i\cos\varphi \\ Z_i'' &= 0\end{aligned} \qquad (5.3.-9)$$

and because of the constancy of the $\underset{\sim}{x}_i^{eq}$ in equations (4.3.1.-9, 10), we need only

$$\dot{X}_i'' = \dot{X}_i \cos\theta\cos\varphi - X_i(\dot{\theta}\sin\theta\cos\varphi + \dot{\varphi}\cos\theta\sin\varphi)$$
$$+ \dot{Y}_i \cos\theta\sin\varphi + Y_i(\dot{\theta}\cos\theta\cos\varphi - \dot{\varphi}\sin\theta\sin\varphi) \qquad (5.3.-10)$$
$$- \dot{Z}_i \sin\theta + Z_i \dot{\theta}\cos\theta$$

$$\dot{Y}_i'' = -\dot{X}_i\sin\varphi - X_i\dot{\varphi}\cos\varphi + \dot{Y}_i\cos\varphi - Y_i\dot{\varphi}\sin\varphi \ .$$

Consequently, the $\dot{X}_i''$ and $\dot{Y}_i''$ are now known in terms of the X_i and $\dot{X}_i$. As a result, so is $\dot{\psi}$.

All the energies to be discussed in this paper have now been defined in terms of the center-of-mass laboratory coordinates and velocities (or momenta).

6. Numerical Methods

6.1. Adams-Moulton Integration

6.1.1. Definition

The numerical integration of the twelve first-order, coupled, differential equations of motion (3.1.-8, 9) was carried out with an Adams-Moulton 5th Order Predictor (32)/6th Order Corrector integrator. The Adams-Moulton method (33) involves a difference polynomial approximation to each first order differential equation. Let $u_i = u_i(t)$ be defined by a first-order differential equation

$$\dot{u}_i = du_i/dt = g_i(U, t) \qquad (6.1.1.-1)$$

where $U = u_1, u_2, \ldots, u_{i-1}, u_i, u_{i+1}, \ldots, u_N$. Thus, in order to solve (6.1.1.-1) we must simultaneously solve the other N-1 equations as well. For notational convenience, let $y = u_i$. The Adams-Moulton n'th order Predictor makes use of the last n values of $\dot{y}$ taken at successive equal intervals, $h = \Delta t$, of the independent variable, t. The value of the dependent variable, y, at step $t = t_0 + (m+1)h$, is predicted to be y^*_{m+1} according to

$$y^*_{m+1} = y_m + h(a_{n+1}\dot{y}_m + a_n\dot{y}_{m-1} + \ldots + a_1\dot{y}_{m-n}). \qquad (6.1.1.-2)$$

This predicted value, y^*_{m+1}, is used in equation (6.1.1.-1) to obtain the predicted value, $\dot{y}^*_{m+1}$, as

$$\dot{y}^*_{m+1} = g_i(U^*_{m+1}, t_{m+1}) \qquad (6.1.1.-3)$$

where the U^*_{m+1} are also predicted values at t_{m+1}. The corrected value, y^c_{m+1}, is taken to be

$$y^c_{m+1} = y_m + h(b_{n+2}\dot{y}^*_{m+1} + b_{n+1}\dot{y}_m + \ldots + b_1\dot{y}_{m-n}). \quad (6.1.1.-4)$$

The coefficients a_i and b_i are determined in Appendix 3.

The y^c_{m+1} could be considered a new prediction for y_{m+1} and as such it could be recycled through equations (6.1.1.-3,4) any number of times. This procedure will converge not to the correct answer, but to the best n'th order approximation thereto. In practice, only one correction cycle is employed.

6.1.2. Truncation Error Analysis

Let us look at the prediction of the y_{n+1} value, assuming that all the $\dot{y}_j (j=0, 1, 2, \ldots, n)$ are correct. Equation (6.1.1.-2) becomes

$$y^*_{n+1} = y_n + h(a_{n+1}\dot{y}_n + \ldots + a_1\dot{y}_0) . \qquad (6.1.2.-1)$$

We may perform a Taylor series expansion for $\dot{y}_j$ in terms of the higher derivatives of $\dot{y}$ taken at j=0. Since the intervals in the independent variable, t, are all the same size, h,

$$\dot{y}_j = \dot{y}_0 + \frac{(jh)}{1!}\ddot{y}_0 + \frac{(jh)}{2!}\dddot{y}_0 + \cdots \qquad (6.1.2.-2)$$

Substitution of equation (6.1.2.-2) into (6.1.2.-1) will give an expression for $\Delta y^* = y^*_{n+1} - y_n$ in terms of powers of (jh) times derivatives of y about time zero.

The true value of Δy (if y is a sufficiently well-behaved function) may be obtained from the difference of two other Taylor series

$$y_j = y_0 + \sum_{k=1}^{\infty} \frac{(jh)^k}{k!} \frac{\partial^k y}{\partial t^k}\bigg|_{t=0} \quad (j=n, n+1)\,. \qquad (6.1.2.-3)$$

Thus

$$\Delta y = y_{n+1} - y_n = \sum_{k=1}^{\infty} \frac{h^k}{k!}[(n+1)^k - n^k] \frac{\partial^k y}{\partial t^k}\bigg|_{t=0} \qquad (6.1.2.-4)$$

where, for example, $\partial^3 y/\partial t^3\big|_{t=0} = \dddot{y}_0$. When equation (6.1.2.-4) is compared term by term with its approximation, Δy^*, described below equation (6.1.2.-2), the n'th order Adams-Moulton Predictor is validated up to the h^{n+2} term. This error analysis is independent of the nature of the differential equation (6.1.1.-1) as long as it yields well-behaved y's.

If we were to continue this standard approach to analyze the error in the corrector, we would run into difficulty. $y^*_{n+1} = y_n + \Delta y^*$ would have to be passed through equation (6.1.1.-1), and

the Taylor series expansion for Δy^* would become unmanageable in the resultant expression for $\dot{y}^*_{n+1}$ unless the differential equation were some simple polynomial in y. Coupling of the other dependent variables, U, in the differential equation (6.1.1.-1) would invalidate this procedure altogether. This error analysis therefore terminates at the predictor level.

6.1.3. 5th Order Predictor/6th Order Corrector

The coefficients for this, the Adams-Moulton routine used in this work, are given in Table 2. When the 5th order predictor coefficients, $a_i^{(5)}$, are used in the error analysis described in Section 6.1.2., the 5th order predictor is shown to have a truncation error of

$$\frac{19087}{60480} h^7 \frac{\partial^7 y}{\partial t^7} \Bigg| \; t_{m-n} < t < t_m \; . \qquad (6.1.3.-1)$$

The seventh derivative may be thought of as having its maximum value over the range of the preceding five integration steps.

In order to test the accuracy of the methods used a 5th order Predictor/5th order Corrector was given the correct $\dot{y}$ table for

$$\dot{y} = 2\pi \cos 2\pi t \qquad (6.1.3.-2)$$

beginning at $t_0 = -2^{-4}$ and taking intervals of $h = \Delta t = 2^{-5}$ through $t_5 = 3 \times 2^{-5}$. The integrator was allowed to take a single predictor/

Table II. Predictor/Corrector Coefficients for the Adams-Moulton Differential Equation Solver Used in this Work.
(See Section 6.1.)

	i		1	2	3	4	5	6	7
1440	$a_i^{(5)}$	=	-475	2877	-7298	9982	-7923	4277	-----
60480	$b_i^{(6)}$	=	-863	6312	-20211	37504	-46461	65112	19087

corrector step. Equation (6. 1. 3. -1) gave an expected predictor accuracy of about $5\frac{1}{2}$ decimal digits for $y(t=2^{-3})$, whereas the integration step gave y to better than $6\frac{1}{2}$ digits. When the step size was reduced to $h = \Delta t = 2^{-8}$, the expected predictor accuracy (12 digits) and the actual predictor/corrector performance (13 digits) were again very close to one another.

Stepping the order of the corrector up by one unit to 6th, takes advantage of all the past values of $\dot{y}$ available to the integrator at a given step, but it does not markedly improve accuracy. From tests other than equation (6. 1. 3. -2), the Adams-Moulton routine with 6th order correction was observed to make less than 1/2 digit improvement over accuracy obtained with the 5th order corrector.

6. 1. 4. Application to Trajectory Study

The Adams-Moulton (AM) integrator of Section 6. 1. 3. was applied to the solution of the dimensionless Hamilton differential equations (3. 1. -8, 9) altered as per Section 3. 2.). A corresponding program was written for an IBM 7094 in 16 decimal digit, floating-point arithmetic (double precision). The double precision arithmetic was found to be necessary in order to delay the growth of round-off error in the integration and in consequence allow us to follow trajectories over many (100) molecular vibration periods. The first five integration steps were taken with a routine which does not require a table of past values of derivatives. This "self-starting" integrator was a 16 decimal digit Runge-Kutta-Gill (34) 4th order integrator (RKG). The RKG was given a step size 1/2 that of the AM routine, which took over from it. This difference in step size

matched the accuracy of the starting routine to that of the AM. The starter RKG was not used for the remainder of the integration because (a) it required twice as many integration steps to maintain the same accuracy as AM, (b) the basic integrator algebra in RKG took almost twice as long to execute for a single step as did that of the AM, but primarily, (c) RKG required twice as many evaluations of derivatives (four) as did AM (two). All these considerations conspired to outweigh RKG's major advantage: its ability to change step size at every step, if necessary.

As suggested by the form of equation (6.1.3.-1) , integrator accuracy is a function of the size of the derivatives of the dependent variables. In trajectory calculations, these derivatives are small when the forces are small and large when the forces are large. Near turning points in the nuclei trajectories, where forces are the highest, the integrator time step sizes should be smaller than when the nuclei are near their equilibrium positions. Changes in integration interval step size require re-starting of AM routines. RKG, not being dependent on tables of past values, can be given different step sizes at each integration cycle. This property was not found to be sufficiently compensatory to warrant the use of the slower integrator.

The AM 5th Order Predictor/6th Order Corrector integrated 1000 steps in all 12 equations of motion in 28 seconds. Typical trajectories involved 4000 steps or less than 2 minutes on the computer.

The accuracy of the integration was determined in a number of ways. Since angular momentum vectors and total energy are rigorous constants of the motion, their values were monitored during the course of the integration. These values were typically conserved

to 0.001% or better. Conservation of the momentum components was usually better than conservation of total energy. However, conservation of these quantities was found to be a necessary but insufficient condition for accuracy of the co-ordinates and momenta.

Hamilton's equations of motion satisfy time reversal. Therefore, a necessary condition for trajectory accuracy is that, under a reversal of all momenta at the end of an integration, the initial positions and momenta should be recovered on integrating in reverse for a number of steps equal to that in the forward integration. From the anharmonic analogs to these equations of motion (15), it was found that recovery of 4 or 5 significant figures indicated that the trajectory had been accurate to 3 significant figures in the forward integration. This was determined by reducing step sizes until the final molecular co-ordinates and momenta were independent of step size. In these tests it was observed that energy and angular momentum conservation were satisfied at larger step sizes than was convergence of the final co-ordinates and momenta.

From the anharmonic analogs, a linear loss of significant digits was observed during the integration. The harmonic trajectories exhibited strange error propagation characteristics. The rate of loss of digits (measured by the rate of divergence of the reverse integration from the forward one) was a monotone descending rather than constant function of number of time steps. We have not found a satisfactory explanation for this behavior. It was not observed in the harmonic trajectories integrated by Bunker (13). The difference may lie in the fact that his computer word length was twice ours.

When an M_3 (harmonic) trajectory was initiated (see Section 6.2.1.) from normal mode energies of $\epsilon_1 = \epsilon_2 = \epsilon_3 = 40$ kcal/mole, and integrated for 3.36×10^{-12} seconds (molecule time) at a step size of 0.84×10^{-15} seconds for a total of 4000 integration steps, momentum reversal lead to recovery of 4 decimal digits of the initial co-ordinates and momenta. Thus the integration could probably have been trusted to 6.72×10^{-12} seconds (8000 steps) with similar accuracy.

6.2. Trajectory Initialization

In order to integrate the equations of motion (3.1.-8, 9) one needs initial values for the twelve quantities X_1, Y_1, Z_1, X_3, Y_3, Z_3, P_{1_X}, P_{1_Y}, P_{1_Z}, P_{3_X}, P_{3_Y}, P_{3_Z} corresponding to desired initial properties. In the following subsections, we describe the methods used to calculate those initial values in terms of different kinds of initial properties. Initially, the molecule is taken to lie in the X-Y laboratory plane, and the Eckart and laboratory axes are coincident without loss of generality. Hence $Z_1(0) = Z_3(0) = 0$. The equilibrium position vectors, $\underset{\sim}{x}_i^{eq}$, are taken such that $\underset{\sim}{r}_2^{eq}$ is parallel to and in the same sense as $\underset{\sim}{x}$. Figure 1 shows the equilibrium configuration of M_3. Figure 2 shows the equilibrium configuration (and normal modes) of nitrosyl chloride. In both cases, it is clear that $y_1^{eq} = y_3^{eq} < 0$.

FIG. 2. Equilibrium configuration and Normal Modes of $ClNO^{18}$. Arrows represent distortion of the molecule due to normal mode motion at 8 times the dissociation energy.

ω_A

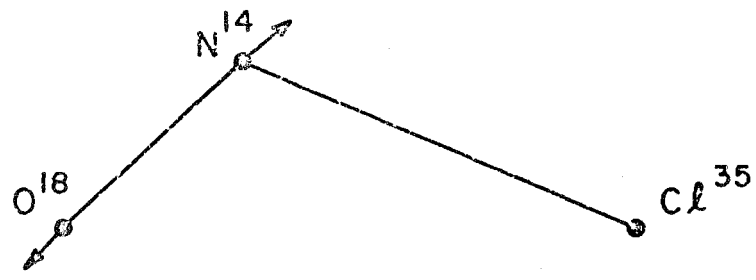

ω_B

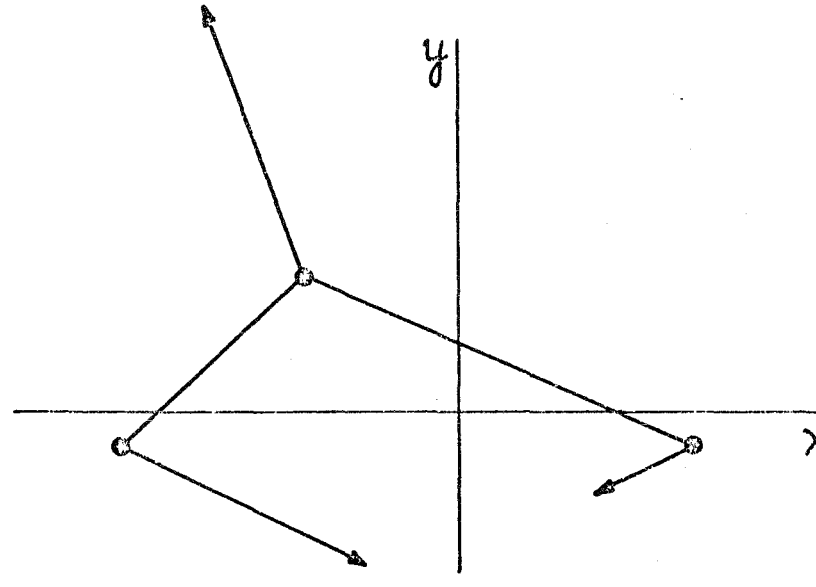

ω_S

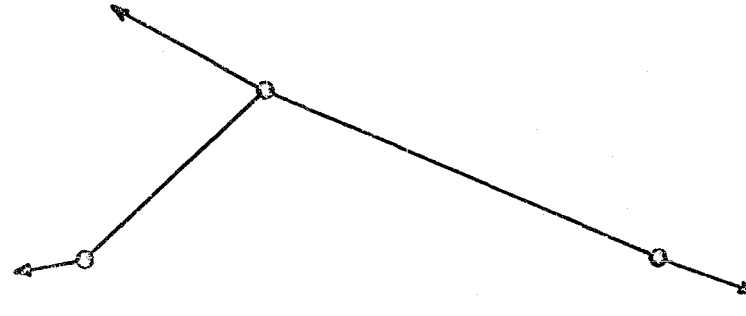

6.2.1. Normal Mode Energies

For each normal mode, i,

$$\epsilon_i = T_{Q_i} + V_{Q_i} \qquad (6.2.1.-1)$$

where

$$2T_{Q_i} = \dot{Q}_i^2 \qquad \text{and} \qquad 2V_{Q_i} = \lambda_i Q_i^2 . \qquad (6.2.1.-2)$$

In the SVA

$$Q_i = (2\epsilon_i/\lambda_i)^{1/2} \cos(\lambda_i^{1/2} t + \delta_i) \qquad (6.2.1.-3)$$

where the δ_i are arbitrary phase angles depending on initial conditions. By definition of the δ_i we make equation (6.2.1.-3) valid at t=0 even for large vibrations. (This does not imply that δ_i or ϵ_i are independent of t for such vibrations.) Therefore,

$$\sin \delta_i = \pm (T_{Q_i}/\epsilon_i)^{1/2}$$

$$\cos \delta_i = \pm (V_{Q_i}/\epsilon_i)^{1/2} . \qquad (6.2.1.-4)$$

We may choose the signs in the above equations arbitrarily. Once this is done, $T_{Q_i}(0)$ and $V_{Q_i}(0)$ determine $Q_i(0)$ and $\dot{Q}_i(0)$ uniquely.

In all the calculations reported in this paper, we made $T_{Q_i}(0) = 0$, $V_{Q_i}(0) = \epsilon_i$, and $\delta_i(0) = 0$. The resultant $Q_i(0)$ yield initial values of $\Delta\mathcal{K}$ through equation (4.3.2.-1). The initial values of the x_1, y_1, x_3, and y_3 follow from equation (4.3.1.-11). By the coincidence of the Eckart and lab. axes, $\underset{\sim}{X}_i(0) = \underset{\sim}{x}_i(0)$. In general, the Eckart axes are rotating with respect to the laboratory ones and

$$\dot{\underset{\sim}{X}}_i(0) = \dot{\underset{\sim}{x}}_i(0) + \underset{\sim}{\omega} \times \underset{\sim}{x}_i(0) \quad . \qquad (6.2.1.-5)$$

The angular velocity vector, $\underset{\sim}{\omega}$, is calculated from the expression for total laboratory angular momentum, $\underset{\sim}{L}$.

Expressing the components of $\underset{\sim}{L}$ in the Eckart system, we may write (31f)

$$\underset{\sim}{L} = \mathrm{II}\,\underset{\sim}{\omega} + \sum_{i=1}^{3} m_i (\underset{\sim}{x}_i \times \dot{\underset{\sim}{x}}_i) \qquad (6.2.1.-6)$$

where II is the moment of inertia matrix, whose elements are defined in terms of the Eckart axes. Equation (6.2.1.-6) can be rearranged to give

$$\underset{\sim}{\omega} = \mathrm{II}^{-1} [\, \underset{\sim}{L} + \sum_{i=1}^{3} m_i (\dot{\underset{\sim}{x}}_i \times \underset{\sim}{x}_i) \,], \qquad (6.2.1.-7)$$

which, with equation (6.2.1.-5) completes the initialization of trajectories from normal mode kinetic and potential energies. Note that when $\underset{\sim}{L} = 0$ and $\dot{\underset{\sim}{x}}_i \neq 0$, $\underset{\sim}{\omega} = 0$ only under the special configurations which render $\sum_{i=1}^{3} m_i(\underset{\sim}{x}_i \times \dot{\underset{\sim}{x}}_i) = 0$. In general, $\underset{\sim}{\omega} \neq 0$ even when $\underset{\sim}{L} = 0$, and the Eckart system rocks with respect to the laboratory system in this case. The $\underset{\sim}{P}_i$ can be obtained from the $\dot{\underset{\sim}{X}}_i$ through (3.1.-2). In the following section, we show how to pick $\underset{\sim}{\omega}$ to give a desired initial rotational energy around a chosen axis.

6.2.2. Rotational Energies

For non-rigid rotors like our triatomic molecules, the definition of rotational energy depends on the choice of rotating co-ordinate axes. Regardless of that choice, the rotational energy is not usually a constant of the motion. It is coupled to the molecule's vibrations because the latter make the moments of inertia be functions of time. Given an instantaneous configuration for the molecule and the Eckart velocity vectors of the nuclei, one can find an angular velocity, $\underset{\sim}{\omega}$, around some chosen axis defined by the unit vector $\hat{\underset{\sim}{\omega}}$ such that the instantaneous rotational energy, T_r, has a desired value. Then,

$$\underset{\sim}{\omega} = \left[\sum_{i=1}^{3} m_i (\hat{\underset{\sim}{\omega}} \times \underset{\sim}{x}_i)^2 / 2T_r \right]^{1/2} \hat{\underset{\sim}{\omega}} . \qquad (6.2.2.-1)$$

Substitution of equation (6.2.2.-1) into (6.2.1.-5) gives the initial nuclei velocities consistent with the chosen energy and axis of rotation.

7. Results and Discussion

7.1. Normal Mode and Bond Energies in the Absence of Rotation

The Slater and RRK theories mentioned in the introduction assume rotation has a negligible effect on the rates of intramolecular energy transfer in unimolecular reactions. In Section 7.2., we will investigate that assumption. Here we study the dynamics of molecules undergoing vibrations only. These studies will suffice to check the validity of the small coupling and small vibration approximations.

The initialization of all trajectories to be discussed in Section 7.1. is accomplished by giving the molecules varying amounts of normal mode potential energy (see Section 6.2.1.). This results in, initially, in-phase vibrations of the normal modes. In the notation of Section 6.2.1., $\delta_i = 0$ $(i = 1, 2, 3)$.

7.1.1. Small Amounts of Vibrational Energy

We initially tested the accuracy of the SVA by introducing into the molecules zero point energies in each of their three normal modes. The parameters for these molecules were taken from the literature (35) and the pertinent ones are summarized in Table I. The molecules studied were divided into two categories. The first contained all the C_{2v} molecules H_2O, D_2S, H_2Se, F_2O, NO_2, and SO_2, and the C_s molecule HOD, which still has a C_{2v} configuration and force field. The second category consisted of the asymmetric FOO and ClNO[18] molecules. The classification

criterion was not the symmetry but the dynamic behavior, as seen below.

The zero point vibration of H_2O exemplified the characteristics of the C_{2v} molecules. The total initial normal mode (potential) energy was 13.43 kcal/mole. Without resorting to any dynamics whatsoever, the total energy of the molecule ($E = \frac{1}{2} \sum_{i=1}^{3} m_i \dot{X}_i^2 + \frac{1}{2} \sum_{i=1}^{3} k_i [r_i - r_i^{eq}]^2$) may be calculated. It is found to be 14.65 kcal/mole. The difference in these energies, 1.22 kcal/mole, is called the normal mode energy defect or normal mode interaction energy and is itself a measure of the initial failure of the SVA for non-linear molecules. The non-zero defect is a direct result of the approximate expressions (A1-2) for internuclear distances implied in getting normal mode energies from displacement co-ordinates. If the molecule were linear, those expressions would have been correct and the energy defect would be zero.

The O-H bond distances, obtained from solving the equations of motion, are given as functions of time in Figure 3a. These bond distances appear to exchange amplitude with one another. They seem to behave as do tuned, coupled pendulums (36) when one is started swinging while the other is at rest. The pendulums exchange the total energy available, and, as is seen in Figure 3b, the O-H bonds in the water molecule do the same. Thus, our intuitive definition of bond energy (see Section 5.2.) is shown to represent the gross behavior of the bonds adequately.

The pendulum analogy is a good one, for it suggests the mechanism for this exchange. When weakly coupled pendulums are started swinging with energy in only one of the normal modes for

FIG. 3. Zero-point energy dynamics of H_2O. τ_{sym} is the symmetric stretch vibration period of 7.62×10^{-15} seconds for the model.

a. Bond Lengths ——— OH, – – – OH, — – — HH.

b. Bond Energies. HH omitted for clarity.

c. Kinetic energy of vibration.

d. Normal Mode Energies. ——— symmetric stretch, – – – asymmetric stretch, — – — bend.

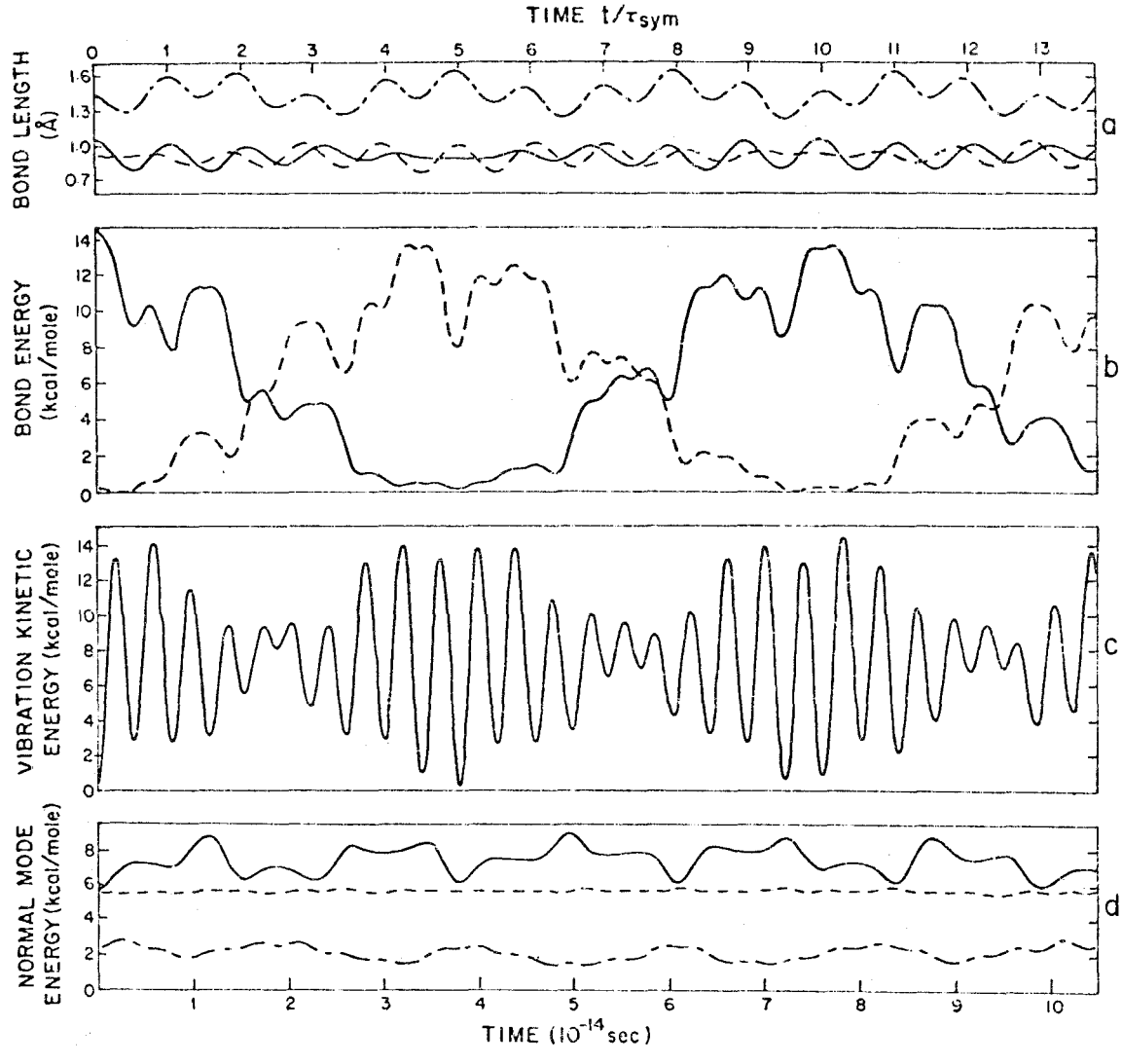
TIME t/τ_{sym}
0 1 2 3 4 5 6 7 8 9 10 11 12 13
BOND LENGTH (Å)
1.6
1.3
1.0
0.7
a
BOND ENERGY (kcal/mole)
14 12 10 8 6 4 2 0
b
VIBRATION KINETIC ENERGY (kcal/mole)
14 12 10 8 6 4 2 0
c
NORMAL MODE ENERGY (kcal/mole)
8 6 4 2 0
d
1 2 3 4 5 6 7 8 9 10
TIME (10^{-14} sec)

that system, no energy transfer between the pendulums takes place. It is only when two normal modes are excited that the pendulum energy exchange occurs, and it results from the beat frequency (i.e., frequency difference) between the two modes.

The normal modes in the water molecule which have the strongest effect on the r_1, r_3 bond lengths are the symmetric and asymmetric stretches. The pendulum analogy would predict that those bonds should exchange energy with the period of 7.5×10^{-14} seconds, which is associated with the symmetric-asymmetric beat frequency of $1.33 \times 10^{+13}$ seconds^{-1}. This is precisely the observed bond energy exchange period. The phenomenon will persist, even under the perturbation of the bending motion, as long as the symmetric and asymmetric mode energies are good constants of the motion. The vibrational kinetic energy of the molecule, T_v, shown in Figure 3c clearly demonstrates the beat. When the energy of one of the O-H bonds is zero, T_v oscillates with twice the frequency of the excited bond. The factor two comes from the existence of two turning points in the bond oscillation. As the other bond becomes equally excited, the O-H bonds oscillate $\pi/2$ out-of-phase with one another, such that the sum of the nuclear kinetic energies is approximately constant. Since the O-H bonds acquire equal energy twice in every beat cycle, the envelope of T_v has twice the beat frequency.

From Figure 3d it is clear that even at zero point energies, normal mode energies are <u>not rigorously</u> conserved! However, the fluctuations in normal mode energies are small (less than about $\pm$ 10%) relative to the total energy. There appears to be no long-term exchange of energy among the normal modes. The ordering

of their energies is conserved, i.e., symmetric stretch always has the most and bend the least energy. The short-term (10^{-14} second) derivations in the normal mode energies are clearly not large enough to obscure the bond energy beat. Thus, the dynamics of the harmonic zero point vibrating water molecule are approximately described by the SVA.

The bond energy beat phenomenon, described above, is observed in all the C_{2v} molecules studied, and it is not a function of their symmetry properties. It follows from the fact that the ω_{sym} and ω_{asym} frequencies happen to be close to one another in these molecules. This propinquity insures beat frequencies much lower than and well separated from the vibration fundamentals.

When the mass symmetry is broken, as in HOD, the character of the zero point motion is not significantly altered. Figure 4a shows that the dynamics has now become a detuned coupling problem (36). The O-H and O-D bonds do not exchange the total amount of energy available to them, but they still wax and wane with an overall period (5.6×10^{-14} seconds) which is related to the symmetric/asymmetric beat period (2.8×10^{-14} seconds) and the asymmetric/bend beat period (1.87×10^{-14} seconds). The periodicity of bond energy exchange observed in Figure 4b is due to the frequency difference in these two beat frequencies. Thus, the two beat frequencies themselves beat against one another to produce the bond energy exchange period.

The initial normal mode energy defect in zero point vibrating HOD between the total energy (12.80 kcal/mole) and the total initial normal mode energy (11.63 kcal/mole) is about 1.17 kcal/mole. This is very close to what it was in H_2O, so we anticipate that the normal mode energies in HOD will show a similar

behavior to that in the former molecule. Figure 4c verifies this expectation. Note that the sum of the normal mode energies is a much better "constant" of the motion than the sum of the bond energies (Figure 4b). The bond energy sum is in error by as much as 60% with respect to the total energy, whereas the sum of normal mode energies deviates from the total energy by less than 10% of the latter. If the RRKM oscillators are construed to be the internuclear bonds, then they appear to be strongly coupled (i.e., have a large bond interaction energy) even in the small vibration limit. Since the potential for the problem is a pairwise one, the choice of the three internuclear distances as bond oscillators is an obvious one. If instead of using the r_2 (H-D) distance, which does not correspond to a bond in the HOD molecule, we had chosen the bond angle opposite r_2 as one of the oscillators, the angle energy would have been like that of the bending normal mode, i.e., nearly constant. Use of this bond angle energy would improve the constancy of the sum of bond energies only if the sum of the r_1 and r_3 bond energies was nearly constant. From Figure 4b, it can be seen that this is not the case. Thus, neither internuclear nor valence bond energies sum to the total energy of the molecule. At least for the small, zero point vibrations considered up to now, the RRKM oscillators should be associated with the normal modes. This insures small coupling energies and oscillator energies which approximately sum to the total energy.

The two asymmetric molecules ClNO[18] (35c) and FOO (35d) fall into the second category of small vibration dynamics. Only the latter exhibited any long-term periodicity---a period of 5.25×10^{-13} seconds arising from the beating of fundamental asymmetric stretch against first overtone bend. The lack of

FIG. 4. Zero-point energy dynamics of HOD. τ_{sym}, the symmetric stretching period for the model is 7.99×10^{-15} seconds.

a. Bond Lengths ——— OH, – – – OD, — – — HD.

b. Bond Energies. — – – — sum of the three bond energies.

c. Normal Mode Energies. — symmetric stretch, – – – asymmetric stretch, — – — bend, — – – — sum of normal mode energies.

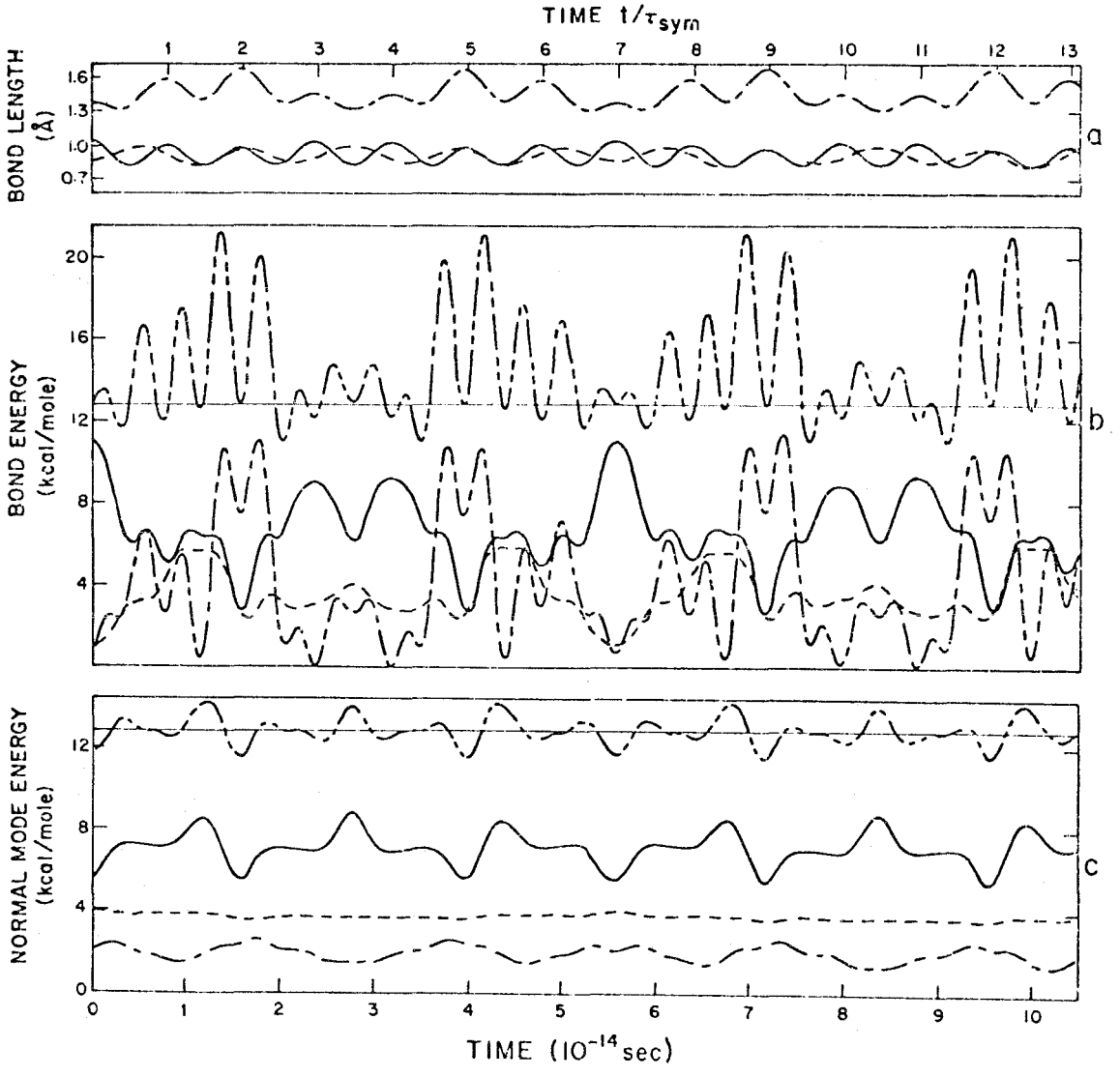
TIME t/τ_{sym}
1 2 3 4 5 6 7 8 9 10 11 12 13
BOND LENGTH (Å)
1.6
1.3
1.0
0.7
a
BOND ENERGY (kcal/mole)
20
16
12
8
4
b
NORMAL MODE ENERGY (kcal/mole)
12
8
4
0
c
0 1 2 3 4 5 6 7 8 9 10
TIME (10^{-14} sec)

periodicity in these molecules is due to their widely separated fundamental frequencies. These provide high frequency beats which are lost in the fundamentals themselves. Both of these molecules have very low bending force constants and one very high stretching force constant. They both correspond to an atom (Cl and F, respectively) loosely attached to a strongly bound diatom (NO and O_2, respectively). Their molecular vibrations are expected to consist of low amplitude, high frequency vibration of the strongly bound diatom and high amplitude, low frequency motion of all other parts of the molecule. It is the latter, loose vibrations which are expected to render the normal mode description of the molecule a poor one.

Nitrosyl chloride containing oxygen-18 (to maximize the mass differences) was given zero point energy in each of its normal modes for a total normal mode energy of 3.7 kcal/mole. The corresponding total energy was 4.6 kcal/mole. As shown in Figure 5c, within 4×10^{-13} seconds (about 20 asymmetric stretch periods) the bending mode (see Figure 2 for a diagram of the $ClNO^{18}$ normal modes) had extracted sufficient energy from the symmetric stretching mode to yield bend amplitudes large enough to cause an erratic behavior of the asymmetric stretch energy. For comparison, $ClNO^{18}$ was given 1/10 of its zero point energy in its normal modes. The resulting normal mode energies were good constants of the motion, showing fluctuations of only a few percent.

These studies indicate that we should not expect <u>rigorous</u> constancy of molecular normal mode energies even for zero point energies in these modes. For the set of molecules studied, the normal mode energies were constant to within $\pm$ 1.5 kcal/mole.

FIG. 5. Zero-point energy dynamics of $ClNO^{18}$. τ_{asym}, the asymmetric stretch period for the model, is 1.905×10^{-14} seconds.

a. Bond Lengths. —— NO^{18}, – – – ClO^{18}, — — — NCl.

b. Bond Energies. — — — — sum of bond energies.

c. Normal Mode Energies. —— asymmetric stretch, – – – symmetric stretch, — — — bend, — — — — sum of normal mode energies.

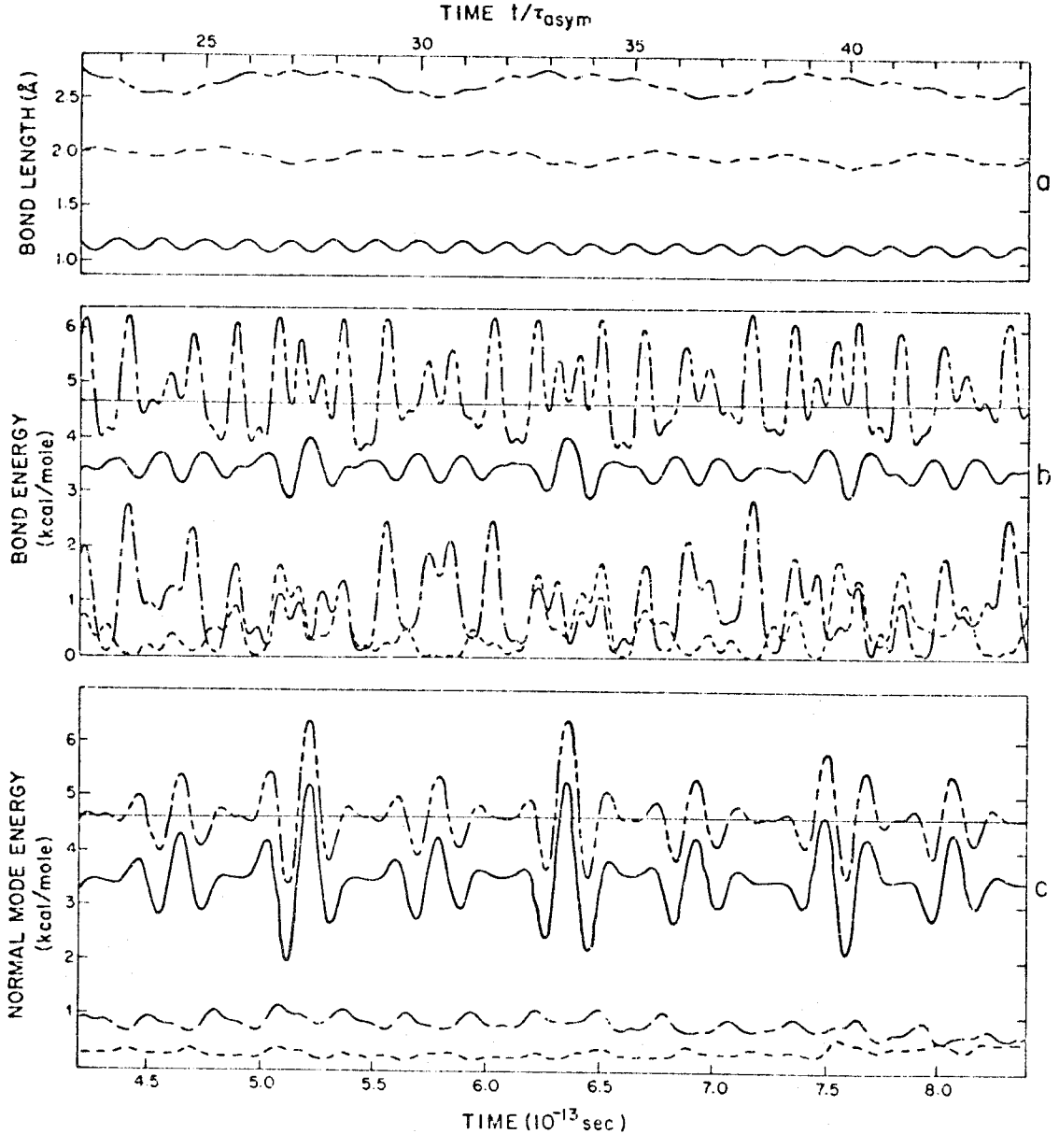
TIME t/τ_{asym}
25
30
35
40
BOND LENGTH (Å)
2.5
2.0
1.5
1.0
a
BOND ENERGY (kcal/mole)
6
5
4
3
2
1
0
b
NORMAL MODE ENERGY (kcal/mole)
6
5
4
3
2
1
c
4.5
5.0
5.5
6.0
6.5
7.0
7.5
8.0
TIME (10^{-13} sec)

Thus, the small vibration approximation furnishes an approximate description of the zero point energy mechanics. However, the fluctuations observed in the normal mode energies could be of importance in the quantum mechanical case as well and therefore in the interpretation of vibrational spectra.

7.1.2. Large Amounts of Vibrational Energy in M_3

In order to investigate the dynamics of molecules at energies approaching those necessary for reaction, the rigid, symmetric M_3 and the loose, asymmetric $ClNO^{18}$ molecules were given half their respective dissociation energies in four ways. First, all this energy was put into one mode at a time, and the dynamics of an initially pure normal mode vibration were followed. Then the same energy was partitioned equally among the three normal modes. In all cases, as in the previous section, normal mode energy was input as normal mode potential energy. Thus, the equipartition energy input resulted in normal modes initially in-phase. The results for $ClNO^{18}$ are described in Section 7.1.3. What follows now are observations on the high energy vibration dynamics of M_3.

The "dissociation" of M_3 requires the rupture of two O_2-like bonds with the expenditure of at least 119.43 kcal/mole for each bond (17). Since the actual dissociation energy of ozone is 24 kcal/mole (37), it is clear that M_3 is a much more tightly bound molecule than O_3. In what follows, half the dissociation energy of M_3 will be denoted by D_o = 119.43 kcal/mole.

From the symmetry of M_3, it is clear that any energy input to the molecule as pure symmetric stretch causes it to execute that normal mode motion forever. Pure symmetric stretch energy is rigorously conserved in M_3. This fact is of value in checking the accuracy of integration routines but does not help in the elucidation of the normal mode coupling phenomenon.

When M_3 is given D_o in its bending mode (see Figure 6), the molecule cannot but retain the initial C_{2v} symmetry in its vibrations. Hence, M_3 is fated to bend forever with these initial conditions. The corresponding normal mode energy, however, changes appreciably with time, for while the exchange of energy with symmetric stretch is confined to less than $0.035\ D_o$, the bending mode energy fluctuates with a period equal to that of the bending motion. The bond angle opens to a maximum of about 95^o and closes to a minimum of about 33^o. These angles are to be compared with the equilibrium angle of 60^o. At the 95^o extension, the bending as well as the total normal mode energy are $1.26\ D_o$ with very little energy in the other two modes. The normal mode interaction energy is therefore about $-0.26\ D_o = -31$ kcal/mole. When the bond angle closes to 33^o, the total normal and bending mode energies both drop to $0.96\ D_o$. Thus, the normal mode energy changes by as much as $0.3\ D_o = 36$ kcal/mole! Fluctuations of this magnitude could have serious consequences.

When the energy D_o is put into asymmetric stretch, the molecular vibrations are not confined to that mode (see Figure 7). Due to the rocking of the Eckart axes (see Section 4.3.1.) under the asymmetric stretching M_3, small Coriolis forces act on the molecule. Since such forces on nucleus i (38) are directed along the vector $\dot{\underset{\sim}{x}}_i \times \underset{\sim}{\omega}$, they convert asymmetric stretch into bend motion and vice versa. Asymmetric normal mode energy is

FIG. 6. High Energy bending motion in M_3. $\tau_{bend} = \tau_{asym}$, the degenerate mode periods in M_3, are 2.43×10^{-14} seconds. Initial bend mode potential energy = D_o = 119.43 kcal/mole.

a. Bond Lengths. — — — bonds 1 and 3, —— bond 2.

b. Bond Energies. — — — — sum of bond energies.

c. Normal Mode Energies. —— bend, — — — sum of all three normal mode energies.

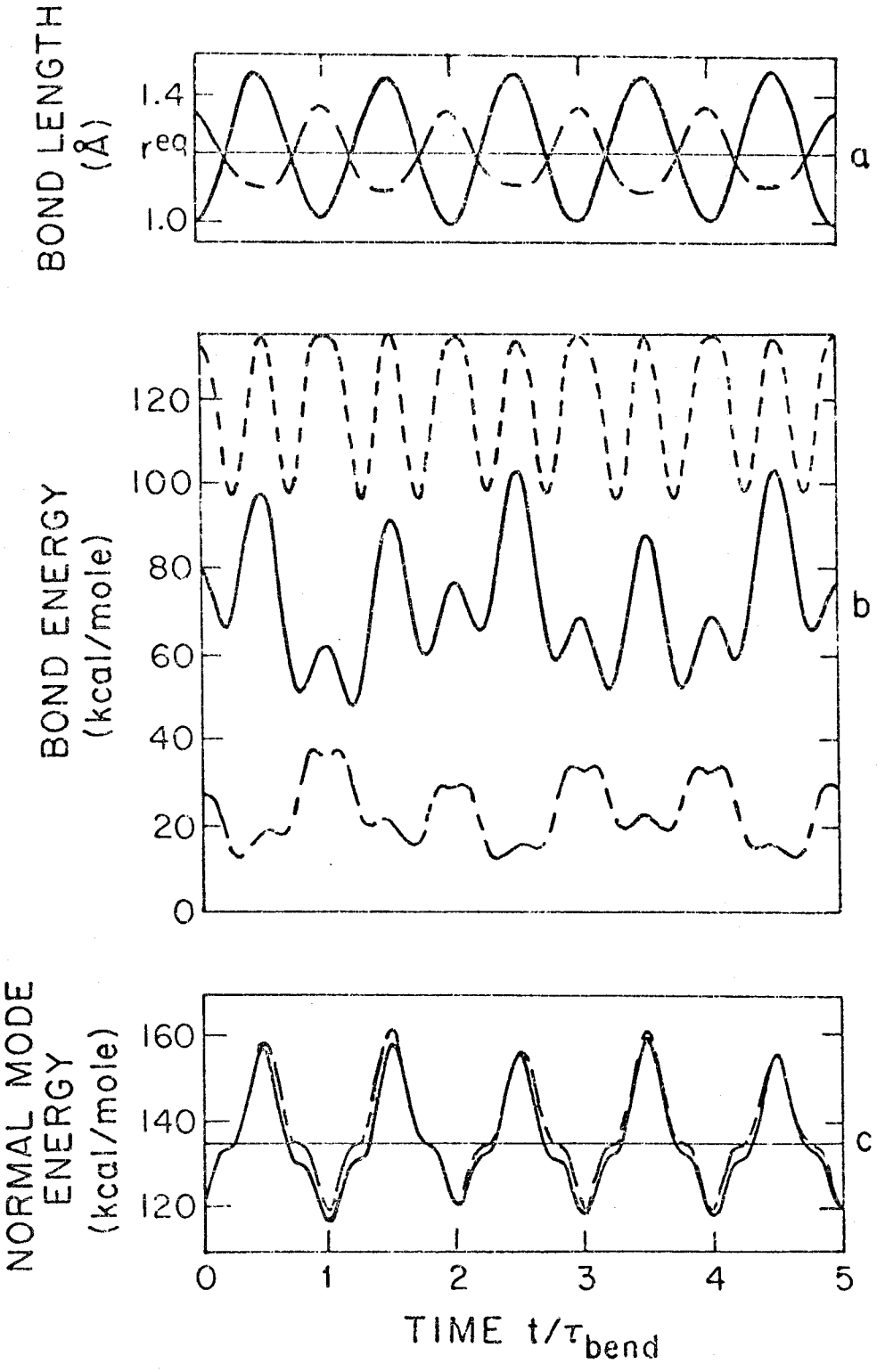
BOND LENGTH (Å)
1.4
r_{eq}
1.0
a
BOND ENERGY (kcal/mole)
120
100
80
60
40
20
0
b
NORMAL MODE ENERGY (kcal/mole)
160
140
120
c
0
1
2
3
4
5
TIME t/τ_{bend}

FIG. 7. High energy asymmetric stretch in M_3. Initial asymmetric stretch mode potential energy = D_o.

a. Bond Lengths. —— bond 1, · · · · bond 2, — — — bond 3.

b. Bond Energies. — — — — sum of bond energies.

c. Normal Mode Energies. —— symmetric stretch, · · · · asymmetric stretch, — — — bend, — — — — sum of normal mode energies.

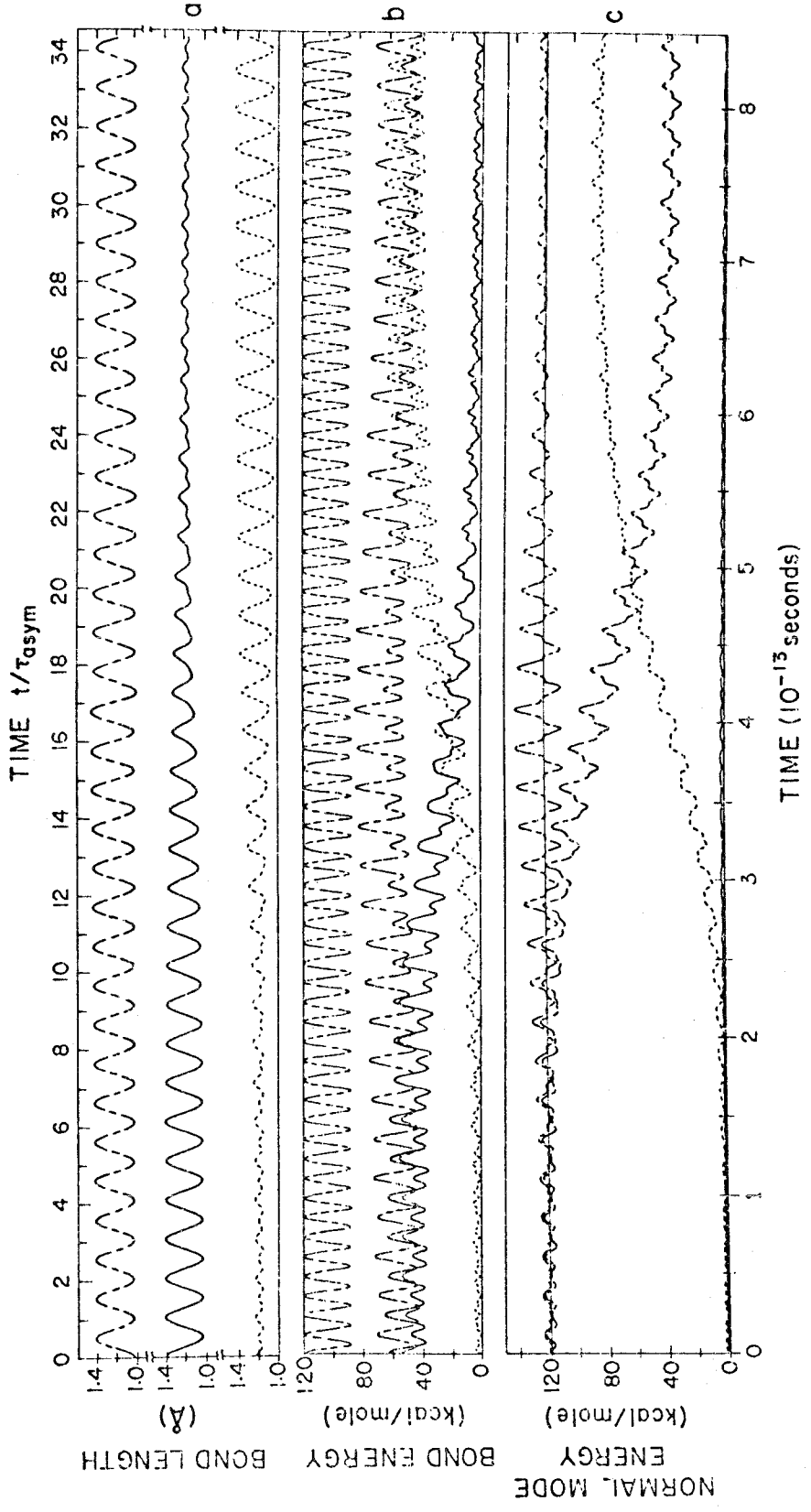
a
b
c
TIME t/τ_{asym}
TIME (10^{-13} seconds)
BOND LENGTH (Å)
BOND ENERGY (kcal/mole)
NORMAL MODE ENERGY (kcal/mole)

observed (Figure 7c) to decay as the small, self-induced Coriolis forces convert it to bend energy. The asymmetric energy cannot go to zero by this mechanism because bend motion, by virtue of its symmetry, does not rock the Eckart axes. As the symmetric bend energy rises to $0.7\ D_o$, the weakened Coriolis forces begin to convert bend energy back into asymmetric stretch energy. Since half this slow oscillation takes about 7.5×10^{-13} seconds, we presume (our integration didn't extend far enough to verify this) that the complete exchange period is about 1.5×10^{-12} seconds. This time is two orders of magnitude smaller than that associated with collision frequencies for gas molecules at standard temperature and pressure, (STP). [CO_2, for example, collides (39) with other CO_2 molecules, under these conditions, once every 2.2×10^{-10} seconds on the average.] Thus, when Slater assumes normal mode energies are constant between collisions, he may apply the assumption to asymmetrically stretching M_3 only if the product, $P\ T^{1/2}$, of the pressure by the square root of the temperature is 400 times greater than at STP. Experimental conditions like that would be very difficult to obtain. Furthermore, if M_3 had sufficient energy to dissociate, (i.e., $2\ D_o$), in its asymmetric normal mode, it would probably exchange asymmetric and bend mode energy faster than 1.5×10^{-12} seconds. Thus, for an asymmetrically stretching M_3 not to go beyond the first quarter of the faster exchange cycle between collisions, we should have $P\ T^{1/2} > 400\ (P\ T^{1/2})_{STP}$.

When all the normal modes in M_3 are excited with $D_o/3$ energy apiece, the bend and asymmetric stretch modes are again weakly coupled and exchange energy with a period of 1.6×10^{-12} seconds. The detailed nuclear motions as well as the overall energy

exchange are very nearly periodic. This may be further evidence of the metric decomposability of harmonic phase spaces suggested by Bunker's results (13).

Neither the sum of bond nor normal mode energies is a good constant of the motion. These two sums are presented in Figure 8 for the case of initially equipartitioned M_3 normal mode energy. The fluctuations in these sums taken over 8 symmetric stretch periods (about 1.4×10^{-13} seconds) are representative of the entire trajectory. It can be seen that RRKM oscillator energies do not sum to the total energy whether the oscillators are associated with the molecule's bonds or its normal modes, though the latter yield energies whose sum is slightly less variable than the bond energy sum.

Thus the high energy vibrations of the M_3 molecule do not satisfy either Slater's assumption of constant normal mode energies or the RRKM assumption that the oscillators are so weakly coupled that their energies sum with small error to the total energy of the molecule. It is unlikely that these conclusions are a function of the high symmetry of the M_3 molecule. In view of the artificiality of M_3, however, the study of a more realistic harmonic model is warranted. The next section describes the high vibration energy dynamics of nitrosyl chloride.

FIG. 8. Bond and Normal Mode energy sums in M_3. Initial energy of $D_o/3$ in each normal mode.

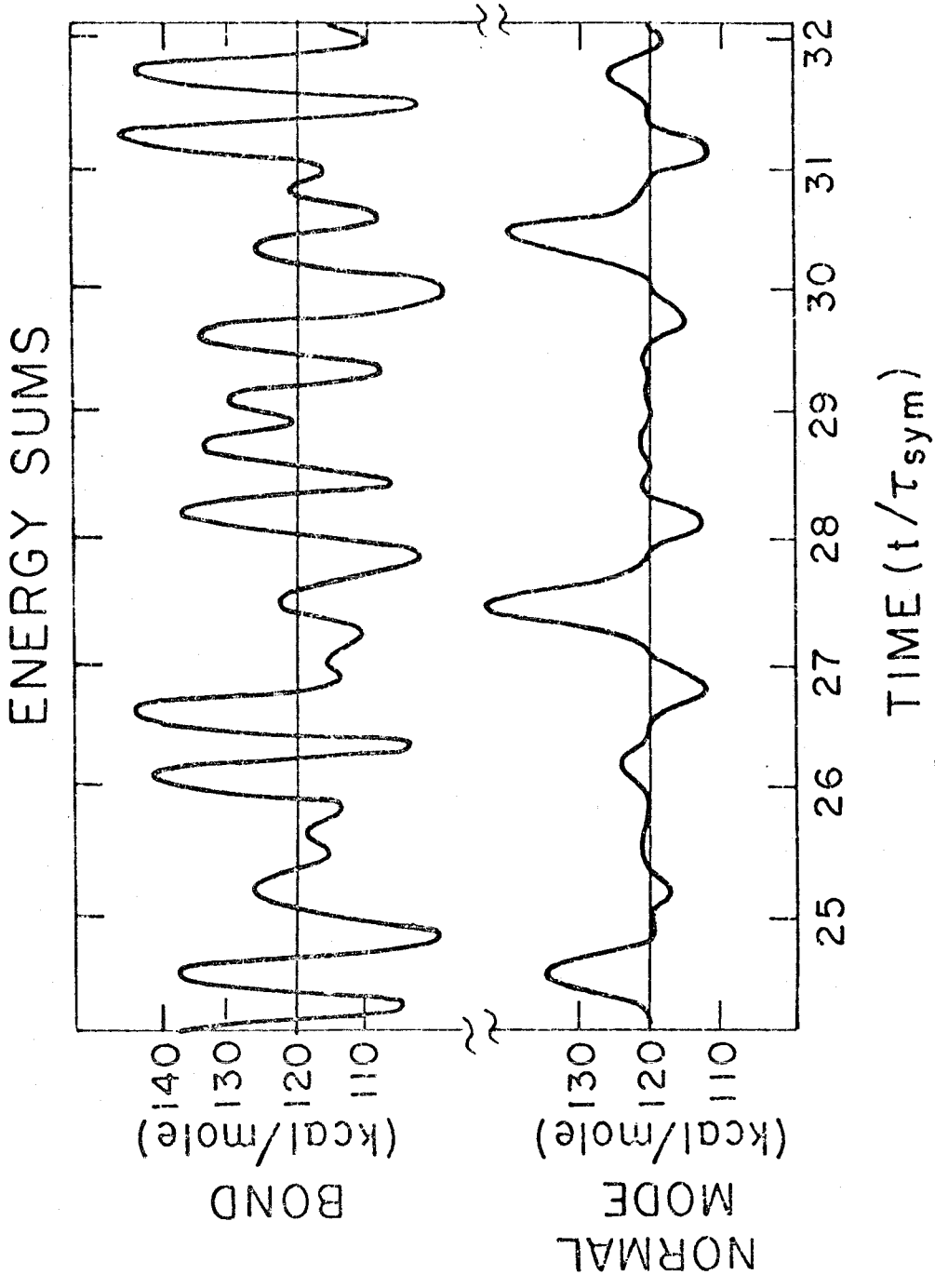
ENERGY SUMS
BOND
(kcal/mole)
140
130
120
110
NORMAL
MODE
(kcal/mole)
130
120
110
25
26
27
28
29
30
31
32
TIME (t/τsym)

7.1.3. Large Amounts of Vibration Energy in $ClNO^{18}$

The dissociation energy of the N-Cl bond in nitrosyl chloride is 38.4 kcal/mole (40). For comparison with the results of Section 7.1.2., we will introduce only half this energy, or 19.2 kcal/mole, into its normal modes.

The high frequency mode of this molecule is an asymmetric stretch-like motion involving, primarily, the vibration of the $N=O^{18}$ bond. Solution of the equations of motion show that 19.2 kcal/mole of energy in this normal mode is conserved to within 0.7% for the 0.84×10^{-12} seconds over which we integrated the trajectory.

Nitrosyl chloride's symmetric stretching (diagrammed in Figure 2) is not a stable mode of motion for energies as high as 19.2 kcal/mole (Figure 9). During the first 5×10^{-13} seconds of the trajectory, the symmetric stretch normal mode energy is reasonably constant. However, a steady increase in bend mode energy gives rise to bend amplitudes large enough for the molecule to pass through linearity at 7.25×10^{-13} seconds (Figure 9a). As a result, the normal mode energies fluctuate chaotically from about 7×10^{-13} to 10×10^{-13} seconds after initialization (Figure 9c). Note that the molecule's asymmetric stretch energy rises off the scale, while the corresponding ($N=O^{18}$) bond energy does not vary by more than about 1 kcal/mole (Figure 9b). This disparity comes about because bond energies measure the projection of atomic displacements along the instantaneous bond configuration, whereas normal mode energies measure projection of the same displacements along the equilibrium configuration. As seen from Figure 2, the velocity vectors in the asymmetric stretch mode, if translated to nuclei which lay on the x axis, would still be assigned to excitation

FIG. 9. High energy symmetric stretch in $ClNO^{18}$. Initial symmetric stretch potential energy = 19.2 kcal/mole.

a. Bond Lengths. —— NO^{18}, – – – ClO^{18}, — — — NCl, — — — — sum of the two smallest bonds, used as a linearity check.

b. Bond Energies. — — — — sum of bond energies.

c. Normal Mode Energies. —— asymmetric stretch, – – – symmetric stretch, — — — bend, — — — — sum of normal mode energies.

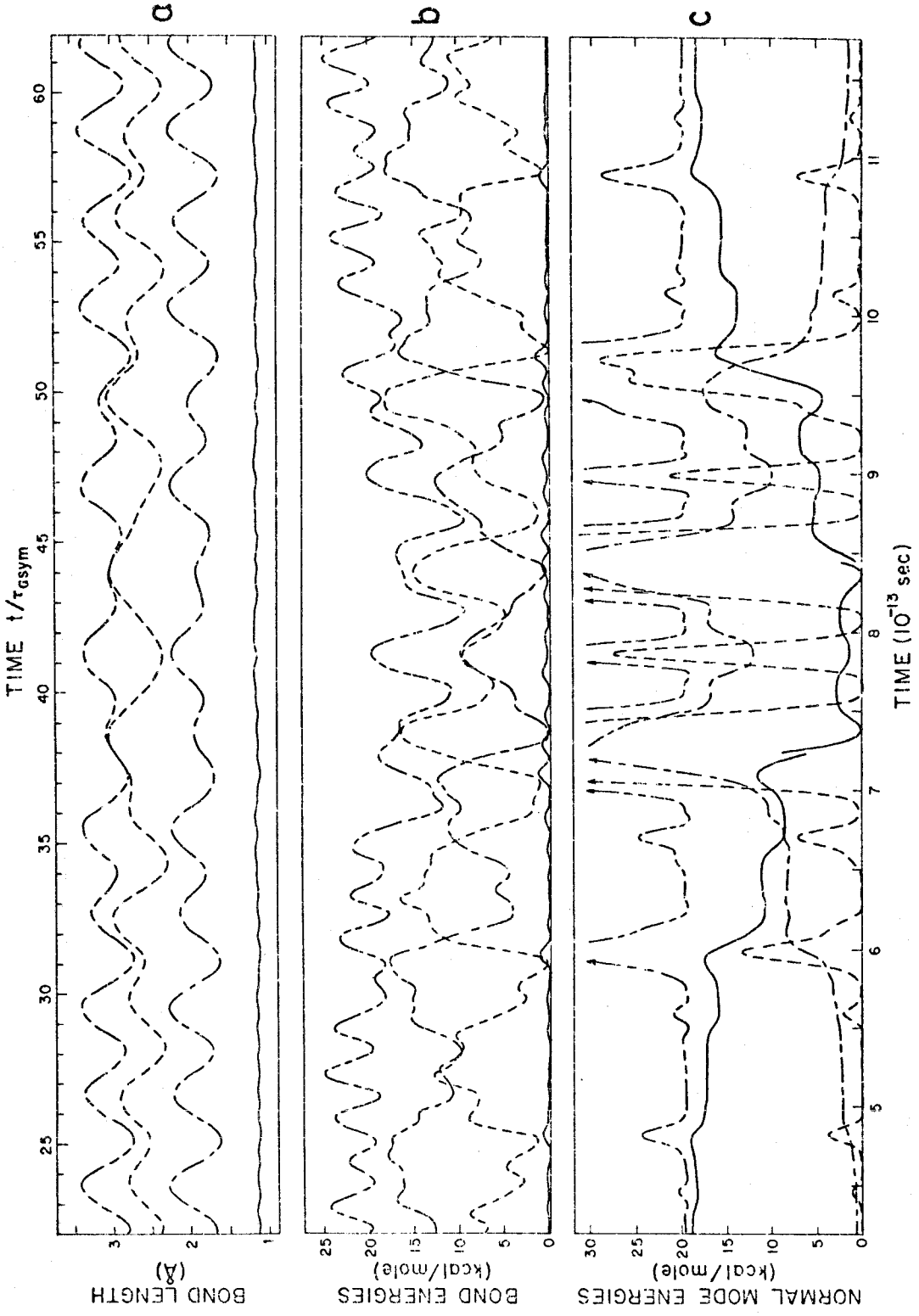
a
b
c
TIME t/τ_{GSym}
BOND LENGTH (Å)
BOND ENERGIES (kcal/mole)
NORMAL MODE ENERGIES (kcal/mole)
TIME (10^{-13} sec)

of the asymmetric stretch mode whereas they would appear to produce bending in the linear molecule. Conversely, bending motion in the linear molecule would be assigned, in part, to excitation of the asymmetric stretch mode. This kind of failure in the decomposition of displacement and velocity vectors renders normal mode energy a useless concept when applied to grossly distorted molecules. Such distortions are clearly not rare, even in molecules with energies less than dissociative.

Returning to Figure 9c, we observe that the symmetric stretch mode eventually recovers its initial energy and the bend energy dies away. We continued the trajectory beyond the terminus of the figure to about 12.6×10^{-13} seconds and the bend energy was still dwindling at that time. Although the trajectory is not perfectly symmetric in time about the instant 7.8×10^{-13} seconds, this exchange of energy between the symmetric stretch and bend modes appears to have a period of about 15.6×10^{-13} seconds.

The definition of nitrosyl chloride's bending mode is so poor that when this mode is given 19.2 kcal/mole of potential energy, the total energy of the molecule is 50.6 kcal/mole. This constitutes a normal mode energy defect of over 150%! In addition, this total energy exceeds the dissociation energy by over 12 kcal/mole. No figure is given for this case as all the energies vary wildly. The significant aspects of the dynamics are summarized in the following discussion. The bond angle opens with such vehemence that all the molecular modes are highly excited within one bend period. Oddly enough, within two more bend periods, the other two modes have drained most of the energy from the bending mode, leaving the molecule in highly excited stretching modes. Since the bond angle

is executing only small amplitude bends, the distortions from equilibrium configuration are not great and a temporary stability is achieved, wherein the normal mode energies are fair constants of the motion. This stability last for only 5×10^{-13} seconds, after which the bend mode has regained sufficient amplitude for the molecular energies to scramble rapidly. The ensuing chaos in the normal mode energies persisted to the termination of the trajectory integration at 1.68×10^{-12} seconds after initiation.

When each of nitrosyl chloride's normal modes is given 6.4 kcal/mole (one-sixth of the dissociation energy), the bending mode energy defect gives rise to a total energy of 40.8 kcal/mole, or 2.4 kcal/mole greater than the dissociation energy. As in the pure bend initiation, the molecule soon deposits most (30 kcal/mole) of its energy in the asymmetric (N=O) stretch. The remainder of the energy shuffles back and forth between the other two modes with a rough 4×10^{-13} second period. Neither the sum of bond nor normal mode energies (Figure 10) indicate small coupling in the molecule. The coupling energies in the RRKM oscillators can be as large as 15 kcal/mole, or almost half the energy of the molecule!

Thus for energies of chemical interest, the normal mode energies in our harmonic model for $ClNO^{18}$ are not conserved over periods of time sufficiently long to be used as constants of the motion between collisions in the gas phase. Furthermore, coupling between RRKM oscillators (either normal modes or bonds) is so strong that the sum of their energies can differ from the total energy by a factor of 2.

Apparently, the consequences of the SVA regarding normal mode energies are approximately correct for zero point energies

FIG. 10. Bond and Normal Mode energy sums in $ClNO^{18}$. Initial energy of 6.4 kcal/mole in each normal mode.

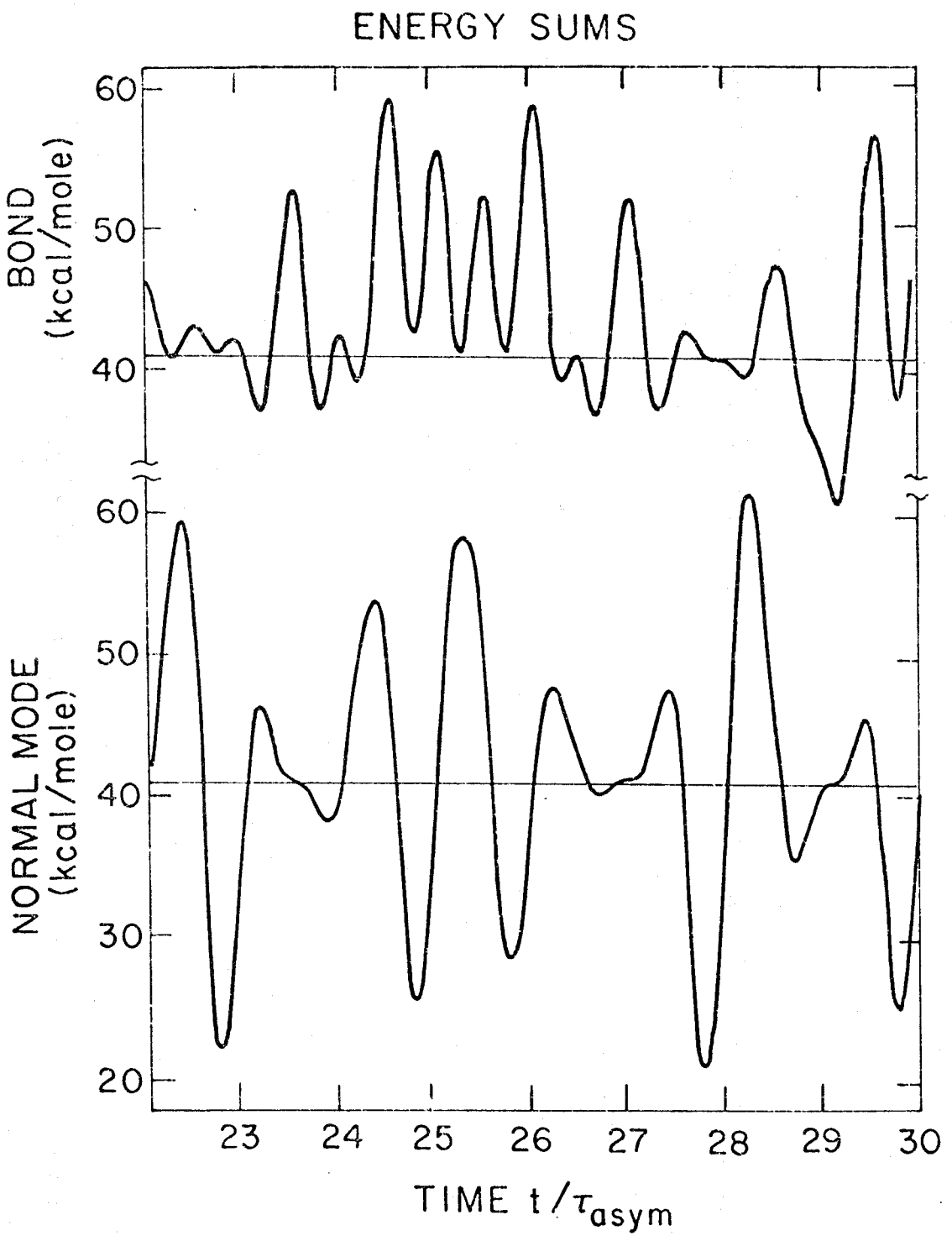
ENERGY SUMS
BOND (kcal/mole)
60
50
40
NORMAL MODE (kcal/mole)
60
50
40
30
20
23
24
25
26
27
28
29
30
TIME t/τasym

but fail for dissociative energies. It is of interest to determine through what energy range the SVA can be trusted. The following section investigates this point.

7.1.4. Onset of Instability in Nitrosyl Chloride's Symmetric Stretching Mode

One suspects that the mixing of one mode into another is an exponential process. Small perturbations yield small admixtures of modes of different symmetries, which, in turn, yield larger perturbations in an ever-accelerating growth. As we have seen in Section 7.1.3., when 19.2 kcal/mole is input to the symmetric stretching mode of $ClNO^{18}$, the molecule's bending mode becomes excited. When the logarithm of the rising bend energy is plotted against time, as in Figure 11, the fit to a straight line (exponential growth) is seen to be good. That line may be taken to represent an average exponential growth. The time it takes the bending mode energy to rise to the total energy of the molecule is a measure of the coupling between the two modes. We shall take the inverse of this time to represent the coupling frequency related to the period of growth and decay of bend energy mentioned in reference to Figure 9c.

We plot a few such symmetric/bend coupling "frequencies" against total energy in Figure 12. It becomes apparent, from this figure, that the SVA, which predicts that these frequencies are zero, fails at energies greater than about 10 kcal/mole in $ClNO^{18}$. The point in Figure 12 at 7.76 kcal/mole total energy represents a case where the bending mode energy did <u>not</u> rise to usurp the total

FIG. 11. Growth of bending mode energy from pure symmetric stretch in $ClNO^{18}$. Initial symmetric stretch potential energy = 19.2 kcal/mole. Semilog plot.

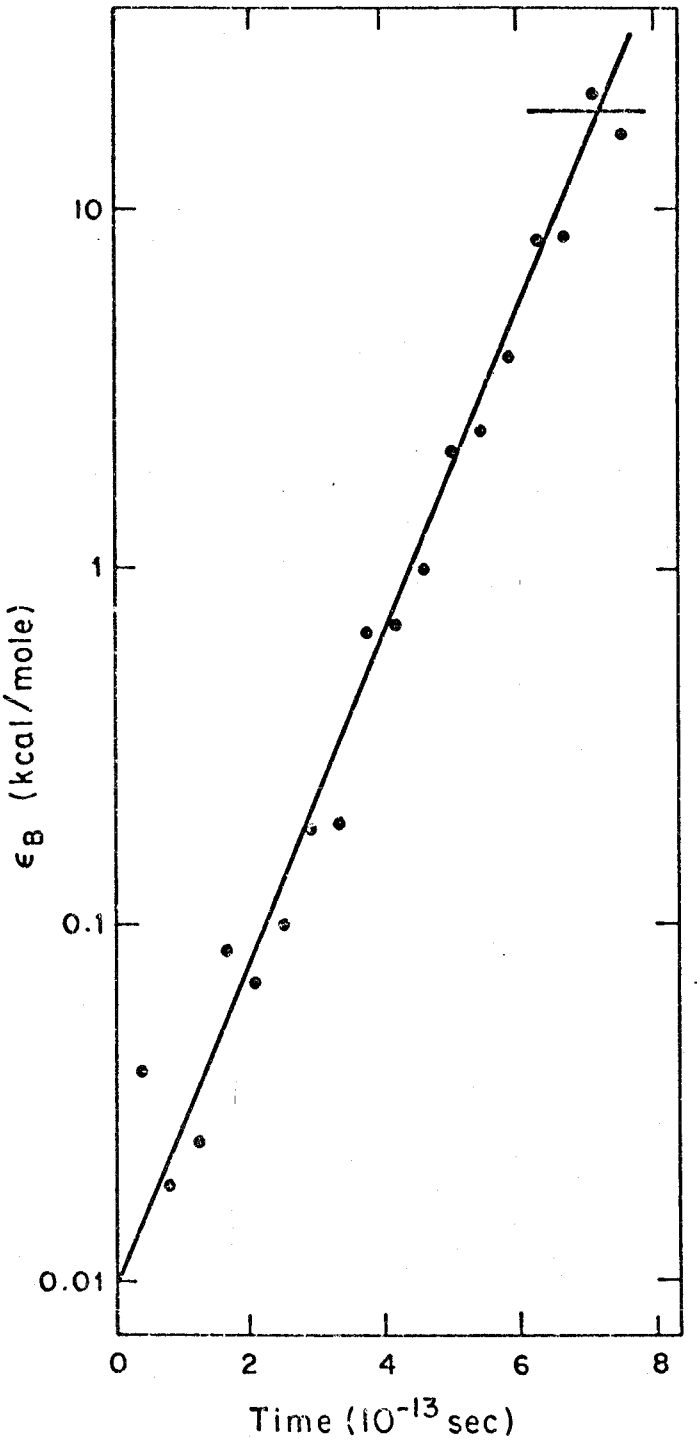
10
1
0.1
0.01
ϵ_B (kcal/mole)
0
2
4
6
8
Time (10^{-13} sec)

FIG. 12. Coupling frequencies for bend mode arising from pure symmetric stretch in $ClNO^{18}$.

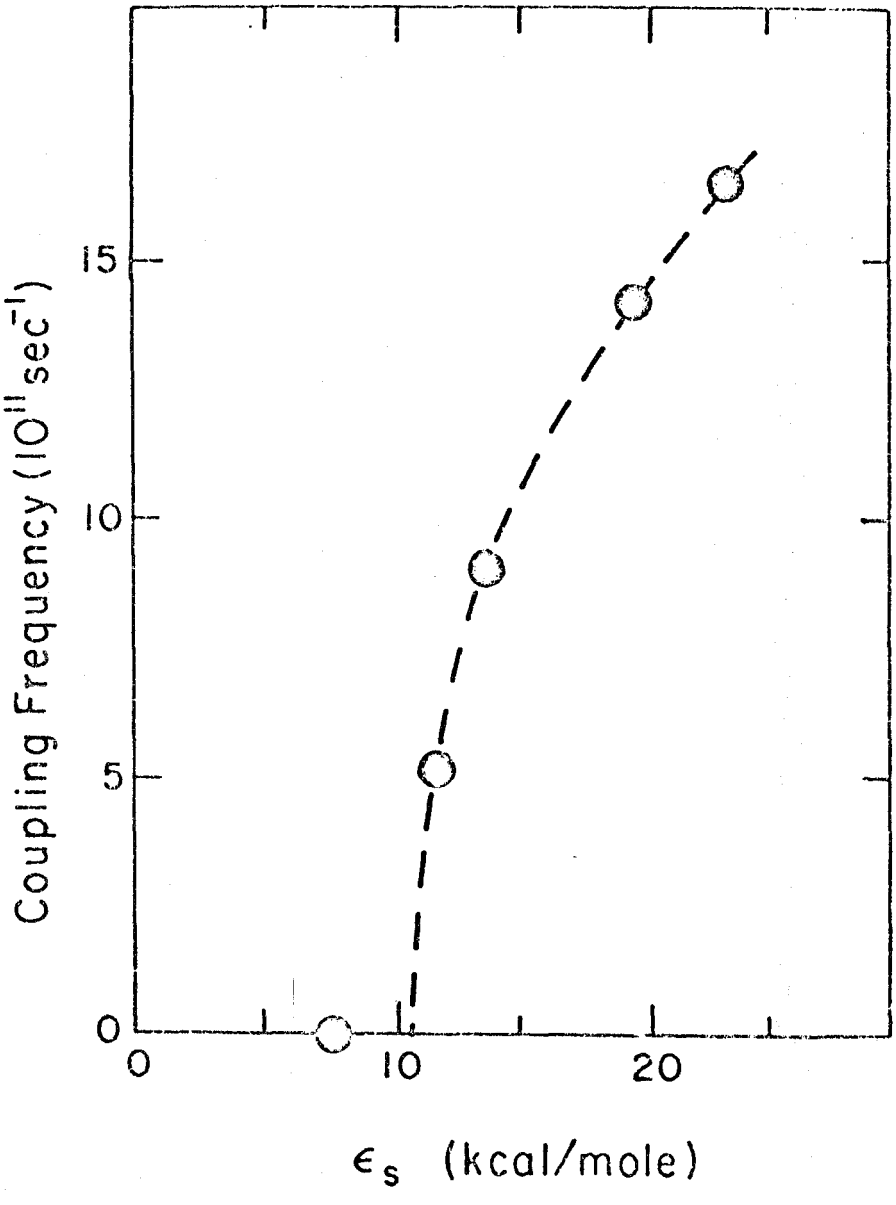
Coupling Frequency (10^{11} sec^{-1})
15
10
5
0
0
10
20
ϵ_s (kcal/mole)

energy of the molecule within the time (1.68×10^{-12} seconds) observed. For this case (Figure 13), the bend energy fluctuated rapidly within double envelopes which rose and fell between 0.01 and 0.001 kcal/mole. The period of the double envelope variation was about 10^{-12} seconds, hence we observed only two of these slow oscillations.

7.1.5. Critical Co-ordinate Dissociation Frequencies

In order to predict dissociation or isomerization rate constants, Slater's harmonic theory requires an expression for the frequencies of excursions of some critical co-ordinate past some critical configuration. The formula he uses comes from an analysis of the reactive excursion frequencies of a sum of sinusoidally varying normal modes of constant energy. This sum weights the normal mode co-ordinates as in footnote 23. The weighting coefficients, α_{ri} are obtained from the definition of the critical co-ordinate, q_r, and the normal mode co-ordinates, Q_i. If the critical co-ordinate is some linear combination of the internal bond displacement co-ordinates (see Appendix 2) such that

$$q_r = \mathbb{IU}\ \$ \qquad (7.1.5.-1)$$

where $\mathbb{IU}$ is a one by three matrix, then by $\$ = \mathbb{IL}\ \mathbb{Q}$ and (7.1.5.-1) , the elements of the one by three matrix $\mathbb{IU}\ \mathbb{IL}$ are the coefficients α_{ri}. Since the equations of motion of non-linear harmonic molecules do not conserve the normal mode energies, we suspected that the reactive excursion frequencies calculated

FIG. 13. Growth of bending mode energy from pure symmetric stretch in $ClNO^{18}$. Initial symmetric potential energy = 7.72 kcal/mole. Semilog plot.

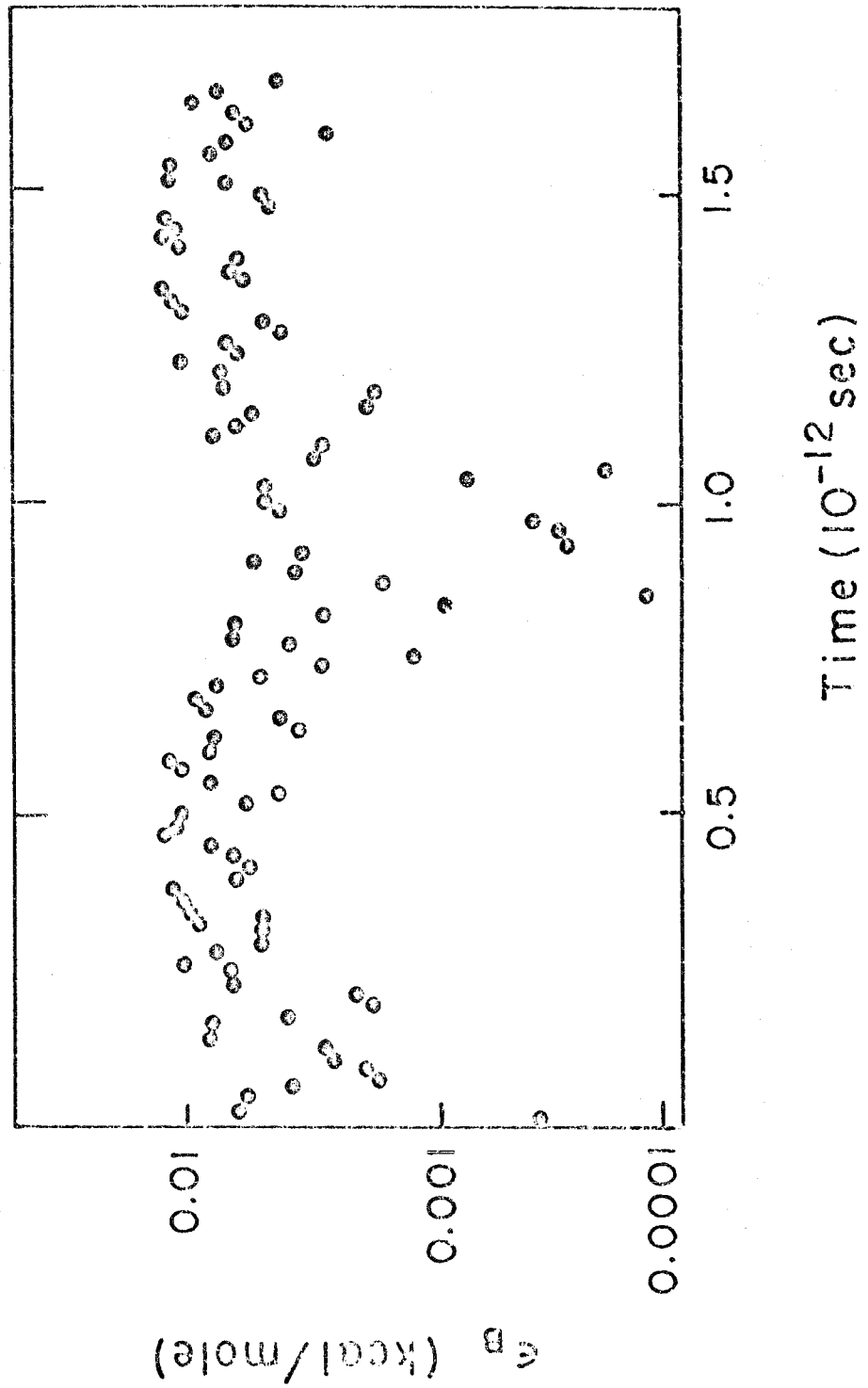
0.01
0.001
0.0001
ϵ_B (kcal/mole)
0.5
1.0
1.5
Time (10^{-12} sec)

by Slater would not agree with those taken directly from trajectory calculations.

The normal mode defect in the trajectories described in Sections 7.1.3. and 7.1.4. lead to total energies as much as a factor of 2.5 higher than the initial normal mode energies. Because of the square root relation between potential energy and bond displacement co-ordinates, the normal mode defect can lead to initial bond displacement co-ordinates different from the SVA ones by a factor as large as 1.6 in the molecules studied. There are two sources of difference between bond distances calculated from the SVA and from the actual harmonic trajectories; both are manifestations of the same approximation, and they cannot be discussed separately with any rigor. First, there is the variation of the normal mode energies with time, which will make the SVA and trajectory calculated $\underset{\sim\sim}{\Delta x}_i$ diverge. Second, the SVA linear approximation, which expresses bond displacements as linear combinations of the components of the $\underset{\sim\sim}{\Delta x}_i$, will give different instantaneous bond distances to the molecule than if they were calculated properly as square roots of squares of differences in the $\underset{\sim}{x}_i$. The SVA rests upon this linear approximation to internuclear distances. Without it, one could not make the potential and kinetic energy functions be simultaneous sums of square terms of normal mode co-ordinates and their derivatives, respectively. As a result, the transformation of the equations of motion into non-coupled normal mode equations could not be performed. Hence, the two effects just mentioned are, in reality, inseparable. However, for comparison purposes, we will consider these two sources of difference to be independent of one another. To achieve this, we

introduce the IVA, which might stand for Intermediate Vibration Approximation, or, in view of the above discussion, the Inconsistent Vibration Approximation. With the IVA, we hope to separate the effects which were inseparable in the SVA. The IVA will retain the same linear relation between the normal mode and Eckart displacement co-ordinates but will use the correct (non-linear) expressions for the internuclear distances. In this way, we may initiate an actual and an IVA trajectory with equal initial normal mode energies from the same molecular configuration and observe the divergence of trajectories due, primarily, to the mixing of normal modes.

We calculated the $\underset{\sim\sim}{\Delta x}_i^{IVA} = \underset{\sim\sim}{\Delta x}_i^{SVA}$ from the inverse of equation (4.3.2.-1) and the sinusoidal $Q_j(t)$ at the same normal mode energies used for the trajectories mentioned earlier. These $\underset{\sim\sim}{\Delta x}_i$ were converted to $\underset{\sim}{x}_i$ via equation (4.3.1.-11)and thence to r_j^{IVA} via the Eckart counterpart to equations(4.1.-5,6) . The r_j^{SVA} were calculated from the bond displacement co-ordinates, S_j (see Appendix 2), via $r_j^{SVA} = S_j + r_j^{eq}$ where

$S_j(t) = \sum_{i=1}^{3} (\mathbb{L})_{ji} Q_i(t)$. The resultant approximations for the internuclear bond distances as a function of time were compared with the actual $r_j(t)$ obtained from the corresponding computed trajectories. A counting procedure was employed to find the frequency with which the function $r_j(t) - r_j^{critical}$ passed through zero in the direction of reaction. The long-time (2×10^{-12} seconds) averages of this frequency for the actual, SVA, and IVA function were plotted against assumed values for $r_j^{critical}$. The comparison is described below.

When a single normal mode is excited, all the $\underset{\sim}{\Delta x}_i^{SVA}$ components oscillate sinusoidally with the same frequency as that of the excited normal mode. They all move in- or 180^o out-of-place with one another. This usually means that the molecule's bonds all execute simple oscillations of this same frequency. Hence, the reactive excursion frequency [the frequency with which $r_j(t) - r_j^{critical} = 0$ occurs with $r_j(t)$ moving toward reaction, abbreviated REF throughout this paper] for a bond is equal to the frequency of the single excited mode for choices of $r_j^{critical}$ within the range r_j^{min} to r_j^{max}.

The REFs for M_3, asymmetrically stretching with D_o energy are shown in Figure 14a. The SVA and IVA REFs, when plotted against assumed critical stretch are step functions, as explained in the last paragraph. It is clear from Figure 14a that neither vibration approximation matches the actual excursion frequencies, but the IVA is not as far wrong as is the SVA. The REFs from the trajectory calculations show the effect of the exchange of energy between the asymmetric stretch and bend modes of the molecule. The trajectory-derived REFs for bonds 1 and 2 would have been coincident in a truly long-time average, i.e., long with respect to the coupling period of 1.5×10^{-12} seconds. However, the average was taken over only 10^{-12} seconds, corresponding to about 58 symmetric stretch periods.

Since M_3's bend mode is a stable mode of motion (i.e., maintenance of C_{2v} symmetry is exact), the REFs for M_3 bonds in the IVA and the actual trajectory are expected to be very much alike. Figure 14b verifies this expectation. Note that the bond displacement co-ordinates in the SVA are almost three times those

FIG. 14. Reactive Excursion Frequencies vs. assumed critical length for the bonds in M_3.

—— actual trajectory, – – – IVA and ····· SVA thereto.

a. Initial asymmetric mode energy = D_o.

b. Initial bend mode energy = D_o.

c. All initial normal mode potential energies = $D_o/3$.

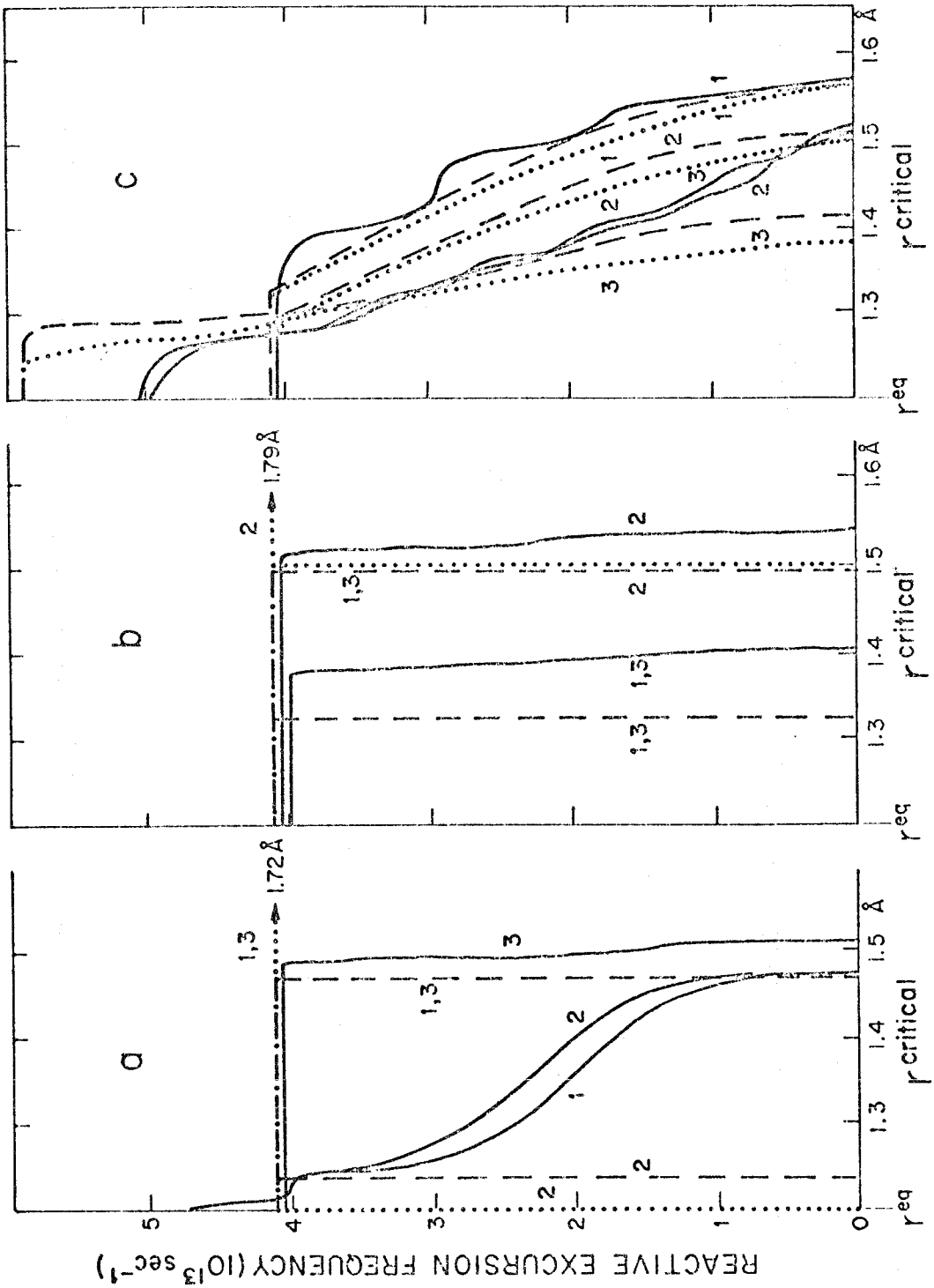
c
b
a
1.72Å
1.79Å
1.6 Å
1.5
1.4
1.3
r critical
r eq
REACTIVE EXCURSION FREQUENCY (10^{13} sec^{-1})
5
4
3
2
1
0

of the IVA. The amplitudes of molecular motion are still not correctly calculated in the latter because the bend mode energy is not a constant of the motion (see Figure 6c) in the actual molecule.

Figure 15 shows the bond distances as a function of time in both the actual and the IVA trajectory wherein the initial normal mode excitation is $D_o/3$ potential energy in each mode. The SVA bond distances (not shown) are within about 2% of the IVA ones over the course of the trajectory. The nuclear motions in the IVA are clearly divergent from those in the actual trajectory after about 3×10^{-13} seconds. The REFs (Figure 14c) of bonds 2 and 3 show the behavior, intermediate to their IVA counterparts, that was observed for bonds 1 and 2 in Figure 14a. The explanation is the same in both cases --bend and asymmetric stretch are coupled modes. What is surprising about Figure 14c is the good agreement between the actual, SVA, and IVA reactive excursion frequencies for bond 1. Figure 15 shows that the IVA is no better an approximation to the oscillations of bond 1 than it is to either of the other bonds, and yet the IVA calculates the correct excursion frequency for large r_1^{critical} in this bond. It is conceivable that this might be an accidental result stemming from M_3's high symmetry.

The long-time averages for the actual, SVA, and the IVA bond excursion frequencies are strictly comparable with one another. They follow from the same initial conditions for the molecule. However, none of these averages is comparable with Slater's phase averaged excursion frequencies (41), since the M_3 molecule's vibration frequencies are linearly dependent ($\omega_{asym} = \omega_{bend}$), which means that Q_{asym} and Q_{bend} always have the same

FIG. 15. Divergence of actual and IVA trajectories in M_3. All initial normal mode potential energies = $D_o/3$. —— actual trajectory, – – – IVA thereto.

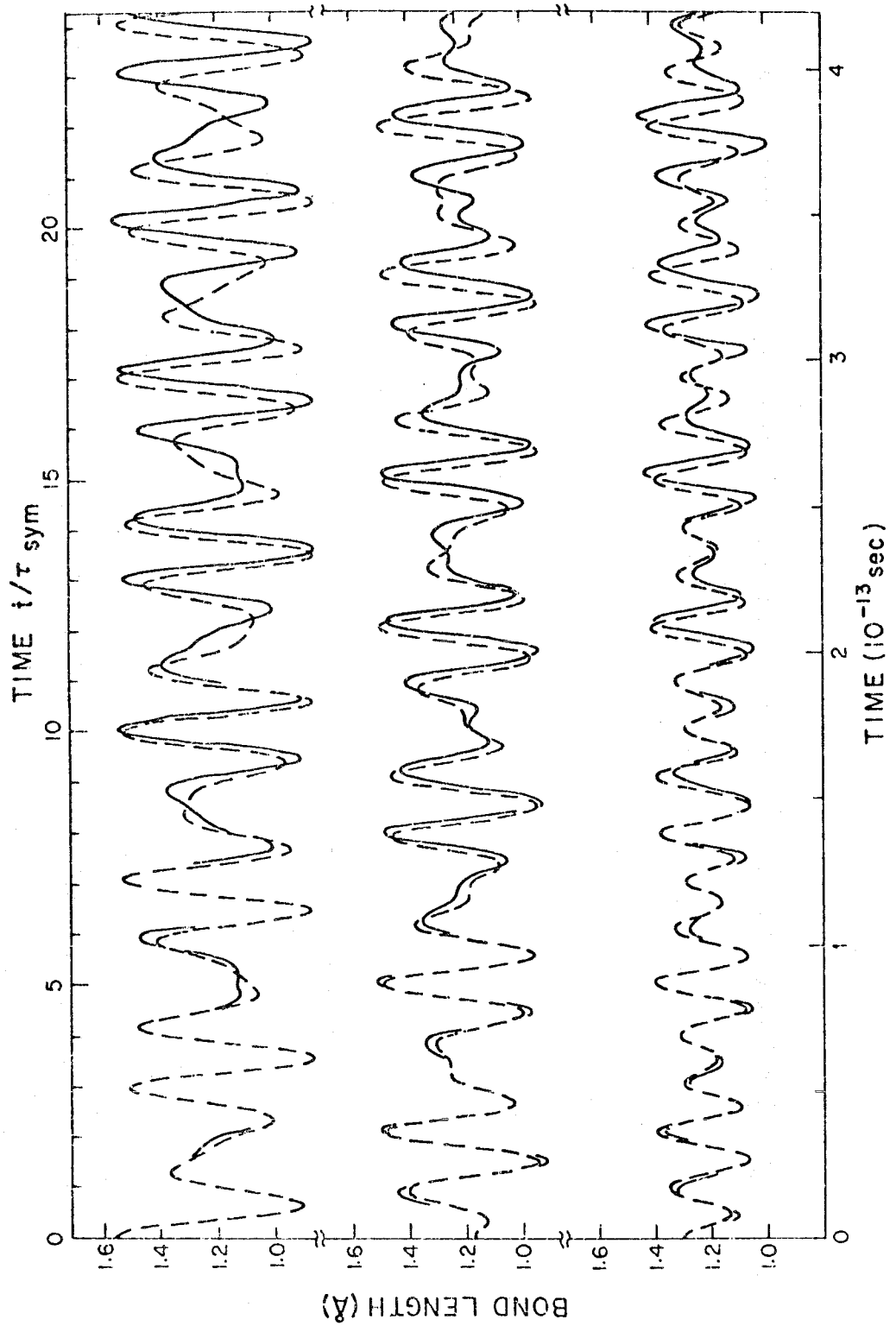
TIME t/τ sym
0
5
10
15
20
TIME (10⁻¹³ sec)
0
1
2
3
4
BOND LENGTH (Å)
1.6
1.4
1.2
1.0

phase relation to one another that they had initially. A long-time average does nothing to break this synchronization, and one expects that the phase averaged frequencies may be different. Indeed, when the IVA to the case of equal normal mode excitation was initiated with the normal modes all 120^{o} out-of-phase with one another, the IVA excursion frequencies were quite different from those with in-phase initiation. The same test was applied to $ClNO^{18}$ with equal normal mode excitation, and it was found that the different initial phases had no appreciable effect on the IVA excursion frequencies. This result follows readily from the fact that nitrosyl chloride has linearly independent molecular frequencies.

The high energy bending mode in $ClNO^{18}$, with its 150% energy defect and instantaneous energy scrambling, does not bear any resemblance to either its SVA or IVA. It is not surprising, then, that the corresponding SVA and IVA REFs in Figures 16abc do not follow those of the actual trajectory, although again the IVA bond displacement amplitudes are better than the SVA. Note that the IVA excursion frequency curve for the N=O bond in Figure 16a is a <u>two</u> step function, with the frequencies being once and twice the bend frequency. A glance at Figure 2 confirms the following argument. As the nuclei are moved along the arrows in the diagram for ω_B in Figure 2, the bond angle opens from its equilibrium value, and the N=O bond stretches to some magnitude r_{NO}^{open}. The bond is also stretched to a different magnitude r_{NO}^{closed} as the nuclei are moved along vectors with senses opposite those for ω_B in Figure 2, that is, as the bond angle closes from its equilibrium value. This means that the N=O bond is opened and closed twice in every bend period. This produces the observed frequency doubling in the IVA

FIG. 16. Reactive excursion frequencies vs. assumed critical length for the bonds in $ClNO^{18}$. Initial bend potential energy = 19.2 kcal/mole. —— actual trajectory, – – – IVA and ····· SVA thereto.

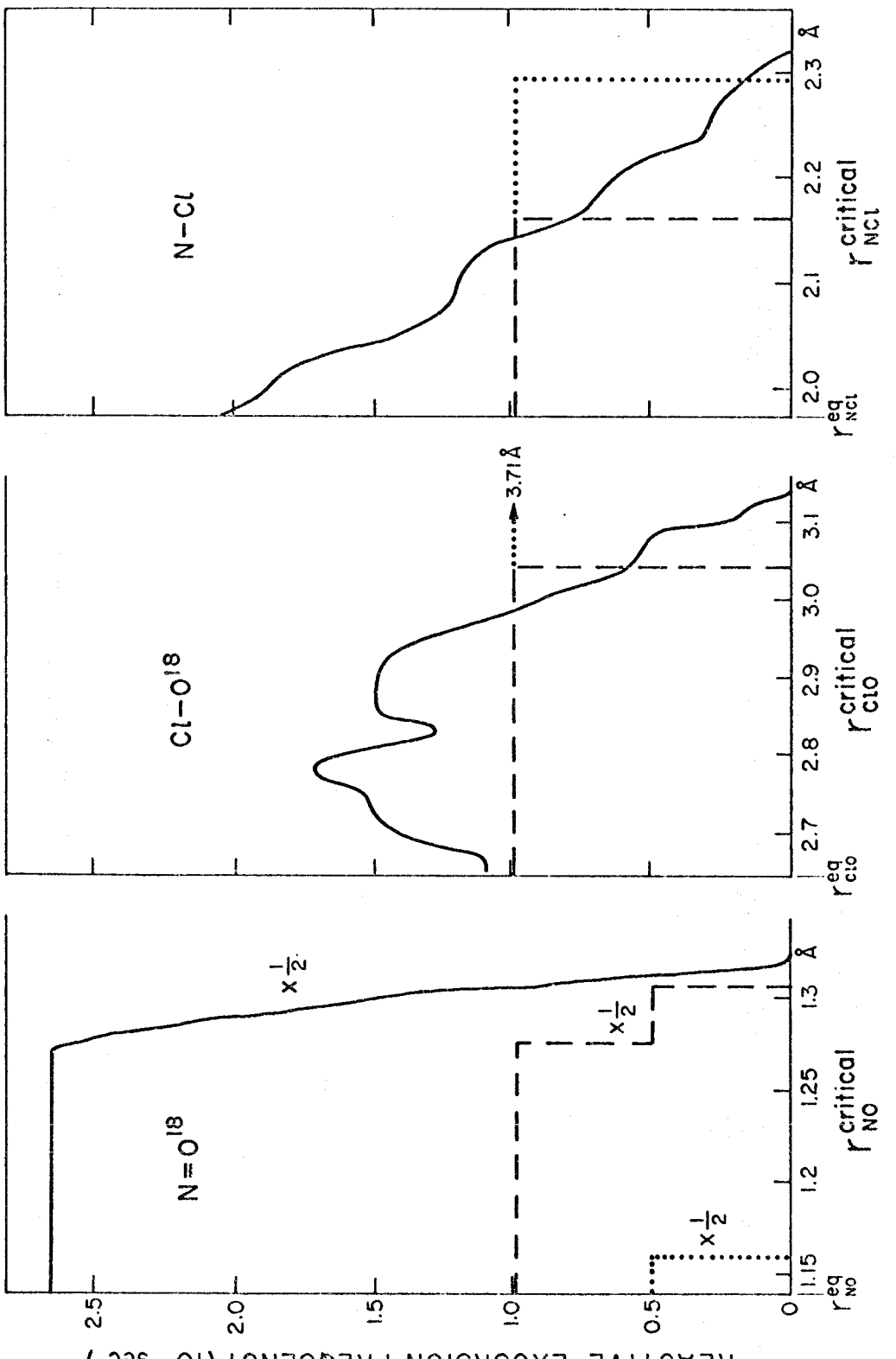
REACTIVE EXCURSION FREQUENCY (10^{13} sec^{-1})
2.5
2.0
1.5
1.0
0.5
0
N≡O^{18}
$\times\frac{1}{2}$
$\times\frac{1}{2}$
$\times\frac{1}{2}$
1.15
1.2
1.25
1.3 Å
r^{eq}_{NO}
$r^{critical}_{NO}$
Cl–O^{18}
3.71Å
2.7
2.8
2.9
3.0
3.1 Å
r^{eq}_{ClO}
$r^{critical}_{ClO}$
N–Cl
2.0
2.1
2.2
2.3 Å
r^{eq}_{NCl}
$r^{critical}_{NCl}$

REF for N=O, and the fact that $r_{NO}^{open} \neq r_{NO}^{closed}$ leads to the two step function for this REF. Frequency doubling, of this nature, should be associated with other loose molecular bending modes, as for the case of initially pure symmetric stretch of 19.2 kcal/mole, as depicted in Figure 17a.

Another observation drawn from Figure 16a is that if a normal mode involves motion in some bond whose natural frequency if much higher than that of the mode itself, one expects it to vibrate with its natural frequency rather than that of the normal mode. This is not the case in the limit of infinitesimal amplitude motion, as all but one of the normal modes would be orthogonal to this bond vibration. In the case of large amplitude motion, as in the excited symmetric stretch of $ClNO^{18}$ (Figure 9a), the N=O vibration takes place at its natural frequency and not that of the symmetric stretch. If, on the other hand, low frequency bonds are stimulated by high frequency modes, one does not expect to find low frequency oscillations observed, as they will be entirely obscured by the rapid normal mode motion.

Since $ClNO^{18}$ with 19.2 kcal/mole as symmetric stretch (see Figure 9c) is stable about 70% of its assumed coupling period (the bend energies being important between 6 and 11 $\times 10^{-13}$ seconds from initiation), the SVA and IVA excursion frequencies in Figures 17abc are a better fit to the actual excursion frequencies than they were in Figure 16. Even the IVA is still far from adequate for a description of the excursion frequencies in either case. However, high energy pure normal mode molecular motions are expected to be produced by collisions only rarely. Errors made in calculating their lifetimes would not greatly affect a unimolecular reaction rate, because such initial conditions have very low statistical weight.

FIG. 17. Reactive excursion frequencies vs assumed critical length for the bonds in $ClNO^{18}$. Initial symmetric stretch potential energy = 19. 2 kcal/mole. —— actual trajectory, – – – IVA and · · · · SVA thereto.

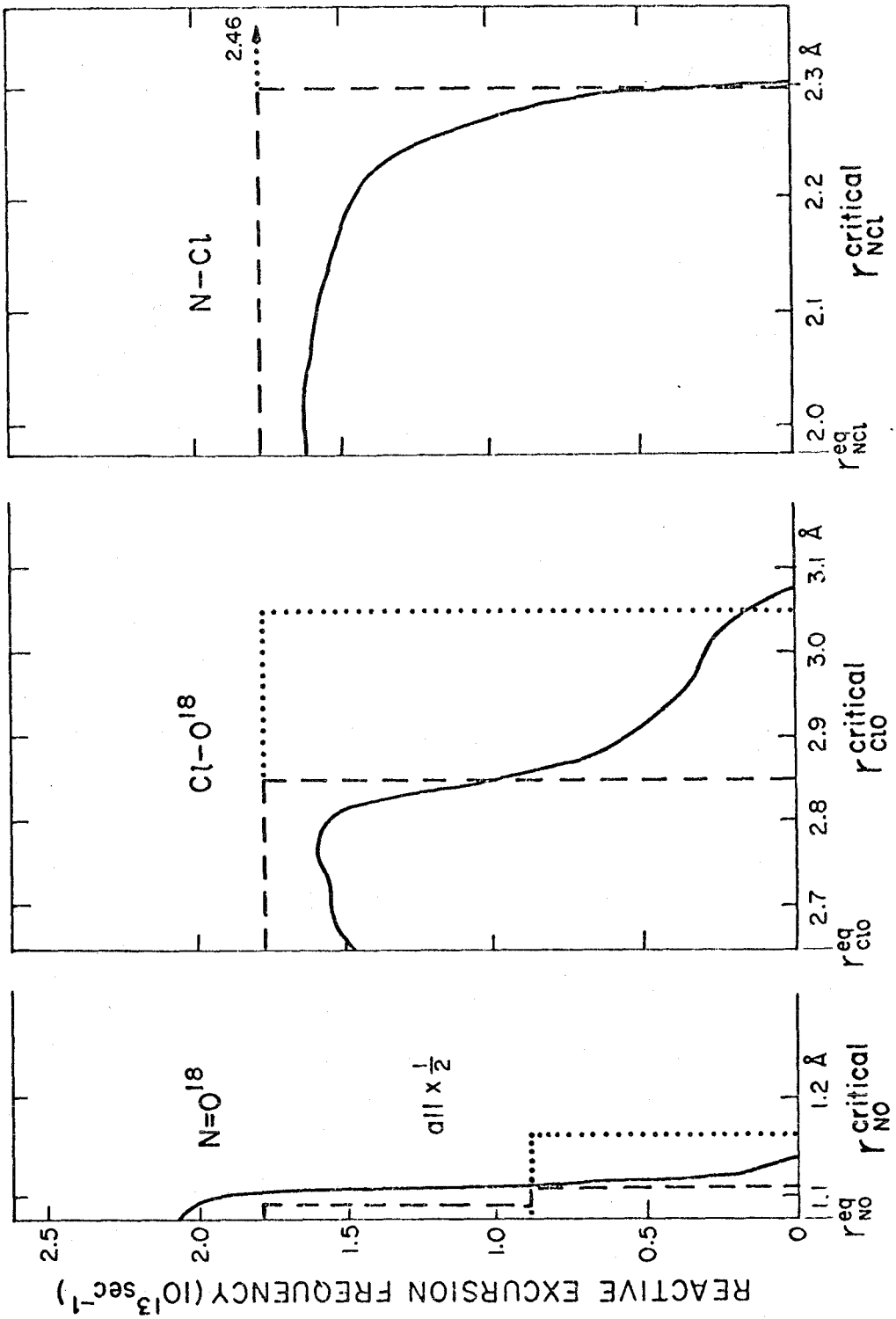
REACTIVE EXCURSION FREQUENCY (10^{13} sec^{-1})
2.5
2.0
1.5
1.0
0.5
0
N=O^{18}
all x 1/2
1.1
1.2 Å
r^{eq}_{NO}
$r^{critical}_{NO}$
Cl-O^{18}
2.7
2.8
2.9
3.0
3.1 Å
r^{eq}_{ClO}
$r^{critical}_{ClO}$
N-Cl
2.46
2.0
2.1
2.2
2.3 Å
r^{eq}_{NCl}
$r^{critical}_{NCl}$

Of greater concern is the way the IVA describes molecules with mixed excitation modes.

When all the modes of nitrosyl chloride are excited with only 6.4 kcal/mole, IVA trajectories (see Figure 18), which differ from the SVA ones by ~ 10%, diverge more rapidly from the actual trajectories than in the case of M_3 with 39.8 kcal/mole energy in each mode (Figure 15). One would then anticipate the IVA excursion frequencies for $ClNO^{18}$ to be less representative of the actual excursion frequencies than they were in M_3. Figure 19 shows that this is not the case. The SVA and IVA reactive excursion frequencies for the bonds which break on dissociation, N--Cl and Cl--O, are good approximations to the actual excursion frequencies exhibited by these bonds. The agreement implies that, although the dynamics of $ClNO^{18}$ are not at all reproduced by either approximation, the molecular quantities of greatest significance to its reaction rate, the reactive excursion frequencies, are accurately calculated in both the SVA and IVA.

7.2. Effects of Rotational Energy

The Slater and RRK theories of unimolecular reaction rates ignore the effect of rotation. Marcus (6) extended the RRK theory to take account of rotations in its statistical part, including their contribution to the density of activated states. The RRKM theory still preserves the assumption of separation of vibration and rotation in the evaluation of partition functions. In using such a rigid rotor treatment, this theory ignores the dynamical effects of rotation. The assumption made in all the theories mentioned is that rotation

FIG. 18. Divergence of actual and IVA trajectories in $ClNO^{18}$. All initial normal mode potential energies = 6.4 kcal/mole. – – – – actual trajectory, —— IVA thereto.

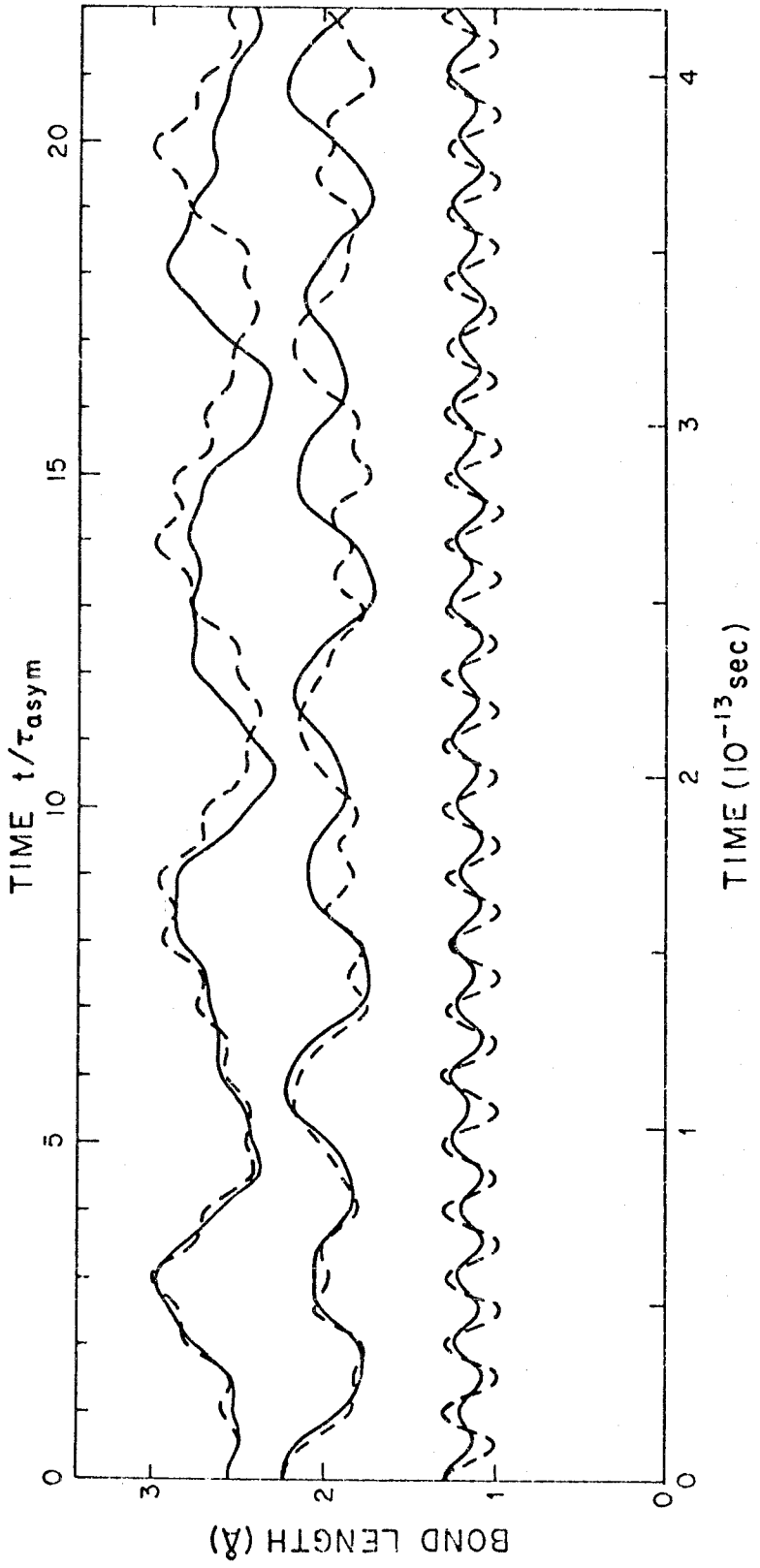
BOND LENGTH (Å)
TIME t/τ_{asym}
TIME (10^{-13} sec)
0
1
2
3
5
10
15
20
0
1
2
3
4

FIG. 19. Reactive excursion frequencies vs assumed critical length for the bonds in $ClNO^{18}$. All initial normal mode potential energies = 6.4 kcal/mole. —— actual trajectory, – – – – IVA and ····· SVA thereto.

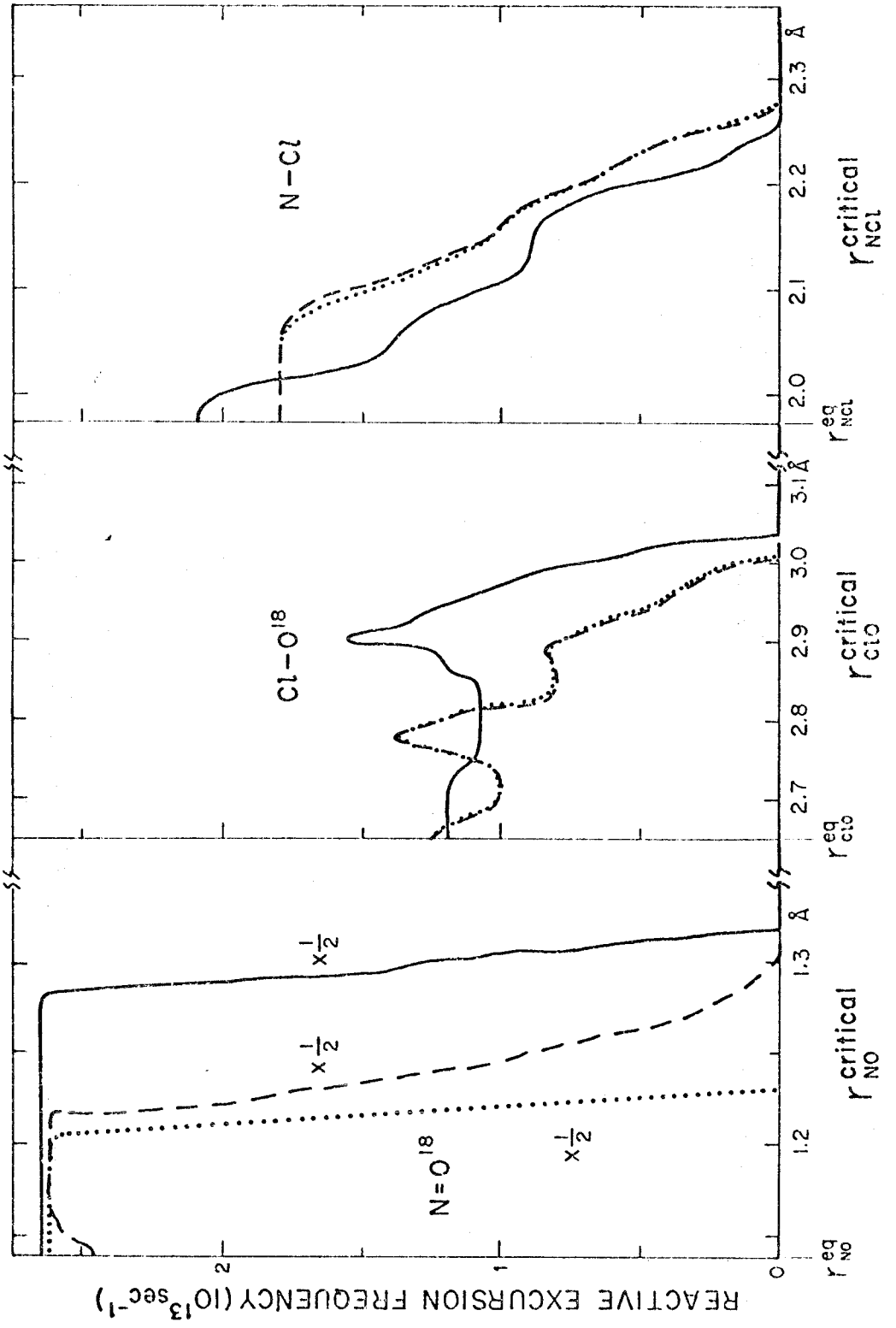
N-Cl
Cl-O18
N=O18
x 1/2
x 1/2
x 1/2
r critical NCl
r critical ClO
r critical NO
r eq NCl
r eq ClO
r eq NO
2.0
2.1
2.2
2.3 Å
2.7
2.8
2.9
3.0
3.1 Å
1.2
1.3 Å
0
1
2
REACTIVE EXCURSION FREQUENCY (10^13 sec^-1)

does not materially enhance intramolecular energy transfer. In this section, we will test this assumption for rotational energies comparable to a) those found in gases at reasonable temperatures and b) dissociation energies.

7.2.1. Small Amounts of Rotational Energy

By the method outlined in Section 6.2.2., a rotational energy of 2.39 kcal/mole was superimposed on the vibrationally excited molecules of Sections 7.1.2. and 7.1.3. This energy corresponds to $\frac{3}{2}$ kT, where T = 800°K. At this temperature many gas phase reaction rates are appreciable. For a symmetric-top, rigid-rotor M_3, this energy (42) is close to the level with quantum numbers K = J = 33. The rotations of this energy to be discussed below were in plane, i.e., taken about the axis perpendicular to the plane of the molecule ($\hat{z}$).

Calculations on symmetrically stretching M_3 were not performed since an in-plane rotation cannot break this symmetry. As a result, this rotation cannot couple the symmetric motion to other vibrational modes.

The bending mode, which is <u>stable</u> in non-rotating M_3 (Figure 6), is coupled to the asymmetric stretch under this rotation (Figure 20). When the initial bending mode energy is D_o, and 2.39 kcal/mole of in-plane rotational energy are added, all the vibrational energy is exchanged between these modes with a period of 4.4×10^{-13} seconds. The bending symmetry is broken by the rotational Coriolis forces as discussed in Section 7.1.2.

FIG. 20. Normal mode energies in vibrating, rotating M_3. Initial bend mode potential energy = 119.43 kcal/mole. Initial in-plane rotational energy = 2.39 kcal/mole. —— symmetric stretch, – – – bend, — – — asymmetric stretch, — – – — sum of normal mode energies.

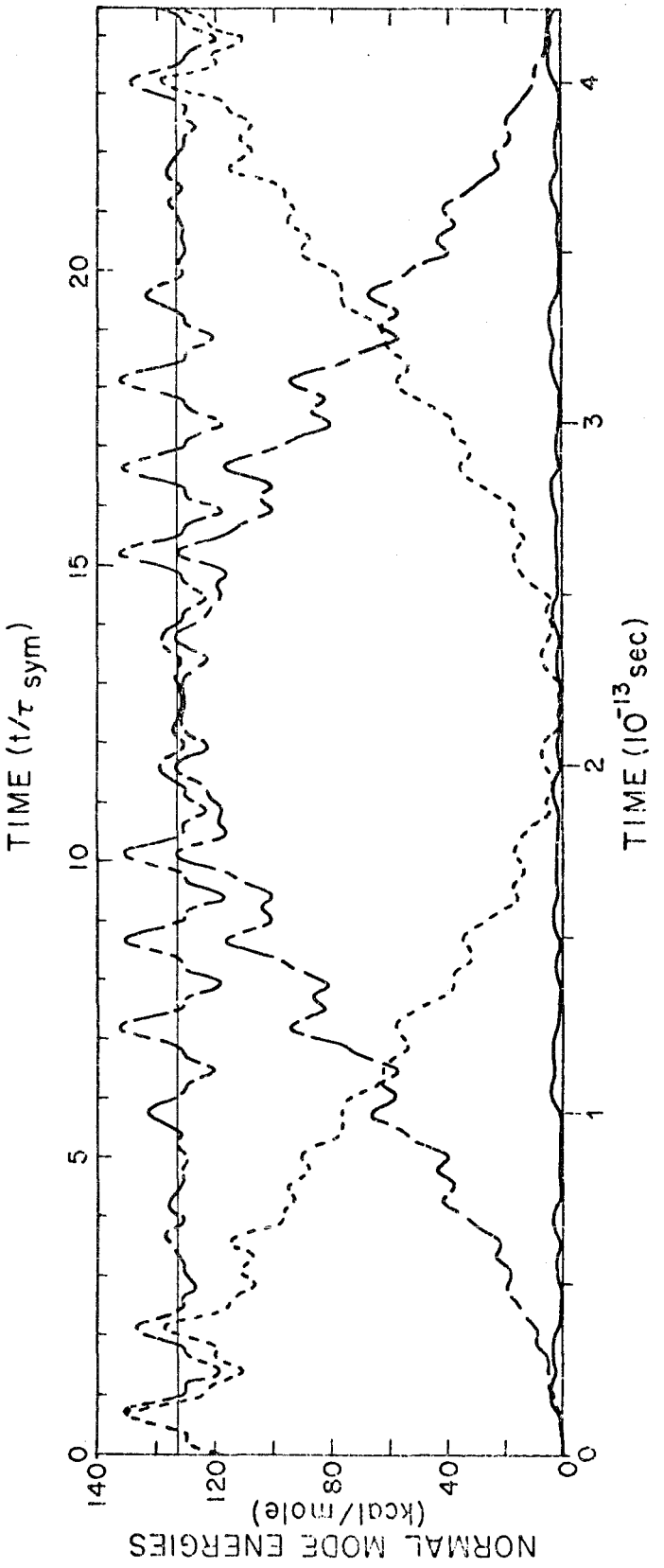
NORMAL MODE ENERGIES
(kcal/mole)
0
40
80
120
140
TIME (t/τ_{sym})
0
5
10
15
20
TIME (10^{-13} sec)
0
1
2
3
4

These forces augment those already present in the asymmetric stretch and when this mode has D_o initial energy, the 1.5×10^{-12} second coupling period observed in the absence of rotation is reduced to 0.37×10^{-12} seconds. Thus, this moderate molecular rotation has more than quadrupled the intramolecular energy transfer rate in this case. This is not a minor perturbation.

When all three of the vibration modes in M_3 are excited to $D_o/3$ energy each and the molecule is given 2.39 kcal/mole of in-plane rotation, the pure vibration coupling period of 1.6×10^{-12} seconds is reduced to 0.32×10^{-12} seconds. Here the intramolecular energy transfer rate increases by a factor of 5.

In summary, there can be no justification for ignoring rotation when treating intramolecular energy exchange in M_3.

The high energy vibrations in ClNO[18] (Section 7.1.3.) exhibit, in the main, intramolecular energy transfer rates which are of the order of the molecules frequencies. It is difficult to imagine how rotation could increase these rates by a factor of 4 or 5, in a molecule that is already "scrambling saturated." Aside from the N=O stretch, nitrosyl chloride's pure symmetric stretch is the only mode with any stability to it. Initially pure 19.2 kcal/mole symmetric stretch energy stays approximately constant for about (Figure 9d) 6×10^{-13} seconds. As seen in Figure 21, the addition of 2.39 kcal/mole of in-plane rotation reduces this metastable lifetime to about 3.7×10^{-13} seconds. The rotation has enhanced the growth of the bending mode by a factor of about 1.6 --- non-negligible, but hardly as impressive as the M_3 rotation results.

FIG. 21. Vibrating, rotating $ClNO^{18}$. Initial symmetric stretch mode potential energy = 19.2 kcal/mole. Initial in-plane rotational energy = 2.39 kcal/mole. Cf. Fig. 9.

a. Bond lengths. —— NO^{18}, – – – ClO^{18}, — – — NCl, — – – – sum of two smallest bond lengths.

b. Bond energies. — – – – sum of bond energies.

c. Eckart energies. – – – vibration kinetic, — – — rotation, —— Coriolis or vibration-rotation interaction.

d. Normal Mode energies. —— asymmetric stretch, — – — symmetric stretch, – – – – bend, — – – – sum of normal mode energies.

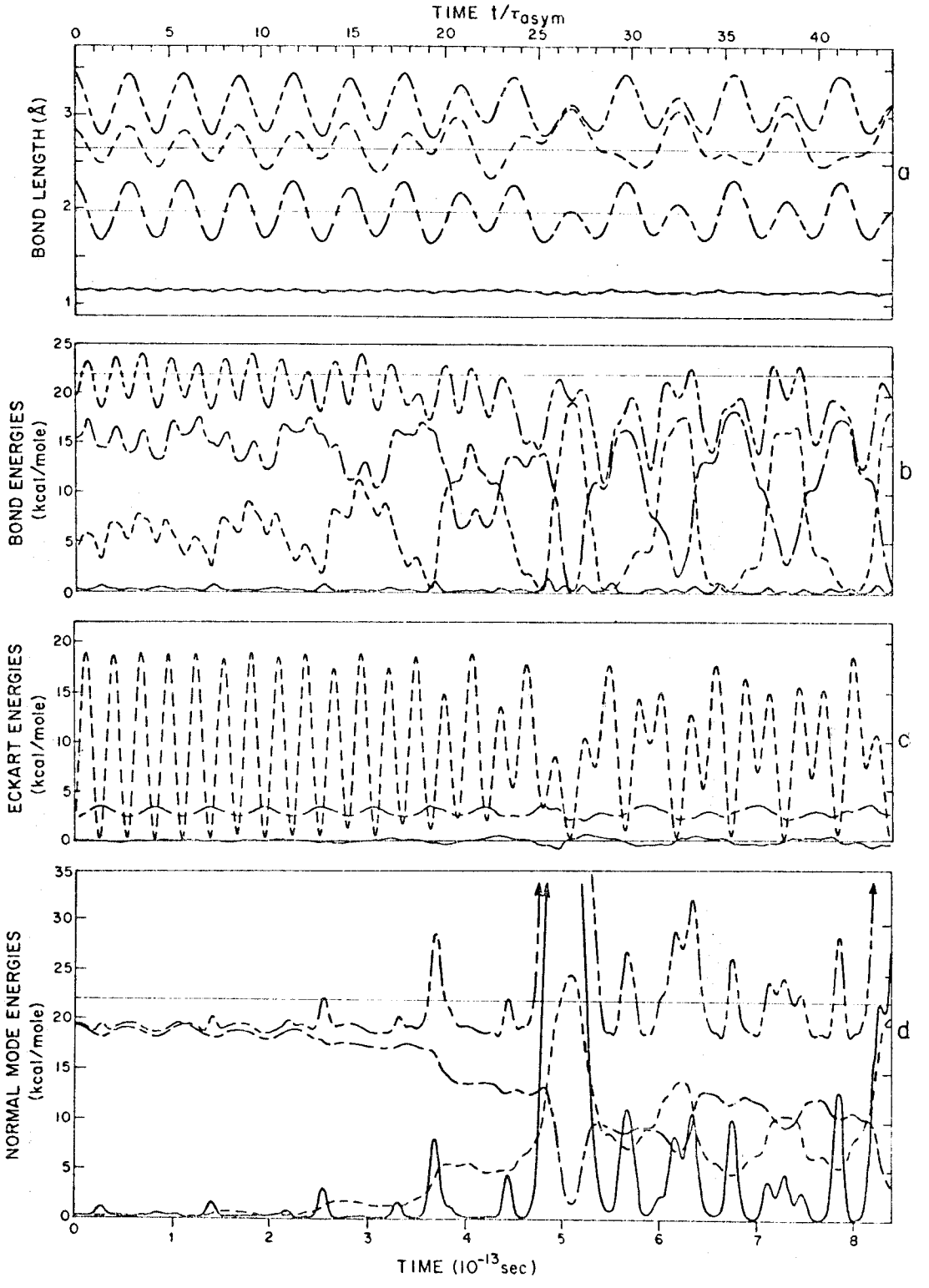
TIME t/τ_{asym}
0
5
10
15
20
25
30
35
40
BOND LENGTH (Å)
1
2
3
a
BOND ENERGIES (kcal/mole)
0
5
10
15
20
25
b
ECKART ENERGIES (kcal/mole)
0
5
10
15
20
c
NORMAL MODE ENERGIES (kcal/mole)
0
5
10
15
20
25
30
35
d
0
1
2
3
4
5
6
7
8
TIME (10^{-13}sec)

One would expect rotation to enhance large bending amplitudes, by virtue of centrifugal forces. In the absence of rotation, initially pure symmetrically stretching (19.2 kcal/mole) $ClNO^{18}$ eventually gained enough bend energy to open the valence angle past 180^{o}. As seen in Figure 21a, the rotation changes the course of the coupling such that the bend energy peaks at a value less than sufficient to make the molecule go through linearity. Thus, the rotation did not automatically enhance bend amplitudes. Its action is more subtle.

Rotation alters the character of the vibrations after the rise of the bend energy. In the non-rotating case, this energy decayed as if the molecule were going to exchange bend and symmetric stretch energy periodically. Even having passed through linearity, the molecule seemed in possession of a memory to allow the reconstruction of the symmetric stretching vibrations. Figure 21c shows that the rotation has erased this memory. If the non-rotating near periodicity of motion was a manifestation of the metric decomposability of harmonic phase spaces, it appears as if rotation destroys this property. This is in contradiction with Bunker's discovery that rotation did not release the sufficiently energized, yet non-dissociating trajectories from their phase space prisons.

With regard to the neglect of rotational effects in the contemporary unimolecular reaction rate theories, the following may be stated with some certainty for harmonic molecules. In rigid complexes, that is, dissociating species whose molecular parameters are not much different from their rigid bound state ones, rotational effects are expected to be large, because their

energy scrambling rates are not saturated by their vibrations. On the other hand, in loose complexes, rotation is likely to alter the details of the nuclear trajectories more seriously than the rate of intramolecular energy transfer.

There is a competing effect mentioned by Marcus (6c) that in energized loose complexes, the moment of inertia in dissociative configurations (called +) is much larger than in non-dissociative configurations (called *). From equation (5.3.-3) and the definition of the moment of inertia matrix, Π, it can be shown that

$$2T_r = \underset{\sim}{\omega} \cdot (\Pi \underset{\sim}{\omega}) \ . \qquad (7.2.1.-1)$$

To the rigid rotor approximation, $\underset{\sim}{\omega} = \Pi^{-1} \underset{\sim}{L}$, where $\underset{\sim}{L}$ is the angular momentum vector. Then to this approximation,

$$2T_r = (\Pi^{-1} \underset{\sim}{L}) \cdot \underset{\sim}{L} \ . \qquad (7.2.1.-2)$$

Since the angular momentum is rigorously conserved, $T_r^+ < T_r^*$, because the elements of Π^+ are larger than those of Π^*, rendering the elements of Π^{-1+} smaller than those of $\Pi^{-1}*$. The decrease in rotational energy in + must have been accomplished by a gain in its vibrational energy, since vibration-rotation energies are usually small and total energy is conserved. Larger initial rotational energies will therefore produce a larger $\Delta E = T_r^* - T_r^+$, which will contribute to the molecule's vibrations in +. At the relatively low energy rotations we have been discussing, ΔE is

likely to be a negligible contribution to the already high energy vibrations. (This effect would be appreciable if the rotational energies were comparable to the vibrational ones.) Therefore, for small amounts of rotational energy, the major effect of rotation should be on the rate of intramolecular energy transfer.

7.2.2. Large Amounts of Rotational Energy

When the total rotational energy is taken to be 38.2 kcal/mole (about $D_o/3$), the corresponding rotational temperature is about 13,000°K. Clearly, we are sampling molecules in the far tail of the rotational energy distribution. If we give these rotations to the highly energized molecules of Section 7.1., such molecules are going to have negligible statistical weight in a gas reacting at temperatures normally attainable in the laboratory, even in high temperature ovens or shock tubes. We sample them not to suggest that they are representative but to examine the effects of large amounts of rotation on vibrating systems. For a symmetric-top, rigid-rotor M_3, this 38.2 kcal/mole of rotation energy corresponds closely to that of the $K = J = 135$ quantum level.

The bending mode in M_3 is stable under rotations about the $\hat{\underset{\sim}{x}}$ and $\hat{\underset{\sim}{y}}$ axes (see Figure 1) in the molecular plane. Neither of these rotations breaks the C_{2v} symmetry of the bending motion (43). They will, however, couple with the bending vibration to make its energy fluctuate with time. In the case of rotation about the $\hat{\underset{\sim}{y}}$ axis, a bend energy initially equal to D_o oscillates from 0.9 to 1.65 D_o. The Coriolis (vibration-rotation interaction) energy remains zero to as many digits as the computer calculates it,

indicating that the residual angular momentum in the Eckart system is zero or that the Eckart axes are rotating perfectly with the molecule. This does not imply, however, that we have made the best choice of displacement co-ordinates in the rotating system. Just as the normal mode energies were defined in the Eckart system to reduce the magnitudes of the model's displacement vectors, so too, Wolfsberg (44) suggests, the model's equilibrium vectors should be reset to their centrifugally distorted values, when the model is rotated. The model, so distorted, would rotate without vibrating, which should therefore be a more consistent choice of the equilibrium configuration. Were our equilibrium vectors to be so redefined, the displacement vectors and resultant normal mode energies would doubtless be smaller. But as the SVA normal mode energies were not rigorous constants of the motion, even in the absence of rotation, the improved definition would not affect our conclusions in this regard.

In plane 38.2 kcal/mole rotation is expected to develop very large Coriolis forces on vibrating systems. These forces couple the bend asymmetric stretch symmetries. It is seen from Figure 22c that D_o bend energy, which gave stable motion without rotation (Figure 6), exchanges all available energy with the asymmetric stretch with a period of only 10^{-13} seconds. The Coriolis energy fluctuates in Figure 22b, rising as high as 0.1 D_o. This too indicates strong interaction between all the internal degrees of freedom.

High energy tumbling (rotation about the $\hat{x}$ or $\hat{y}$ axes) causes the asymmetric stretch in M_3 (for an initial asymmetric stretch energy of D_o) to couple with the bend mode with a period

FIG. 22. High energy vibrating, rotating M_3. Initial bend mode potential energy = 119.43 kcal/mole. Initial in-plane rotational energy = 38.2 kcal/mole.

a. Bond lengths. —— bond 1, – – – bond 2, — – — bond 3.

b. Eckart energies. —— vibration kinetic, – – – – rotation, — – — Coriolis.

c. Normal mode energies. —— symmetric stretch, – – – – bend, — – — asymmetric stretch, — – – — sum of normal mode energies.

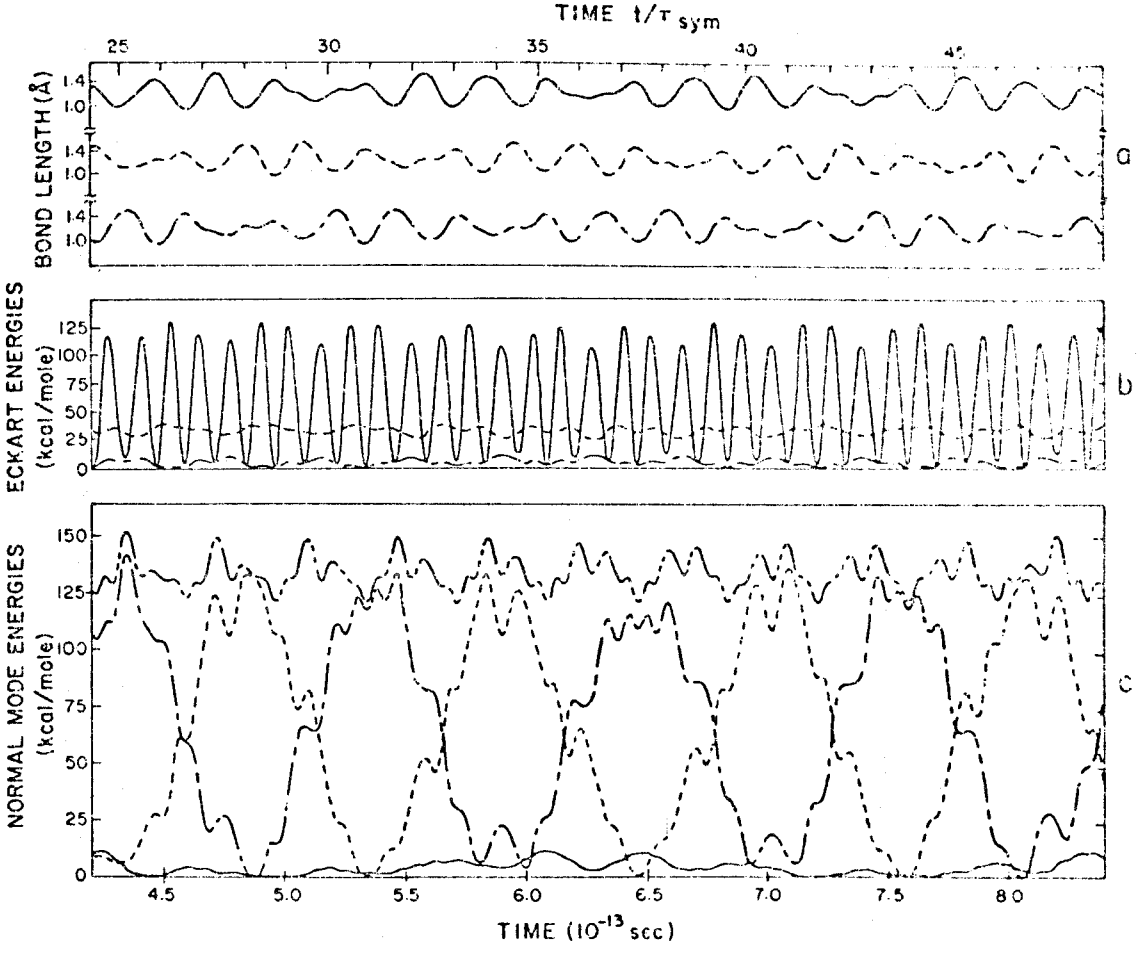
TIME t/τ_{sym}
25
30
35
40
BOND LENGTH (Å)
1.4
1.0
a
ECKART ENERGIES
(kcal/mole)
125
100
75
50
25
0
b
NORMAL MODE ENERGIES
(kcal/mole)
150
125
100
75
50
25
0
c
4.5
5.0
5.5
6.0
6.5
7.0
7.5
8.0
TIME (10^{-13} sec)

of 4.2×10^{-13} seconds when the rotational energy is about 38.2 kcal/mole ($D_o/3$). The inefficiency of tumbling to enhance energy scrambling is now apparent, since a mere 2.39 kcal/mole (0.02 D_o) of in-plane rotation energy caused the asymmetric and bend modes to couple faster than this with a period of only 3.72×10^{-13} seconds. As anticipated then, in-plane 38.2 kcal/mole rotation couples these two modes with great speed. The energy exchange period under this rotation is now 4.3×10^{-14} seconds. Since the natural periods of both bend and asymmetric stretch are 2.44×10^{-14} seconds, this massive in-plane rotation energy seems to have almost saturated the coupling rate in this stiff model.

The degree of enhancement of intramolecular energy exchange rate for this rotation is extremely high. Consider that Coriolis forces vary directly (38) with the angular velocity. By equation (7.2.1.-1), the angular velocity varies with the square root of the rotational energy. Thus, Coriolis forces vary with the square root of the rotational energy (to a zeroth order approximation). The Coriolis forces in the 38.2 kcal/mole rotation should be four times as large as those in the 2.39 kcal/mole rotation. Yet, the coupling frequency is not 4 but almost 9 times greater in the former.

Being separated in frequency from the other modes, the symmetric stretch in M_3 does not couple well with them. It couples to all the rotations since symmetric stretch produces large changes in all the moments of inertia. For example, when D_o is introduced into the symmetric stretching mode of M_3 which is then rotated about the $\hat{y}$ axis with an additional $D_o/3$ energy, the symmetric mode energy fluctuates by about $0.3\ D_o$. Nevertheless,

all vibration and/or rotation combinations mentioned thus far fail to excite any appreciable energy in the symmetric mode. It is then fairly surprising to find that under $D_o/3$ energy rotation about either the $\hat{\underset{\sim}{x}}$ or $\hat{\underset{\sim}{z}}$ axes, M_3, initialed with $D_o/3$ in each of its normal modes, exhibits evidence of coupling of its symmetric stretch to the other modes. This is most clear for the $\hat{\underset{\sim}{z}}$ axis rotation (Figure 23), wherein the strongly coupled bend and asymmetric stretch modes exchange energies rapidly (2×10^{-14} seconds) within an energy envelope which appears coupled to the symmetric stretch energy. The latter varies slowly (2×10^{-13} seconds) over a 0.5 D_o range.

In summary, we conclude that massive rotational energies are capable of producing intramolecular energy scrambling on time scales of the order of the molecular vibration periods themselves. Modest rotational energies enhance the scrambling rate in vibrationally excited molecules by factors of 1.5 for loose to 5 for rigid complexes.

FIG. 23. Normal modes in high energy vibrating, rotating M_3. All initial normal mode energies = 39.8 kcal/mole. Initial in-plane rotational energy = 38.2 kcal/mole. —— symmetric stretch, – – – – bend, — – — asymmetric stretch, ——— sum of normal mode energies.

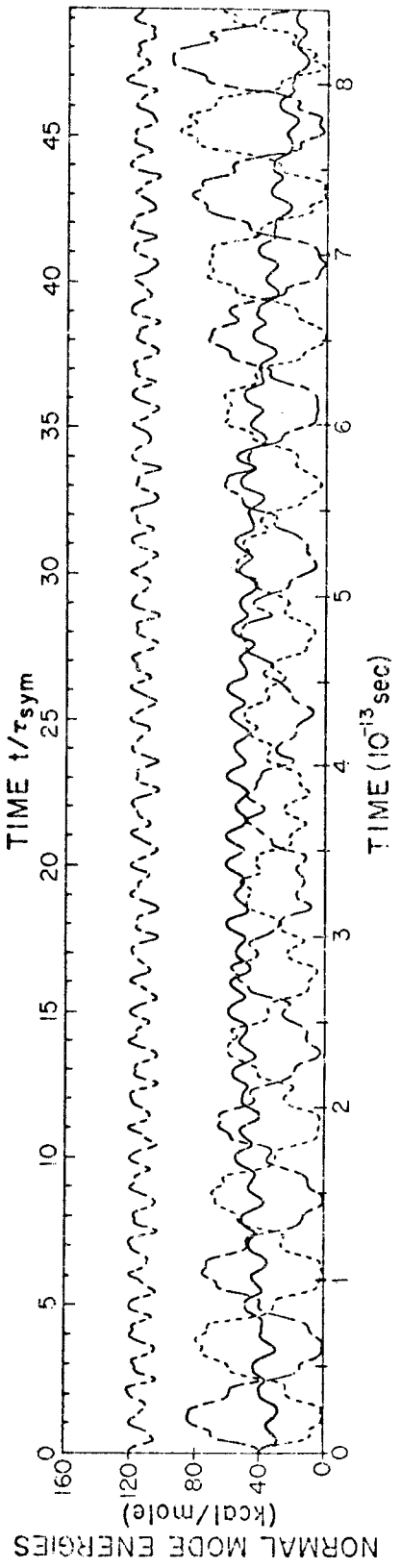
NORMAL MODE ENERGIES
(kcal/mole)
160
120
80
40
0
TIME t/τsym
0
5
10
15
20
25
30
35
40
45
TIME (10⁻¹³ sec)
0
1
2
3
4
5
6
7
8

8. Summary

We have shown that Slater's small vibration approach to the classical dynamics of bent triatomic molecules is inapplicable at energies approaching those necessary for reaction. Slater's assumption of constancy of the normal mode energies fails for the harmonic $ClNO^{18}$ model at energies above 25% of the dissociation energy for the molecule. This failure is due to the breakdown of the small vibration approximation at these energies. Despite this failure, Slater's formulae for reaction frequencies is shown to give values in good agreement with the actual reaction frequencies in our harmonic models.

The assumption of weak coupling between molecular harmonic oscillators, used in the RRKM theories, is shown to be a poor one at all energies, if the oscillators are taken to be the interatomic bonds. If, instead, the RRKM oscillators are assumed to be the normal modes, they are indeed weakly coupled at low energies (of the order of zero-point energies). As the energy in the molecule approaches that necessary for reaction, the oscillators couple strongly, and not only their individual energies but also the sum of those energies fail to be constants of the motion. The difference between this sum and the constant total energy is the oscillator coupling energy, which is not negligible, as assumed in the RRKM theories.

None of the theories mentioned treats the effect of rotation on the intramolecular energy transfer rates. These effects can be quite large. At rotational energies corresponding to $800^{o}K$, the energy scrambling rates in $ClNO^{18}$ (vibrating with 19.2 kcal/mole)

are increased by 60%. The enhancement is expected to be larger in molecules more rigid than nitrosyl chloride.

Thus, some basic assumptions in contemporary theories of unimolecular reaction are shown to be inadequate when applied to the high energy dynamics of this simplest of molecular models --- the bent harmonic triatom.

REFERENCES

1. N. B. Slater, Theory of Unimolecular Reactions, Cornell University Press, Ithaca, 1959, Chapters 2, 5, 7, 9.

2. L. S. Kassel, Kinetics of Homogeneous Reactions, Chemical Catalog Company, Inc., New York, 1932, Chapter V and references therein.

3. S. W. Benson, Foundations of Chemical Kinetics, McGraw-Hill Book Company, Inc., New York, 1960, Chapters X and XI.

4. H. S. Johnston, Gas Phase Reaction Rate Theory, Ronald Press Company, New York, 1966, Chapter 15.

5. D. L. Bunker, Theory of Elementary Gas Reaction Rates, International Encyclopedia of Physical Chemistry and Chemical Physics, Topic 19, Volume 1, Permagon Press, New York, 1966, Chapter 3.

6. (a) R. A. Marcus, J. Chem. Phys. 20, 359 (1952); (b) G. M. Wieder and R. A. Marcus, J. Chem. Phys. 37, 1835 (1962); (c) R. A. Marcus, J. Chem. Phys. 43, 2658 (1965); and references therein.

7. L. Pauling and E. B. Wilson, Jr., Introduction to Quantum Mechanics, McGraw-Hill Book Company, Inc., New York, 1935, Section X-37, pp. 282-290.

8. Reference 1, Chapter 5.

9. (a) E. Thiele and D. J. Wilson, J. Phys. Chem. 64, 473 (1960); (b) N. B. Slater, J. Phys. Chem. 64, 476 (1960).

10. Reference 2, Chapter V, Footnote 11.

11. Reference 1, p. 30 Footnote.

12. E. Thiele and D. J. Wilson, J. Chem. Phys. 35, 1256 (1961).

13. D. L. Bunker, J. Chem. Phys. 37, 393 (1962).

14. D. L. Bunker, J. Chem. Phys. 40, 1946 (1964).

15. C. A. Parr, A. Kuppermann, and R. N. Porter, forthcoming.

16. L. I. Schiff, Quantum Mechanics, McGraw-Hill Book Company, Inc., New York, 1955, pp. 131-134. A dynamical function is a classical constant of the motion if it has no explicit time dependence and its Poisson bracket with the Hamiltonian is zero. It is a quantal constant of the motion if its associated operator exists and commutes with the Hamiltonian and, again, there is no explicit time dependence. The relation between the commutator and the Poisson bracket given in Schiff's equation (23.9), $[A, B] = i\hbar \{A, B\}$, verifies the statement made in the text, which refers only to dynamical functions which are defined both classically and quantum mechanically.

17. G. Herzberg, Molecular Spectra and Molecular Structure. I. Spectra of Diatomic Molecules, D. Van Nostrand Company, Inc., Princeton, 1950, Second Edition, pp. 558-560.

18. J. R. Durig and R. C. Lord, Spectrochim. Acta. 19, 421 (1963).

19. W. B. Eberhardt and T. G. Burke, J. Chem. Phys. 20, 529 (1953).

20. (a) G. V. Calder and W. F. Giauque, J. Phys. Chem. 69, 2443 (1965); (b) W. H. Evans, T. R. Munson, and D. D. Wagman, J. Res. Nat'l. Bur. Std. 55, 147 (1955). Calder and Giauque misquote Evans et al. by interchanging the ΔH_0^o values for the dissociation of Cl_2 and I_2.

21. A. Kuppermann and R. N. Porter, Abstracts of Papers, 141st Meeting of the American Chemical Society, March 1962, pp. 9R, 10R.

22. For our purposes, phase space is metrically decomposable if trajectories can be trapped in some subvolume in the constant energy hypershell and are incapable of crossing the boundaries of that volume. In the SVA, all trajectories are so contained, since they may not wander into regions of the hypershell wherein the normal mode energies differ from their initial values.

23. Reference 1, pp. 58, 91. Slater's high pressure rate constant is $k_\infty = \bar{\nu} \exp(-E_o/kT)$, where E_o is the minimum energy for dissociation, k and T are the Boltzmann constant and absolute temperature and the frequency factor, $\bar{\nu}$, is a root mean square of the model's normal mode frequencies, ν_i, according to

$$\bar{\nu} = \left\{ \sum_{i=1}^{n} \alpha_{ri}^2 \nu_i^2 / \sum_{i=1}^{n} \alpha_{ri}^2 \right\}^{1/2}$$

where the α_{ri} are defined by the expression which relates the normal mode co-ordinates, Q_i, to the reaction co-ordinate, q_r:

$$q_r = \sum_{i=1}^{n} \alpha_{ri} Q_i \cdot$$

24. The notation used in these equations will be defined by the following example. Let

$$\dot{\underset{\sim}{X}}_i = \dot{X}_i \hat{\underset{\sim}{X}} + \dot{Y}_i \hat{\underset{\sim}{Y}} + \dot{Z}_i \hat{\underset{\sim}{Z}}$$

and $$\underset{\sim}{P}_i = P_{i_X} \hat{\underset{\sim}{X}} + P_{i_Y} \hat{\underset{\sim}{Y}} + P_{i_Z} \hat{\underset{\sim}{Z}} \cdot$$

Then the equation $\dot{\underset{\sim}{X}}_i = \partial \mathcal{H} / \partial \underset{\sim}{P}_i$ will be taken to mean $\dot{X}_i = \partial \mathcal{H} / \partial P_{i_X}$ and $\dot{Y}_i = \partial \mathcal{H} / \partial P_{i_Y}$ and $\dot{Z}_i = \partial \mathcal{H} / \partial P_{i_Z}$.

25. As an example, $|\underset{\sim}{X}_1 - \underset{\sim}{X}_3| = [(\underset{\sim}{X}_1 - \underset{\sim}{X}_3) \cdot (\underset{\sim}{X}_1 - \underset{\sim}{X}_3)]^{1/2}$.

26. Reference 17, p. 101 and references therein.

27. This choice does not sacrifice generality, since it simply specifies the initial orientation of r_2 vector with respect to the X axis. This initial orientation is arbitrary anyway.

28. H. Margenau and G. M. Murphy, The Mathematics of Physics and Chemistry, D. Van Nostrand Company, Inc., Princeton, 1956, Second Edition, pp. 319-322, 331.

29. See, for example, F. Villars, Nucl. Phys. 3, 240 (1957).

30. C. Eckart, Phys. Rev. 47, 552 (1935).

31. (a) E. B. Wilson, J. C. Decius, and P. C. Cross, Molecular Vibrations, McGraw-Hill Book Company, Inc., New York, 1955; (b) p. 275, footnote 1; (c) Appendix I, p. 285.

Note that our ψ is WDC's x; (d) Chapter 4; (e) Chapter 11; (f) p. 277, equation (2) where $\underset{\sim}{L} \equiv \underset{\sim}{\mathfrak{M}}$, $\underset{\sim}{x}_i \equiv \underset{\sim}{r}_i$, $\dot{\underset{\sim}{x}}_i \equiv \underset{\sim}{v}_i$ in WDC's notation. The first term on the rhs of equation (2) is $\Pi \underset{\sim}{\omega}$; (g) Appendix VIII.

32. This routine was extended from one donated to us by Dr. T. Latta. His 4th order version of this integrator is in IBM 7090 machine language at the University of Illinois Computer Library under D2-UØI-ADM3-36-SR.

33. J. B. Scarborough, Numerical Mathematical Analysis, Johns Hopkins Press, Baltimore, 1962, 5th Edition, pp. 318-325.

34. S. Gill, Proc. Camb. Philos. Soc. 47, 96 (1951). This reference contains extensive derivational and error analysis sections.

35. The following references gave valence not central field (pairwise) force constants. We used k_1 and k_3 as they were and approximated k_2, the non-bonded force constant, from the valence bending force constant, k_θ, by the relation $k_2 = k_\theta(r_2^{eq}\sin\theta^{eq})^2/r_1^{eq}r_3^{eq}$. (a) D. Papousek and J. Pliva, Coll. Czech. Chem. Comm. 29, 1973 (1964); (b) K. Kuchitsu and Y. Morino, Bull. Chem. Soc. Japan 38, 814 (1965); (c) L. Landau and W. H. Fletcher, J. Molec. Spectrosc. 4, 276 (1960); (d) R. D. Sprateley, J. J. Turner, and G. C. Pimentel, J. Chem. Phys. 44, 2063 (1966).

36. A. Sommerfeld, Lectures on Theoretical Physics. Volume I Mechanics, Academic Press, New York, 1964, pp. 106-110.

37. G. Herzberg, Molecular Spectra and Molecular Structure. III. Electronic Spectra and Electronic Structure of Polyatomic Molecules, D. Van Nostrand Company, Inc., Princeton, 1966, p. 604.

38. H. Goldstein, Classical Mechanics, Addison-Wesley Publishing Company, Inc., Reading, Mass., 1950, pp. 135-140.

39. Reference 3, pp. 154-155, Table VII. 2.

40. $D_e(Cl{-}{-}NO^{18}) = \Delta H_0^o(Cl{-}{-}NO^{16}) + \frac{hc}{2}\left[\sum_{i=1}^{3} \omega_i(ClNO^{16}) - \omega(NO^{16})\right]$ where the molecular frequencies are obtained from references (18) and (17), and $\Delta H_0^o(Cl{-}{-}NO^{16})$ comes from references (20a) and (20b), which give $\Delta H_0^o(ClNO^{16} \longrightarrow NO^{16} + \frac{1}{2}Cl_2)$ and $\Delta H_0^o(\frac{1}{2}\, Cl_2 \longrightarrow Cl)$ respectively.

41. Reference 1, Chapter 4.

42. N. Davidson, Statistical Mechanics, McGraw-Hill Book Company, Inc., 1962, p. 172, Equation (11-7).

43. A rotation about the axis $\hat{\underset{\sim}{x}} + \hat{\underset{\sim}{y}}$, for example, would break the C_{2v} symmetry, but such rotations were not performed.

44. M. Wolfsberg, personal communication.

45. These λ_i are not pure numbers, as they were in Section 4. 2. Here they have the same dimensions as the GG IF elements, namely, the units of force constants divided by the units of mass, or seconds^{-2}.

Appendix 1. General Form for the SVA Solution of the Equations of Motion M_3

The internuclear distances can be obtained as functions of the displacement vectors for M_3 by substitution of (4.1.-7) into (4.1.-5):

$$\begin{aligned} \underset{\sim}{r}_1 &= \underset{\sim\sim}{\Delta X}_1 + 2\underset{\sim\sim}{\Delta X}_3 + \underset{\sim}{X}_1^{eq} + 2\underset{\sim}{X}_3^{eq} \\ \underset{\sim}{r}_2 &= \underset{\sim\sim}{\Delta X}_1 - \underset{\sim\sim}{\Delta X}_3 + \underset{\sim}{X}_1^{eq} - \underset{\sim}{X}_3^{eq} \\ \underset{\sim}{r}_3 &= 2\underset{\sim\sim}{\Delta X}_1 + \underset{\sim\sim}{\Delta X}_3 + 2\underset{\sim}{X}_1^{eq} + \underset{\sim}{X}_3^{eq} \ . \end{aligned} \tag{A1-1}$$

The length of these vectors, to first order in the components of $\underset{\sim\sim}{\Delta X}_i/r^{eq}$, are given by

$$\begin{aligned} r_1 &\simeq r^{eq} + (\underset{\sim\sim}{\Delta X}_1 + 2\underset{\sim\sim}{\Delta X}_3) \cdot (\underset{\sim}{X}_1^{eq} + 2\underset{\sim}{X}_3^{eq})/r^{eq} \\ r_2 &\simeq r^{eq} + (\underset{\sim\sim}{\Delta X}_1 - \underset{\sim\sim}{\Delta X}_3) \cdot (\underset{\sim}{X}_1^{eq} - \underset{\sim}{X}_3^{eq})/r^{eq} \\ r_3 &\simeq r^{eq} + (2\underset{\sim\sim}{\Delta X}_1 + \underset{\sim\sim}{\Delta X}_3) \cdot (2\underset{\sim}{X}_1^{eq} + \underset{\sim}{X}_3^{eq})/r^{eq} \ . \end{aligned} \tag{A1-2}$$

Substitution of these equations into (4.1.-3) and (4.1.-4) and retaining only first order terms in $\underset{\sim\sim}{\Delta X}_i/r^{eq}$ gives

$$\dot{\underset{\sim}{P}}_1 \simeq -\frac{k}{r^{eq\,2}}\Big\{(\underset{\sim}{X}_1^{eq} + 2\underset{\sim}{X}_3^{eq})[(\underset{\sim\sim}{\Delta X}_1 + 2\underset{\sim\sim}{\Delta X}_3)\cdot(\underset{\sim}{X}_1^{eq} + 2\underset{\sim}{X}_3^{eq})]$$

$$+ (\underset{\sim}{X}_1^{eq} - \underset{\sim}{X}_3^{eq})[(\underset{\sim\sim}{\Delta X}_1 - \underset{\sim\sim}{\Delta X}_3)\cdot(\underset{\sim}{X}_1^{eq} - \underset{\sim}{X}_3^{eq})] \qquad \text{(A1-3)}$$

$$+ 2(2\underset{\sim}{X}_1^{eq} + \underset{\sim}{X}_3^{eq})[(2\underset{\sim\sim}{\Delta X}_1 + \underset{\sim\sim}{\Delta X}_3)\cdot(2\underset{\sim}{X}_1^{eq} + \underset{\sim}{X}_3^{eq})]\Big\}$$

and

$$\dot{\underset{\sim}{P}}_3 \simeq -\frac{k}{r^{eq\,2}}\Big\{2(\underset{\sim}{X}_1^{eq} + 2\underset{\sim}{X}_3^{eq})[(\underset{\sim\sim}{\Delta X}_1 + 2\underset{\sim\sim}{\Delta X}_3)\cdot(\underset{\sim}{X}_1^{eq} + 2\underset{\sim}{X}_3^{eq})]$$

$$- (\underset{\sim}{X}_1^{eq} - \underset{\sim}{X}_3^{eq})[(\underset{\sim\sim}{\Delta X}_1 - \underset{\sim\sim}{\Delta X}_3)\cdot(\underset{\sim}{X}_1^{eq} - \underset{\sim}{X}_3^{eq})] \qquad \text{(A1-4)}$$

$$+ (2\underset{\sim}{X}_1^{eq} + \underset{\sim}{X}_3^{eq})[(2\underset{\sim\sim}{\Delta X}_1 + \underset{\sim\sim}{\Delta X}_3)\cdot(2\underset{\sim}{X}_1^{eq} + \underset{\sim}{X}_3^{eq})]\Big\}\,.$$

These are the small vibration approximation to the equations of motion for $\dot{P}$. They can be rewritten as

$$\dot{\mathbb{P}} = -k\,\mathbb{B}\,\mathbb{X}/r^{eq\,2} \qquad \text{(4.1.-11)}$$

where $\mathbb{B} = (b_{ij})$ is given by

$$b_{11} = (X_1^{eq} + 2X_3^{eq})^2 + (X_1^{eq} - X_3^{eq})^2 + 4(2X_1^{eq} + X_3^{eq})^2$$

$$b_{12} = b_{21} = (X_1^{eq} + 2X_3^{eq})(Y_1^{eq} + 2Y_3^{eq}) + (X_1^{eq} - X_3^{eq})(Y_1^{eq} - Y_3^{eq})$$

$$+ 4(2X_1^{eq} + X_3^{eq})(2Y_1^{eq} + Y_3^{eq})$$

$$b_{13} = b_{31} = 2(X_1^{eq} + 2X_3^{eq})^2 - (X_1^{eq} - X_3^{eq})^2 + 2(2X_1^{eq} + X_3^{eq})^2$$

$$b_{14} = b_{41} = 2(X_1^{eq} + 2X_3^{eq})(Y_1^{eq} + 2Y_3^{eq}) - (X_1^{eq} - X_3^{eq})$$

$$\cdot (Y_1^{eq} - Y_3^{eq}) + 2(2X_1^{eq} + X_3^{eq})(2Y_1^{eq} + Y_3^{eq})$$

$$b_{22} = (Y_1^{eq} + 2Y_3^{eq})^2 + (Y_1^{eq} - Y_3^{eq})^2 + 4(2Y_1^{eq} + Y_3^{eq})^2 \qquad \text{(A1-5)}$$

$$b_{23} = b_{32} = 2(X_1^{eq} + 2X_3^{eq})(Y_1^{eq} + 2Y_3^{eq}) - (X_1^{eq} - X_3^{eq})(Y_1^{eq} - Y_3^{eq})$$

$$+ 2(2X_1^{eq} + X_3^{eq})(2Y_1^{eq} + Y_3^{eq})$$

$$b_{24} = b_{42} = 2(Y_1^{eq} + 2Y_3^{eq})^2 - (Y_1^{eq} - Y_3^{eq})^2 + 2(2Y_1^{eq} + Y_3^{eq})^2$$

$$b_{33} = 4(X_1^{eq} + 2X_3^{eq})^2 + (X_1^{eq} - X_3^{eq})^2 + (2X_1^{eq} + X_3^{eq})^2$$

$$b_{34} = b_{43} = 4(X_1^{eq} + 2X_3^{eq})(Y_1^{eq} + 2Y_3^{eq}) + (X_1^{eq} - X_3^{eq})(Y_1^{eq} - Y_3^{eq})$$

$$+ (2X_1^{eq} + X_3^{eq})(2Y_1^{eq} + Y_3^{eq})$$

$$b_{44} = 4(Y_1^{eq} + 2Y_3^{eq})^2 + (Y_1^{eq} - Y_3^{eq})^2 + (2Y_1^{eq} + Y_3^{eq})^2 \ .$$

The matrix $\mathbb{C}$ defined by (4.1.-16) is therefore given by $\mathbb{C} = (c_{ij})/(r^{eq})^2$, (i = 1, 2, 3, 4) where

$$c_{11} = (X_1^{eq} - X_3^{eq})^2 + 2(2X_1^{eq} + X_3^{eq})^2$$

$$c_{12} = c_{21} = (X_1^{eq} - X_3^{eq})(Y_1^{eq} - Y_3^{eq}) + 2(2X_1^{eq} + X_3^{eq})(2Y_1^{eq} + Y_3^{eq})$$

$$c_{13} = 2(2X_1^{eq} + X_3^{eq})^2 - (X_1^{eq} - X_3^{eq})^2$$

$$c_{14} = c_{23} = (2X_1^{eq} + X_3^{eq})(2Y_1^{eq} + Y_3^{eq}) - (X_1^{eq} - X_3^{eq})(Y_1^{eq} - Y_3^{eq})$$

$$c_{22} = (Y_1^{eq} - Y_3^{eq})^2 + 2(2Y_1^{eq} + Y_3^{eq})^2$$

$$c_{24} = (2Y_1^{eq} + Y_3^{eq})^2 - (Y_1^{eq} - Y_3^{eq})^2 \qquad \text{(A1-6)}$$

$$c_{31} = (X_1^{eq} + 2X_3^{eq})^2 - (X_1^{eq} - X_3^{eq})^2$$

$$c_{32} = c_{41} = (X_1^{eq} + 2X_3^{eq})(Y_1^{eq} + 2Y_3^{eq}) - (X_1^{eq} - X_3^{eq})(Y_1^{eq} - Y_3^{eq})$$

$$c_{33} = (X_1^{eq} - X_3^{eq})^2 + 2(X_1^{eq} + 2X_3^{eq})^2$$

$$c_{34} = c_{43} = (X_1^{eq} - X_3^{eq})(Y_1^{eq} - Y_3^{eq}) + 2(X_1^{eq} + 2X_3^{eq})(Y_1^{eq} + 2Y_3^{eq})$$

$$c_{42} = (Y_1^{eq} + 2Y_3^{eq})^2 - (Y_1^{eq} - Y_3^{eq})$$

$$c_{44} = (Y_1^{eq} - Y_3^{eq})^2 + 2(Y_1^{eq} + 2Y_3^{eq}) \quad .$$

Using the initial equilibrium positions given by (4.1.-13), we may reduce $\mathbb{C}$ to

$$\mathbb{C} = \begin{pmatrix} 3/2 & -\sqrt{3}/2 & -3/4 & -\sqrt{3}/4 \\ -\sqrt{3}/2 & 3/2 & -\sqrt{3}/4 & 3/4 \\ -3/4 & \sqrt{3}/4 & 3/2 & \sqrt{3}/2 \\ \sqrt{3}/4 & 3/4 & \sqrt{3}/2 & 3/2 \end{pmatrix} \qquad \text{(A1-7)}$$

from which (4.1.-29) can easily be obtained.

The physical significance of the ϵ_i given in equation (4.2.-7) becomes clear when we return to the q_i notation.

$$2\epsilon_i = \left[\sum_{j=1}^{3} (\mathbb{N}^{-1})_{ij}\, \dot{q}_j\right]^2 + \frac{k}{m}\left[\sum_{j=1}^{3} (\mathbb{N}^{-1})_{ij}\, q_j\right]^2 \qquad \text{(A1-8)}$$

$$\mathbb{N}^{-1} = \begin{pmatrix} -1 & -\sqrt{3} & -2 \\ -1/2 & \sqrt{3}/2 & -1 \\ 3\sqrt{3}/2 & 3/2 & \sqrt{3} \end{pmatrix} \quad . \qquad \text{(A1-9)}$$

The expansion of $\sum_{i=1}^{3} \left[\sum_{j=1}^{3} (\mathbb{N}^{-1})_{ij} \dot{q}_j \right]^2$ in terms of the $\dot{\Delta X}_i$

gives the same expression as does the kinetic energy

$$2T = m[2(\dot{\Delta X}_1)^2 + 2\dot{\Delta X}_1\dot{\Delta X}_3 + 2(\dot{\Delta X}_3)^2 + 2(\dot{\Delta Y}_1)^2 + 2\dot{\Delta Y}_1\dot{\Delta Y}_3 + 2(\dot{\Delta Y}_3)^2] \qquad \text{(A1-10)}$$

when the ΔY_3 in the latter are substituted by the first derivative of the rhs of equation (4.1.-26) . We conclude that

$$2T = \sum_{i=1}^{3} \dot{Q}_i^2 . \qquad \text{(4.2.-9)}$$

Similarly, substituting the SVA expressions for the r_j from (A1-2) into the expression for the potential energy (3.1.-14) , it may be shown that

$$2V = \frac{k}{m} \sum_{i=1}^{3} \lambda_i Q_i^2 . \qquad \text{(4.2.-10)}$$

Therefore,

$$E = \sum_{i=1}^{3} \epsilon_i \qquad \text{(A1-11)}$$

in the SVA.

Appendix 2. The GF Treatment for Triatomic Molecules with Pair-wise Bonds

In Section 4.3.2., matrices transforming Eckart displacement co-ordinates into normal mode ones were discussed. In this appendix, we outline the procedures used to obtain these matrices.

The GF method of Wilson, Decius, and Cross (31d) utilizes a set of co-ordinates intermediate to the transformation from displacement to normal mode ones. This new set is made up of the internal co-ordinates, S_i, the bond displacement co-ordinates. In the SVA, they are approximated by equations (A1-2), wherein the laboratory co-ordinates, $\underset{\sim}{X}_i$, are replaced by the Eckart ones, $\underset{\sim}{x}_i$. Those equations are specific to M_3. In our more general case

$$S_i = \sum_{j=1}^{3} \underset{\sim}{s}_{ij} \cdot \underset{\sim}{\Delta x}_j \qquad \text{(A2-1)}$$

where $\underset{\sim}{s}_{ij}$ is the unit vector in the direction of greatest increase of S_i due to displacements of nucleus j. In view of our numbering system (see Figure 1),

$$\underset{\sim}{s}_{ij} = (\underset{\sim}{x}_j^{eq} - \underset{\sim}{x}_k^{eq})/r_i^{eq} \quad \text{and} \quad \underset{\sim}{s}_{ij} = -\underset{\sim}{s}_{ik} \qquad \text{(A2-2)}$$

where i, j, k is a cyclic permutation of 1, 2, 3.

Equation (A2-1) may be rewritten as

$$\mathbb{S}' = \mathbb{M}' \Delta\mathbb{X}' \tag{A2-3}$$

where $\mathbb{S}'$ is the four by one matrix with elements S_1, S_2, S_3, and zero. The elements of the four by one matrix, $\Delta\mathbb{X}'$, are Δx_1, Δy_1, Δx_3, and Δy_3. The fourth row of the four by four matrix, $\mathbb{M}'$, contains the coefficients of the $\Delta\underset{\sim}{x}_i$ in the Eckart condition. If we then replace Δy_3 by using the Eckart relation between the displacement co-ordinates, we may rewrite (A2-3) as

$$\mathbb{S} = \mathbb{M} \Delta\mathbb{X} \tag{A2-4}$$

where these matrices have dimensions 3×1, 3×3, and 3×1 respectively. The general elements of the $\mathbb{M}$ matrix, $(\mathbb{M})_{ij} = M_{ij}$, become

$$M_{ij} = M'_{ij} + M'_{i4}M'_{4j}/M'_{44} \tag{A2-5}$$

where

$$M'_{11} = m_1 s_{1_x}/m_2$$

$$M'_{12} = m_1 s_{1_y}/m_2$$

$$M'_{13} = (1 + m_3/m_2)s_{1_x}$$

$$M'_{14} = (1 + m_3/m_2)s_{1_y}$$

$$M'_{21} = 1 = -M'_{23} \; ; \; M'_{22} = M'_{24} = 0$$

$$M'_{31} = (1 + m_1/m_2)s_{3_x}$$

$$M'_{32} = (1 + m_1/m_2)s_{3_y} \qquad \text{(A2-6)}$$

$$M'_{33} = m_3 s_{3_x}/m_2$$

$$M'_{34} = m_3 s_{3_y}/m_2$$

$$M'_{41} = m_1 s_{3_y} r_3^{eq}$$

$$M'_{42} = -m_1 s_{3_x} r_3^{eq}$$

$$M'_{43} = m_3 s_{1_y} r_1^{eq}$$

$$M'_{44} = -m_3 s_{1_x} r_1^{eq}$$

and

$$s_{1_x} = [m_1 x_1^{eq}/m_2 + (1 + m_3/m_2)x^{eq}]/r_1^{eq}$$

$$s_{1_y} = [m_1 y_1^{eq}/m_2 + (1 + m_3/m_2)y_3^{eq}]/r_1^{eq}$$

$$s_{3_x} = [(1 + m_1/m_2)x_1^{eq} + m_3 x_3^{eq}/m_2]/r_3^{eq}$$

$$s_{3_y} = [(1 + m_1/m_2)y_1^{eq} + m_3 y_3^{eq}/m_2]/r_3^{eq} .$$

When we substitute equations (4.1.-13) into the above, we obtain the $\mathbb{M}$ matrix for M_3 as

$$\mathbb{M} = \begin{pmatrix} -7/2 & -3\sqrt{3}/2 & -4 \\ 1 & 0 & -1 \\ -1/2 & -3\sqrt{3}/2 & -1 \end{pmatrix} . \qquad \text{(A2-7)}$$

For our problem, the matrix of force constants, $\mathbb{F}$, is diagonal, $(\mathbb{F})_{if} = k_i \delta_{ij}$, and

$$2V = \sum_{ij} (\mathbb{F})_{ij} S_i S_j . \qquad \text{(A2-8)}$$

Defining a matrix $\mathbb{G}$ by the elements

$$G_{ij} = \sum_{\ell=1}^{3} \underset{\sim}{s}_{i\ell} \cdot \underset{\sim}{s}_{\ell j}/m_\ell \qquad \text{(A2-9)}$$

the total kinetic energy of vibration may be expressed as

$$2T = \sum_{ij} (\mathbb{G}^{-1})_{ij} \dot{S}_i \dot{S}_j \qquad \text{(A2-10)}$$

where

$$\dot{S}_i = \sum_{j=1}^{3} \underset{\sim}{s}_{ij} \cdot \underset{\sim}{\dot{\Delta x}}_j = \sum_{j=1}^{3} \underset{\sim}{s}_{ij} \cdot \underset{\sim}{\dot{x}}_j \qquad \text{(A2-11)}$$

since $\underset{\sim}{\dot{x}}_j^{eq} = 0$. In matrix notation, equations (A2-8) and (A2-10) become

$$2T = \dot{\$}^{\dagger} \mathbb{G}^{-1} \dot{\$} \qquad \text{(A2-12)}$$

and

$$2V = \$^{\dagger} \mathbb{F} \$ \ . \qquad \text{(A2-13)}$$

We wish to obtain a set of normal mode co-ordinates, $\mathbb{Q}$ and velocities, $\dot{\mathbb{Q}}$, such that

$$2T = \dot{\mathbb{Q}}^{\dagger} \dot{\mathbb{Q}} \qquad \text{(A2-14)}$$

and

$$2V = \mathbb{Q}^{\dagger} \mathbb{\Lambda} \mathbb{Q} \ . \qquad \text{(A2-15)}$$

$\mathbb{Q}$ will be related to $\$$ according to

$$\$ = \mathbb{L} \mathbb{Q} \qquad \text{(A2-16)}$$

where $\mathbb{L}$ must satisfy

$$\mathbb{L}^{\dagger}\,\mathbb{F}\,\mathbb{L} = \mathit{\Lambda} \tag{A2-17}$$

and

$$\mathbb{L}^{\dagger}\,\mathbb{G}^{-1}\,\mathbb{L} = \mathbb{E} \tag{A2-18}$$

$\mathbb{E}$ being the identity matrix and $\mathit{\Lambda}$ a diagonal matrix. Following the treatment in WDC (31g), substitution of equation (A2-18) into (A2-17) yields

$$\mathbb{G}\,\mathbb{F}\,\mathbb{L} = \mathbb{L}\,\mathit{\Lambda} \tag{A2-19}$$

where $\mathit{\Lambda}$ is the diagonal matrix of eigenvalues of $\mathbb{G}\,\mathbb{F}$, $(\mathit{\Lambda})_{ij} = \lambda_i\,\delta_{ij}$ (45). The elements are the solutions to the cubic equation

$$|\mathbb{G}\,\mathbb{F} - \lambda_n\,\mathbb{E}| = 0. \tag{A2-20}$$

For M_3, $\mathbb{F} = k\,\mathbb{E}$, where k is the single force constant common to all three pairwise bonds. In this case

$$\mathbb{G} = \frac{1}{2m}\begin{pmatrix} 4 & 1 & 1 \\ 1 & 4 & 1 \\ 1 & 1 & 4 \end{pmatrix} \tag{A2-21}$$

where m is the mass common to all nuclei in M_3. The eigenvalues, λ_i, of the resultant $\mathbb{G}\mathbb{F}$ matrix for M_3 are 3k/m, 3k/2m, and 3k/2m (cf. footnote 45 and Section 4. 2.).

In general, once the eigenvalues are determined, the elements, L_{jn}, of the matrix $\mathbb{L}$ can be obtained from equations (A2-19) and (A2-17). The first of these gives

$$\sum_{j=1}^{3} [(\mathbb{G}\mathbb{F})_{ij} - \lambda_n \delta_{ij}] L_{jn} = 0 \quad (i, n=1, 2, 3) \ . \qquad \text{(A2-22}$$

But since its determinant is zero (A2-20), the matrix $\mathbb{G}\mathbb{F} - \lambda_n \mathbb{E}$ is singular, and the equations (A2-22) for L_{jn} are linearly dependent.

We now choose two linearly independent equations for L_{jn} (j=1, 2, 3) from among the three linearly dependent ones in (A2-22). Let the independent equations be

$$\sum_{j=1}^{3} \beta_{nj} L_{jn} = 0$$

and (A2-23)

$$\sum_{j=1}^{3} \gamma_{nj} L_{jn} = 0 \ .$$

The coefficients in (A2-23) are

$$\beta_{nj} = P_{ij} - \lambda_n \delta_{ij}$$

and (A2-24)

$$\gamma_{nj} = P_{kj} - \lambda_n \delta_{kj}, \quad \text{where } i \neq k.$$

Simultaneous solution of equations (A2-23) gives

$$L_{2n} = -L_{1n}(\gamma_{1n}\beta_{3n} - \beta_{1n}\gamma_{3n})/(\gamma_{2n}\beta_{3n} - \beta_{2n}\gamma_{3n})$$

$$L_{3n} = L_{1n}(\gamma_{1n}\beta_{2n} - \beta_{1n}\gamma_{2n})/(\gamma_{2n}\beta_{3n} - \beta_{2n}\gamma_{3n}) . \quad \text{(A2-25)}$$

The expression for L_{1n} comes from the equation (A2-17), and, can be written

$$\sum_{j=1}^{3} k_j L_{jn}^2 = \lambda_n \quad (n=1, 2, 3) \quad . \quad \text{(A2-26)}$$

Substitution of equations (A2-25) into (A2-26) gives

$$L_{1n} = \pm \left[k_1 + k_2 \frac{(\gamma_{1n}\beta_{3n} - \beta_{1n}\gamma_{3n})^2}{(\gamma_{2n}\beta_{3n} - \beta_{2n}\gamma_{3n})^2} + k_3 \frac{(\gamma_{1n}\beta_{2n} - \beta_{1n}\gamma_{2n})^2}{(\gamma_{2n}\beta_{3n} - \beta_{2n}\gamma_{3n})^2} \right]^{\frac{1}{2}} . \quad \text{(A2-27)}$$

We choose the plus sign in the last equation so that, for example, positive symmetric stretching normal mode co-ordinates will increase the bond displacement co-ordinates.

Once the three eigenvalues, λ_n, have been found, equations (A2-25, 27) produce the required $\mathbb{L}$, if none of the λ_n are equal. In the case of M_3, $\lambda_2 = \lambda_3$, and the procedure breaks down. One is then free to choose any L_{j2} (j=1, 2, 3) which satisfy equations (A2-22, 26). Once this choice is made, L_{j3} (j=1, 2, 3) must satisfy (A2-26) and the orthogonality conditions

$$\sum_{j=1}^{3} L_{j3} L_{ji} = 0 \quad (i=1, 2). \tag{A2-28}$$

If we impose the condition that the Q_2 normal mode co-ordinate in M_3 have C_{2v} symmetry about $\hat{\underset{\sim}{y}}$, we find

$$\mathbb{L} = \frac{1}{\sqrt{m}} \begin{pmatrix} 1 & 1/2 & 3/2 \\ 1 & -1 & 0 \\ 1 & 1/2 & -3/2 \end{pmatrix} \tag{A2-29}$$

and

$$\mathbb{L}^{-1} = \frac{\sqrt{m}}{3} \begin{pmatrix} 1 & 1 & 1 \\ 1 & -2 & 1 \\ 1 & 1/2 & -3/2 \end{pmatrix} \tag{A2-30}$$

It is readily verified that the matrices $\mathbb{L}^{-1}$ and IM of equations (A2-7, 30) give the product $(\mathbb{N}')^{-1}$ whose elements are given in equation (4. 3. 2. -4).

Appendix 3. Adams-Moulton Integrator Coefficients

In order to find the best Predictor/Corrector orders for our calculation, we developed a recursion method for the determination of the a_i and b_i of equations (6.1.1.-2) and (6.1.1.-4). This method is described below.

Using the notation of Section 6.1.1.,

$$y^*_{m+1} = y_m + h\left[\dot{y}_m + \sum_{i=1}^{n} g^*_i \Delta_i \dot{y}_m\right] . \qquad \text{(A3-1)}$$

The $\Delta_i \dot{y}_m$ are differences in $\dot{y}$ at various times t and are defined by

$$\Delta_i \dot{y}_m = \Delta_{i-1} \dot{y}_m - \Delta_{i-1} \dot{y}_{m-1} , \qquad \text{(A3-2)}$$

where

$$\Delta_1 \dot{y}_j = \dot{y}_j - \dot{y}_{j-1} . \qquad \text{(A3-3)}$$

It is clear from equation (A3-2) that

$$\Delta_i \dot{y}_m = \sum_{j=0}^{i} c^i_j \dot{y}_{m-j} \qquad \text{(A3-4)}$$

where

$$c_j^i = c_j^{i-1} - c_{j-1}^{i-1} \quad (0 \le j \le i)$$

$$c_{-1}^i = c_{i+1}^i = 0 \qquad (i > 0) \tag{A3-5}$$

and

$$c_0^i = -c_1^1 = 1 \ .$$

Scarborough (33) shows that

$$g_i^* = \frac{1}{i!} \int_0^1 u\,(u+1) \cdots (u+i-1)\, du. \tag{A3-6}$$

Thus

$$g_i^* = \frac{1}{i!} \sum_{j=1}^{i} \frac{d_{i-j+1}^i}{j+1} \tag{A3-7}$$

where

$$d_j^i = d_j^{i-1} + (i-1)\, d_{j-1}^{i-1} \qquad (j=1, \ldots, i)$$

$$d_1^i = 1 \quad \text{and} \quad d_0^i = d_{i+1}^i = 0 \ . \tag{A3-8}$$

Tables of c and d may be made up from the recursion relations (A3-5, 8). Given these coefficients and equations (A3-4, 7), equation (A3-1) becomes

$$y^*_{m+1} = y_m + h\,\dot{y}_m + \sum_{i=1}^{n} \sum_{k=0}^{i} c_k^i\, g_i^*\, \dot{y}_{m-k} \,. \qquad \text{(A3-9)}$$

A comparison of equations (6.1.1.-2) and (A3-9) shows that for n'th order prediction

$$a_i = a_i^{(n)} = \sum_{j=1}^{i} g^*_{n+1-j}\, c^{n+1-j}_{n+1-i} \quad (i=1, 2, \ldots, n)$$

and (A3-10)

$$a_{n+1} = a^{(n)}_{n+1} = 1 + \sum_{j=1}^{n} g^*_{n+1-j} \,.$$

If one is interested in tabulating the $a_i^{(n)}$ for various orders, n, it is useful to note that

$$a_i^{(n+1)} = a_i^{(n)} + c_i^{n+1}\, g^*_{n+1} \,. \qquad \text{(A3-11)}$$

The correction coefficients may be derived in a similar way. The g_i^* are replaced by g_i^{corr} which come from

$$g_i^{corr} = \frac{1}{i!} \int_{-1}^{0} u\,(u+1) \cdots (u+i-1)\, du \qquad \text{(A3-12}$$

and

$$g_i^{corr} = \frac{1}{i!} \sum_{j=1}^{i} (-1)^j \, \frac{d^i_{i-j+1}}{j+1} \qquad \text{(A3-13)}$$

The d_j^i still obey equations (A3-8). Thus the difference formula for y_{m+1}^{corr},

$$y_{m+1}^{corr} = y_m + h(\dot{y}^*_{m+1} + \sum_{i=1}^{n+1} g_i^{corr} \Delta_i \dot{y}_{m+1}) \qquad \text{(A3-14)}$$

becomes, via equations (A3-4),

$$y_{m+1}^{corr} = y_m + h(\dot{y}^*_{m+1} + \sum_{i=1}^{n+1} \sum_{k=0}^{i} c_k^i g_i^{corr} \dot{y}_{m-k+1}). \qquad \text{(A3-15)}$$

By comparison of equations (6.1.1.-4) and (A3-15),

$$b_i = b_i^{(n)} = \sum_{j=1}^{i} g_{n+1-j}^{corr} c_{n+1-i}^{n+1-j} \quad (i=1, 2, \ldots, n)$$

$$b_{n+1} = b_{n+1}^{(n)} = 1 + \sum_{j=1}^{n} g_{n+1-j}^{corr} . \qquad \text{(A3-16)}$$

As with the predictor coefficients, the use of

$$b_j^{(n+1)} = b_j^{(n)} + c_j^{n+1} g_{n+1}^{corr} \qquad \text{(A3-17)}$$

results in a more efficient tabulation of b_j for sequential orders, (n).

Part II. Dynamics of Energized Anharmonic Molecules

DYNAMICS OF ENERGIZED ANHARMONIC MOLECULES

1. Introduction

The accepted mechanism for unimolecular reaction, proposed by Lindemann (1), involves three elementary processes: collisional activation to and collisional deactivation from molecular states with energy in excess of that required for reaction (hereafter called energized states) and the reactive process itself. When this mechanism is expanded by adoption of the strong collision assumption, whereby energized molecules are deactivated by a single collision with heat bath molecules, Slater (2) shows that the fate of energized molecules can be described by a probability of reaction

$$P_{rxn} = e^{-\omega \tau(s)}. \qquad (1.-1)$$

Here ω is the heat bath collision frequency, and τ is the lifetime of the energized molecule which a prior collision has left in the state s. This is a deterministic, classical-mechanical formulation. Only in classical mechanics will a specific energized state, determined by $s \equiv s(q_1^0, \ldots, q_n^0, p_1^0, \ldots, p_n^0)$, with the q_i^0, p_i^0 being the set of initial coordinates and momenta of the n degrees of freedom of the molecule, react in some definite time, $\tau(s)$. The applicability of classical mechanics to reacting molecules is discussed in Section 3. If $\tau(s)$ is known and the fraction, f(s)ds, of molecules in energized states s to s + ds can be found, then the first-order rate constant for thermal unimolecular reaction becomes (2)

$$k = \omega \int f(s)\, e^{-\omega \tau(s)}\, ds\,, \qquad (1.-2)$$

where the integral is taken over all values of s corresponding to unreacted molecules.

The problem of calculating f(s) has been considered by many workers (3, 4). Slater (5) evaluates this quantity in terms of the action-angle variables of the system using the small vibration approximation (SVA). He then relates the vibration phase average of $\omega e^{-\omega\tau(s)}$ to the "asymptotic frequency of up-zeroes" or reactive excursion frequency (REF) of a critical coordinate. In the preceding paper (6), hereafter called Paper I, it has been shown that for harmonic molecules, the REF is adequately described by its SVA analog. However, for an ensemble of energized anharmonic molecules, the SVA is not expected to furnish a good REF for reasonable values of critical coordinates. It would be useful, then, to develop other methods for evaluating $\tau(s)$ as a function of state, s, in order to apply equation (1.-2) to unimolecular reactions. In part, this paper shows the behavior of $\tau(s)$ in some regions of the classical phase space of anharmonic bent triatomic molecules.

When a polyatomic molecule is given energy slightly in excess of that required for dissociation, it executes large amplitude internal motions before decomposing (7). During these motions, energy exchanges among the bonds until the requisite amount finds its way into the modes which yield dissociation. The fact that energized molecules do not necessarily decompose within a single characteristic vibration period suggests that the motion on the constant energy hypersurface in the phase space for these molecules is fairly complex. The representative point in phase space does not head directly to the dissociative regions but may pass near them several times before passing into them (7). Still, as the energy of the molecule is raised above that required for dissociation,

one expects the passage into the dissociative regions to increase in cross-sectional hyperarea faster than does the non-dissociative region of the constant energy hypersurface. Since the lifetime of the excited molecule is inversely related in some way to the ratio of hyperareas in phase space corresponding to dissociated and non-dissociated states, molecular lifetimes might be expected to be monotonically decreasing functions of molecular energy. This simple model will be tested in this paper.

The molecule models used are the relatively rigid equilaterally symmetric M_3 and the loose asymmetric $ClNO^{18}$ ones of Paper I. In the present paper, both these bent triatoms have three pairwise Morse bonds connecting the nuclei. The Morse parameters were chosen to yield the proper dissociation energy and harmonic force constants and are given in Sections 6.1. and 5.3. for M_3 and $ClNO^{18}$, respectively.

2. Equations of Motion

The classical equations of motion of our triatomic models are given in equations (3.1.-8 through 13) of Paper I. Instead of the harmonic internuclear potential, V_i, of equation (3.1.-14) in that paper, we will use the Morse potential

$$V_i = D_i\{1 - \exp[-\beta_i(r_i - r_i^{eq})]\}^2. \qquad (2.-1)$$

In this equation, D_i is the dissociation energy of bond i measured from the bottom of the potential well, and β_i is chosen such that

$$k_i = 2\beta_i^2 D_i, \qquad (2.-2)$$

where k_i is the harmonic force constant for bond i. Equation (2.-2) is

obtained by expanding (2.-1) in a power series in $(r_i - r_i^{eq})$ and equating the result with equation (3.1.-14) of Paper I in the limit of vanishingly small $(r_i - r_i^{eq})$.

It is clear that a sum of pairwise Morse functions like (2.-1) gives only an approximation to the potential surface of molecules. The assumption that the bond potential parameters of the free diatom and the diatom in the molecule are the same is a very poor one. A more realistic potential would take into account the perturbations on the diatom by other atoms in the molecule. Thus, when we solve the equations of motion for the dynamical behavior of molecular models held together by Morse bonds, we cannot claim that the real molecules they are to represent will exhibit the same dynamical behavior in every particular. The present paper concerns itself with the dynamics of these classical Morse models.

3. Validity of Classical Molecular Mechanics

The avowed purpose of Paper I was the study of the time dependence of dynamical variables which were constants of the motion in the SVA or weak coupling approximation. It was shown (see footnote 16 of that paper) that a classical mechanical study was sufficient to determine whether or not the expectation value of a dynamical variable was time independent for the corresponding quantum mechanical system. In this paper, however, we cannot fall back on this property to justify the use of classical equations of motion. We want to study the evolution of the paths of representative points in phase space in order to determine their residence time in the regions which we declare to be non-dissociated.

In the quantum analog of these studies, we would determine the time evolution of the wave packets in configuration space representing analogous initial conditions. If the wave packets didn't broaden excessively during the molecule's lifetime, the passage of their centers through a dissociated configuration would furnish lifetimes. If, on the other hand, the spread is appreciable, the concept of a unique classical lifetime breaks down and one is reduced to a discussion of distribution functions of reactive decay times.

In the classical case, a uniquely energized molecule will decompose in a definite time to a definite final state. The quantal description of unimolecular decomposition (8) involves excitation of an ensemble of molecules to some metastable resonance state followed by decay into the many continuum states coupled to it. Classically, the existence of many product channels for each initial state can be rationalized by the fact that the quantal state specification does not set the relative vibration phases, and different initial phases can dissociate into different product channels. It is also clear that classical mechanics cannot define the metastable resonance states a priori. However, this defect does not guarantee that the results of quantal and (suitably averaged) classical mechanical decomposition studies will disagree.

3.1. Mechanics of Bound States

Classical mechanics cannot, of course, be used to derive the quantized states of bound molecules. Thus, it is surprising that a minimum wave packet displaced from the center of a harmonic well executes the classical sinusoidal motion without change of shape (9).

However, the harmonic potential is unique in classical mechanics as well; it is the only force field in which the characteristic frequencies are not functions of the energy of the system. This means that the probability distribution for a swarm of one-dimensional classical harmonic trajectories will recover its initial shape in contrast to the anharmonic analog (10). Their studies in the quantum dynamics of anharmonic oscillators have led Wilson and co-workers (11) to the conclusion that the similarity of the classical and quantum dynamics of "harmonic oscillators is an accidental peculiarity of the system and does not imply that corresponding similarities exist between classical and quantal anharmonic oscillators" (11a). In particular, the similarities were not found in one-dimensional linear well, square well, and Morse oscillators nor in two-dimensional square wells. While the potential models were not sufficiently complex to serve as approximations to bent triatomic molecules, we believe the evidence gathered thus far indicates that classical and quantal dynamics of these systems will show the divergences found in the one-dimensional cases.

The results obtained by Wilson et al. (11) tend to indicate that if, in a classical trajectory the energy of some oscillator in a polyatomic molecule is well below (30%, for example) that oscillator's dissociation energy for a time which is long compared to the oscillator's natural period, then that classical trajectory would be divergent from its quantum analog. If, on the other hand, the oscillators of the energized polyatomic molecule exchange large amounts of energy in times comparable to oscillator periods, then no single oscillator would remain in its low energy bound states long enough for the classical and quantal

trajectories to diverge appreciably. The question then becomes whether the small differences in the two dynamics yield trajectories stable in the sense used by Born and Hooten (10). I.e., are small changes in the initial conditions of classical or quantal trajectories amplified or dampened by the subsequent dynamics? Amplification of the divergence between two initially similar trajectories would indicate instability. Directing their attention to classical anharmonic dynamics, Born and Hooten make the statement that "all motion is unstable" (10). The results of Section 5.1 will be seen to bear them out.

3.2. Mechanics in the Continuum and in Metastable Molecules

The usual justification (11a) for the use of classical trajectories in chemical dynamics involves appeal to the correspondence principle. When the density of quantum levels becomes so high that energy eigenvalues need no longer be considered discrete, the solutions to the quantum and classical equations of motion for the system approach one another (12). Thus, classical mechanics should be adequate to describe the dynamics of polyatomic molecules with sufficient energy to undergo complete decomposition into its constituent atoms. But such molecules are not of primary interest in chemical kinetics. It is rather molecules with energy distributions sufficient to break but one or two bonds that are of most concern in chemistry. Such decompositions yield at least one molecular fragment or isomeric species. In this case, the use of classical mechanics is questionable because the problem calls for the solution of the dynamics of at least one bound oscillator. However, the formalism developed recently(8, 13ab) for quantum mechanical solutions

to the unimolecular reactions of these metastable molecules require detailed knowledge of the position and broadening of the quasi-stationary (resonance) states above chemically realistic potential wells. As such information is not yet available, the only mechanics capable of solving the dynamics of unimolecular reaction at present is classical. In the absence of direct evidence to the contrary, one can only hope that it provides a fair first approximation to the dynamics of unimolecular chemistry. If and when subsequent quantum mechanical calculations are done, the present classical results will furnish an interesting basis for comparison.

4. Numerical Methods

4.1. Integration

Some of the trajectories to be described in this work were obtained by integrating the classical equations of motion with an Adams-Moulton integrater described in Section 6.1. of Paper I. The predictor series was 5^{th} order and the corrector was 6^{th} order. The coefficients for these orders in the Adams-Moulton formulae were given in Table II, Section 6.1.3. of Paper I. Many of the earlier trajectories determined in this study came from Adams-Moulton 11^{th} Order Predictor/11^{th} Order Corrector integrations. In the results, the distinction between these integraters is dropped because they give solutions of comparable accuracy when applied to the differential equations of motion of our anharmonic molecules.

4.1.1. Adams-Moulton Eleventh Order Predictor/Corrector Integrater (AM11)

The basic equations for Adams-Moulton integration were given in Section 6.1.1. of Paper I. A method for obtaining the n'th order prediction and correction coefficients, $a_i^{(n)}$ and $b_i^{(n)}$ ($i = 1, \cdots, n+1$), was given in Appendix 3 of that paper, and the results for orders one through eleven are given here in Table I. The formulae utilizing these coefficients are given in Paper I as equations (6.1.1.-2) and (6.1.1.-4). The truncation error analysis appears in Section 6.1.2. of that paper. However, truncation error in the n'th order predictor is related to the coefficient of the first ignored term which appears explicitly in the $n + 1^{st}$ predictor. A comparison of the 5^{th} order error, given as $\frac{19087}{60480} h^7 \partial^7 y/\partial t^7$ in equation (6.1.3.-1) of Paper I, with the coefficient $a_1^{(6)}$ from Table I gives the following relation for the truncation error, $\mathcal{E}^{(n)}$, of the n'th order Adams-Moulton predictor as

$$\mathcal{E}^{(n)} = |a_1^{(n+1)}| \; h^{n+2} \; \partial^{n+2} y/\partial t^{n+2} . \qquad (4.1.1.-1)$$

In this equation, as in (6.1.3.1-1) of Paper I, $h = \Delta t$ is the integration step size and y and t are the dependent and independent variables of the first order differential equation being solved. Thus, the truncation error of the eleventh order Adams-Moulton predictor is found to be

$$\mathcal{E}^{(11)} = \frac{703604254357}{2615348736000} \; h^{13} \; y^{XIII} \qquad (4.1.1.-2)$$

$$\cong 0.269 \; h^{13} \; y^{XIII} .$$

Table I. Table of Adams-Moulton Integrater Coefficients

i	$2a_i^{(1)}$	$2b_i^{(1)}$	$12a_i^{(2)}$	$12b_i^{(2)}$	$24a_i^{(3)}$	$24b_i^{(3)}$	$720a_i^{(4)}$	$720b_i^{(4)}$	$1440a_i^{(5)}$	$1440b_i^{(5)}$	$60480a_i^{(6)}$	$60480b_i^{(6)}$	$120960a_i^{(7)}$	$120960b_i^{(7)}$
1	-1	1	5	-1	-9	1	251	-19	-475	27	19087	-863	-36799	1375
2	3	1	-16	8	37	-5	-1274	106	2877	-173	-134472	6312	295767	-11351
3			23	5	-59	19	2616	-264	-7298	482	407139	-20211	-1041723	41499
4					55	9	-2774	646	9982	-798	-688256	37504	2102243	-88547
5							1901	251	-7923	1427	705549	-46461	-2664477	123133
6									4277	475	-447288	65112	2183877	-121797
7											198721	19087	-1152169	139849
8													434241	36799

i	$3628800a_i^{(8)}$	$3628800b_i^{(8)}$	$7257600a_i^{(9)}$	$7257600b_i^{(9)}$	$479001600a_i^{(10)}$	$479001600b_i^{(10)}$	$958003200a_i^{(11)}$	$958003200_i^{(11)}$
1	1070017	-33953	-2082753	57281	134211265	-3250433	-262747265	5675265
2	-9664106	312874	20884811	-583435	-1479574348	36284876	3158642445	-68928781
3	38833486	-1291214	-94307320	2687864	7417904451	-184776195	-17410248271	384709327
4	-91172642	3146338	252618224	-7394032	-22329634920	567450984	58189107627	-1305971115
5	137968480	-5033120	-444772162	13510082	44857168434	-1170597042	-131365867290	3007739418
6	-139855262	5595358	538363838	-17283646	-63176201472	1710774528	211103573298	-4963166514
7	95476786	-4604594	-454661776	16002320	63716378958	-1823311566	-247741639374	6043521486
8	-43125206	4467094	265932680	-11271304	-46113029016	1446205080	214139355366	-5519460582
9	14097247	1070017	-104995189	9449717	23591063805	-890175549	-135579356757	3828828885
10			30277247	2082753	-8271795124	656185652	61633227185	-2092490673
11					2132509567	134211265	-19433810163	1374799219
12							4527766399	262747265

The eleventh order integrator was chosen because it minimized the error in a single integration step of size $h = 2^{-5}$ in the double precision (sixteen significant decimal digits) solution of

$$\dot{y} = 2\pi \cos 2\pi t \, . \qquad (4.1.1.-3)$$

For $n < 11$, the accuracy of such an integration increases exponentially with order, n, as is to be expected from the h^{n+2} form of the truncation error of equation (4.1.1.-1). For $11 \leq n \leq 17$, however, the double precision Adams-Moulton predictor/corrector integration step gives a constant eleven significant digit answer. This is due to the limitation of word length. The integrater coefficients were supplied correct to ± 3 in the sixteenth significant figure. As can be seen from Table I, these coefficients for eleventh order differ among themselves by about 5 orders of magnitude. This means that truncation in the computer's arithmetic operations reduce the accuracy to 16 - 5 = 11 significant figures.

Optimization of order is a function of step size, h. When $h = 2^{-4}$, the optimal order for a single step of (4.1.1.-3) is about n = 20. The eleventh order was chosen because we anticipated small step sizes for the anharmonic equations we were to solve.

4.1.2. Application of AM11 to Trajectories

Since Adams-Moulton integrators are not self-starting (see Paper I, Section 6.1.4.), an integration initiation routine is required. The 12th integration step is taken by the 11th order routine, AM11, which derives its table of past $\dot{y}$ values from a 10th order routine, AM10,

operating at a step size of h/2. AM10 derives its past value table from AM9, which takes steps of h/4. The cascade of integrators reaches down to AM4, a fourth order Adams-Moulton routine, operating at a step size of h/128. The first entries in the $\dot{y}$ table come from a 4th order Runge-Kutta-Gill (RKG) integrator (see Paper I, Section 6.1.4.) running at this same h/128 step size. Thus, by the time the independent variable, t, reaches the value 11h, the initiation routine has taken 72 integration steps of increasing sizes and supplied AM11 with a set of past values of $\dot{y}$ which is roughly compatible with its own accuracy.

The accuracy compatibility requirement relating the step size of Adams-Moulton integrators of order n and n+1 is by equation (4.1.1.-1).

$$h_n = h_{n+1}^2 \left| \frac{a_1^{(n+2)}}{a_1^{(n+1)}} \cdot \frac{\partial^{n+3} y/\partial t^{n+3}}{\partial^{n+2} y/\partial t^{n+2}} \right| . \qquad (4.1.2.-1)$$

The ratio of a_1's is always near unity. If we assume that the maximum values of the n + 2nd and n + 3rd derivatives of y are the same, then $h_n \cong h_{n+1}^2$ insures compatible accuracies. It can be shown that when $h_n = \frac{1}{2} h_{n+1}$, compatible tables of past values of $\dot{y}$ are obtained when $h_{11} \geq 2^{-6}$. Typically, the anharmonic trajectory integrations were carried out with $h_{11} = 2^{-5} \Rightarrow 5.25 \times 10^{-17}$ seconds of molecule time.

4.1.3. Comparison of Integraters

The integrater accuracies discussed in the previous section involve a single integration step. Trajectory calculations, for anharmonic molecules at chemically interesting energies, involve six to twelve thousand such steps. Thus, overall accuracy in such integra-

tions is greatly affected by truncation characteristics of the computer, stability of the equations to be solved, and other factors which do not significantly influence the accuracy of a single step. The merit of a numerical integrater is best tested by observing its long-term accuracy.

The Adams-Moulton 11th Order (AM11) and Runge-Kutta-Gill 4th Order (RKG) integraters were used to solve the equations of motion of M_3, an equilaterally symmetric molecular model with masses equal to that of O^{16} and pairwise Morse potentials whose parameters are those of O_2. The initial conditions in these comparison test integrations corresponded to in-phase compressional potential energy in the three bonds of 0.0197 D_0, 1.40 D_0, and 0.90 D_0, respectively, where $D_0 = D_e(O_2) =$ 119.43 kcal/mole. This trajectory is dissociative. After about 3.2×10^{-13} seconds of high amplitude vibrations, the molecule begins to decompose. Bonds 2 and 3 break, leaving bond 1 as the molecular fragment. The point in the trajectory at which the molecule is said to have dissociated may be taken as the point when the two breaking bonds are stretched to at least some minimum length. This minimum length was taken to be 4 $r^{eq} = 4.828$ Å. The molecular lifetime, τ_4, is the time it takes any two bond lengths to exceed this value. It was found that none of our trajectories lead to "healing" bonds beyond τ_4. It is not dynamically impossible to create such a trajectory, but they are rare. Since the potential surface has a long-range attractive tail, it would be possible to create a healing trajectory beyond τ_∞, but the probability of encountering such cases becomes negligible for τ_n with $n \geq 4$. Less ambiguous reaction criteria involving minimum kinetic energy of fragment separation, passage over rotational barriers or through phase

space "bottlenecks" (14) have been suggested, but τ_4 is adequate for our purposes in this paper.

Table II shows the effect of integration step size on τ_4 for both integraters. The superiority of AM11 over RKG is manifest. The usual test of integration accuracy is the comparison of the initial co-ordinates and momenta with those obtained by integrating the equations of motion backward from the final to the starting time. Although AM11, integrating at a step size of $h = 7 \times 2^{-7}$ t*, preserves almost 3 digits in all the co-ordinates and momenta on reverse integration, the lifetime of this trajectory is in error by about 6% or 135 h! When the step size is dropped to $h = 3 \times 2^{-5}$ t*, 4 digits are recovered and τ_4 is still off by 36 h It is clear that the lifetime of this (and other) anharmonic metastable molecule cannot be trusted unless reverse integration recovers at least 6 or 7 significant digits for each of the initial co-ordinates and momenta. Such accuracy is obtained with AM11 operating at a step size of about $h = 2^{-5}$ t* $= 5.25 \times 10^{-17}$ seconds. (t* is the reduced time unit for our equations of motion. See Paper I, Section 3.2.) Integrater accuracy begins to fall off for step sizes smaller than 2^{-6} t* as the number of steps necessary to reach a constant molecular time increases beyond n = 12000.

The accuracy is also a function of the total energy of the molecule. Higher energies lead to more vigorous vibrations with larger changes in momenta at turning points. The larger momentum derivatives make for larger integration error. The test cited above involves an M_3 molecule with 277.1 kcal/mole total energy. If we raise the total energy to 290 kcal/mole, we expect larger errors. This latter energy

Table II. Metastable Lifetime (τ_4) vs Integrater and Integration Step Size (h) for an M_3 Trajectory[a]

h		AM11		RKG	
t*	10^{-17} sec	τ_4 10^{-13} sec	Digits[b] Recovered	τ_4 10^{-13} sec	Digits[b] Recovered
2^{-3}	20.96	4.0996	1.9		
$\frac{7}{8} \cdot 2^{-3}$	18.34	4.1316	2.8		
$\frac{3}{4} \cdot 2^{-3}$	15.72	4.3214	3.8		
2^{-4}	10.48	4.3801	6.0		
2^{-5}	5.24	4.3786	7.9	4.6690	2.6
2^{-6}	2.62	4.3786	6.9	4.4120	3.9

[a]See text for initial conditions for M_3.

[b]Number of decimal digits recovered by reverse integration from dissociation back to initial state.

was given to anharmonic M_3 as symmetric stretch. The equilateral symmetry of the equations forbids any but D_{3h} motion. However, RKG, AM11, and the AM5/6 of Paper I all integrating at a step size of $h = 2^{-5}$ t* give appreciably asymmetric solutions after 3.6 to 3.9 $\times 10^{-13}$ seconds. This failure is integration order independent and must result from the truncation to 16 decimal digit arithmetic.

Other accuracy criteria, such as constancy of total energy and angular momentum components, for AM11 and RKG are essentially as useless as they were for the AM5/6 integrater of Paper I.

Finally, one thousand steps taken with each of the three integraters, RKG, AM11, and AM5/6, required 51, 38, and 28 seconds of IBM 7094 computer time, respectively.

4.2. Trajectory Initiation

4.2.1. Vibration Initiation

The few trajectory initiations from normal mode energies were accomplished via the algebra of Section 6.2.1. in Paper I. The remainder of the pure vibration trajectories were initiated from bond potential energy conditions, i.e., the bonds were stretched or compressed individually to specified potential energy values. Solving equation (2.-1) for r_i, we obtain

$$r_i = r_i^{eq} - \frac{1}{\beta_i} \log_e(1 \pm \sqrt{V_i/D_i}) \quad (i = 1,2,3) \qquad (4.2.1.-1)$$

which produces the three required bond lengths satisfying the three given potential energies as long as no $V_i \geq D_i$ when the minus sign is used

before the square root. As all such initiations in this paper are made with compressed bonds, the plus sign is used before the radical, and no initial r_i exceeds r_i^{eq}. With the three bond lengths determined, the co-ordinates of the molecule are specified by assuming that bond 2 lies parallel to and in the same sense as the $\hat{\underset{\sim}{X}}$ axis of the laboratory (non-rotating) center of mass system. This does not sacrifice generality.

Commencing all trajectories from a turning point in all the vibrations forces them to be in-phase with one another initially. This is done for convenience, but it is not necessary. The results show that for asymmetric initial configurations, the phase lock is broken in less time than the fastest vibration period. It is felt that these trajectories are representative ones for the model inspite of the unique initialization.

Had out-of-phase initiation been deemed necessary, it would have been accomplished via the input of non-zero values for bond kinetic energy, T_{B_i}. The definitions governing T_{B_i} are given in Paper I, Section 5.2. Briefly, the required bond kinetic energies specify three bond velocities to within a sign, which determines whether the bond is opening or closing. The three velocities and the Eckart condition (15)

$$\sum_{i=1}^{3} m_i \left(\underset{\sim}{x}_i^{eq} \times \dot{\underset{\sim}{x}}_i\right) = 0 \qquad (4.2.1.-2)$$

suffice to determine the four required atomic velocities $\dot{x}_1$, $\dot{y}_1$, $\dot{x}_3$, and $\dot{y}_3$ in the Eckart co-ordinate frame. These are related to the laboratory atomic velocities via equation (5.2.-4) of Paper I. The angular velocity in that equation is determined by the $\dot{\underset{\sim}{x}}_i$ and the choice of angular momen-

tum vector through equation (6.2.1.-7) of the same source.

4.2.2. Initial Rotation

The initiation from rotational energies is described fully in Paper I, Section 6.2.

4.3. Dynamic Variables for Decomposition Products

In our trajectory calculations, reaction is recognized when two molecular bonds stretch to greater than some factor n times their equilibrium values. The lifetime, τ_n, is then measured from initiation to this point. When such dissociations are found, the dynamical variables of the fragments are calculated from the final generalized co-ordinates and momenta of the system. These are the Cartesian co-ordinates of two of the three atoms and their conjugate momenta. The items of interest are the internal energies of the diatomic fragment and the kinetic energy of separation of the fragments. The latter quantity is of importance in guaranteeing that reaction has taken place. If the sum of the potential energy of the breaking bonds and the kinetic energy of separation is not greater than the dissociation energy, the molecule is merely undergoing a high amplitude stretch.

The atomic velocity vectors in the non-rotating center of mass system are obtained from the momenta via equations (3.1.-8) of Paper I and the time derivative of equation (3.1.-1). The kinetic energy of separation of the fragments, T_s, may be shown to be

$$2\,T_s = \frac{m_a\,M}{m_b + m_c}\,(\dot{\underset{\sim}{X}}_a \cdot \hat{\underset{\sim}{X}}_a)^2 \qquad (4.3.-1)$$

where $\hat{\underset{\sim}{X}}_a$ is the unit vector in the direction of the fragment atom, a, and $\dot{\underset{\sim}{X}}_a$ is the atomic velocity vector of a. Once the velocity of the center of mass of the diatomic fragment,

$$\dot{\underset{\sim}{X}}_{bc} = (m_b\dot{\underset{\sim}{X}}_b + m_c\dot{\underset{\sim}{X}}_c)/(m_b + m_c), \qquad (4.3.-2)$$

is subtracted from the velocities of the atoms in the diatom fragment, the resulting atomic velocities with respect to the diatom center of mass, $\dot{\underset{\sim}{x}}_b$ and $\dot{\underset{\sim}{x}}_c$, may be used to obtain the instantaneous diatomic internal energies. The kinetic energy of vibration becomes

$$2\,T_{bc} = \frac{m_c\,(m_b + m_c)}{m_b}\,(\dot{\underset{\sim}{x}}_c \cdot \hat{\underset{\sim}{x}}_c)^2 \qquad (4.3.-3)$$

where $\hat{\underset{\sim}{x}}_c = (\underset{\sim}{X}_c - \underset{\sim}{X}_b)/|\underset{\sim}{X}_c - \underset{\sim}{X}_b|$. The total instantaneous vibration energy is

$$E_v = T_{bc} + V_{bc} \qquad (4.3.-4)$$

where V_{bc} is the potential energy of the bc diatom. The rotational energy becomes

$$2\,E_{rot} = \frac{m_c\,(m_b + m_c)}{m_b}\,[\,\dot{x}_c^2 - (\dot{\underset{\sim}{x}}_c \cdot \hat{\underset{\sim}{x}}_c)^2], \qquad (4.3.-5)$$

or the difference between the total diatomic kinetic energy,

$$E_{bc} - V_{bc} = (m_b\dot{x}_b^2 + m_c\dot{x}_c^2)/2, \qquad (4.3.-6)$$

and the vibration kinetic energy, equation (4.3.-3).

5. Results and Discussion

5.1. Vibration Dynamics of Anharmonic Molecules

The molecules to be discussed are M_3 and $ClNO^{18}$. Their assumed pairwise potential parameters are given in Table III. These parameters give the molecules the same harmonic force constants they had in Paper I. The experimental structure (16) is used for $ClNO^{18}$. The D values are constrained by the experimental dissociation energy such that $D(ClO^{18}) + D(NCl) = 38.4$ kcal/mole. If we use the free diatom dissociation energy (17) for NO^{18} and Johnston's rare gas analogue (18) approach to estimate D(NCl), then $D(ClO^{18})$ and the Morse parameters follow from D(ON---Cl) and the experimental central field force constants (19).

5.1.1. Normal Mode Energies Below Dissociation

Trajectories for harmonic models in Paper I were initiated with half the ABC → A + BC dissociation energy either in one molecular mode or divided equally between the three modes. It was shown that initially pure asymmetric stretch in harmonic M_3 exchanged half its initial energy with the bending mode in about 5×10^{-13} seconds. When the same initial configuration is used to start a trajectory for anharmonic M_3, the asymmetric stretch mode (see Figure 1) exchanges half its energy with the other modes in about 5×10^{-15} seconds, which is about 1/4 of the fastest (symmetric stretch) period. It is clear that anharmonic M_3, oscillating with half its dissociation energy, is <u>not</u> executing normal mode motion. It does not show even the short term stability of motion (lack of normal mode inter-

Table III. Molecular Potential Parameters

Molecule	Bond	r^{eq} (Å)	β ($Å^{-1}$)	D_e (kcal/mole)	k (mdyn/Å)	ω (cm^{-1})
M_3	M_2	1.207	2.663	119.43	11.77	1580
ClNO[18]	NO	1.139	2.569	152.3	13.97	1730
	ClO	2.650	2.340	17.0	0.98	375
	NCl	1.975	2.401	21.4	1.92	570

FIG. 1. Normal mode energies of anharmonic M_3 with the initial conditions of half the dissociation energy in the asymmetric stretch mode. —— symmetric stretch; - - - - - bend; —— - —— asymmetric stretch; and —— - - —— sum of the normal mode energies.

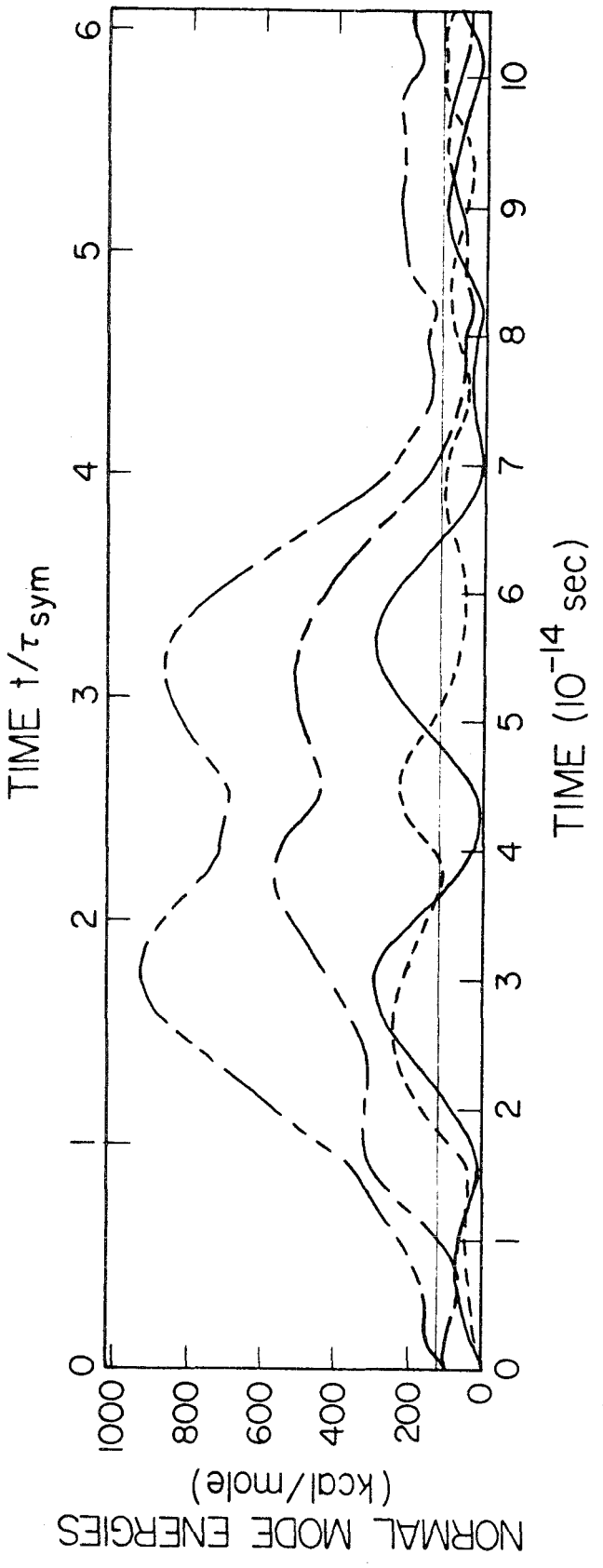
NORMAL MODE ENERGIES
(kcal/mole)
1000
800
600
400
200
0
TIME t/τsym
0
1
2
3
4
5
6
TIME (10⁻¹⁴ sec)
0
1
2
3
4
5
6
7
8
9
10

action) exhibited by the harmonic counterpart in Figure 7c of Paper I. While the total energy of the anharmonic M_3 remains 144.32 kcal/mole throughout the integration, the total normal mode energy at times exceeds 900 kcal/mole. It is evident that a normal mode description of energized anharmonic M_3 is highly inaccurate.

When the harmonic model for $ClNO^{18}$ is given half its dissociation tion (ON---Cl) energy in its symmetric stretching mode, that mode is stable for about 5×10^{-13} seconds (see Figure 9c of Paper I). When an anharmonic $ClNO^{18}$ trajectory (see Figure 2) is given the same initial conditions, the symmetric stretching mode is stable for only about half that length of time. In contrast to the harmonic case, the symmetric stretch energy is not even an approximate constant of the motion over its range of stability. It varies by about 75% of its initial value, 19.2 kcal/mole. The normal mode defect (as defined in Paper I) is very large for these initial conditions, as the total energy is only about half the initial symmetric stretch energy. It is this low total energy which is responsible for the reasonably well-behaved normal mode energies in Figure 2. One expects that the normal mode energies in trajectories with total energies nearer dissociation will be at least as chaotic as those of Figure 1. Figure 2 cannot be used as evidence that the small vibration approximation (SVA), which underlies the normal mode analysis, is better for the loose $ClNO^{18}$ model than it is for the relatively rigid M_3 one. Their relative energies are not comparable.

FIG. 2. Normal mode energies of anharmonic $ClNO^{18}$ initially given half its dissociation energy in symmetric stretch. —— asymmetric stretch; - - - - - bend; —— - —— symmetric stretch.

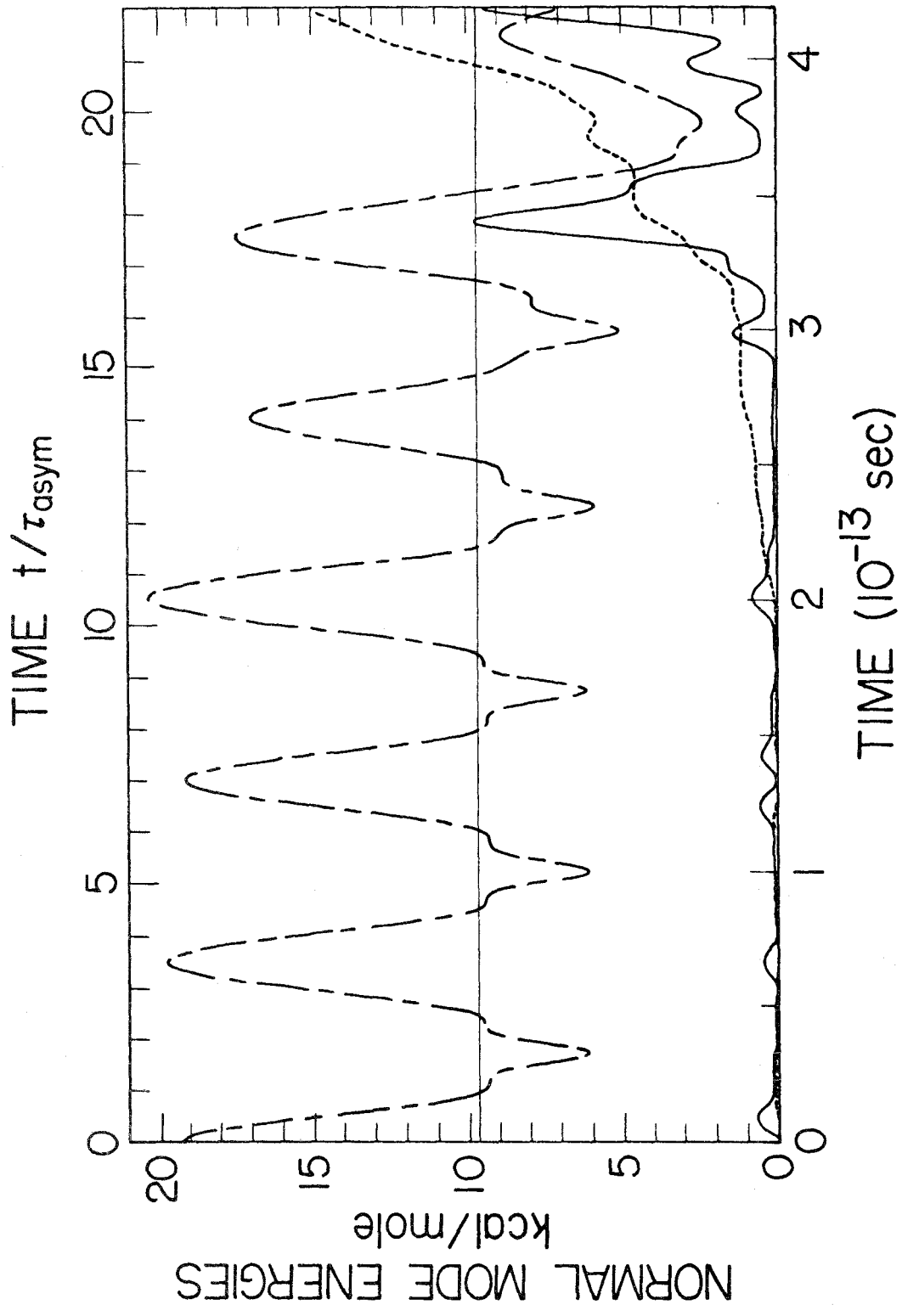
NORMAL MODE ENERGIES
kcal/mole
20
15
10
5
0
TIME t/τ_{asym}
0
5
10
15
20
TIME (10^{-13} sec)
0
1
2
3
4

5.1.2. Vibration Dynamics of M_3 Above Dissociation

All the M_3 trajectories to be discussed in this section are initiated with constant amounts of potential energy in compression of bonds 1 and 3. These energies are $V_1(0) = 0.0197\ D_o = 2.35$ kcal/mole (which is close to the 2.26 kcal/mole zero-point energy for an M_2 bond) and $V_3(0) = 0.90\ D_o = 107.49$ kcal/mole. All the initial momenta (and hence the initial kinetic energy) are zero, and $V_2(0)$ is varied from run to run. Its lowest value is $1.10\ D_o = 131.37$ kcal/mole, corresponding to a lowest total energy of $2\,D_o + 2.35$ kcal/mole. This exceeds the dissociation energy of M_3 ($2\,D_o = 238.86$ kcal/mole) by about the zero-point energy of M_2.

As $V_2(0)$ is varied systematically, the point in phase space, representative of the initial conditions for the trajectory, traces out some continuous curve, the total energy, E, increasing linearly with $V_2(0)$. When $V_2(0) > 1.581\ D_o = 188$ kcal/mole, the distance between the fragment atom (atom 1) and the center of mass of the fragment molecule (bond 1, in the numbering system of Paper I) increases monotonically with time during the entire trajectory, indicating <u>direct</u> decomposition. At these high energies ($E > 2.5\,D_o$), the M_3 molecule is not observed to execute any vibrations as a whole before decomposing.

The product diatom, M_2, comes away from the reaction site excited both vibrationally and rotationally. As $V_2(0)$ is raised above the critical energy for direct decomposition, the M_2 internal energies (see Figure 3) increase linearly but only 1/5 as fast as the total energy. Thus, this direct decomposition apparently yields a molecular fragment of almost

FIG. 3. M_2 fragment energies vs initial potential energy in bond 2 of M_3. O vibration energy; ● internal (vibration + rotation) energy. Top line represents the maximum energy available to the M_2 fragment. Arrow marks the minimum $V_2(0)$ necessary to produce direct decomposition.

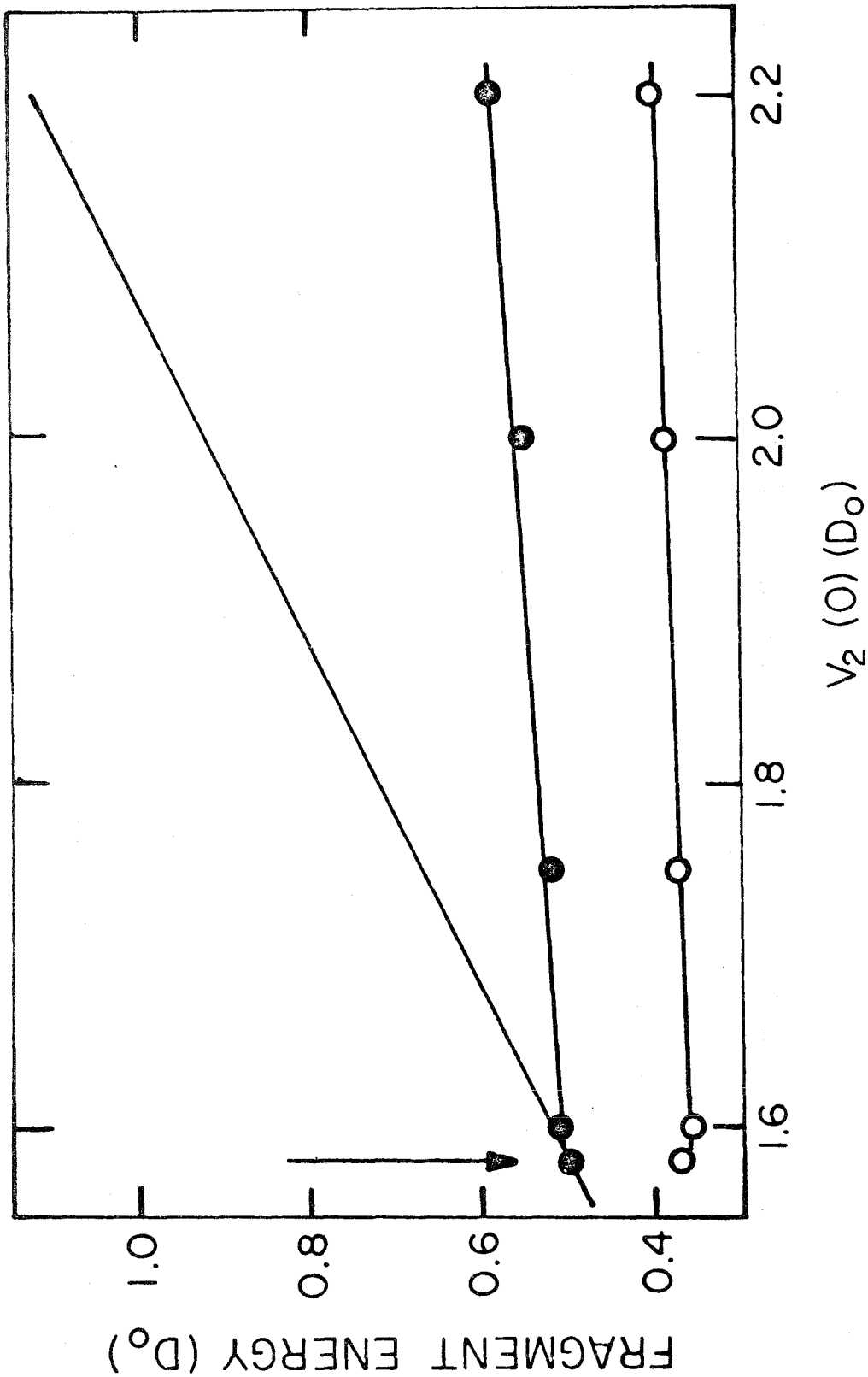
FRAGMENT ENERGY (D_o)
1.0
0.8
0.6
0.4
V_2 (O) (D_o)
1.6
1.8
2.0
2.2

constant internal excitation. The excess energy appears preferentially as relative translation of the products. This phenomenon is probably due to the fact that the molecular lifetime of excited M_3 approaches a constant value at very high energies. This constant is of the order of half the period of a molecular vibration, corresponding to the expansion time from the compressed initial configuration to dissociation. Apparently, only a constant 60 - 70 kcal/mole can be transferred into the molecular fragment in this time.

When $V_2(0) \leq 1.58\ D_o$, the energized M_3 molecule executes several molecular vibrations before dissociation, indicating delayed decomposition. (See, for example, Figure 4b.) The molecule vibrates until sufficient energy ($\geq D_o$) has accumulated in each of two bonds (1 and 3 in Figure 4b) which then break. It had been supposed that increasing the total molecular energy systematically, via increases in $V_2(0)$, would result in a monotonic decrease of molecular lifetimes. This is found not to be the case. Figure 4a represents the trajectory of an anharmonic M_3 with $V_2(0) = 170.03$ kcal/mole and $E = 279.87$ kcal/mole. The lifetime, τ_4, of this energized molecule is about 3.4×10^{-13} seconds, corresponding to almost 20 harmonic symmetric stretch periods. When the total energy is raised by about one part in 10,000, by increasing $V_2(0)$ to 170.06 kcal/mole, the lifetime (see Figure 4b) does not decrease by some small amount but increases to about 4.8×10^{-13} seconds or almost 28 symmetric stretch periods. Therefore, an increase in the total energy of about 0.01% increases the lifetime of this molecule by about 40%.

Figure 4 points up a general property of the unimolecular tra-

FIG. 4. Bond lengths vs time for anharmonic M_3 trajectories. Initial conditions: $V_1(0) = 2.35$ kcal/mole, $V_3(0) = 107.48$ kcal/mole; —— bond 1; - - - - bond 2; —— - —— bond 3.

a) $V_2(0) = 170.03$ kcal/mole

b) $V_2(0) = 170.06$ kcal/mole.

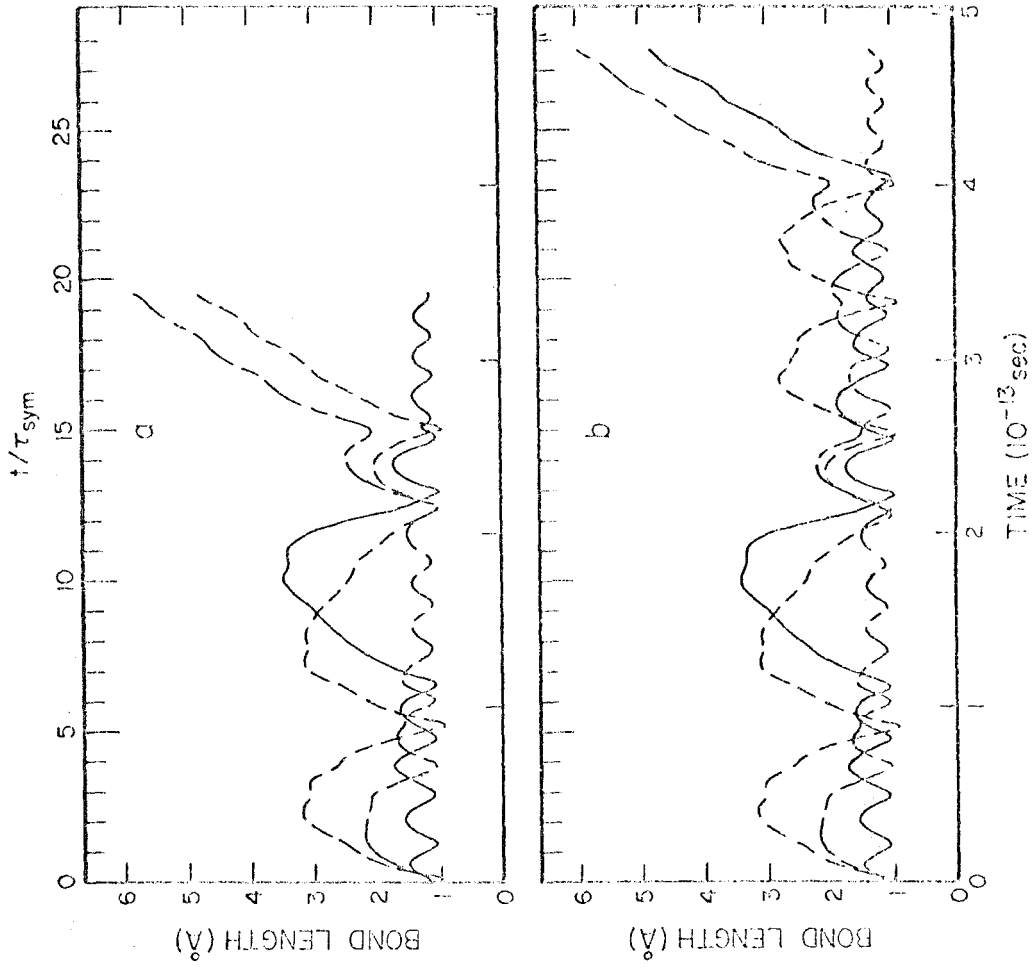
a
b
BOND LENGTH (Å)
BOND LENGTH (Å)
t/τ_{sym}
TIME (10^{-13} sec)
0
5
10
15
20
25
1
2
3
4
5
6

jectories we encountered. They are almost always highly sensitive to changes in their initial conditions. This is direct evidence in support of the statement by Born and Hooten (10) that "all motion is unstable." An additional indication of this sensitivity is the vibrational phase dependence in inter-bond energy transfers. Such exchanges of energy among the bonds occur when two or more of them are near their compressed turning points. The magnitude and direction of such transfers depend strongly upon the relative phase of the oscillators involved. For example, in Figure 4b at $t = 4 \times 10^{-13}$ seconds, the high energy bond 2 has just contracted and is beginning to expand, while the low energy bond 1 is just about to reach its compressed turning point. Thus, at this time, bond 2 is vibrating slightly out-of-phase with bond 1 and ahead of it by a few degrees. Such conditions are always associated with excitation of the lagging oscillator by the leading one. Indeed, in Figure 4b for $t > 4 \times 10^{-13}$ seconds, bond 1 extracts sufficient energy from bond 2 to dissociate. The slightly different phase relation between bonds 2 and 3 at $t = 2.1 \times 10^{-13}$ seconds in the same figure yields a different degree of excitation for the laggard bond 3. Thus, small perturbations introduced in the initial conditions are amplified by every energy transfer event. This high sensitivity may lead to strong differences between classical and quantum mechanical lifetimes, as discussed in Section 3.

For $V_2(0) < 186.7$ kcal/mole, the first energy transfer event, which occurs as all the bonds are expanding, does not transfer enough energy into bonds 2 and 3 for them to break. Thus, they must both contract at least once more to redistribute the oscillator energies. The

second energy transfer event (for $V_2(0) < 182.7$ kcal/mole) occurs when bond 3 contracts and exchanges energy with bond 1. Since the bonds are anharmonic, their periods are functions of their energy. Thus, the period of bond 3 and the time to the second transfer event increases with increasing $V_2(0)$, as seen in Figure 5. For successively higher values of $V_2(0)$, the second transfer event catches bond 1 in a different phase of its vibration, rendering the subsequent sections of the trajectory different from one another.

The molecular lifetime (20) is found to be a chaotic function of $V_2(0)$, as Figure 6 attests. Aside from the region of direct decomposition for $V_2(0) > 1.58 D_o$, only three regions of relative stability of lifetime with respect to $V_2(0)$ are found. These are shown in Figure 6 centered about $V_2(0) = 1.34$, 1.43, and $1.51 D_o$, respectively. All the trajectories in these regions led to dissociation in the same manner, that is, the last energy transfer event was the same. Outside these regions, no two neighboring $V_2(0)$ values, given by the abscissas of points in Figure 6, led to the same reactive event. Continuity, within the scale of the grid used for $V_2(0)$, exists only within these three zones. The zonal boundaries consist of dissociations in which the last energy transfer event leaves the breaking bonds with no energy in excess of that required for dissociation. In other words, reactive events near the zonal boundaries are characterized by near zero relative translational energy. Hence, these lifetimes become arbitrarily long as one approaches these boundaries from either side. Thus, there exist poles in these plots of lifetime vs energy. Furthermore, one suspects that there must exist more narrow zones of continuous dynamic character,

FIG. 5. Vibration period of bond 3 in M_3 vs initial potential energy of bond 2. Other initial conditions as in Figure 4.

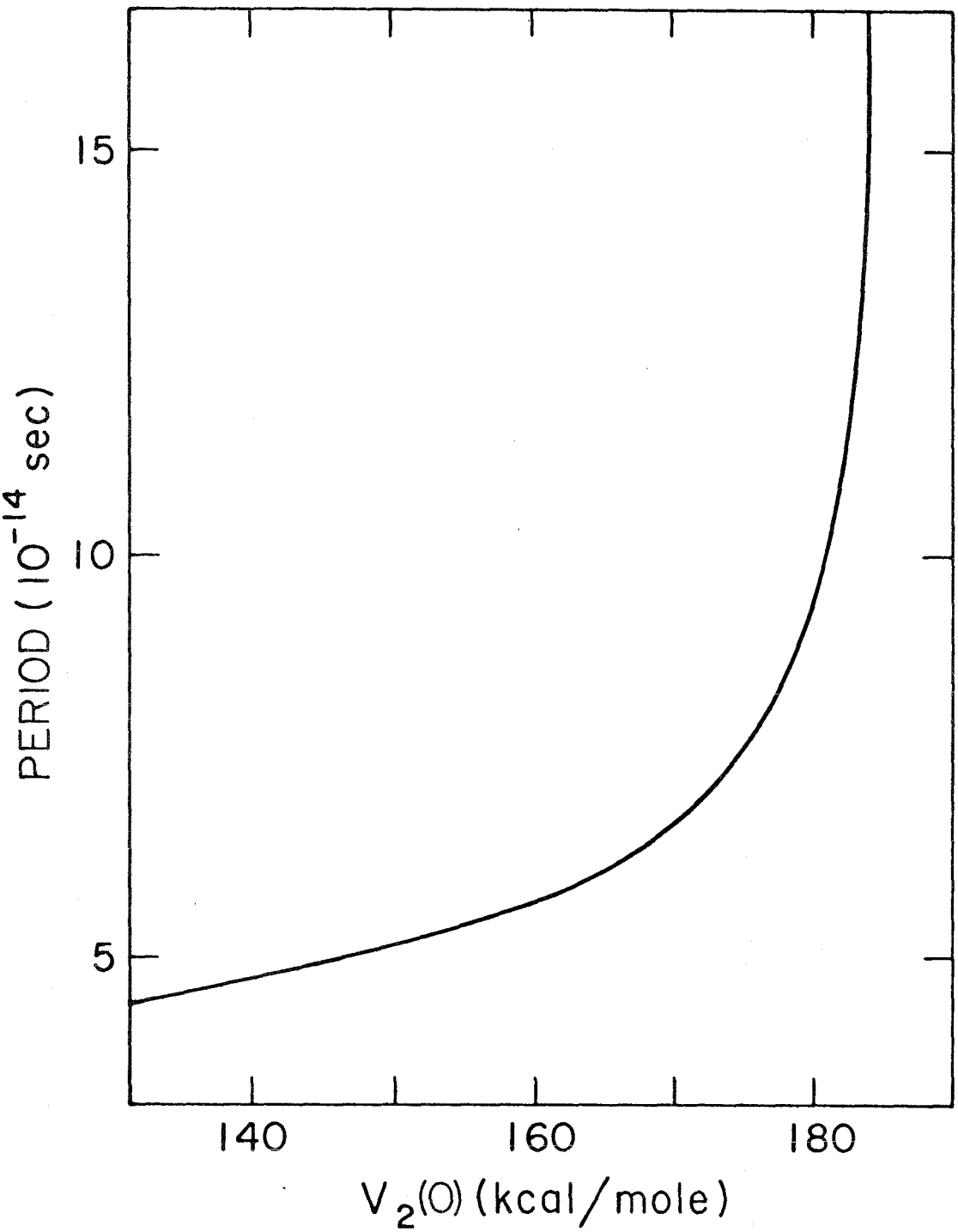
15
10
5
PERIOD (10^{-14} sec)
140
160
180
$V_2(0)$ (kcal/mole)

FIG. 6. Lifetime of metastable anharmonic M_3 vs the initial potential energy of bond 2. $V_1(0)$ and $V_3(0)$ as in Figure 4. Solid lines have been drawn through points corresponding to increasing values of $V_2(0)$ when no evidence for discontinuity was present.

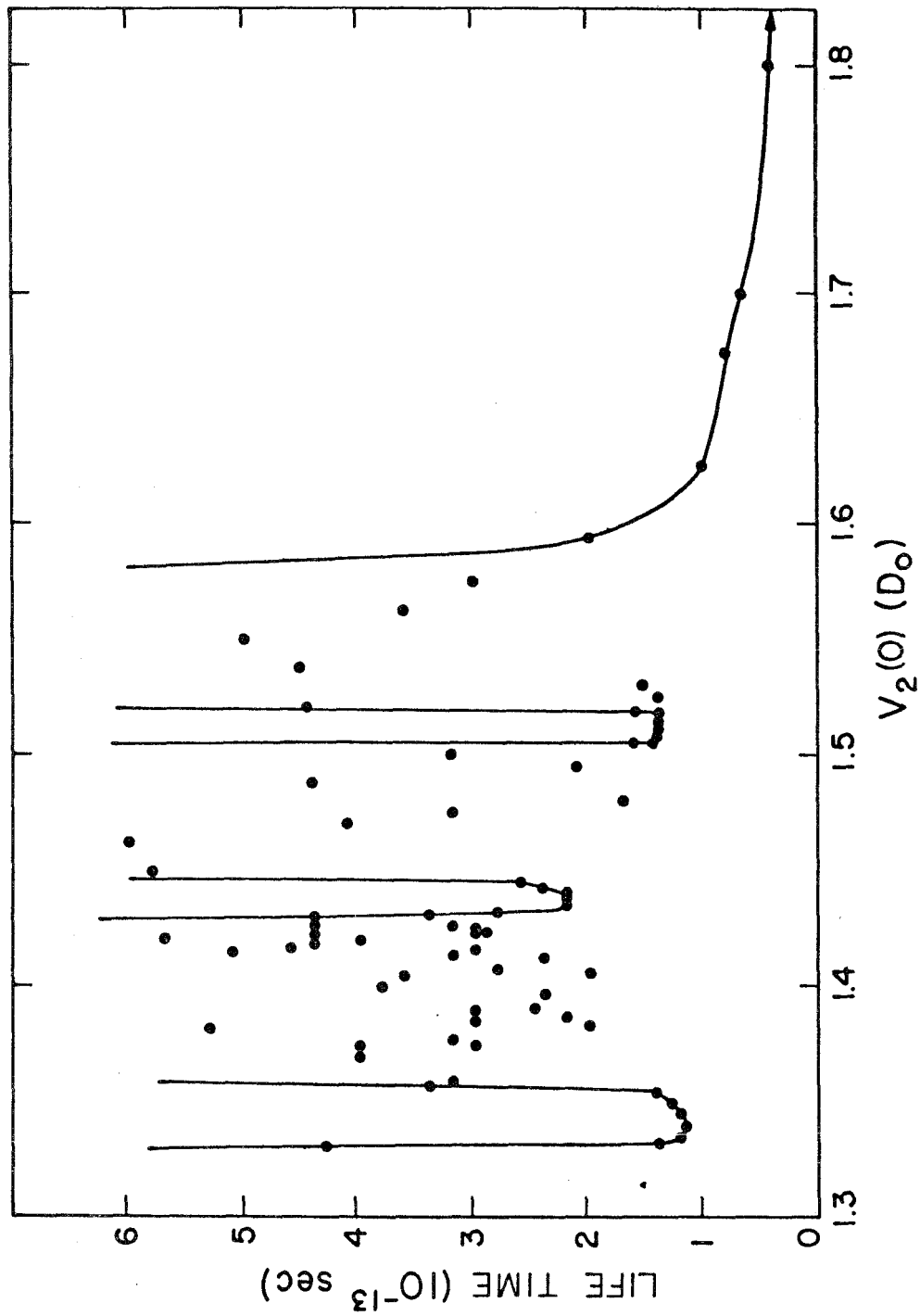
LIFE TIME (10^{-13} sec)
0
1
2
3
4
5
6
$V_2(0)$ (D_0)
1.3
1.4
1.5
1.6
1.7
1.8

visible with a finer grid in $V_2(0)$ than that used in this work. These will also exhibit arbitrarily long lifetimes at their boundaries. Indeed, regions of $V_2(0)$ might be found over which molecular lifetimes are discontinuous on any practical $V_2(0)$ grid size even if the equations of motion could be solved over indefinitely long times. In practice, our integrators fail at molecular times beyond about 6×10^{-13} seconds, so that this prediction cannot be verified.

Classical mechanical solutions of anharmonic molecular dynamics appears to involve extreme variations of lifetime with oscillator energy and, probably, any other progress variable. Hence, it is impractical, at this time, to obtain analytic or even numerical values for $\tau(s)$ from the classical equations of motion. This does not imply that unimolecular rate constants cannot be obtained from classical trajectory calculations. The Monte Carlo calculations of Bunker et al. (14) prove otherwise, at least for the high pressure limit. However, it seems unlikely that equation (1.-2), in its present form, will be useful in connection with the decomposition of anharmonic molecules. In view of the observed instability, accurate classical expressions for $\tau(s)$ will not be forthcoming. It is possible that $\tau(s')$, where s' represents a vibration phase average over s, may show the continuity sought in this paper for $\tau(s)$. The number of trajectories performed in this work does not permit statistically significant phase averaging for our $\tau(s)$ to test this important point.

5.1.3. Vibration Dynamics of $ClNO^{18}$ Above Dissociation

The extreme sensitivity of classical trajectories to perturbations, discussed in the last section for M_3, is found in the model for $ClNO^{18}$ also. Figure 7 shows a representative trajectory for anharmonic $ClNO^{18}$ at an energy of 46.1 kcal/mole, or about 7.5 kcal/mole above dissociation into Cl + NO^{18}. Figure 7b confirms the fact that energy transfers among the oscillators when they are near their contracted turning points. Note that the high frequency NO bond exchanges energy with the other bonds much more readily in this anharmonic $ClNO^{18}$ than it did in the harmonic model of Paper I. In that work, it was observed that modes of very different frequency rarely interact. The harmonic frequency of the NO bond is almost three times that of the next highest one (NCl). Hence, resonance coupling of these bonds should be poor. In the anharmonic situation, however, the force "constant" of a bond varies throughout its vibration cycle and its frequency is a function of its energy. These factors help couple oscillators which were relatively independent in the harmonic force field.

Figure 7c strongly confirms the inapplicability of normal modes or the SVA to highly energized anharmonic molecules. To that approximation, the normal mode energies are constants of the motion. According to Figure 7c, these energies vary by as much as 80 times the total energy of the molecule while it remains undissociated. The use of results from harmonic theories in describing anharmonic dynamics is clearly hazardous.

FIG. 7. Dynamics of anharmonic $ClNO^{18}$. Initial conditions $V_{NO}(0) = V_{ClO}(0) = 12.86$ kcal/mole, $V_{NCl}(0) = 20.37$ kcal/mole.

a) Bond lengths: —— NO; - - - - ClO; —— - —— NCl; —— - - —— sum of the two shortest lengths used as a check for linear configurations.

b) Bond energies: —— - - —— sum of bond energies.

c) Normal mode energies: —— asymmetric stretch; - - - - bend; —— - —— symmetric stretch.

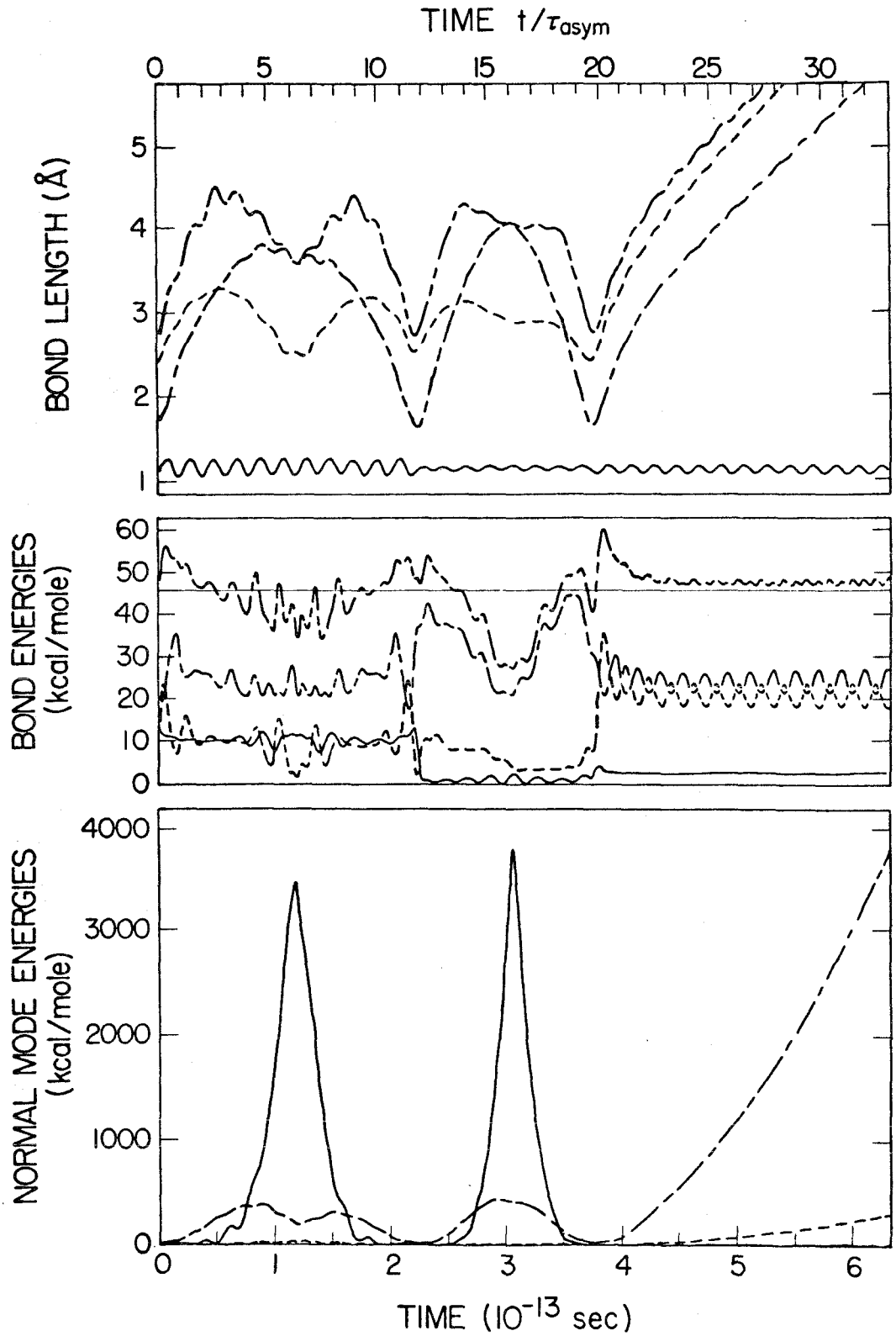
TIME t/τ_{asym}
0
5
10
15
20
25
30
BOND LENGTH (Å)
1
2
3
4
5
BOND ENERGIES (kcal/mole)
0
10
20
30
40
50
60
NORMAL MODE ENERGIES (kcal/mole)
0
1000
2000
3000
4000
0
1
2
3
4
5
6
TIME (10^{-13} sec)

5.2. Vibration-Rotation Dynamics of Anharmonic Molecules

In Paper I it was discovered that any rotation of harmonic molecules enhanced the rate of intramolecular energy exchange, thereby increasing the reaction rate. From Figure 7b, it is obvious that anharmonic molecules change their oscillator energies at every contraction of the molecule. With no significant barrier to free flow of anharmonic molecular energies to overcome, rotation is not expected to have as marked an effect on anharmonic dynamics as it had on the harmonic one. We tested this expectation by subjecting some of the vibrating M_3 cases mentioned in Section 5.1.2. to systematic increase in rotational energy about the laboratory axes. In all these studies, the high sensitivity of metastable lifetime to perturbations in the initial conditions was again evident.

When M_3 is given potential energy in compression such that $V_1(0) = 2.35$, $V_2(0) = 160.72$, and $V_3(0) = 107.49$ kcal/mole, the molecule dissociates, expelling atom 2, with a metastable lifetime, τ_4, of about 1.7×10^{-13} seconds, as shown in Figure 8a. (This lifetime in insensitive to changes in $V_2(0)$ on the order of 8 kcal/mole. It lies in the first zone of dynamic continuity found in Figure 6.) When the same initial configuration is given less than 0.01 kcal/mole of rotational energy, $T_r(0)$, about the axis normal to the molecular plane, the reaction to give different products (atom 3 is released) occurs in 4.7×10^{-13} seconds as can be seen in Figure 8b. This rotational energy falls between the first and second rotational levels of the symmetric top molecule M_3. Thus, it is clear that there is no general continuity of

FIG. 8. Bond lengths for anharmonic M_3 trajectories. $V_1(0)$, $V_3(0)$ as in Figure 4. $V_2(0) = 160.62$ kcal/mole. —— bond 1; - - - - bond 2; —— - —— bond 3.

a) No initial rotational energy.

b) Initial rotational energy $T_r(0) = 0.00985$ kcal/mole about axis perpendicular to molecule and passing through its center of mass.

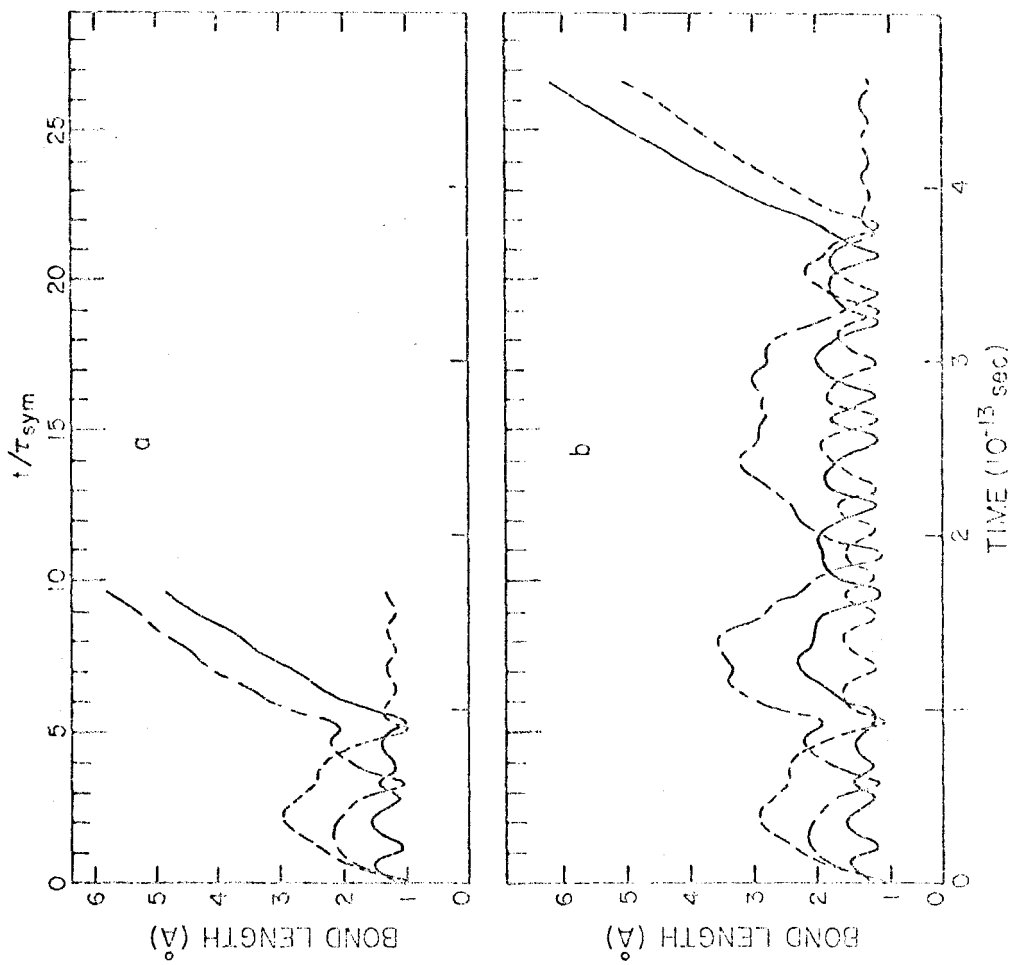
t/τsym
0
5
10
15
20
25
a
b
BOND LENGTH (Å)
0
1
2
3
4
5
6
TIME (10-13 sec)

(classical) molecular lifetimes even on the smallest scale of energy differences allowed by quantum mechanics.

It is found that when $V_1(0)$ and $V_3(0)$ have the constant values used in Section 5.1.2., and the variable $V_2(0)$ is in the range $188.69 < V_2(0) < 188.84$ kcal/mole, the transition between delayed and direct decomposition takes place. Table IV gives the corresponding ranges found for various vibrating-rotating anharmonic M_3 molecules. For the higher values of $V_2(0)$, it appears as if rotation about the Z axis (initially normal to the molecular plane) facilitates direct decomposition, that is, the molecule decomposes directly at lower total energies if it is rotating as well as vibrating. However, when the molecule has barely enough vibration energy to dissociate (a mere 2.35 kcal/mole excess), it requires an additional 119 kcal/mole of in-plane rotational energy for direct decomposition, whereas 57 kcal/mole of extra vibrational energy (in the absence of rotation) would make the molecule decompose directly. From this, it might be implied that rotational energy is somehow less available for the breaking of bonds than is vibrational energy. However, a change in the axis of rotation can reduce the rotational energy required for direct decomposition to values below the addition vibrational energy necessary to accomplish the same end. Hence, rotational energy cannot be dismissed as ineffective in the dissociation process. This corroborates a similar conclusion reached in connection with the harmonic molecules of Paper I.

Table IV. Minimum Direct Decomposition Energies[a] for M_3

$V_2(0)$[b]	$E_{rot}(0)$	Axis	Total Energy
188.69 - 188.84	0	-	298.52 - 298.67
180.33[c]	0 - 1.19	$\hat{z}$	290.16 - 291.35
171.97[c]	0 - 4.78	$\hat{z}$	281.80 - 286.58
160.62[c]	13.14 - 14.33	$\hat{z}$	283.59 - 284.78
131.37[d]	119.42 - 131.37	$\hat{z}$	360.21 - 372.13
"	71.65 - 74.64	$\hat{x}$	312.85 - 315.84
"	59.71 - 62.70	$\hat{y}$	300.91 - 303.90
"	35.83 - 41.80	$\hat{x} + \hat{y}$	277.03 - 283.00
"	38.81 - 40.31	$\hat{x} + \hat{y} + \hat{z}$	280.01 - 281.51

[a]Ranges in energies imply that the trajectory with the high value decomposed the molecule directly while its nearest neighbor, with the low value, did not.

[b]$V_1(0) = 2.35$, $V_3(0) = 107.48$. All energies in kcal/mole.

[c]τ stable with respect to variation in $V_2(0)$ near this value.

[d] $\sum_{i=1}^{3} V_i(0) = 2D_o + 2.35$ kcal/mole ($D_o = 119.42$ kcal/mole).

6. Summary

Classical-mechanical anharmonic trajectories differ from harmonic ones in the expected ways. At energies above dissociation, anharmonic bonds exchange vibrational energy at rates governed by the frequency of bond compression. Modes of very different harmonic frequency appear to exchange energy as rapidly as degenerate ones. The usual definitions of normal modes lead to normal mode energies which fluctuate widely as does their sum. As with the harmonic models (6), rotational energies have a strong effect upon the detailed dynamics of anharmonic molecules.

Metastable classical-mechanical lifetimes of anharmonic molecular models are not monotonic functions of vibrational-rotational energies. The great sensitivity of lifetime to (0.01%) perturbations in vibration-rotation energies renders calculation of $\tau(s)$, lifetime as a function of initial (classical) energized state, impractical as a means of obtaining unimolecular rate constants. The general instability of anharmonic classical dynamics suggests that there may be a serious divergence between classical and quantum trajectories for the same energized states. Confirmation of this suspicion awaits investigation of the behavior of classical trajectory swarms (11) for these systems. The averaging process inherent in such swarms <u>may</u> moderate the instabilities observed in this paper.

REFERENCES

1. F.A. Lindemann, Trans. Faraday Soc. 17, 599 (1922).
2. N.B. Slater, Theory of Unimolecular Reactions, Cornell University Press, Ithaca, 1959, Chap. 9, pp. 190-2.
3. E.W. Schlag, R.A. Sandmark, and W.G. Valance, J. Chem. Phys. 40, 1461 (1964) and references therein.
4. J.C. Tou, J. Phys. Chem. 71, 2721 (1967) and references therein.
5. Reference 2, pp. 195-8.
6. C.A. Parr, A. Kuppermann, and R.N. Porter, preceding paper.
7. S.W. Benson, Foundations of Chemical Kinetics, McGraw-Hill Book Company, Inc., New York, 1960, Chap. X.
8. See, for example, F.H. Mies and M. Krauss, J. Chem. Phys. 45, 4455 (1966).
9. L.I. Schiff, Quantum Mechanics, McGraw-Hill Book Company, Inc., New York, 1955, pp. 67-9.
10. M. Born and D.J. Hooten, Proc. Cambridge Phil. Soc. 52, 287 (1956).
11. (a) E.B. Alterman, C.T. Tahk, and D.J. Wilson, J. Chem. Phys. 44, 451 (1966); (b) R.C. Baetzold, C.T. Tahk, and D.J. Wilson, J. Chem. Phys. 45, 4209 (1966); (c) P.F. Endres and D.J. Wilson, J. Chem. Phys. 46, 425 (1967).
12. A. Messiah, Quantum Mechanics, John Wiley and Sons, Inc., New York, 1966, Vol. I, p. 29.
13. (a) R.D. Levine, J. Chem. Phys. 44, 2029 (1966) and references therein; (b) R.B. Frey and E. Thiele, J. Chem. Phys. 48, 3240 (1968).

14. D. L. Bunker and M. Pattengill, J. Chem. Phys. 48, 772 (1968).

15. The Eckart system and its application to these unimolecular trajectory studies are described in Section 4.3.1. of Paper I. The remaining three linear equations in the atomic velocities are

$$\left[\frac{M_1}{M_2}\dot{X}_1 + \left(1 + \frac{M_3}{M_2}\right)\dot{X}_3\right]\rho_{1_x} + \left[\frac{M_1}{M_2}\dot{Y}_1 + \left(1 + \frac{M_3}{M_2}\right)\dot{Y}_3\right]\rho_{1_y} = v_1 r_1$$

$$(\dot{X}_1 - \dot{X}_3)\rho_{2_x} + (\dot{Y}_1 - \dot{Y}_3)\rho_{2_y} = v_2 r_2$$

$$\left[\left(1 + \frac{M_1}{M_2}\right)\dot{X}_1 + \frac{M_3}{M_2}\dot{X}_3\right]\rho_{3_x} + \left[\left(1 + \frac{M_1}{M_2}\right)\dot{Y}_1 + \frac{M_3}{M_2}\dot{Y}_3\right]\rho_{3_y} = v_3 r_3$$

where $\underset{\sim}{\rho}_i$ is the i^{th} bond vector in the Eckart frame and v_i is (minus) the bond velocity. Inversion of these four equations is straightforward.

16. J. R. Durig and R. C. Lord, Spectrochim. Acta 19, 421 (1963).

17. M. Brook and J. Kaplan, Phys. Rev. 96, 1540 (1954).

18. H. S. Johnston, Adv. Chem. Phys. 3, 131 (1960).

19. W. B. Eberhardt and T. G. Burke, J. Chem. Phys. 20, 529 (1953).

20. These lifetimes, τ, are not the τ_4 discussed in Section 4.3., but rather the average of τ_4 and τ_c, the time to the last contraction of the last bond to break. Thus $\tau < \tau_4$ but still a good measure of the molecule's stability.

Part III. The H + DX Reactions

THE H + DX REACTIONS

1. Introduction

Detailed information about the progress and outcome of elementary bimolecular chemical reactions is rapidly becoming available through ab initio calculations. The solution of classical and quantum mechanical equations of motion of various intra- and intermolecular models provide predictions to be tested against the results of the new, sophisticated experiments in beams, chemiluminescence, hot atom studies, and photochemistry. The system of highest interest for the theoretician is the ortho-para conversion of molecular hydrogen. Ab initio calculations of the forces of the H_3 intermediate (1) are possible due to the simplicity of the system. For the same reason, the quantum dynamics of the reaction may be attempted (2). At present, however, in systems with many more than three electrons, ab initio potential surface calculations are prohibitively expensive. They may yield total electronic energies correct to within a per cent, but chemical energies are of the order of magnitude of the errors. Thus, even these small errors in molecular potentials render them untrustworthy for the very demanding chemical reaction purposes. Furthermore, given the correct force fields, quantum mechanical solution of the many-body problem posed by chemical reactions is a formidable task. Thus, to date, the majority of effort expended in the study of the dynamics of reacting molecules has been in obtaining classical-mechanical solutions to reactions between atoms and molecules taking place on ad hoc or semi-empirical potential surfaces.

The earliest such work was Hirschfelder's (3a) laborious hand

calculation of part of the trajectory of a hydrogen atom incident upon a hydrogen molecule. The co-linear collision took place on the London-Eyring-Polanyi (LEP) potential surface (3b) for H_3. That pioneering effort stood alone for 22 years before the availability of high speed electronic computers obviated the human labor of numerical integration. Many of the recent bimolecular trajectory studies have been reviewed by Bunker (4).

This paper includes some of the results of a trajectory study of the abstraction and exchange reactions occuring when hydrogen atoms strike deuterium bromide. The motivation for the study came from recent photolysis experiments (5) involving monochromatic photo-dissociation of DX (X = Br or I). The resultant monoenergetic D atoms react with hydrogen molecules releasing hydrogen atoms. The latter attack undissociated DX and complicate the HD yield analysis with their subsequent reactions. The experiments have shown that at room temperature, the reactions

$$H + DX \xrightarrow{k_a} HD + X \qquad (1.-1)$$

and

$$H + XD \xrightarrow{k_e} HX + D \qquad (1.-2)$$

have an abstraction fraction, $k_a/(k_a + k_e)$, of 0.88 and 0.85 for X = Br and I, respectively. Such quantities are used here to calibrate a semi-empirical HDX potential surface for transition state and trajectory calculations. The results of these calculations aid in understanding the experiments in a kind of chemical bootstrap operation.

Phase space theory calculations have been carried out on these

reactions (6). Comparison of the details of these calculations with the trajectories provides further incentive for the present studies.

2. Methods

The classical equations of motion of the three-body system, the Monte Carlo methods for the choice of initial trajectory parameters, the calculation of final state properties, and reaction cross-sections are all taken, with slight modifications, from Section II of the monumental work of Karplus, Porter, and Sharma (7). Vibration-rotation constants for DBr, given in Table I, were calculated from those for the hydrogen isotope (8) through Dunham's formulae (9). The test for trajectory termination outlined in Ref. 7 was modified to accomodate unequal atomic masses, and a single precision (eight significant decimal digits) Adams-Moulton 5^{th} order Predictor/Correcter integration routine (10) was employed to solve Hamilton's equations of motion. The potential function used in this work was a modified London-Eyring-Polanyi-Sato (11,12) (LEPS) one discussed in the next section.

With the chosen potential, it was found that H + DBr trajectories could be followed for about 1.5×10^{-13} seconds (molecule time) with an integration step size of about 3×10^{-16} seconds. These figures pertain to collisions with relative energies of about 0.5 eV. Collisions at higher energies required somewhat smaller step sizes to maintain the desired accuracy (10) over the course of the encounter. Computer time was a function of both step size and relative energy. For example, a batch of 200 trajectories of 0.25 eV collisions integrated with a step size $\Delta t = 3.25 \times 10^{-16}$ seconds (molecule time) took about 13 minutes of IBM 7094

Table I. Vibration-Rotation Constants for DBr[a,b]

$G_1 = 0.23363$	$G_2 = -2.837 \times 10^{-3}$	$G_3 = -1.3 \times 10^{-7}$
$F_{11} = 5.311 \times 10^{-4}$	$F_{21} = -1.5 \times 10^{-8}$	$F_{31} = 2 \times 10^{-13}$
$F_{12} = -7.41 \times 10^{-6}$	$F_{22} = 9 \times 10^{-11}$	$F_{32} = -9 \times 10^{-15}$
$F_{13} = 1.4 \times 10^{-8}$	$F_{23} = -4 \times 10^{-12}$	$F_{33} = 0$

[a] Durham isotope calculations (9) on the HBr data of Rank, Fink, and Wiggins (8).

[b] All values are in eV. See Eqn. 15 in Ref. 7 for the energy expression involving these coefficients. Durham (9) uses $W(v,J) = \sum_{m,n\neq 0} Y_{mn}(v + \frac{1}{2})^m \cdot J^n(J+1)^n$, where $Y_{io} = G_i$ and $Y_{j-1,i} = F_{ij}$.

time. Collision trajectories with relative energies near 1 eV had to be integrated with step sizes of only 2.5×10^{-16} seconds. Two hundred such trajectories were generated by the computer in about 11 minutes. The programs were written in FORTRAN IV.

3. Potential Surface for H + DX

Potential surfaces are defined only within the Born-Oppenheimer approximation for separation of nuclear and electronic motions. If this approximation fails, the potential is not a function of atomic co-ordinates alone but becomes a function of momenta as well, destroying the conservative system so far as the nuclei are concerned. But to the extent to which the Born-Oppenheimer approximation is valid (relative energies of chemical interest fall within this domain), potential energies are independent of isotopic substitution. Thus, a potential surface valid for $H + DBr^{79}$ will be satisfactory for $T + HBr^{81}$ and so on. The generic name to be applied in this paper to all reactions involving one halogen isotope and two hydrogen isotopes will be H_2X. The H_2X potential surfaces should vary only with X.

3.1 Previous H_2X Potential Surfaces

To date, all H_2X potentials have been obtained from approximate three-electron valence bond methods. Glasstone, Laidler, and Eyring (GLE) (13) describe LEP surfaces for H_2X (X = Cl, Br, I). These are obtained, in part, from the London equation specialized to three s electrons. This expression is derived from the valence bond method when triple exchange integrals and overlap of atomic orbitals

are ignored. It has been argued (14) that the terms, which have been dropped, give rise to energies larger than some of the unique features in the LEP surfaces. These potentials characteristically show deep minima corresponding to stable or metastable H_2X complexes. For example, HClH is found to be stable with respect to Cl + H_2 by 0.75 eV. As no such molecule as HClH has been found spectroscopically, it must be concluded that these minima are at best analomously deep and, at worst, artifacts of the LEP approximations.

GLE (13) claimed that support for these minima arose from the calculations of Magee (15). He applied the valence bond method to one p and two s electrons hoping to obtain a better three-electron model for H_2X. Magee's calculation also ignored triple exchange and approximated three-center integrals. With an invariant orbital exponent of 2 for the p electron (a propos fluorine), he obtained a potential surface for H_2Cl, which rendered one isoceles symmetric configuration of the complex over 1 eV stable with respect to Cl + H_2.

In an effort to eliminate the rather modest 1.5 kcal/mole minimum, comprising "Lake Eyring," in the LEP surface (3b) for H_3, Sato (11,16) postulated an "anti-Morse" function for any diatom's lowest repulsive electronic state. When this function was coupled with the standard Morse function for the ground electronic state of the diatom, Sato obtained the valence bond coulomb and exchange energies directly, without the LEP assumption of a constant ratio between them. This ratio had been LEP's empirical parameter, which allowed for fitting of the potential surface to some experimental datum, such as "activation energy." Sato introduced such a parameter, which he associated (16) with the square of a single

constant overlap integral.

It has long been supposed (17) that Sato's method and modifications (12) thereof yield potential surfaces which are free of the spurious wells mentioned above. Persky and Klein (18), Timmons and Weston (19), and Sullivan (20) have all used Sato surfaces to correlate isotope effects in the reactions of $X + H^iH^j$ (i,j = 1,2, and sometimes 3 and X = Cl, Br, I, respectively, in these three papers). Timmons et al. and Sullivan obtained rather poor fits to their experimental data of activated complex theory (ACT) isotope effects using a Sato surface with a single adjustable parameter. Persky and Klein, however, using the multi-parameter modification suggested by Polanyi (12) were able to reproduce the effects of five of the isotopic combinations in $Cl + H^iH^j$ very well. Their calculations, as well as those of Sullivan and Timmons et al., dealt only with the linear XHH complexes. The present work required the potential surface for these three atoms for all possible geometric configurations, including, for example, linear HXH.

3.2. Present Sato Surface for H_2X

It was found that the Sato parameters a propos $Cl + H_2$ used by Persky and Klein (18) (their Sato II) gave a potential well for HClH over 6 kcal/mole deep with respect to the most stable products, $Cl + H_2$. This "Lake Sato" was over 9 kcal/mole stable with respect to the linear dissociation giving HCl + H. The Sato surfaces for HBrH (19) and HIH (20) with the single parameter set to 0.2 were also found to harbor basins of over 5 and 4 kcal/mole depth with respect to HBr + H and HI + H , respectively.

Some of the three-dimensional trajectories, which we had planned to investigate, would have probed these basins. In the absence of a fourth body to carry away energy, our computer simulated collisions would never have produced stable HXH molecules, but the existence of wells in the potential surface would have led to metastable, long-lived HXH complexes. It has been suggested (21) that such metastable classical mechanical trajectories are less likely to follow the results of an accurate quantum mechanical scattering treatment than would the classical trajectories of direct collisions. With this (and the hope that such basins were indeed spurious) in mind, we varied the Sato parameters k_{H_2} and k_{HX} independently to remove the wells and retain agreement with experiment.

The modified (12) Sato potential for A + BC is

$$V = V_o + Q_{AB} + Q_{BC} + Q_{CA} - [(\alpha_{AB} - \alpha_{BC})^2 + (\alpha_{BC} - \alpha_{CA})^2 + (\alpha_{CA} - \alpha_{AB})^2]^{\frac{1}{2}}/\sqrt{2} \qquad (3.2.-1)$$

where

$$Q_{ij} = \frac{D_{ij}X_{ij}[(k_{ij} + 3)X_{ij} - 2(3k_{ij} + 1)]}{4(k_{ij} + 1)}$$

$$\alpha_{ij} = \frac{D_{ij}X_{ij}}{4(k_{ij} + 1)}[(3k_{ij} + 1)X_{ij} - 2(k_{ij} + 3)] \qquad (3.2.-2)$$

and

$$X_{ij} = \exp[-\beta_{ij}(r_{ij} - r_{ij}^{eq})] \ .$$

The k_{ij} in the above equations are the Sato parameters for the diatoms ij.

The D_{ij}, r_{ij}^{eq}, and β_{ij} are the ij^{th} diatom's potential energy of dissociation equilibrium internuclear distance, and Morse parameter, respectively. If we set V_o equal to the largest D_{ij}, the zero of energy lies at the bottom of the channel with the most stable diatom. The diatom constants (and final Sato parameter choices) are given in Table II.

3.2.1. Stable and Unstable HXH

Since the potential surface for linear HXH is symmetric about the line r(HX) = r(XH), we need only find the minimum value of the potential along that line and we have located an extremum. If a normal mode analysis of this extremum gives characteristic frequencies which are all real, the extremum is a basin. If one of the frequencies is imaginary, the extremum is a symmetric col or saddlepoint. We used Newton's Method of Slopes (22) to search out these symmetric extrema on Sato surfaces defined by points in a two-dimensional grid of Sato parameters for H_2 and HX. The parameters were varied independently from 0 to 1, and the nature of the symmetric extrema for HXH (X = Cl, Br, I) was determined as a function of grid location. The results of this investigation are shown in Figure 1. Any $k(HX) \gtrsim 0.08$ gives rise to a Sato surface with a stable or metastable HXH complex. The larger the value of k(HX), for a given $k(H_2)$, the deeper is the resulting basin. For $k(HX) \sim 0.2$, the bottom of the basin is at a lower potential than HX + H, and for X = Cl the well is even deeper than the Cl + H_2 channel! Clearly, only small k(HX) parameters give chemically sensible potential surfaces if we hold that the Sato parameters are not functions of the geometry of H_2X.

Table II. Sato Potential Parameters[a]

Diatom ij	H_2	HBr	HI
D_{ij} (kcal/mole)	109.43	90.33	73.78
r_{ij}^{eq} (Å)	0.7417	1.4138	1.604
β_{ij} ($Å^{-1}$)	1.942	1.8109	1.750
k_{ij}	0.225	0.076	0.0915

[a]See text for definitions.

FIG. 1. Sato Parameters which give Rise to Basins in the Potential Surface for Linear HXH. Vertical hatching, X = Cl. Horizontal hatching, X = Br. Dots, X = I. Basins become deeper as the HX Sato parameter increases.

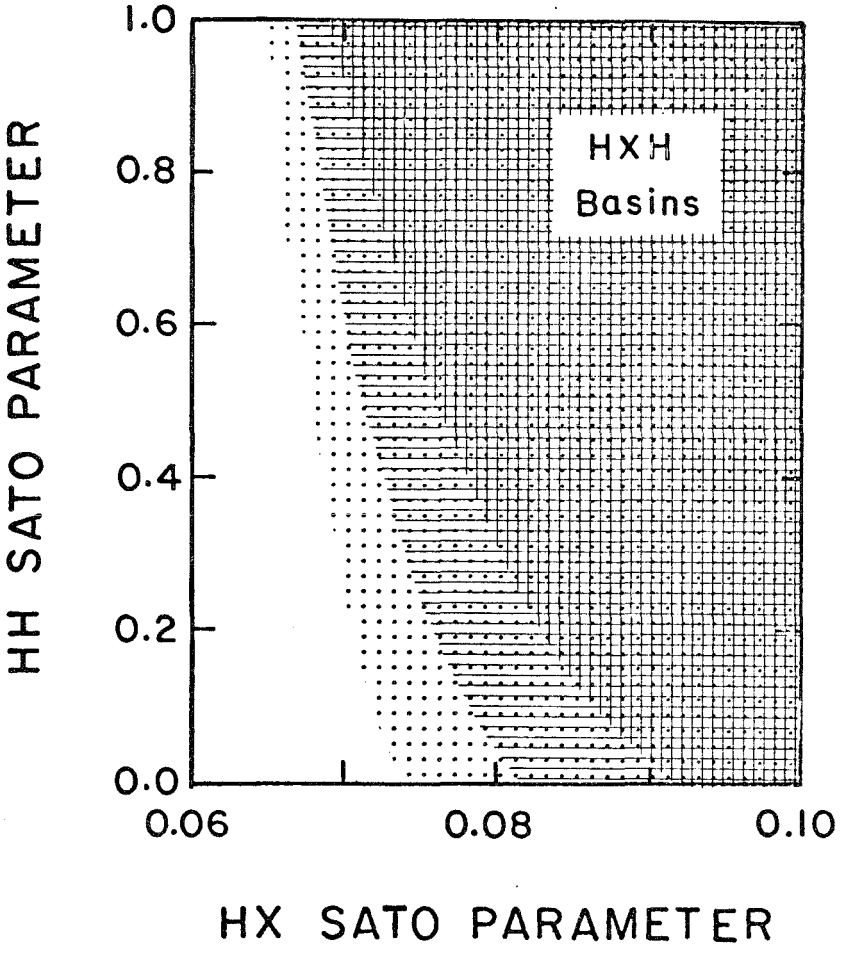
1.0
0.8
0.6
0.4
0.2
0.0
HH SATO PARAMETER
HXH
Basins
0.06
0.08
0.10
HX SATO PARAMETER

3.2.2. Activation Energies Calibration

Little is known about the activation energy for H attack on the halogen end of hydrogen halides. It is assumed that these energies are small, probably no greater than the 5 kcal/mole value found by Steiner and Rideal (23) using the LEP technique. However, the activation energies of $X + H_2$ reactions are better documented (24).

It is not clear what aspects of the chosen potential surface per se should be considered in comparison with experimental Arrhenius activation energies. Ideally, one calculates the rate constant as a function of temperature from reaction cross-sections obtained by accurate solution of the collision dynamics on the given surface. This rate constant data is fit to an Arrhenius form as is the experimental data. Thus the dynamics are central to activation energy calculation. Such a method would prove tedious if used to calibrate the surface by matching the experimental and calculated Arrhenius activation energies.

A more common (13,25) calibration procedure is comparison of a calculated "activation energy at absolute zero," E_o, with the experimental Arrhenius activation energy, E_a. The quantity E_o has no dynamic dependence and represents the classical potential energy barrier height, $V^{\ddagger}$, corrected for zero point energies of the reactants and complex. A potential surface, so calibrated, is usually used in a transition state calculation to derive reaction rates or isotope effects. However, transition state theory (or ACT) yields rate constants with temperature-dependent pre-exponential factors, that is, non-Arrhenius forms. If the potential surface is to be calibrated to a level of approximation consistent with its

subsequent use, E_a should be compared with an activation energy (26) derived from the ACT rate expression, an energy which we shall call $E_a'(T)$. Table III shows that E_o, which is equal to $E_a'(0°K)$, can differ significantly from $E_o'(T)$ when T lies in the range of interest for chemical reactions.

Since trajectory calculations on simple potential surfaces (without basins) have shown molecular collisions to be impulsive rather than "sticky," the activation energy calculated rigorously from the dynamics may be very different (27) from either E_o or $E_a'(T)$. However, we calibrated (see Appendix 1) our H_2X surfaces, in part, by matching the calculated $E_a'(1000°K)$ to the experimental E_a for Br + H_2 and Br + D_2 to within their experimental errors. The loci of points of constant $E_a'(1000°K)$ are essentially straight lines in the regions of interest in the Sato parameter plane. In other words, when the Sato parameters, $k(H_2)$ and k(HBr), are varied in such a way that the resulting Sato surfaces yield constant ACT activation energies (26), evaluated at 1000°K, it turns out that the variation relates the parameters to one another almost linearly. The lines corresponding to the experimental activation energies (Table III) for Br + H_2 and Br + D_2 cross in the Sato parameter plane near the point $k(H_2) = 0.245$, $k(HBr) = 0.058$. The Sato surface determined by these parameters yields $E_a'(1000°K)$ which satisfy both experimental values simultaneously.

3.2.3. Abstraction Fraction Calibrations

Unfortunately, no reasonable variation of the Sato parameters gives $E_a'(1000°K)$ in agreement with the experimental Arrhenius activa-

Table III. Activation Energies for $X + H_2$[a]

Reaction	Experimental Arrhenius[b]	Sato[c]			
		$V^{\ddagger}$	E_o	E_a' (1000°K)	
$Br + H_2$	19.7 ± 0.4	20.85	18.28	20.02	d
$Br + D_2$	21.4 ± 0.4	20.85	19.04	21.54	d
$I + H_2$[f]	32.80 ± 0.25	35.71	33.04	35.88	d
$Cl + H_2$	5.48 ± 0.14	7.76	5.50	6.48	e

[a]All values in kcal/mole.

[b]Ref. 24.

[c]See text for definitions of $V^{\ddagger}$, E_o, and E_a'.

[d]This paper's Sato surface (see Table II).

[e]Single parameter Sato surface (k = 0.177) from Ref. 25.

[f]E_a, experimental Arrhenius activation energy taken from J. H. Sullivan, J. Chem. Phys. 36, 1925 (1962).

tion energy for $I + H_2$. However, experimental values of rate ratios for reactions (1.-1,2) are available (5) from photochemistry experiments. ACT rate ratios may be fit to these values to calibrate the surfaces. If we let the ACT rate for a reaction, r, be given by

$$k_r(T) = B_r(T) \exp(-V_r^{\ddagger}/RT) \ . \qquad (3.2.3.-1)$$

Then the abstraction fraction (AF) from ACT becomes

$$AF = 1/(1 + B_e e^{-V_e^{\ddagger}/RT} / B_a e^{-V_a^{\ddagger}/RT}). \qquad (3.2.3.-2)$$

In this expression, $V_e^{\ddagger}$ is the potential barrier to the exchange reaction (1.-2) and $V_a^{\ddagger}$ the barrier to abstraction (1.-1). Equation (3.2.3.-2) may be inverted to give

$$V_a^{\ddagger} - V_e^{\ddagger} = RT \ln\left\{\frac{B_a}{B_e}\left[\frac{1}{AF} - 1\right]\right\} \qquad (3.2.3.-3)$$

enabling one to calculate the difference in potential barrier heights given the ACT pre-exponential factors and the abstraction fraction (see Section 1) at some temperature. In general, this potential difference will not agree with that taken from the surface whose saddlepoint ‡ gave rise to the ACT B's. The Sato parameters are varied until this discrepancy vanishes, whereupon the potential surfaces consistent with a given AF to the ACT approximation have been found.

The loci of points in the Sato parameter plane which satisfy the above condition for X = Br is a curve which crosses the lines of experimental E_a at almost right angles. Thus there is only a small area in the

parameter plane which gives rise to Sato surfaces which simultaneously satisfy the experimental AF and activation energies to within their uncertainties. The Sato surface with $k(H_2) = 0.225$ and $k(HBr) = 0.076$ is such a one and will be taken as the potential surface for H_2Br throughout this paper.

If we insist that the Sato parameters for both HX diatoms in an arbitrary configuration of H_2X are the same constant, we may transfer the Sato parameter for H_2 from the H_2Br surface to the H_2I surface with the same degree of approximation. Thus, the experimental AF for X = I serves to calibrate the Sato H_2I potential surface. The resultant best fit parameters appear in Table II. The characteristics of both surfaces are given in Table IV.

The chosen potential surfaces were used to determine the temperature dependence of the abstraction fractions for both halides, X = Br and I, with some of the possible hydrogen isotopic combinations. ACT calculations (see Appendix 2) gave the results shown in Figures 2 and 3. Although ACT provides better predictions for rate ratios than for the rates themselves (through some cancellation of errors), these AF's should be regarded as more indicative of general trends than as reliable absolute values. Caution should be exercised in interpreting the AF at the extreme temperatures in the range shown, because for low temperatures (less than 300°K for Br or 200°K for I) the parabolic tunneling approximation breaks down, while for high temperatures (above 800°K for Br or 300°K for I) the classical bending vibration amplitude (28) of the linear HXH complex sweeps out over π radius, a physical impossibility. Nevertheless, it is clear from the figures that there is a marked tempera-

Table IV. H_2X Saddlepoint Characteristics

Linear Complex	R_1 (Å)	R_2	F_{11}	F_{22} mdyn/Å	F_{12}	F_ϕ 10^{-13}ergs/rad^2	$V^\ddagger$ kcal/mole[a]
H—H—Br	1.148	1.490	0.064	2.277	0.938	6.500	1.75
H—Br—H	1.577	1.577	0.984	0.984	0.985	0.688	3.95
H—H—I	1.984	1.608	-0.004	3.067	0.041	0.701	0.06
H—I—H[b]	2.028	1.652	0.026	2.142	0.435	0.229	2.17

[a] $V^\ddagger$ is the classical potential energy difference between the complex, A—B—C, and reactants, A + B—C.

[b] There is a very shallow symmetric basin (< 1/5 kcal/mole with respect to the barrier height) situated at r(HI) = r(IH) = 1.75 Å.

FIG. 2. Abstraction Fraction for $H^i + H^jBr$ vs Temperature. Upper curve, i = 1 and j = 1,2,3; lower curve, i = 2 and j = 1,2,3. Dashed line indicates failure of parabolic tunneling. ACT treatment of bending vibrations in HBrH breaks down above T = 785°K.

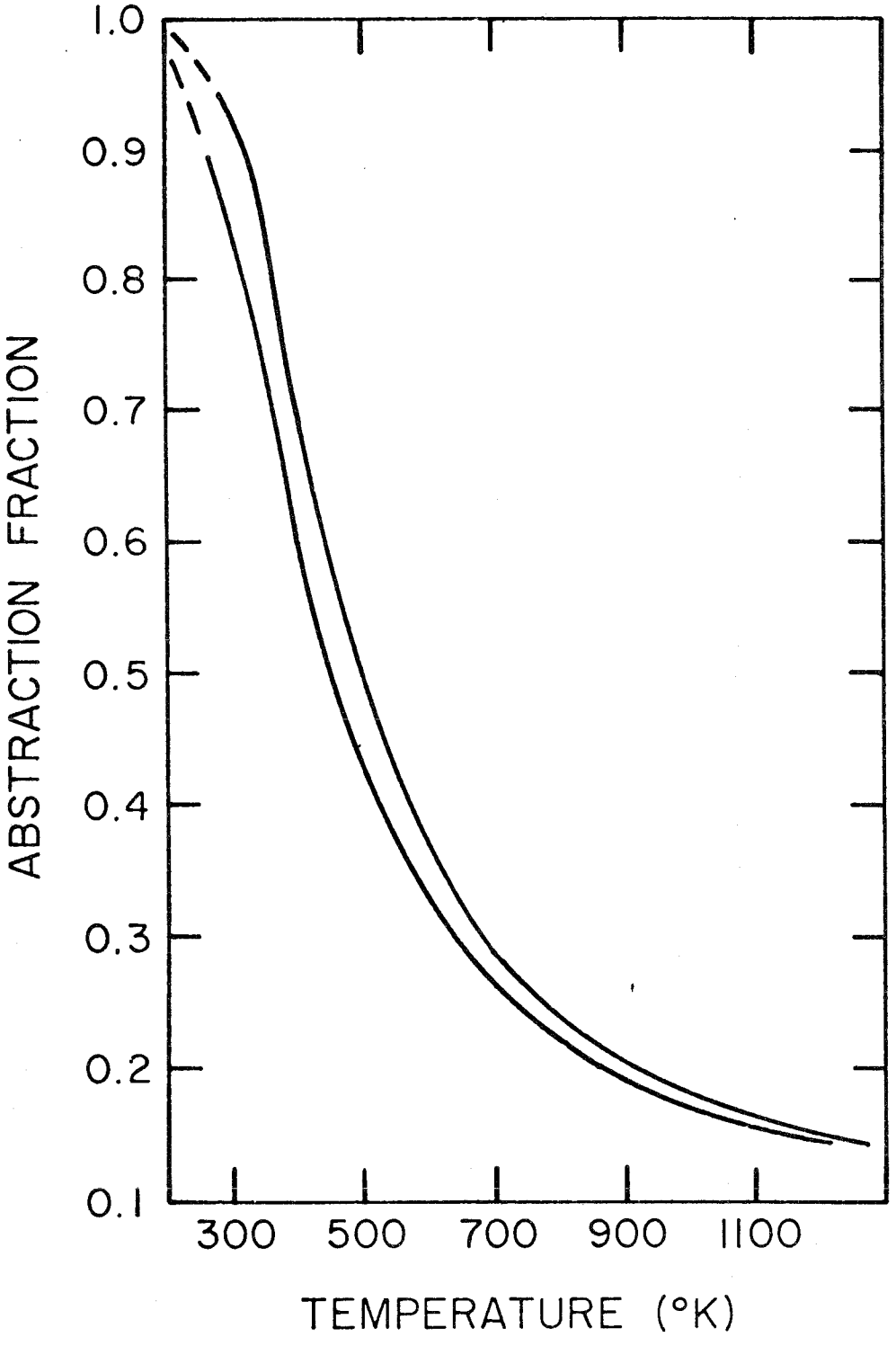
1.0
0.9
0.8
0.7
0.6
0.5
0.4
0.3
0.2
0.1
ABSTRACTION FRACTION
300
500
700
900
1100
TEMPERATURE (°K)

FIG. 3. Abstraction Fraction for $H^i + H^jI$ vs Temperature. Upper curve, i = 1,2,3 and j = 2; lower curve, i = 1, 2,3 and j = 1.

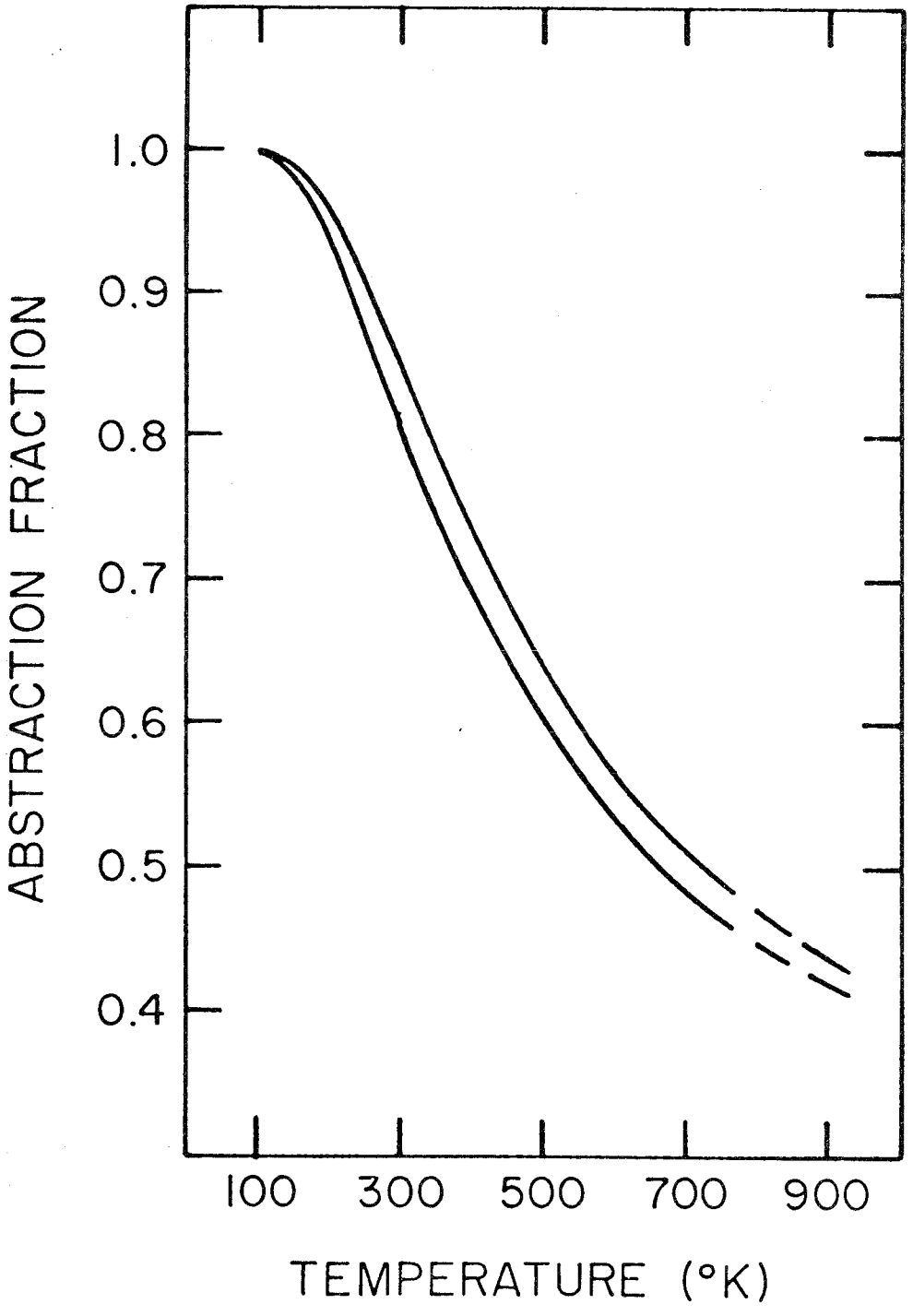
ABSTRACTION FRACTION
1.0
0.9
0.8
0.7
0.6
0.5
0.4
100
300
500
700
900
TEMPERATURE (°K)

ture dependence in both abstraction fractions, indicating very different energetics for the two reactions (1.-1 and 2). The difference in potential energies of activation (Table IV) insures the dominance of abstraction at low energies, while the very low bending force constant of HXH enhances exchange at the higher ones. The latter effect follows from the fact that partition functions for low frequency vibrations are larger than those for high ones at the same temperature. Since the bending vibrations in a linear complex are doubly degenerate, the exchange rate enhancement goes as the square of the larger partition function.

3.2.4. Properties of the Potential

The contour diagram (29) of the potential surface of linear H—H—Br is shown in Figure 4. This surface is quite repulsive in Polanyi's terminology (12,30). Since the majority of the potential drop occurs after the "reaction path" (31) has "turned the corner," one expects little product excitation in abstraction. The same situation prevails on the H—H—I potential energy surface, which has the same general shape as Sullivan's (20). On our HHI surface, the energy release is only 9% attractive (32) and 91% repulsive, leading again to the expectation of vibrationally cold H_2 product. Of course, for the thermoneutral exchange reactions, there is no energy release. One anticipates cold products from these reactions due to their thermoneutrality.

In the preceding section, the dominance of exchange at high temperatures was related to the difference in bending frequencies between the linear HHX and HXH complexes. A more physical explanation is available from the potential surfaces themselves. If we hold the target

FIG. 4. Potential Energy Surface for Linear H—H—Br. Sato parameters given in Table II. Contour values from 5.5 to 30.0 kcal/mole in steps of 0.5 kcal/mole. Product channel, lower right, drops to 0 kcal/mole as $x \rightarrow \infty$. Reactant channel, top left, drops to 19.1 kcal/mole as $y \rightarrow \infty$. Saddlepoint potential $V^* = 20.85$ kcal/mole with respect to product, $H_2 + Br$.

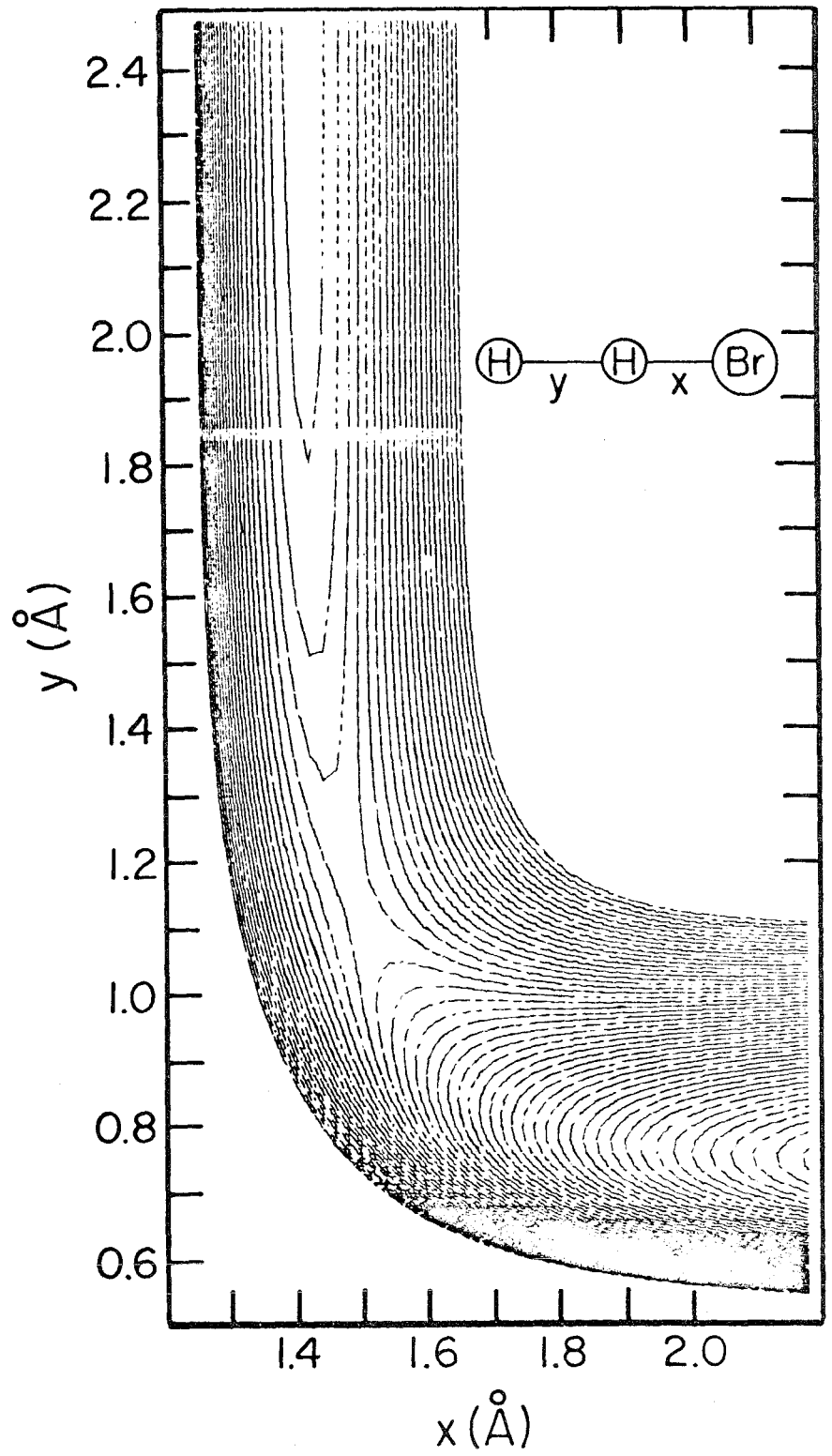
2.4
2.2
2.0
1.8
1.6
1.4
1.2
1.0
0.8
0.6
y (Å)
1.4
1.6
1.8
2.0
x (Å)
H
y
H
x
Br

HBr diatom at a constant bond length of 1.58 Å (the value it has at the symmetric HBrH complex) and determine the potential energy as a function of the distance between the Br and incident H atoms and the H—Br—H external angle, we obtain the diagram in Figure 5. A strong orientation force is evident. There is a potential ridge lying along $\theta \simeq 146^\circ$ which divides the abstraction domain from the exchange. The ridge becomes more evident when one views the surface in 3-D perspective (33), as in Figure 6.

In a simple-minded view of the dynamics, one suspects that hot hydrogen atoms incident upon DBr within a solid angle of 146° half-width about the Br are deflected to collide with that end of the molecule. Incident H atoms falling within a solid angle of only 34° half width about the D atom will be directed to that end of the molecule. (Clearly the more energetic hydrogen atoms will experience less deflection for a given force. The assumption that any deflection suffices to direct the incoming atom to one end of the DBr or the other breaks down at high energies.) If we make the further assumption that once a hot hydrogen atom (with translational energy significantly above either potential barrier) "strikes" either end of the DBr molecule, the probability of reaction is the same, then abstraction fraction is simply the ratio of the area associated with the 34° solid angle to that of the unit sphere. With this naive picture, the high energy abstraction fraction should be

$$AF \longrightarrow \frac{1 - \cos(\pi - \theta_r)}{2} \qquad (3.2.4.-1)$$

where θ_r is the angle associated with the spine of the ridge in figures

FIG. 5. Potential Energy Surface for Bent H—Br—H. Sato parameters given in Table II. Contour values from 20 to 29 kcal/mole relative to Br + H_2 (or 0.9 to 9.9 kcal/mole relative to H + HBr) in steps of 1 kcal/mole. Highest contour is the left most. Depressions at (x = 1.58, $\theta = 0^\circ$) and (x = 2.5, $\theta = 180^\circ$) represent exchange and abstraction configurations, respectively.

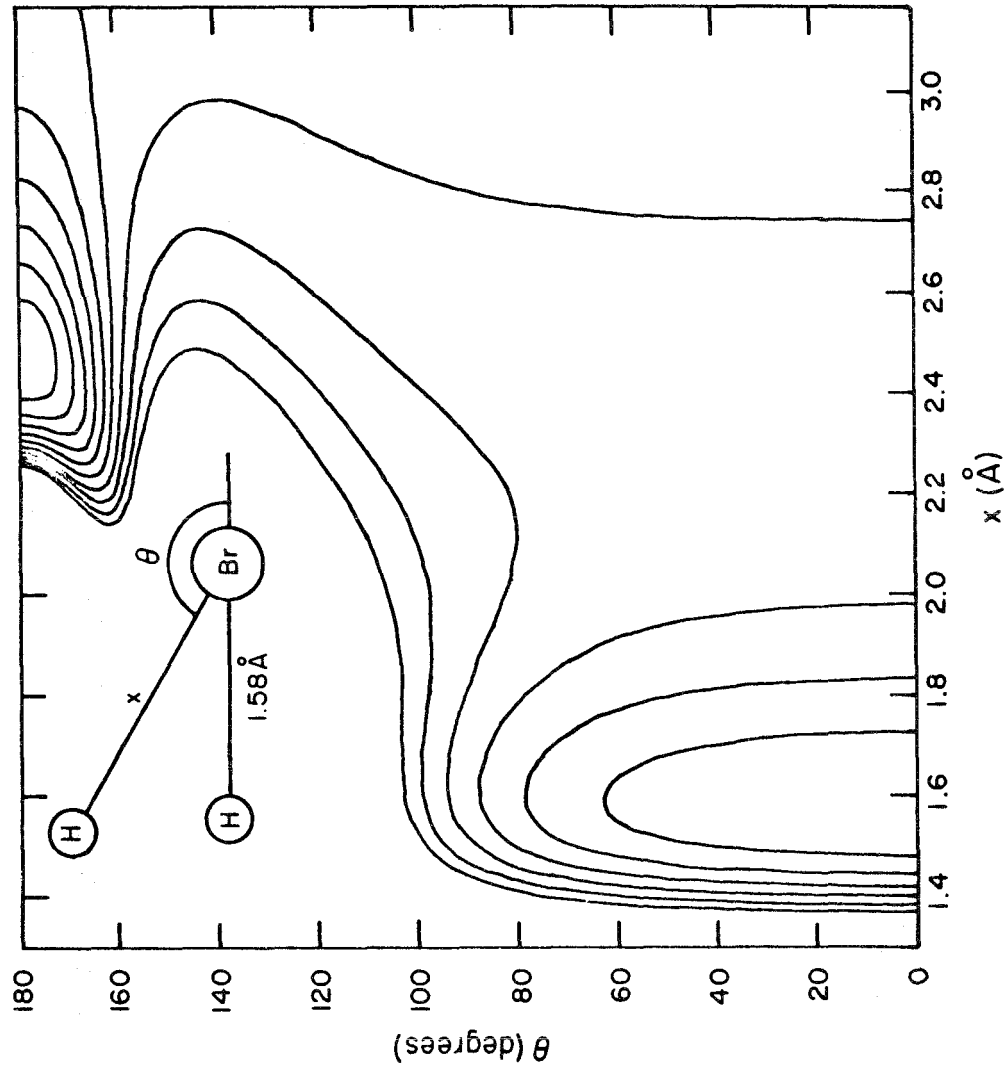
θ (degrees)
180
160
140
120
100
80
60
40
20
0
x (Å)
1.4
1.6
1.8
2.0
2.2
2.4
2.6
2.8
3.0
H
Br
H
1.58Å
x
θ

FIG. 6. Potential Energy Surface for Bent H—Br—H. Sato parameters given in Table II. x and θ are defined in Figure 5. H—Br target diatom internuclear distance set at 1.58 Å. Viewing angle: 60° colatitude, 25° azimuth. Potential energies with respect to Br + H_2.

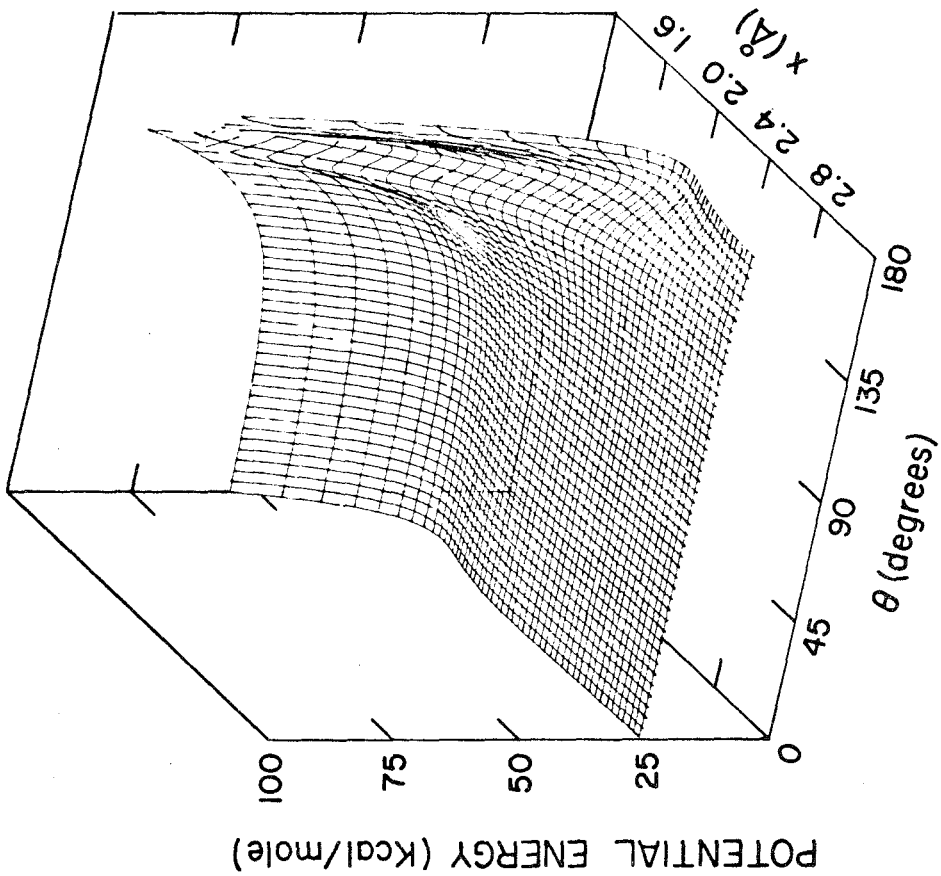
POTENTIAL ENERGY (kcal/mole)
100
75
50
25
0
45
90
135
180
θ (degrees)
2.8
2.4
2.0
1.6
x (Å)

like 5 and 6. Thus AF(X = Br) → 0.08 when the collision energy exceeds both barrier heights.

The fixed 1.58 Å target HBr bond distance corresponds to a diatomic potential energy of about 6.3 kcal/mole, that is, 2.5, 3.6, and 4.1 kcal/mole in excess of the zero point energies of HBr, DBr, and TBr. Thermal hydrogen halide target molecules should be in their ground vibrational state. (This was assumed for the trajectories of Section 4.2.) The fixed bond length for the target HBr was thus too large. The distance was reduced to 1.49 Å (H—Br distance in the linear HHBr complex), corresponding to a diatomic potential of only 1.4 kcal/mole. With this bond distance held fixed θ_r became 150°, changing AF(X = Br) → 0.07 for high energy collisions.

During the course of a collision, the target diatom would not be frozen at some stretched or compressed configuration as is assumed for Figures 5 and 6. The way in which the target diatom bond length would change would surely depend on the initial conditions and subsequent dynamics of each collision. In order for the target diatom to appear stationary, the incident H atom would have to have a flyby time at least an order of magnitude shorter than the diatom vibration period. If we use the HBr vibration period and its equilibrium bond length to determine this minimum velocity ($v_H = 10\, r^{eq}_{HBr}\, \nu_{HBr}$), the H atom must have over 65 eV translational energy! This is high indeed; in fact, it is unattainable in the monochromatic photochemical studies (5) mentioned in the introduction. If, instead, we assume that the target diatom is always relaxed, that is, for every position of the approaching H atom, the target HBr bond length (but not orientation angle) adjusts to the value

which minimizes the total potential energy, we obtain the potential surface (see Appendix 3) shown in Figure 7. From this diagram, $\theta_r = 155°$. Thus, for case of the perpetually relaxed target, AF (X = Br) → 0.05 at relative energies high with respect to the potential barriers, yet low enough to allow the target to equilibrate to each position of the advancing H atom. These last are mutually exclusive criteria, no doubt.

The fixed and relaxed target angular potentials for X = I are shown in Figures 8 and 9. These diagrams give θ_r as 146° and 148°, respectively. The corresponding high energy abstraction fractions are AF (X = I) → 0.08 and 0.075.

3.2.5. Disadvantages

The disadvantage to <u>any</u> potential energy surface used in a classical trajectory calculation is that only <u>one</u> such surface may be used. All classical trajectories are adiabatic; they cannot cross over to surfaces leading to electronically excited products. When the excited state surfaces are well separated from the ground state, or when the reactions producing electronically excited products are highly endothermic, we may be justified in ignoring their contribution to the dynamics. Unfortunately, the assumption of electronic adiabaticity is a poor one for the reactions at hand. Free ground state halogen atoms are $^2P_{3/2}$. The lowest excited state for halogens is the $^2P_{1/2}$ state at an energy (6) of 0.11, 0.46, and 0.94 eV above the ground state for X = Cl, Br, and I, respectively. These values render the heats of reaction to produce X* ($^2P_{1/2}$) as +1.5, -6.0, and -11.0 kcal/mole for X = Cl, Br, and I, respectively (34). Thus X* should be important even in thermal reactions.

FIG. 7. Potential Energy Surface for Bent H—Br—H. Sato parameters given in Table II. x and θ have the same meaning as in Figures 5 and 6, but the target diatom bond distance varies to minimize total potential energy at every point. Contour values from 19.5 to 24.0 in 0.5 kcal/mole steps. Highest contour is left most. All potential energies relative to zero at Br + H_2.

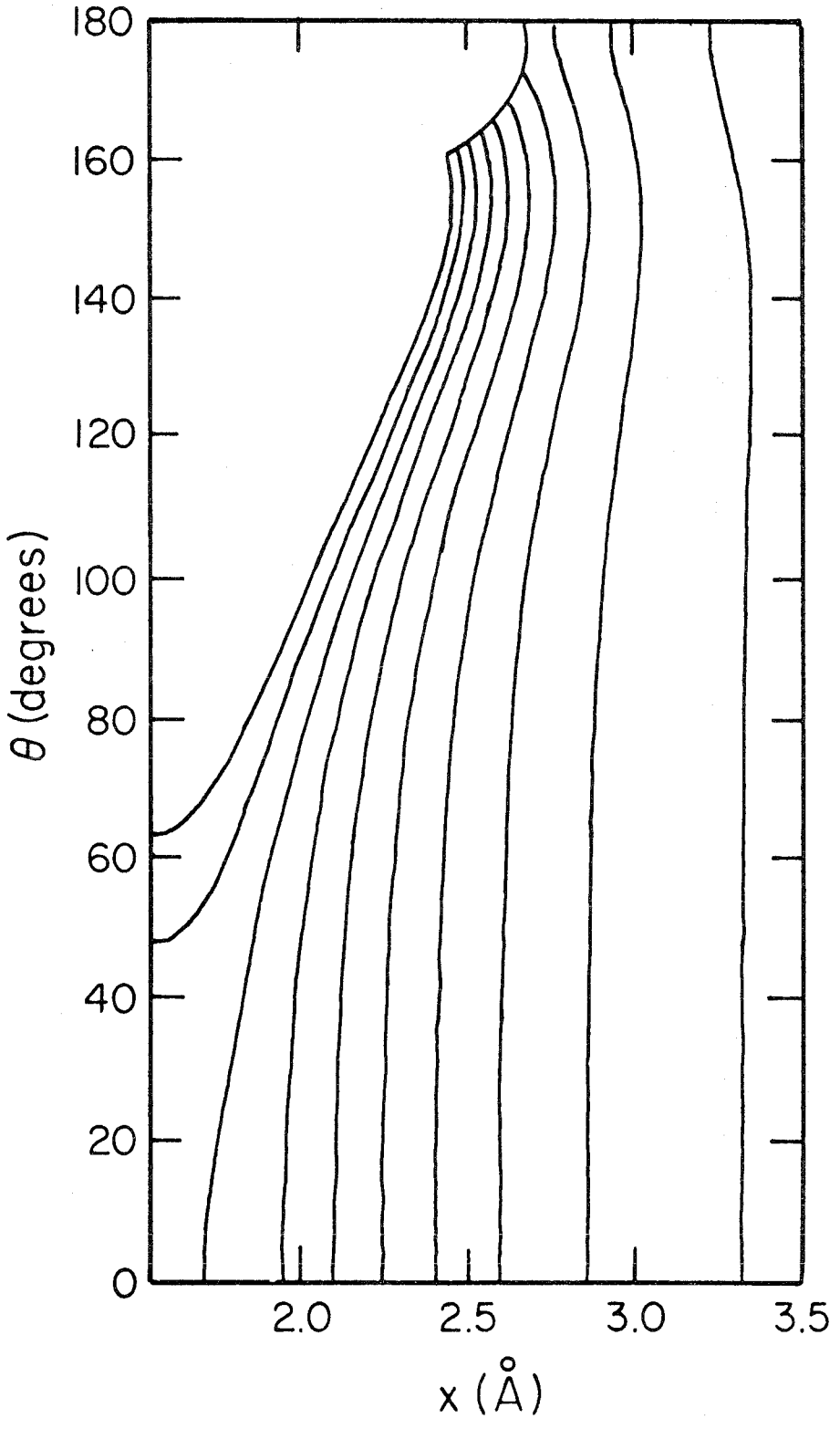
180
160
140
120
100
80
60
40
20
0
θ (degrees)
2.0
2.5
3.0
3.5
x (Å)

FIG. 8. Potential Energy Surface for Bent H—I—H. Sato parameters given in Table II. Contour values from 32 to 50 in steps of 1 kcal/mole. Highest contour is left most. All potentials are relative to zero for $I + H_2$.

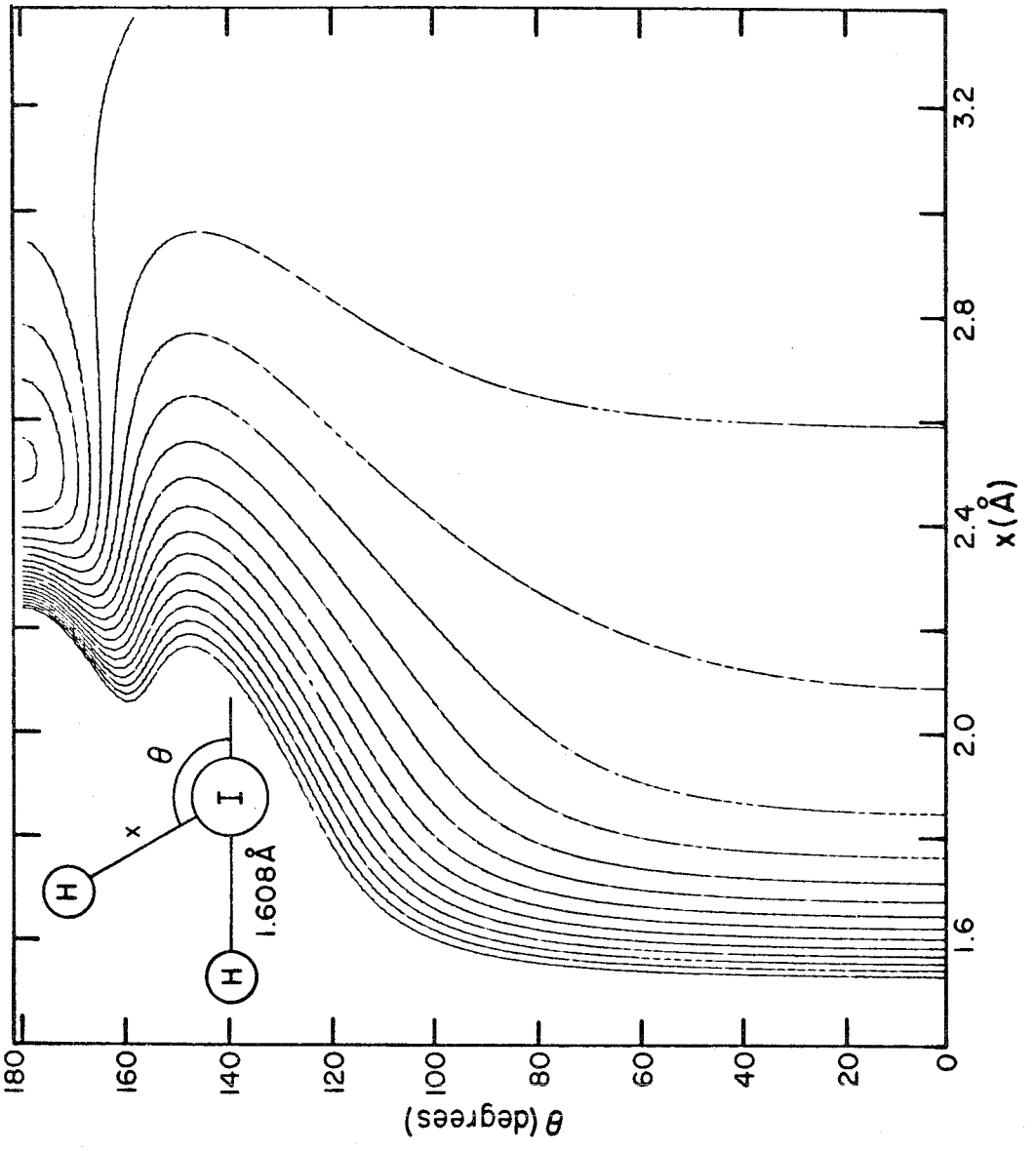
θ (degrees)
180
160
140
120
100
80
60
40
20
0
x (Å)
1.6
2.0
2.4
2.8
3.2
H
x
θ
I
1.608Å
H

FIG. 9. Potential Energy Surface for Bent H—I—H. Sato parameters given in Table II. x and θ have the same meaning as in Figure 8, but the target diatom bond distance varies to minimize total potential energy at every point. Contour values from 35.5 to 40.0 in steps of 0.5 kcal/mole. Highest contour is left most. All potentials are relative to zero for $I + H_2$.

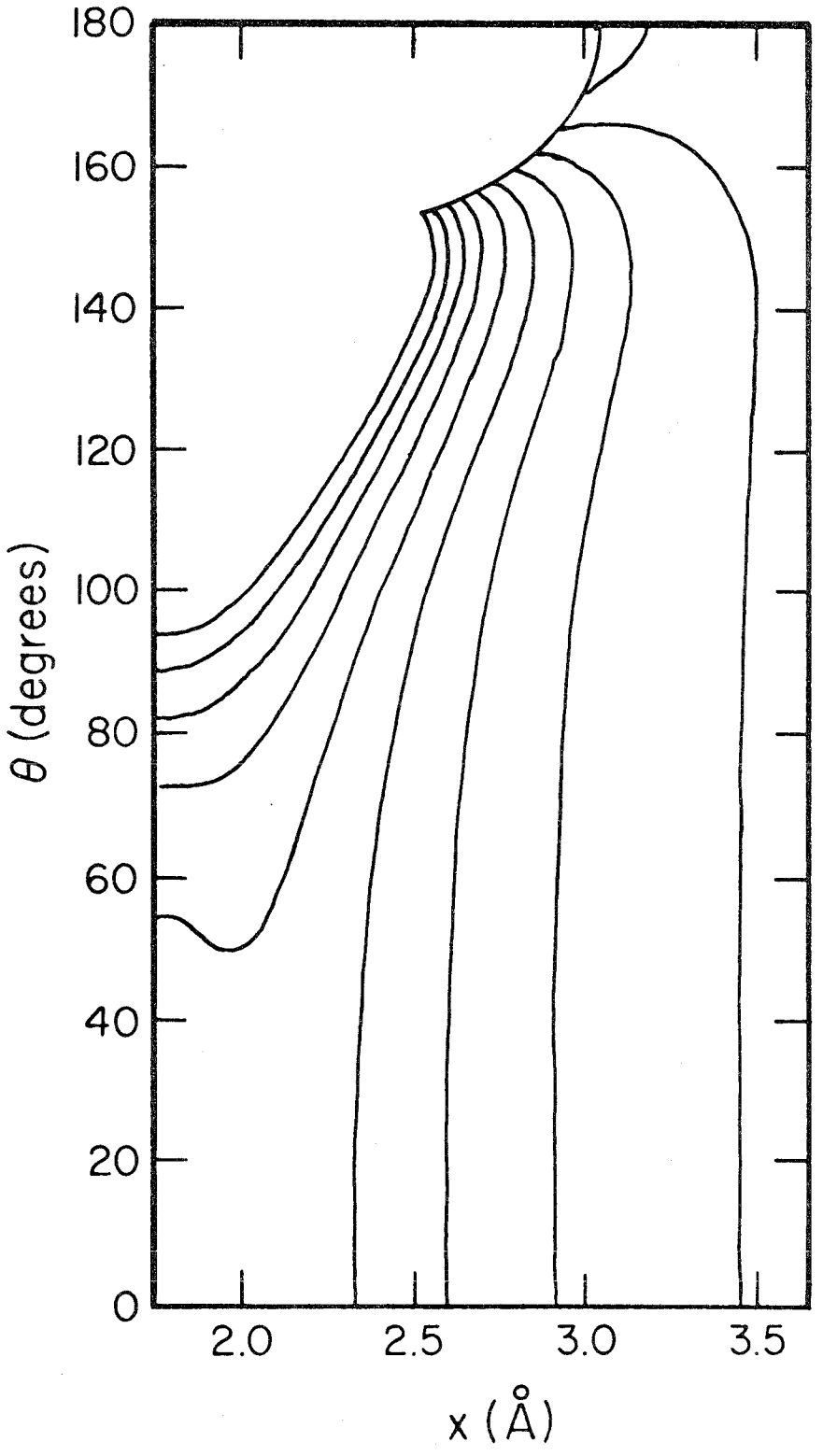
180
160
140
120
100
80
60
40
20
0
θ (degrees)
2.0
2.5
3.0
3.5
x (Å)

Indeed, Cadman and Polanyi (35) have found Br* as a product in these reactions, but it constitutes less than 2% of the total Br product. While this may appear negligible at low relative energies, there are phase space calculations (36) indicating the percentage of product excitation may rise above 20% at relative energies of 1 eV and more. Clearly the inability to predict any such excitation in a classical trajectory calculation is a serious disadvantage, not only because of the inherent interest in such results but also because transitions between surfaces of different electronic energies during the course of a trajectory could have serious effects on its dynamics.

Even for the ground state surface, the Sato method itself has the disadvantage that it is neither a straightforward approximation to nor a truncation of any rigorous quantum mechanical calculation. The inclusion of the semi-empirical parameters, k_{ij}, in equations (3.2.-1 and 2) does not result from any improvement in the approximations used in the derivation of valence bond potentials like the LEP. The success or failure of Sato surfaces cannot be used to comment on the ignorability or importance of "higher order" terms included in a more complete derivation. The utility of the Sato surface lies only in the hope that its general topology can be adjusted to match that of the true surface well enough to allow trajectory calculations to reproduce the basic features of reaction dynamics.

A third disadvantage inherent in this work is the lack of a long range attractive potential due to dispersion forces. Such forces would lead to larger reaction cross sections than those found for our Sato surface and would also yield more impulsive collisions and a closer approach

to the behavior of the statistical models.

4. Dynamics of H + DBr Reactions

All of the trajectories to be discussed in this paper were initiated with DBr in its zero-point vibrational state, i.e., with 2.7 kcal/mole of vibration energy in the target molecule. While this energy is more than 1.2 kcal/mole below the potential barrier to exchange, it is almost 1 kcal/mole above the potential barrier to abstraction. This means that, in principle, the abstraction threshold energy is zero. This point will be discussed further in Section 4.2. Initiation from the vibration-rotation quantum states rather than the classical distribution of internal energies in the DBr target facilitates comparison with forthcoming phase space theory results (36), and, as pointed out by Karplus, Porter, and Sharma (7), this "quasi-classical" initiation simplifies establishment of the thermal distribution of DBr internal energies.

4.1. Reaction Probability vs Impact Parameter

Trajectory calculations are costly. Large numbers of trajectories are necessary to average over target orientation, vibration phase, and impact parameter in order to obtain cross sections for various events at a single relative energy and initial energy state of the target. If reaction cross sections are to be measured, maximum impact parameters, b_{max}, must be chosen such that reaction probabilities for collisions with larger impact parameters are negligible. What is really desired is the least upper bound on b_{max}, since we wish to minimize fruitless collisions without missing any potential reactive events. The optimal b_{max} for

H + DBr was found as follows. Energetic H atoms were shot at normal incidence to the bond direction in zero-point-vibrating, non-rotating DBr molecules as in the diagram in Figure 10. The impact parameter was increased systematically until no reactions occurred. In this way, b_{max} (ϵ_{rel} = 1 eV), the maximum impact parameter for 1 eV barycentric energy collisions, was found (37) to be about 4.6 a_o. This is a fairly high value, considering that the Sato surface has no long-range attractive forces. At similar barycentric energies (1.3 eV), Karplus, Porter, and Sharma (7) found that H atoms ceased to react with hydrogen molecules at impact parameters larger than 2.5 a_o. The difference between these two b_{max} lies not in any fundamental differences in the surfaces involved but rather with the location of the centers of mass and force. In the symmetric H_2 molecule, the center of mass lies midway between the centers of force at a distance of 0.7 a_o from either nucleus. Thus a b_{max} of 2.5 a_o (measured from the center of mass) implies a maximum distance for reaction of 1.8 a_o from a center of force, i.e., one of the hydrogen nuclei. In DBr, however, the center of mass is essentially buried in the Br atom. When undergoing zero-point vibration, the D atom is 2.7 ± 0.2 a_o from both the Br atom and the center of mass. Thus, for this system, a b_{max} of 4.6 a_o implies a maximum separation of 1.9 a_o between the incident H and target D atoms in order for abstraction to take place at 1 eV relative energy. The agreement between these values in the two different chemical systems may be significant, implying some dynamic justification for transferable hard sphere radii.

The normal incidence collisions themselves merit some attention. It may be seen from Figure 10 that high impact parameter collisions

FIG. 10. Product Diatom Internal Energy vs Impact Parameter in 1 eV Normal Incident Collisions of H Atoms with DBr (v = 0, J = 0) Molecules. Circles, DBr product; triangles, HD product; open symbols, reactant DBr extended at instant of collision; filled symbols, reactant DBr compressed at collision instant. Δr indicates the bond vibration amplitude. Maximum energies available: DBr, 1.116 eV; HD, 1.944 eV. The curves are merely smooth fits through the data points.

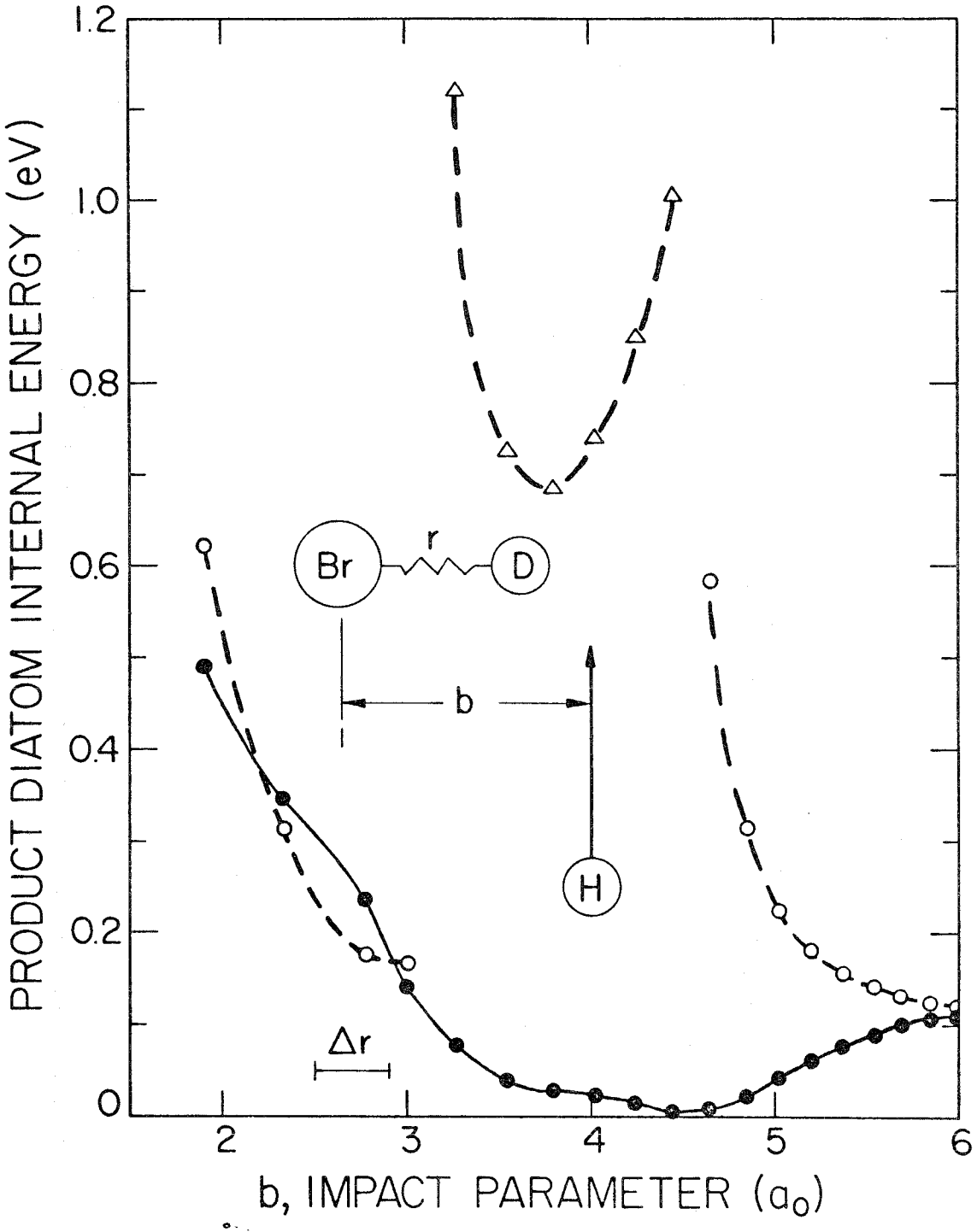
PRODUCT DIATOM INTERNAL ENERGY (eV)
1.2
1.0
0.8
0.6
0.4
0.2
0
Br
r
D
b
H
Δr
2
3
4
5
6
b, IMPACT PARAMETER (a0)

($b \geq 6\ a_o$) hardly perturb the DBr molecule. It is left with almost the same internal energy as it had initially, viz, 0.116 eV, zero point energy, regardless of the vibration phase at the instant of collision (point of closest approach). However, as the impact parameter drops to 5 a_o, the dynamics of the collision become more sensitive to the DBr vibration phase. If the DBr bond is near its compression turning point (solid circles in Figure 10) at the instant of impact, it loses energy to the passing H atoms. The molecule apparently expends some of its energy by pushing the atom away during its expansion cycle. On the other hand, if, at the time of impact, the DBr bond is near its expansion turning point (open circles), it gains energy from the incident H atom. The mechanism for this exchange is no doubt a weakening of the DBr bond restoring forces preparative to an abstraction which never takes place because of the rapid transit of the atom. In its weakened condition, the DBr bond stretches beyond its zero-point vibration turning point. Hence, upon departure of the H atom, the DBr bond snaps closed with more than its original energy. If this reasoning is valid, one would expect the right hand branch of the dashed curve to rise smoothly to 1.116 eV (the maximum energy available to a DBr molecule at this relative energy) near $b = 4.6\ a_o$.

At slightly smaller impact parameters, the DBr bond is so weakened that D is just able to break away, forming excited HD (open triangles). As the impact parameter, b, falls to about 3.8 a_o, the reaction becomes more direct but product HD excitation energy never drops below 0.68 eV = 35% of the available energy. This is not what is expected of our "repulsive" surface, and the discrepancy between expectations and performance is due to our reliance on the linear complex map (Figure 4)

to predict the outcome of 3-D collisions.

HD product excitation appears to be maximized at both ends of the range in b which leads to abstraction, viz., $3.2 \lesssim b_{abs} \lesssim 4.6\ a_o$ for normal incidence 1 eV collisions of H upon stretched DBr. One assumes that at high b, in this range, the H atom flys by, dragging the D in its wake, whereas the low b collisions involve significant rebound of the H atom before the heavier D can break away from Br and follow. In either mechanism, highly excited HD molecules are produced. In the range $1.8 \leq b \leq 3.2\ a_o$, the collisions leave excited DBr regardless of the vibration phase of that molecule. The exchange reaction appears to take over at $b \lesssim 1.8\ a_o$, again independent of the DBr phase. If we accept this last figure as the radius of a disk within which exchange is 100% guaranteed, the cross-section for exchange at this relative energy is approximately $10.2\ a_o^2$. The cross section for abstraction is not as straightforward. Since $3.2 \lesssim b_{abs} \lesssim 4.6\ a_o$, let us assume that abstraction may not take place within $3.2\ a_o$ of Br and is possible only within a disk of radius $4.6 - (r_{HBr}^{max} = 2.9) = 1.7\ a_o$ about the D atom. The area of the half moon defined by these overlapping disks is $3.64\ a_o^2$, but abstraction only occurs when DBr is stretched. Thus, the cross section for abstraction at 1 eV relative energies should be around $1.8\ a_o^2$. The abstraction fraction at this energy (no temperature average) should be about 0.15, close to the solid angle minimum of 0.08 found in the last section.

Clearly, these cross sections should be taken with a grain of salt. They are not the proper average over all orientation angles and vibration phases. Indeed, when the relative energy of normal incidence collisions was dropped to 0.57 eV, no reactions took place at any $b \geq$

1.34 a_o (the lowest impact parameter used). The low reaction barriers would lead one to expect some reaction at this high a: energy. When the proper averages are taken at this relative energy, the exchange probability is almost 0.6 at b = 0 and drops to ~0.3 at b = 2.0 a_o and to zero between 2 and 3 a_o. Abstraction probability stays ~0.06 for the range $0 \leq b \leq 3\ a_o$ and drops to ~0.01 between 3 and 4 a_o.

Because of the small number of trajectories studied, the statistical fluctuations in the impact parameter studies were too large to make meaningful fits to simple functions. The reaction possibilities were monotone decreasing functions of impact parameter within their (2/3 confidence) error bars even though the average values of the abstraction probabilities appeared to peak off zero impact parameter. At least four times the number of trajectories used at each impact parameter (~ 150) would have been required to document or destroy this analomous behavior, but we felt the effort was best made elsewhere, as in the reaction cross-section studies to follow.

4.2. Reaction Cross Sections and Product Energy Distributions

Reaction cross sections were obtained as per the methods of Section IId of Ref. 7. First, the probability of reaction, $P_{rxn}(\epsilon_{rel}, v, J)$, at constant values of relative energy, ϵ_{rel}, and DBr initial quantum state, v, J, was determined by randomizing DBr orientation, vibration phase, and b^2 over many (N = 200 to 250) trajectories. The reaction cross section, $S_{rxn}(\epsilon_{rel}, v, J)$ was approximately

$$S_{rxn}(\epsilon_{rel}, v, J) \simeq \pi b_{max}^2 P_{rxn}(\epsilon_{rel}, v, J) . \qquad (4.2.-1)$$

The standard (2/3 confidence) error was taken as

$$\sigma \xrightarrow[\lim N_{rxn} \ll N]{} (1/N_{rxn}^{\frac{1}{2}})\, S_{rxn} \qquad (4.2.-2)$$

for a given set of trajectories. The same ϵ_{rel}, v, and J were then used in another set of trajectories (N = 200 to 250) and the average of the two values for S_{rxn} was used in the figures of Sections 4.2.1. and 4.2.2. The halfwidth of the error bars in these figures is the larger of the following numbers: $|S_{rxn} - \langle S_{rxn}\rangle|$, the deviation of each S_{rxn} from their average, or $\sigma(2N) \xrightarrow[\lim N_{rxn} \ll 2N]{} \langle S_{rxn}\rangle/N_{rxn}^{2}$; thus these errors bars are fairly pessimistic, being $\geq$ 84% confidence limits.

4.2.1. DBr (v = 0, J = 0)

The circles in Figure 11 represent abstraction cross sections derived from at least 400 trajectories at each relative energy. The reaction threshold appears to be very close to zero relative energy. The lowest value shown is for ϵ_{rel} = 0.063 eV ~1.45 kcal/mole. (Collisions with smaller relative energies are rarely reactive and thus require larger numbers of trajectories for accuracy in the dynamics and statistical significance in the cross sections.) Within 1 eV of the threshold energy, the abstraction cross section has peaked and begun to fall off. In the range $0 < \epsilon_{rel} \leq 1$ eV, the abstraction cross section, $S_{abs}(\epsilon_{rel}, 0, 0)$, is a simple function of ϵ_{rel} with a single maximum of $\sim 2.3\ a_o^2$ around ϵ_{rel} = 0.6 eV. The cross section value of $1.6\ a_o^2$ for ϵ_{rel} = 1.0 eV compares well with the $1.8\ a_o^2$ value calculated by the normal incident collisions. The agreement is probably fortuitous. $S_{abs}(\epsilon_{rel} \geq 1.14$ eV, 0, 0) is also a simple

FIG. 11. Abstraction Cross Section vs Relative Energy for H + DBr (v = 0, J = 0). Error bars are > 84% confidence.

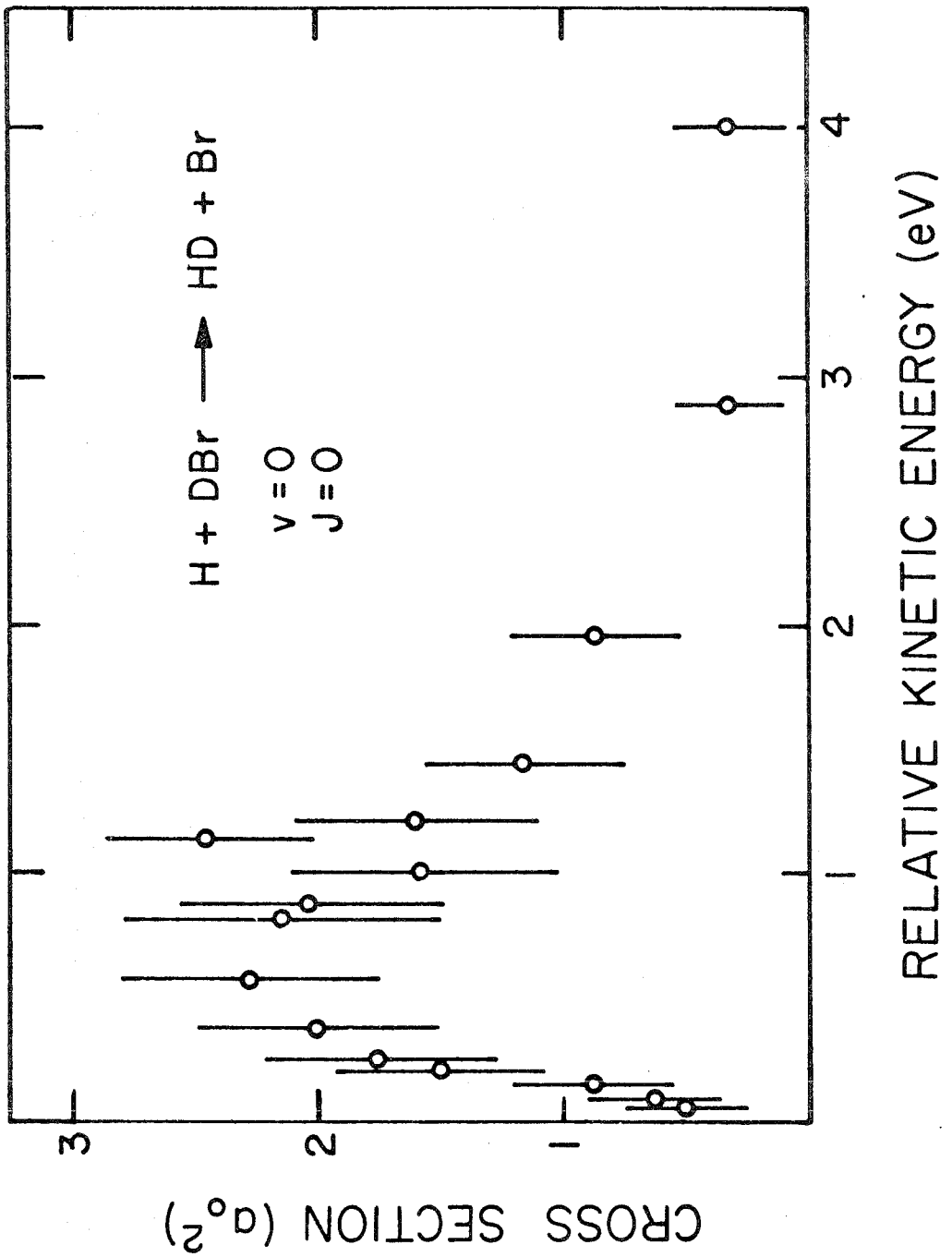
H + DBr ⟶ HD + Br
v=0
J=0
CROSS SECTION (a_o^2)
RELATIVE KINETIC ENERGY (eV)
1
2
3
4

function, monotone decreasing with ϵ_{rel}. However, there appears to be a discontinuity in S_{abs} between $\epsilon_{rel} = 1.0$ and 1.14 eV. The cross section for the latter relative energy was re-determined, using a total of 800 trajectories. The S_{abs} (1.14,0,0) value of 2.46 a_o^2 shown in Figure 11 is the result of this double sized sample. No function with a single maximum can be made to fit the data to within the error bars. Therefore, $S_{abs}(\epsilon_{rel},0,0)$ appears to have something more than trivial structure.

The cross section for exchange (Figure 12) suffers the same discontinuity at the same values of ϵ_{rel}. Rising from a $\sim$0.15 eV threshold, the exchange cross section appears to peak at $\sim$12 a_o^2 near ϵ_{rel} = 0.9 eV. There follows a statistically significant falloff to $\sim$9.2 a_o^2 at ϵ_{rel} = 1 eV (38), a rise to 11.6 a_o^2 at ϵ_{rel} = 1.14 eV, and monotone decreasing behavior thereafter. It is not clear to what dynamic effects we owe this structure. The only discontinuity observed in other reaction parameters is that the average reactive collision time (39) in the 1.142 eV collisions (2.38×10^{-14} seconds) was about 7/10 of a DBr vibration period longer than average reactive collision times for 0.81, 0.90, and 1.0 eV collisions. In the absence of an exhaustive study of the detail of the reactive trajectories, this fact does not do much to illuminate the cause of the structure in cross section curve.

We may calculate abstraction fraction as a function of energy from these cross sections, if we're willing to assume relatively small dependence of S_{rxn} on J. The AF falls from 0.54 $\pm$ 0.07 at ϵ_{rel} = 0.20 eV to 0.09 $\pm$ 0.03 (2/3 confidence) at the highest relative energy used, ϵ_{rel} = 4 eV. This high energy value agrees very well with the solid angle calculations of AF in Section 3.2.4.

FIG. 12. Exchange Cross Section vs Relative Energy for H + DBr (v = 0, J = 0).

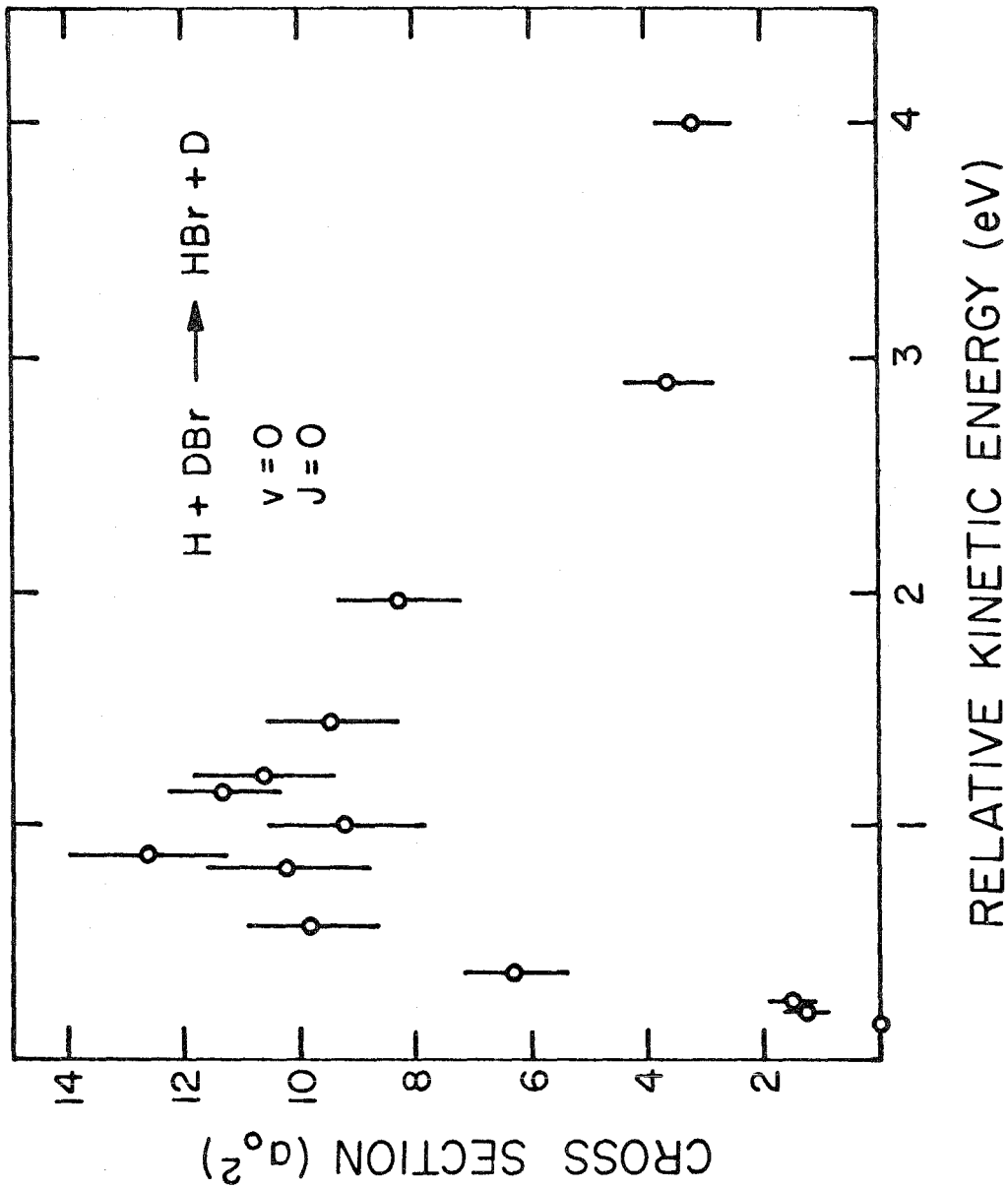
H + DBr ⟶ HBr + D
v = 0
J = 0
CROSS SECTION (a₀²)
RELATIVE KINETIC ENERGY (eV)
2
4
6
8
10
12
14
1
2
3
4

The average internal (vibration + rotation) energies of both product diatoms (HD and HBr) increase with relative energy in such a way as to leave an almost constant fraction of the total available (40) energy in the diatom. This fraction is about 0.3 for HD and about 0.5 for HBr. Over 25% of the abstraction events give HD excited with 40-60% the available energy. This seems analamously high for our "repulsive" (in the Polanyi (30) sense) surface. The spread in internal energies is rather broad and fairly symmetric about the average as seen in Figure 13a. This results in a broad range of product kinetic energies, 40-80% of the available energy for HD + Br and 7-85% of that for HBr + D.

At relative energies in excess of about 3.8 eV, it is energetically possible for the HDBr collision complex to break up into three atoms, that is, possible for H atoms to collisionally dissociate DBr. None of the 400 trajectories integrated at 4 eV relative energy gave rise to atomization.

4.2.2. DBr (v = 0, J = 6)

The population of the rotation states of DBr peaks at J = 4 for a temperature of 300°K. This state is almost six times as probable as J = 1 or 12, for example. However, in view of the slow falloff of population number with J value, it was concluded that J = 6 (92% as probable as J = 4) would be a better representative of room temperature rotation effects. Moreover, the J = 6 state was one of six J states chosen for a recent phase space theory calculation (6) on this system, and the overall results for J = 6 was found to agree with the results obtained by averaging over a room temperature distribution of rotational levels.

The cross section for abstraction of D from DBr (v = 0, J = 6)

FIG. 13. Differential Cross Section for Product Excitation.

a) $\epsilon_{rel} = 1.142$ eV. Initial DBr state v = 0, J = 0. Number of reactions involved: 34 abstractions, 155 exchanges.

b) $\epsilon_{rel} = 0.57$ eV. Initial DBr state v = 0, J = 6. Number of reactions involved 35 abstractions, 117 exchanges.

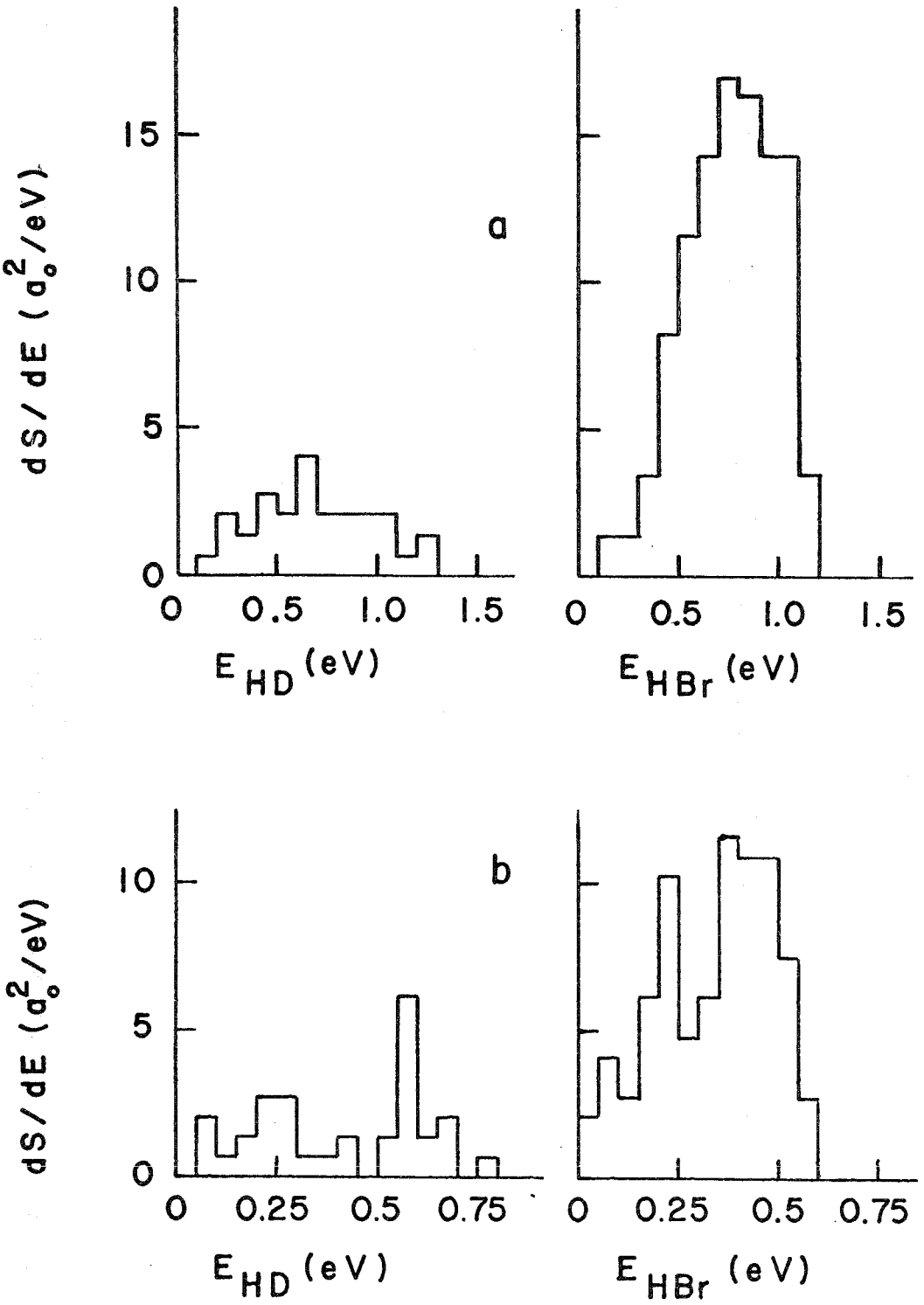
dS / dE (a_o^2/eV)
15
10
5
0
a
0
0.5
1.0
1.5
E_{HD} (eV)
E_{HBr} (eV)
b
0.25
0.75

is given as a function of relative energy, ϵ_{rel}, in Figure 14. The substantial minimum around 0.8 eV is statistically significant. It cannot be due to a resonance between the rotation and flyby periods as this occurs at relative energies near 0.01 eV. There is no statistically significant structure in average collision times, average reaction impact parameters or average product energies over the relative energy range from 0 to 1 eV. The average collision times at low energies are negative (39) indicating strong repulsive deflections of the H atom, even during abstraction. They become less negative with increasing relative energy, which is consistent with a smaller deflection of more energetic particles. The average HD product internal energies are again about 0.3 of the total available energy, and again the distribution of product energies is broad (Figure 13b). The differences in the shapes of the abstraction product energy distributions for J = 0 or 6 cannot be laid to the rotation of the target diatom, for, although 1000 trajectories were investigated at ϵ_{rel} = 0.57 eV, the number of abstractions recorded was a paltry 35. In consequence, the HD energy distributions are more a function of statistical fluctuation than dynamics, and all that may be profitably drawn from them is that their relative breadths are comparable.

Figure 15 shows the cross section for exchange of hydrogen isotopes in rotating DBr. It is not significantly different from the non-rotating case of Figure 12. The average collision times are about the same as for the non-rotating exchanges and are again about one DBr vibration period longer than the abstractions. The average HBr product energies do not vary significantly from the 0.5 fraction of available energy also found in the J = 0 trajectories, and the breadths of the distri-

FIG. 14. Abstraction Cross Section vs Relative Energy for H + DBr (v = 0, J = 6).

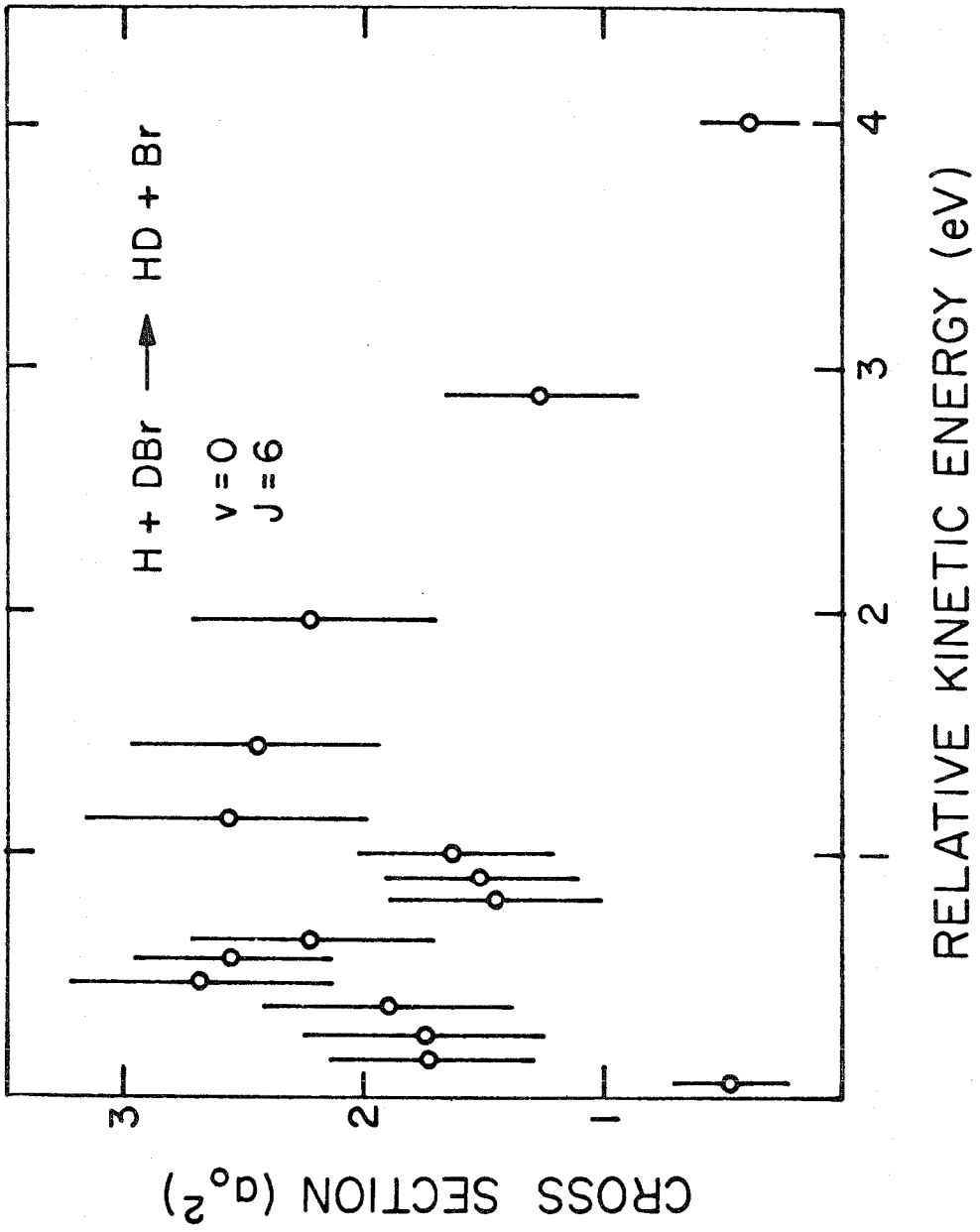
H + DBr ⟶ HD + Br
v=0
J=6
CROSS SECTION (a_o^2)
RELATIVE KINETIC ENERGY (eV)
1
2
3
4

FIG. 15. Exchange Cross Section vs Relative Energy for H + DBr (v = 0, J = 6).

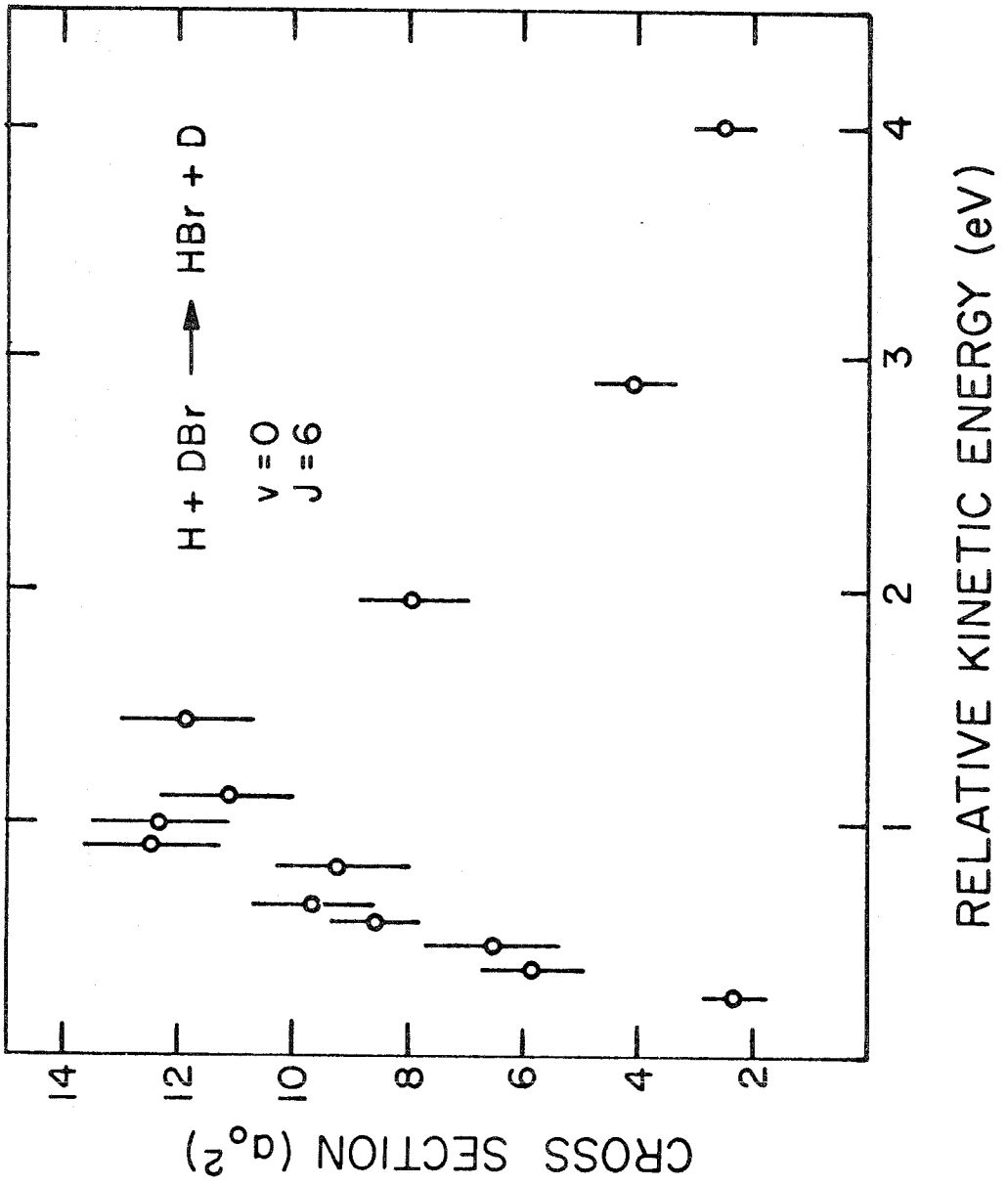
H + DBr → HBr + D
v=0
J=6
CROSS SECTION (a_o^2)
RELATIVE KINETIC ENERGY (eV)
2
4
6
8
10
12
14
1
2
3
4

bution, relative to the available energy, are the same in either case (see Figure 13b). Again there was no record of atomization at 4 eV, the highest relative energy investigated.

In short, except for the unexplained structure in the abstraction cross section, the dynamics of collisions between H atoms and rotating DBr molecules appears to be the same as for the non-rotating case. Confirmation of this statement awaits extension of these trajectories to collisions with $J > 6$ and a four-or fivefold increase in the number of trajectories run at each relative energy to increase our confidence in the results which depend on the statistics.

4.3. Abstraction Fraction

If, as suggested in the last section, the cross section for either reaction (1.-1 or 2) is independent of the J state of DBr, then we may be justified in combining $S_{rxn}(\epsilon_{rel}, v = 0, J = 0)$ and $S_{rxn}(\epsilon_{rel}, v = 0, J = 6)$ to obtain an average $S_{rxn}(\epsilon_{rel}, v = 0)$ from, essentially, a double-sized sample of trajectories. If, in addition, we assume a negligible contribution from $S_{rxn}(\epsilon_{rel}, v \neq 0)$ to the thermal reaction rates, we may attempt to fit a simple functional form to the $S_{rxn}(\epsilon_{rel}, v = 0)$ data to obtain thermal abstraction fractions. The statistical fluctuation in even the double sampled $S_{rxn}(\epsilon_{rel}, v = 0)$ is too large to find any detailed functional form, but it is found that linear and quadratic fits satisfy the data over energy ranges of about 0.2 and 0.8 eV, respectively. Consequently, the linear dependences

$$S_{HD} = 7.5\,\epsilon_{rel} \qquad \epsilon_{rel} \geq 0$$

$$S_{HBr} = 0 \qquad 0 \leq \epsilon_{rel} \leq 0.17 \text{ eV}$$

$$= 35.6\,\epsilon_{rel} - 6.06 \qquad \epsilon_{rel} \geq 0.17 \text{ eV}$$

and the quadratic ones

$$S_{HD} = 2.4 - 8.0\,(\epsilon_{rel} - 0.55) \qquad \epsilon_{rel} \geq 0$$

$$S_{HBr} = 0 \qquad 0 \leq \epsilon_{rel} \leq 0.18$$

$$= 11.8 - 2.0\,(\epsilon_{rel} - 0.95) \qquad \epsilon_{rel} \geq 0.18$$

$$(\epsilon_{rel} \text{ in eV},\ S_{rxn} \text{ in } a_o^2)$$

were used in the following calculation. The abstraction fraction was taken as

$$AF = 1/(1 + R)$$

where

$$R = \frac{\int_0^\infty \epsilon\, S_{HBr}(\epsilon)\, e^{-\epsilon/kT}\, d\epsilon}{\int_0^\infty \epsilon\, S_{HD}(\epsilon)\, e^{-\epsilon/kT} d\epsilon} \quad .$$

The resultant AF as a function of temperature, T, are given in Table V, along with those from the transition state calculation (described in Section 3.2.3.) and from statistical phase space theory (6).

It is clear from the table that both crude fits to S_{rxn} give surprisingly similar abstraction fractions. They differ from the ACT cal-

Table V. Abstraction Fractions for H + DBr

T(°K) Model	200	300	400	500	600	700	800	900	1000
ACT[a]	1.00	0.90	0.67	0.50	0.37	0.30	0.25	0.21	0.19
Linear S^{b}_{rxn}	0.99	0.82	0.57	0.41	0.32	0.32	0.33	0.22	0.20
Quadratic S^{b}_{rxn}	0.99	0.86	0.65	0.50	0.36	0.29	0.33	0.30	0.22
PST[c]		0.97		0.92		0.89			

[a]Activated complex theory applied to this paper's Sato surface.

[b]Integration of trajectory cross sections with linear or quadratic relative energy dependencies

[c]Phase space theory of Truhlar and Kuppermann (6).

culations primarily in the fact that they predict non-monotonic dependence of AF on T around T = 750°K. But the otherwise good agreement (41) suggests that some ACT calculations may agree with trajectory results without the reactions proceeding through long-lived transition states. The collisions observed here, as in most other trajectory studies, involved complexes too short-lived to come to equilibrium in all their degrees of freedom.

The phase space theory (PST) calculations contained no non-statistical corrections. Also, there were no valence electronic potential energy barriers to reaction in the reported PST results (6). However, both these assumptions can be and indeed are being removed from the PST. Preliminary results (36) indicate closer agreement with the trajectory studies in all particulars.

5. Summary

It has been shown that Sato surface is not necessarily free of the spurious wells found in other semi-empirical potentials. However, in the case of H_2X, these wells may be avoided by judicious choice of the Sato parameters. Furthermore, a Sato surface for H_2Br may be found which fits the experimental values for Br + H_2 and Br + D_2 activation energies as well as the experimental ratio of abstraction to total reaction rate. The latter fit is made via activated complex theory, which may be used to demonstrate a large temperature dependence for the abstraction fraction. This dependence is very similar to that obtained from the classical trajectory calculations on the same Sato surface.

The large separation between the centers of mass and force in the DBr molecule (as opposed to a homonuclear diatomic) lead to large impact parameters for abstraction reactions. The large impact parameters require very many Monte Carlo trajectories for statistical significance in cross sections and other dynamic properties. The maximum reaction cross sections occur at relative energies about 1 eV. They are about 3 a_o^2 for abstraction and about 13 a_o^2 for exchange. The product internal energies show a broad energy distribution centered about 30% and 50% of the energy available to HD and HBr, respectively.

Appendix 1. Saddlepoint Search

Activation energy determination from potential surface data requires (26) a knowledge of (a) the minimum potential energy barrier to the reaction, $V^{\ddagger}$, and (b) the frequencies of the normal modes of the activated complex. These quantities are obtained from the saddlepoint region of the potential surface. If but one surface is involved, this information is found by evaluating the potential expression at various geometric configurations for the atoms in the complex until the col is located. One then obtains force constants at the col as described in Appendix B of Ref. 26 and vibration frequencies via the formulae of Appendix D in the same work. However, if one wants activation energies and other ACT data from several thousand potential surfaces, as required by the calibrations performed in this paper, automation is essential.

Since the Sato surface has an analytic form, the required force constants can be determined exactly given the location of the saddlepoint. In principle, one could write down the expressions for the first derivatives of the potential with respect to the interatomic distances and solve for the saddlepoint through the transcendental equations obtained by setting these derivatives to zero. This procedure would locate any of four or more extrema, the saddlepoint of interest being recognized by its characteristic imaginary frequency. Such transcendental equations are often solved by Newton's Method of Slopes (22). In one dimension, the method corrects a good guess about the location of an extremum by subtracting the ratio of the first derivative over the second from the guess. At the extremum, the first derivative vanishes and with it, the correction. Saddlepoints

represent extrema in two dimensions. Position guesses may be corrected by applying the one-dimensional method simultaneously in both dimensions. Unfortunately, as one turns a co-ordinate system centered in a saddlepoint, the second derivatives change sign. Clearly, orientation angles may be found where at least one of the second derivatives vanishes. Since the correction term in the method

$$\Delta r = -V'/V'' \tag{A1-1}$$

bears that derivative in its denominator, the correction may become arbitrarily large, destroying the convergence. Such a situation occurs without co-ordinate axis rotation in the search for some HHBr saddlepoints and indeed for many saddlepoints occuring outside the reactant channel.

The solution to this problem rests in rotating the co-ordinate system so that $|V''|$ is large. Let the original co-ordinates be x and y. Another pair, u and v, are rotated by angle θ with respect to x and y. By the chain rule and the formulae governing rotation of axes,

$$\frac{\partial V}{\partial u} = \frac{\partial V}{\partial x}\cos\alpha - \frac{\partial V}{\partial y}\sin\alpha$$

and

$$\frac{\partial V}{\partial v} = -\frac{\partial V}{\partial x}\sin\alpha + \frac{\partial V}{\partial y}\cos\alpha . \tag{A1-2}$$

Using the shorthand $F_{st} = \partial^2 V/\partial s \partial t$,

$$F_{uu} = F_{xx}\cos^2\alpha + 2F_{xy}\sin\alpha\cos\alpha + F_{yy}\sin^2\alpha . \tag{A1-3}$$

We may now use Newton's method to maximize F_{uu} with respect to α. Actually, all we need do is enlarge F_{uu}, so we needn't carry the method to convergence. Since the method finds only extrema, we must take steps to avoid minima. The obvious modification to the method results in

$$\Delta\alpha = \frac{(\partial F_{uu}/\partial\alpha)}{(\partial^2 F_{uu}/\partial\alpha^2)} \text{ sign } (\partial^2 F_{uu}/\partial\alpha^2) \qquad \text{(A1-4)}$$

where

$$\frac{\partial F_{uu}}{\partial\alpha} = 2 \sin\alpha \cos\alpha (F_{yy} - F_{xx}) + 2 F_{xy} (\cos^2\alpha - \sin^2\alpha)$$

and (A1-5)

$$\frac{\partial^2 F_{uu}}{\partial\alpha^2} = 2 (\cos^2\alpha - \sin^2\alpha)(F_{yy} - F_{xx}) - 4 F_{xy} \sin\alpha \cos\alpha .$$

Alternation of "maximizing" F_{uu} with Newton's method correction of guesses to the saddlepoint location suffices to locate the saddlepoint on all but the most pathological surfaces, those with reaction paths along nearly perfect parabolic channels, i.e., near thermoneutral reactions with very broad cols.

Appendix 2. Pre-Exponential Term Ratios

Calculation of abstraction fractions, $k_a/(k_a + k_e)$ in reference to equations (1.-1,2), to the activated complex theory (ACT) approximation requires a ratio of temperature dependent pre-exponential factors. In this paper, these were evaluated by the local properties method (42). The ratio of the pre-exponential factors, $B^{(T)}$, for two reactions x + yz and x + zy with linear complexes xyz and xzy, reduces to

$$\frac{B_{xyz}}{B_{xzy}} = \frac{\omega^*_{xyz}}{\omega^*_{xzy}} \left[\frac{R_{xy}\, R_{yz}\, \Gamma_b\, xyz}{R_{xz}\, R_{zy}\, \Gamma_b\, xzy}\right]^2 \frac{(\Gamma_s \Gamma_*)\, xyz}{(\Gamma_s \Gamma_*)\, xzy} \cdot$$

$$\frac{F_\phi\, xzy}{F_\phi\, xyz} \cdot \left[\frac{(F_{11}F_{22} - F_{12}^2)_{xzy}}{(F_{11}F_{22} - F_{12}^2)_{xyz}}\right]^{\frac{1}{2}} \cdot \qquad \text{(A2-1)}$$

The ω^* are the imaginary frequencies associated with the reaction path through the complexes. The F_{ij} are $\partial^2 V/\partial R_i \partial R_j$ evaluated at the complex configuration. The Γ terms (28a) are ratios of the quantum to classical partition functions for s,b, the stretching and bending vibrations, and *, the reaction co-ordinate. The latter term is calculated in this paper for one-dimensional tunneling through a parabolic barrier (43). This approximation to the actual tunneling through the true barrier in three dimensions is good only at relatively high temperatures or for relatively broad cols; in other words, where $u_* = hc\omega_*/kT \ll 2\pi$.

The B ratio requires not only the force constants (Table IV) but also the frequencies, ω, of the complex. These frequencies are given

in Table VI for some of the isotopically substituted complexes of interest.

Table VI. Complex Frequencies for H + HX[a]

Complex	ω_s	ω_b	ω_*
H—H—Br	1420	588	1034 i
H—D—Br	1164	463	897 i
D—H—Br	1257	552	831 i
H—H—I	2256	135	88 i
H—D—I	1602	103	88 i
D—H—I	2256	129	63 i
H—Br—H	1826	98	39 i
D—Br—H, H—Br—D	1581	85	32 i
H—I—H	1947	49	321 i
H—I—D	1405	41	315 i
D—I—H	1929	44	230 i

[a]All values in cm^{-1}. $i \equiv \sqrt{-1}$.

Appendix 3. Discontinuous Potentials

The relaxed target angular potential energy surfaces (Figures 7 and 9) have discontinuities in them (middle top) where the contour lines close abruptly. The reason for this real discontinuity is best shown by an examination of the surface for linear H—H—Br (Figure 4). The reactant channel is upper left. Minimization of the potential at fixed values of x + y by variation of x is accomplished by locating energy minima along a family of lines with -45° slope in Figure 4. The critical line passes through the saddlepoint. All lines in the family above this one have two energy minima, one each in the reactant and product channel. The minimum of interest is the one in the reactant channel. The critical line has one in the product channel and an energy inflexion point at the col. All lines in the family below the critical line have only the product channel minimum. Thus as one passes smoothly through the family, i.e., toward the smaller values of x along $\theta = 180°$ in Figures 7 and 9, one encounters a discontinuity in the minimum energy at the saddlepoint. The argument is unaltered for other values of θ.

The algebra for obtaining relaxed target potential energies follows. One solves

$$\partial V/\partial r_{BC}\,|_{r_{AB},\,\theta} = 0 \qquad \text{(A3-1)}$$

for r_{BC} via Newton's method (22), where if r_{BC}' is a good guess for the solution to (A3-1), a better guess, r_{BC}'' is obtained by

$$r_{BC}'' = r_{BC}' - \frac{(\partial V/\partial r_{BC})}{(\partial^2 V/\partial r_{BC}^2)} \quad \text{sign}\left(\frac{\partial^2 V}{\partial r_{BC}^2}\right)\Bigg|_{r_{AB},\theta} \quad . \qquad \text{(A3-2)}$$

Differentiating equation (3.2.-1) with respect to r_{BC}, we obtain

$$\frac{\partial V}{\partial r_{BC}}\Bigg|_{r_{AB},\theta} = \frac{\partial Q_{BC}}{\partial r_{BC}} + \frac{\partial Q_{AC}}{\partial r_{BC}} - \frac{1}{\sqrt{2}\,R}\left[(2\,\alpha_{BC} - \alpha_{AB} - \alpha_{AC}) \cdot \right.$$

$$\left. \frac{\partial \alpha_{BC}}{\partial r_{BC}} + (2\,\alpha_{AC} - \alpha_{AB} - \alpha_{BC})\right] \qquad \text{(A3-3)}$$

where

$$\frac{\partial Q_{AC}}{\partial r_{BC}} = \frac{\partial Q_{AC}}{\partial r_{AC}} \frac{\partial r_{AC}}{\partial r_{BC}} \quad , \qquad \frac{\partial \alpha_{AC}}{\partial r_{BC}} = \frac{\partial \alpha_{AC}}{\partial r_{AC}} \frac{\partial r_{AC}}{\partial r_{BC}} \quad ,$$

and, of course,

$$r_{AC} = (r_{AB}^2 + r_{BC}^2 - 2\,r_{AB} r_{BC} \cos\theta)^{\frac{1}{2}}.$$

The symbol R stands for the radical

$$[(\alpha_{AB} - \alpha_{BC})^2 + (\alpha_{BC} - \alpha_{CA})^2 + (\alpha_{CA} - \alpha_{AB})^2]^{\frac{1}{2}} \quad .$$

Equations (3.2.2-2) provide the partials, such as,

$$\frac{\partial Q_{ij}}{\partial r_{ij}} = \frac{-\beta_{ij} D_{ij} X_{ij}}{2(1 + k_{ij})} [(k_{ij} + 3) X_{ij} - (3k_{ij} + 1)]$$

and (A3-4)

$$\frac{\partial \alpha_{ij}}{\partial r_{ij}} = \frac{-\beta_{ij} D_{ij} X_{ij}}{2(1 + k_{ij})} [(3k_{ij} + 1) X_{ij} - (k_{ij} + 3)] .$$

Thus equation (A3-3) can be expanded with the aid of (A3-4) and given

$$\frac{\partial r_{AC}}{\partial r_{BC}} = (r_{BC} - r_{AB} \cos \theta)/r_{AC} . \quad \text{(A3-5)}$$

Newton's method requires one further differentiation, namely,

$$\left.\frac{\partial^2 V}{\partial r_{BC}^2}\right|_{r_{AB},\theta} = \frac{\partial^2 Q_{BC}}{\partial r_{BC}^2} + \frac{\partial^2 Q_{AC}}{\partial r_{BC}^2} - \frac{1}{\sqrt{2}R} \left\{ (2\alpha_{BC} - \alpha_{AB} - \alpha_{AC}) \cdot \right.$$

$$\frac{\partial^2 \alpha_{BC}}{\partial r_{BC}^2} + 2\left[\left(\frac{\partial^2 \alpha_{BC}}{\partial r_{BC}^2}\right)^2 - \left(\frac{\partial \alpha_{BC}}{\partial r_{BC}}\right)\left(\frac{\partial \alpha_{AC}}{\partial r_{BC}}\right) + \left(\frac{\partial \alpha_{AC}}{\partial r_{BC}}\right)^2\right] +$$

$$(2\alpha_{AC} - \alpha_{AB} - \alpha_{BC}) \frac{\partial^2 \alpha_{AC}}{\partial r_{BC}^2} - \left[(2\alpha_{BC} - \alpha_{AB} - \alpha_{AC}) \frac{\partial \alpha_{BC}}{\partial r_{BC}} + \right.$$

$$\left. \left. (2\alpha_{AC} - \alpha_{AB} - \alpha_{BC}) \frac{\partial \alpha_{AC}}{\partial r_{BC}} \right]^2 / R^2 \right\} . \quad \text{(A3-6)}$$

It is readily shown that

$$\frac{\partial^2 Q_{AC}}{\partial r_{BC}^2} = \frac{\partial^2 Q_{AC}}{\partial r_{AC}^2}\left(\frac{\partial r_{AC}}{\partial r_{BC}}\right)^2 + \frac{\partial Q_{AC}}{\partial r_{AC}}\frac{\partial^2 r_{AC}}{\partial r_{BC}^2} ,$$

and a similar form holds for $\partial^2\alpha_{AC}/\partial r_{BC}^2$, where $\partial^2 r_{AC}/\partial r_{BC}^2 = [1 - (\partial r_{AC}/\partial r_{BC})^2]/r_{AC}$. Thus all that is required to expand (A3-6) is

$$\frac{\partial^2 Q_{ij}}{\partial r_{ij}^2} = \frac{\beta_{ij}^2 D_{ij} X_{ij}}{2(1 + k_{ij})}[2(k_{ij} + 3)X_{ij} - (3k_{ij} + 1)]$$

and (A3-7)

$$\frac{\partial^2 \alpha_{ij}}{\partial r_{ij}^2} = \frac{\beta_{ij}^2 D_{ij} X_{ij}}{2(1 + k_{ij})}[2(3k_{ij} + 1)X_{ij} - (k_{ij} + 3)] .$$

The method used to obtain Figures 7 and 9 was to solve (A3-2) for a given θ, starting at large r_{AB} with the good assumption that $r_{BC}' = r_{BC}^{eq}$. The solution for r_{BC} was used as the r_{BC}' for the next smaller r_{AB} at the same θ.

REFERENCES

1. (a) S. F. Boys and I. Shavitt, University of Wisconsin Technical Report, WIS-AF-13 (1959); (b) H. Conroy and B. L. Bruner, J. Chem. Phys. 47, 921 (1967); (c) I. Shavitt, R. M. Stevens, F. L. Minn, and M. Karplus, J. Chem. Phys. 48, 2700 (1968).
2. (a) E. M. Mortensen, J. Chem. Phys. 48, 4029 (1968); (b) M. Karplus and K. T. Tang, Disc. Faraday Soc. 44, 56 (1967).
3. (a) J. O. Hirschfelder, H. Eyring and B. Topley, J. Chem. Phys. 4, 170 (1936); (b) H. Eyring, H. Gershinowitz, and C. E. Sun, J. Chem. Phys., 3, 786 (1935).
4. D. L. Bunker, Theory of Elementary Gas Reaction Rates, Permagon Press, New York, 1966, pp. 39-44.
5. J. M. White, A. Kuppermann, D. R. Davis, and J. Betts (Asay), to be published.
6. D. G. Truhlar and A. Kuppermann, to be published.
7. M. Karplus, R. N. Porter, and R. D. Sharma, J. Chem. Phys. 43, 3259 (1965).
8. D. H. Rank, U. Fink, and T. A. Wiggins, J. Mol. Spectroscopy 18, 170 (1965).
9. J. L. Dunham, Phys. Rev. 41, 421 (1932).
10. C. A. Parr, A. Kuppermann, and R. N. Porter, Dynamics of Energized Harmonic Molecules, Section 6.1.
11. S. Sato, Bull. Chem. Soc. (Japan), 28, 450 (1955).
12. J. C. Polanyi, J. Quant. Spectroscopy Radiative Transfer 3, 471 (1963).

13. S. Glasstone, K. J. Laidler, and H. Eyring, The Theory of Rate Processes, McGraw-Hill Book Company, New York, 1941, Chap. V.

14. A. S. Coolidge and H. M. James, J. Chem. Phys. 2, 811 (1934).

15. J. L. Magee, J. Chem. Phys. 8, 677 (1940).

16. S. Sato, J. Chem. Phys. 23, 592, 2465 (1955). See also R. E. Weston, Jr., J. Chem. Phys. 31, 892 (1959).

17. See, for example, K. J. Laidler and J. C. Polanyi, Progr. Reaction Kinetics 3, 1 (1965).

18. A. Persky and F. S. Klein, J. Chem. Phys. 44, 3617 (1966).

19. R. B. Timmons and R. E. Weston, Jr., J. Chem. Phys. 41, 1654 (1964).

20. J. H. Sullivan, J. Chem. Phys. 39, 3001 (1963).

21. C. A. Parr, A. Kuppermann, and R. N. Porter, preceeding paper, Section 3.

22. Also known as the Newton-Raphson method. See H. Margman and G. M. Murphy, The Mathematics of Physics and Chemistry, D. Van Nostrand Company, Inc., Princeton, N.J., 1956, 2nd edition, p. 492.

23. W. Steiner and E. K. Rideal, Proc. Roy. Soc. (London), 173A, 503 (1939).

24. See G. C. Fettis and J. H. Knox, Prog. Reaction Kinetics 2, 1 (1964) and references therein.

25. J. Bigeleisen, F. S. Klein, R. E. Weston, and M. Wolfsberg, J. Chem. Phys. 30, 1340 (1959).

26. H. S. Johnston, Gas Phase Reaction Rate Theory, Ronald Press Company, New York, 1966, pp. 169, 199.

27. Such a comparison has been made in Ref. 7. In the language of this paper, the activation energies for H + H_2 were found by Karplus, Porter, and Sharma to be E_a (from dynamics) = 7.435, E_o = 8.79, E_a'(300°K) = 8.60, and E_a'(1000°K) = 9.68 kcal/mole.

28. (a) Ref. 26, p. 92. (Tables of classical vibration amplitude are given on p. 223.); (b) S. W. Mayer and L. Schieler, J. Phys. Chem. 72, 236 (1968).

29. Contour routines for the Calcomp plotter were sent to us by Dr. R. E. Weston, Jr. at Brookhaven. The authors wish to thank Dr. Weston for these programs. They are available in FORTRAN IV at the Caltech Booth Computing Center under the title of TØPØG.

30. P. J. Kuntz, E. M. Nemeth, J. C. Polanyi, S. D. Rosner, and C. E. Young, J. Chem. Phys. 44, 1168 (1966).

31. H. S. Johnston, Adv. Chem. Phys. 3, 131 (1961).

32. This division of energy release (-ΔV for the reaction) into attractive and repulsive components is described in Case (b) of Ref. 17.

33. Three-dimensional perspective plotting routines for the Calcomp plotter were obtained from Dr. David L. Nelson at the University of Maryland. We are grateful to Dr. D. C. Cartwright for revision of the FORTRAN IV listings.

34. Compare the heats of reaction to produce ground state X($^2P_{3/2}$) of -1.0, -16.6, and -32.6 kcal/mole for X = Cl, Br, and I, respectively.

35. P. Cadman and J. C. Polanyi, Symposium on Photochemistry and Radiation Chemistry, U. S. Army Natick Laboratories (Natick, Mass., April 22, 1968).

36. D. G. Truhlar, unpublished data.

37. Of course, b_{max} is a function of the relative energy, ϵ_{rel}. It would be expected to be smaller for lower ϵ_{rel} values and larger for high ones.

38. This value of the cross section compares with the 10.2 a_o^2 estimated from the normal incidence collisions of Section 4.1.

39. The collision time is not merely the duration of a trajectory integration. Since the H atoms are shot at DBr at different impact parameters and initial separations (the latter to randomize vibration phase), and since the end test stops the integration when an atom is further than some chosen distance from a diatom, the collision time is the difference between the actual trajectory duration and the time it would have taken the H atom to fly by DBr in the absence of any intermolecular forces. Thus we are describing the amount of time the collision delays the hot atom in its flight.

40. The heat of reaction, 0.828 eV, was included in that energy available to HD. It is of course not available to HBr since this product is isoelectronic to the reactant DBr.

41. It must be remembered that the potential surface upon which the trajectories were observed was chosen to give the exp'l. AF(300°K) ~ 0.88 in an ACT calculation. This fit to experiment in no way detracts from the observed agreement between the ACT and trajectory AF's.

42. Ref. 26, p. 188.

43. Ref. 26, p. 190.

Part IV. Propositions

Abstracts of Propositions

by Christopher Alan Parr

A. It is proposed that quartic contributions to bending forces in linear triatomic reaction intermediates be included in transition state theory. An example is given.

B. It is proposed that the bond-energy-bond-order (BEBO) method be used to obtain isotope effects in the $H + H_2$ reaction. Modifications of the method are suggested.

C. It is proposed that free, ultra-thin films may be obtained by vacuum deposition on substrates which may be removed by sublimation. The uses of such films are reviewed.

D. It is proposed that the time-dependent Schroedinger equation be solved for unibound minimum wave packets in the square well potential. The analytic nature of the corresponding classical trajectory swarms makes comparison of quantal and classical results especially simple.

E. It is proposed the potassium metaborate (KBO_2) be investigated as a wall poison to recombination of hydrogen and halogen atoms. The utility of such a poison is described.

Proposition A. Harmonic-Quartic Vibrations in Reaction Rate Theory

It is proposed that quartic contributions to bending forces in linear triatomic reaction intermediates be included in transition state theory. An example is given.

Molecular vibrations are usually anharmonic. Often, however, when one deals with states near extrema in a molecule's potential surface, satisfactory results are obtained for spectral, thermochemical, and even "absolute reaction rate" calculations with harmonic approximations to the potential. This is especially true for large harmonic force constants, which swamp the higher order contributions, and for low temperatures where only the lowest vibrational states are involved. High frequency stretching vibrations are very well represented by harmonic models at chemically interesting temperatures, since their harmonic force constants, F, are large. They range (1a) from 2 to 20 millidynes/Å and yield Boltzmann average classical amplitudes (2a),

$$\ell_H = \int_{-\infty}^{+\infty} \exp(-Fx^2/2kt)\,dx = (2\pi kT/F)^{\frac{1}{2}}, \qquad (A\text{-}1)$$

smaller than 0.21 Å at 1000°K. However, bending force constants for stable molecules are considerably weaker, ranging between 0.1 and 0.7 millidynes/Å, when tabulated (1a) as $F_\varphi/r_1^{eq}r_2^{eq}$. The r_i^{eq} correspond to the equilibrium lengths of the bonds enclosing the valence angle, φ.

One of the stronger bending force constants is that of CO_2. Here $F_\varphi = 0.77 \times 10^{-11}$ ergs/radian^2. Over 99% of the potential comes from the quadratic term for zero-point bending CO_2 (3). At 1000°K,

the classical bending vibration amplitude,

$$\Phi_H = \int_{-\infty}^{+\infty} \exp(-F_\varphi \varphi^2/2kT)d\varphi = (2\pi kT/F\varphi)^{\frac{1}{2}}, \qquad (A\text{-}2)$$

is about 19° for CO_2. The weaker bending force constant for HCN (0.246×10^{-11} ergs/radian^2) leads to a 34° angular deformation at the same temperature. The potential function for weak angular bonds like that of HCN probably contain anharmonic terms which become important at deformations as large as 34°.

However, there are species of chemical interest with still smaller harmonic force constants and larger Boltzmann average deformations at a given temperature. These are the reaction intermediates, or transition states, of absolute rate theory. The literature values for properties of most of these short-lived species are conjectural. This may be seen from the many estimates for the bending force constant of the H_3 intermediate, collected in Table I. At 1000°K, the largest of these force constants gives a 44° deformation while the smallest yields an average angular amplitude of almost 79°.

Mayer et al. (10a) show that many H atom abstraction reactions involve weak bending force constants. In reference 10a and subsequent papers (10b and c), the authors warn against application of absolute rate theory to a reaction at temperatures above $F_\varphi/1.38 \times 10^{-16}$ °K (F in ergs/radian^2). At that temperature, the doubly degenerate bending vibrations in a linear reaction intermediate sweep out a 2π solid angle, or half the unit sphere. This restricts the application of activated complex theory (ACT) in the $H + H_2$ reaction to temperatures below 3260°K.

Table I. Bending Force Constant for H_3

Method	BEBO[2b]	CH[4]	LEPS[5]	PK[6]	BS[7]	SSMK[8]	HMP[9]
F_φ (10^{-11} ergs/rad^2)	0.045	0.062	0.066	0.076	0.080	0.116	0.142

Similarly, ACT cannot be applied to the O + NH → OH + N reaction at temperatures above 150°K (10a). This is a serious handicap to an otherwise useful tool. Mayer and Schieler (10c) show that BEBO-ACT rate constants are in much better agreement with known rates than are the collision theory results to which the authors turn when Φ_H becomes too large. The ACT agreement with experiment appears (10c) to be improving even as the temperature approaches the maximum consistent with the ACT model.

It is clear that the introduction of higher powers in the potential of the bending mode may reduce the Boltzmann average deformation, Φ_H, and widen the range of applicability of the ACT. It is therefore proposed that the quartic contribution to the potential energy of (at least) the bending vibrations of these intermediate species be included to correct the ACT rate constant. As an example of the possibilities of this approach, the harmonic-quartic bending potential,

$$V = \frac{1}{2!} F_\varphi \varphi^2 + \frac{1}{4!} Q_\varphi \varphi^4 , \qquad \text{(A-3)}$$

for the linear H_3 complex will be determined and used to obtain Φ_{HQ} and the correction to the ACT rate constant via harmonic-quartic partition functions. The latter are readily obtained from the energy eigenvalues available through Truhlar's variation-perturbation method (11).

The quartic force constant, Q_φ, for H_3 may be estimated by a number of methods, some of which have already been mentioned in Table I. Numerical potential surfaces may be fit to polynomials in φ^2, and the coefficient of φ^4 is identified with $Q_\varphi/4!$. For example,

Harris et al. (9) give a numerical surface for H_3 in a form convenient for numerical fitting. Using a fifth order fit to all nine data points in HMP (9), one finds $Q_\varphi \cong 0.35 \times 10^{-11}$ ergs/radian^4. This means that at one radian deformation, 17% of the potential energy comes from the quartic term. Other methods give analytic expressions for the potential energy, from which Q_φ may be derived by differentiation. In Appendix 1, the BEBO (2c) expression for the potential energy of the general linear ABC complex is differentiated to obtain Q_φ. Again for the H_3 complex, BEBO predicts $Q_\varphi = 0.122 \times 10^{-11}$ ergs/radian^4. This implies that about 10% of the potential energy comes from the quartic term at one radian deformation, in fair agreement with HMP (9).

The Boltzmann average vibration amplitude for the mixed harmonic-quartic oscillator is (12)

$$\ell_{HQ} \text{ or } \Phi_{HQ} = \int_{-\infty}^{\infty} \exp\left[-Fx^2/2 + Qx^4/24)/kT\right] dx$$

$$= \tfrac{1}{2}(a/b)^{\frac{1}{2}} \exp(a^2/8b)\ K_{1/4}(a^2/8b) \qquad \text{(A-4)}$$

where $a = F/2kT$, $b = Q/24kT$ and K_γ is the γ'th order modified Bessel function of the 2nd kind. Tables of $K_{1/4}$ do not yet exist. They may be generated from Basset's formula (13)

$$K_\gamma(z) = \frac{\Gamma(\gamma + 1/4)\ (2z)^\gamma}{\Gamma(1/2)} \int_0^\infty \frac{\cos u}{(u^2 + z^2)^{\gamma + 1/2}}\, du$$

by numerical integration, but for a simple estimate, approximate values of $e^x K_{1/4}(x)$ are obtained by linear interpolation between the values in the existing tables for $e^x K_0(x)$ and $e^x K_{1/3}(x)$ in Watson (14).

Table II gives the multiplicative factor for the bending modes in the classical ACT rate for $H + H_2$, $\Phi^2/2\pi$, as a function of temperature. Note that for low temperatures, which correlate with small angular displacements, the quartic perturbation is negligible, whereas at 3260°K, where the harmonic ACT fails, the harmonic-quartic ACT factor is 26% smaller than the quartic one. Table II indicates that when the quartic nature of H_3 bends are taken into account, the range of applicability of the ACT is extended by more than 1200°K.

The harmonic-quartic correction to the classical harmonic ACT rate expression is $(\Phi_{HQ}/\Phi_H)^2$ as far as the bending modes are concerned. The quantum mechanical rate expression involves quantum partition functions, pf. The correction, mentioned above, becomes $(pf_{HQ}/pf_H)^2$. The well-known harmonic oscillator partition function is

$$pf_H = \exp(-h\nu/2kT)/[1 - \exp(-h\nu/kT)] , \qquad (A-5)$$

where ν is the frequency of the harmonic oscillator. The partition function for the mixed, harmonic-quartic oscillator is

$$pf_{HQ} = \sum_{n=1}^{\infty} \exp(-W_n^{HQ}/kT) , \qquad (A-6)$$

where W_n^{HQ} are the harmonic-quartic energy levels. These may be approximated (to better than 0.5%) by a variation-perturbation method due to Truhlar (11).

$$\frac{W_n^{HQ}}{W_n^H} = \tfrac{1}{2}(\lambda_n^2 + \lambda_n^{-2}) + \frac{Q_\varphi \langle \varphi^4 \rangle_n^H}{24\, W_n^H} \lambda_n^{-4} \qquad (A-7)$$

Table II. Temperature Dependence of Bending Deformations in H_3

T(°K)	$e^x K_0(x)$[a]	$e^x K_{1/4}(x)$[b]	$e^x K_{1/3}(x)$[a]	$\Phi_{HQ}^2/2\pi$	$\Phi_H^2/2\pi$
45	0.279	0.28_0	-----	0.0138	0.0138
100	0.412	0.41_4	0.415	0.030	0.031
300	0.698	0.70_7	0.709	0.087	0.096
600	0.958	0.98	0.98	0.168	0.184
900	1.144	1.17	1.191	0.241	0.276
1000	1.20	1.24	1.25	0.269	0.307
1125	1.258	1.30	1.320	0.298	0.346
1500	1.417	1.48	1.503	0.386	0.46
2250	1.663	1.77	1.799	0.55	0.69
3260	1.91	2.05	2.11	0.74	1.00
4500	2.141	2.35	2.418	0.97	1.38

[a]Ref. 14.

[b]$e^x K_{1/4}(x) \cong \frac{1}{4} e^x K_0(x) + \frac{3}{4} e^x K_{1/3}(x)$.

where

$$\lambda_n^6 - \lambda_n^2 - \frac{Q_\varphi \langle \varphi^4 \rangle_n^H}{6\, W_n^H} = 0 . \qquad \text{(A-8)}$$

With the aid of reference 15, it may be shown that

$$\langle \varphi^4 \rangle_n^H = 3\hbar^2 G_{\varphi\varphi}^3 (2n^2 + 2n + 1)/4F_\varphi . \qquad \text{(A-9)}$$

The $G_{\varphi\varphi}^3$ is the valence angle element of the G matrix (1b) for the general linear triatom,

$$G_{\varphi\varphi}^3 = \frac{1}{m_A r_1^2} + \frac{1}{m_C r_2^2} + \frac{1}{m_B}\left(\frac{1}{r_1^2} + \frac{1}{r_2^2} + \frac{2}{r_1 r_2}\right), \qquad \text{(A-10)}$$

where the triatom is $m_A \cdots (r_1) \cdots m_B \cdots (r_2) \cdots m_C$. When the parameters of the BEBO H_3 complex are inserted in the above equations, the resulting energy levels are those found in Table III. The energy units (°K) are for convenience in evaluation of $\exp(-W_n^{HQ}/kT)$.

Table IV shows the quantum partition functions for the H_3 bending vibrations and the multiplicative correction factor for the quantum version of the ACT rate. Thus, the proposed treatment of quartic terms not only expands the utility of the ACT but also makes a significant correction to the rate constant itself. For example, it halves the discrepancy between the BEBO-ACT and Karplus, Porter, and Sharma (2d,16) computer-similated rates for $H + H_2$. The effect on rates involving complexes with still weaker harmonic force constants is expected to be even more important.

Table III. Bending Vibration Energy Levels

n	λ_n^2	W_n^H (°K)	W_n^{HQ} (°K)
0	1.000	525	554
1	1.005	1575	1724
2	1.218	2625	2936
3	1.282	3675	4240
4	1.329	4725	5600
5	1.410	5775	7090

Table IV. H_3 Bending Mode Partition Functions and Quantum Correction Factor for Harmonic ACT Rates

T(°K)	pf_H	pf_{HQ}	$(pf_{HQ}/pf_H)^2$
500	0.40	0.36_5	0.84
1000	0.91	0.83	0.83
2000	1.88	1.68	0.80

Appendix 1

The BEBO potential (2c) can be expressed as

$$V = V_B + V_{Tr} , \tag{A-11}$$

where V_B is the bonding contribution from r_1 and r_2, while V_{Tr} is the antibonding triplet repulsion between the end atoms in the ABC complex. V_{Tr} is a function of r_3, where

$$r_3^2 = r_1^2 + r_2^2 - 2\, r_1 r_2 \cos\theta , \tag{A-12}$$

by the law of cosines, and $\theta = \pi - \varphi$. At constant r_1 and r_2, the only variable part of the potential will be

$$V_{Tr} = (D_e/2) \exp(-\beta r_3) [\, 1 + \tfrac{1}{2} \exp(-\beta r_3)] , \tag{A-13}$$

where D_e and β are the dissociation energy and Morse parameter for the AC molecule. Substitution of (A-12) into (A-13) and repeated differentiation yields

$$F_\varphi = (\partial^2 V/\partial\varphi^2)_\ddagger = \alpha[\, 1 + \exp(-\beta r_3^\ddagger)] \tag{A-14}$$

$$Q_\varphi = (\partial^4 V/\partial\varphi^4)_\ddagger = \alpha \{3\, \beta\, r_1^\ddagger r_2^\ddagger [\, 1 + 2 \exp(-\beta r_3^\ddagger)] / r_3^\ddagger +$$

$$+ [\, 3\, r_1^\ddagger r_2^\ddagger / r_3^{\ddagger 2} - 1] [\, 1 + \exp(-\beta r_3^\ddagger)] \} \tag{A-15}$$

where

$$\alpha = (D_e/2)\, \beta\, (r_1^\ddagger r_2^\ddagger / r_3^\ddagger) \exp(-\beta r_3^\ddagger) . \tag{A-16}$$

The ‡ sign means that all quantities are evaluated at the saddlepoint in the potential surface. The values a propos the H_3 surface are D_e = 109.43 kcal/mole, $\beta = 1.9420 \text{Å}^{-1}$, and $r_1^‡ = r_2^‡ = \frac{1}{2} r_3^‡ = 0.92 \text{Å}$.

REFERENCES

1. (a) E. B. Wilson, J. C. Decius, and P. C. Cross, Molecular Vibrations, McGraw-Hill Book Company, Inc., New York, 1955, pp. 175-6; (b) pp. 61-63, 303-305.
2. (a) H. S. Johnston, Gas Phase Reaction Rate Theory, Ronald Press, New York, 1966, pp. 92, 223; (b) Bond Energy-Bond Order, p. 189; (c) p. 340; (d) p. 198.
3. K. Kuchitzu and Y. Morino, Bull. Chem. Soc. Japan, 38, 805 (1965).
4. J. K. Cashion and D. R. Herschbach, J. Chem. Phys. 40, 2358 (1964).
5. London-Eyring-Polanyi-Sato. See R. E. Weston, J. Chem. Phys. 31, 892 (1959).
6. R. N. Porter and M. Karplus, J. Chem. Phys. 40, 1105 (1964).
7. S. F. Boys and I. Shavitt, University of Wisconsin Naval Laboratory Tech. Report WIS-AF-13, 1959.
8. I. Shavitt, R. M. Stevens, F. L. Minn, and M. Karplus, J. Chem. Phys. 48, 2700 (1968).
9. F. E. Harris, D. A. Micha, and H. A. Pohl, Arkiv Fysik 30, 259 (1965). The authors reported $F_{\varphi} = 0.088 \times 10^{-11}$ ergs/rad^2. This is inconsistent with their Table 1, which is assumed to be correct.
10. (a) S. W. Mayer, L. Schieler, and H. S. Johnston, J. Chem. Phys. 45, 385 (1966); (b) S. W. Mayer, L. Schieler, and H. S. Johnston, Proceedings of the Eleventh Symposium on Combustion, The Combustion Institute, Pittsburgh, Pa., 1967; (c) S. W. Mayer

and L. Schieler, J. Phys. Chem. 72, 236 (1968).

11. D. G. Truhlar, Ph.D Candidacy Exam, California Institute of Technology, March 10, 1967, Proposition I.

12. The integral is found in I. S. Gradshteyn and I. M. Ryzhik, Tables of Integrals, Series, and Products, Academic Press, New York, 1965, p. 307, # 3.323 3.

13. M. Abramowitz and F. A. Stegun, Handbook of Mathematical Functions, National Bureau of Standards, Applied Mathematics Series 55, 1964, p. 376, # 9.6.25.

14. G. N. Watson, Treatise on the Theory of Bessel Functions, Macmillan Company, New York, 1944, second ed., pp. 698, 714.

15. A. M. Shorb, R. Schroeder, and E. R. Lipponcott, J. Chem. Phys. 37, 1043 (1962).

16. M. Karplus, R. N. Porter, and R. D. Sharma, J. Chem. Phys. 43, 3259 (1965).

Proposition B. Isotopic Reaction Rates

It is proposed that the bond-energy-bond-order (BEBO) method be used to obtain isotope effects in the $H + H_2$ reaction. Modifications of the method are suggested.

In an earlier proposition (1), it was suggested that the empirical BEBO method (2) be used to evaluate the rates of all the isotopic variations of the $H + H_2$ reaction. It was shown (1) that the BEBO potential was better justified for ground state hydrogen atom interactions than for any other and that the method was intended for linear triatomic complexes, such as H_3. Since that writing, it has become apparent that it will soon be possible to obtain such rates a priori. Configuration interaction methods (3) are slowly converging on the actual H_3 potential. Finite-difference quantum dynamics methods (4) are being developed which can handle the linear H_3 reaction on any of the existing or forthcoming potential surfaces. When available, these a priori rates may be compared with the very accurate (error $< 10\%$) ESR detection results (5) for $A + BC \rightarrow ABC \rightarrow AB + C$ where $A \neq C$. In view of the factor of 2 uncertainty in the experimental $A + A_2$ rate constants available from thermal conductivity (6) and mass spectrometric (7) detection methods, the ESR results probably provide a finer test of the theories.

The a priori theories mentioned above have not yet been pushed to their ultimate accuracies. Furthermore, they require a great deal more computer time than the simple BEBO method. Recently, several suggestions have been made for improving the BEBO rates. A more appropriate fit of the Sato anti-Morse function (8) to theoretical H_2

triplet data has been suggested (9). Quartic corrections to the bending vibrations have been proposed (11). The least certain aspect of the method, however, is the quantum correction to the reaction co-ordinate, that is, the tunneling correction. The original method was to make one-dimensional Eckart barrier (12) corrections on a reaction path from the zero point of the reactants to the zero point of the products through the classical potential pass. The zero-point energy of the complex was not taken into account because, in Johnston's words (13), "the quantum correction for one supposedly separable co-ordinate does not constitute potential energy for the reaction co-ordinate."

It has been demonstrated (14) that the assumption of vibrational adiabaticity in the H_3 reaction satisfactorily reproduces all but the very high energy reaction cross sections. This implies that at least the symmetric stretching mode of the H_3 complex has a good quantum number, which is the same as that of the reactant and product H_2 molecule for vibration. The representative trajectories must pass over the saddle with at least zero-point symmetric stretch energy in addition to the classical barrier height. It is not yet clear (14) whether the other vibration-rotation modes of the complex exhibit adiabaticity. It is therefore proposed that the tunneling correction for the $H + H_2$ isotopic reactions (1) be made for the one-dimensional Eckart reaction path (15) through the symmetric stretching zero point at the complex. As the bending mode frequencies are only about one-third that of the symmetric stretching mode, the latter accounts for about 60% of the total zero-point energy of the complex.

Mortensen (4b) has obtained a two-dimensional "transmission coefficient" (tunneling correction) for the Sato-Weston (8,17) H_3 potential. Comparison of this with his one-dimensional zero point path Eckart and Johnston's (13) 1-D Eckart ignoring all zero-point energy in the complex, shows non-negligible two-dimensional effects (see Table I). Proper accounting of the bending motion may yield even larger differences. The inclusion of only symmetric stretch zero-point energy in the 1-D Eckart barrier height would probably lead to better agreement with the 2-D tunneling correction than full complex zero-point energy at the low temperatures ($\sim 300^\circ K$) but poorer agreement at the intermediate temperatures ($\sim 500^\circ K$). No change in the amount of zero-point energy available to the complex is likely to bring the 1-D Eckart tunneling correction into accord with the 2-D one at the higher temperatures.

Mortensen (4b) found that he could bring the 1-D and 2-D "permeabilities" (Eyring's transmission coefficient (18)) as functions of energy into good agreement by shifting the 1-D values upscale by some energy $E_s \sim$ zero-point energy of the reactants and reducing the imaginary frequency of the complex. The first alteration follows Marcus' suggestion (19) for comparing the one and two-dimensional "permeabilities" at comparable translational energies. The <u>second</u> alteration, however, is interpreted by Mortensen (4b) as evidence of the need for effective reaction co-ordinate frequencies, obtained by some average of the actual potential surface frequencies over the possible crossing points at along the col. The imaginary frequency is maximized along the reaction path and any averaging of off-path crossings will necessarily reduce it.

Table I. H_3 Tunneling Corrections

T(°K)	333	500	1000
2-D	16	4.72	1.90
1-D Eckart			
ZPE‡	19	3.69	1.45
no ZPE‡	6.7	3.0	1.5
Classical path	23.0	3.9	1.4

It is clear from the above discussion that the tunneling correction is almost wholly unknown. Until exact numerical studies (16) are made, it is not obvious which approximate method should be employed. The one-dimensional Eckart tunneling is surely no more crude an approximation to the quantum correction in the reaction co-ordinate than the anti-Morse function fit is to the H_3 triplet potential. One finds (2) the isotope effects to be less sensitive to these simplifications than are the absolute rates. It is in the spirit of this last observation that this proposition is put forth.

REFERENCES

1. C. Parr, Ph.D Candidacy Exam, Caltech, March 12, 1965, Proposition I.
2. H. S. Johnston and C. Parr, J. Am. Chem. Soc. 85, 2544 (1963).
3. I. Sharett, R. M. Stevens, F. L. Minn, and M. Karplus, J. Chem. Phys. 48, 2700 (1968).
4. (a) D. J. Diestler and V. McKoy, J. Chem. Phys. 48, 2951 (1968); (b) E. M. Mortensen, J. Chem. Phys. 48, 4029 (1968).
5. A. A. Westenberg and N. de Haas, J. Chem. Phys. 47, 1393 (1967).
6. M. van Meersche, Bull. Soc. Chim. Belges 60, 99 (1951).
7. G. Boato, G. Careri, A. Cimino, E. Molinari, and G. G. Volpi, J. Chem. Phys. 24, 783 (1956).
8. S. Sato, J. Chem. Phys. 23, 2465 (1955).
9. S. W. Mayer, L. Schieler, and H. S. Johnston, Proceedings of the Eleventh International Symposium on Combustion, The Combustion Institute, Pittsburgh, Pa., 1967, p. 837. The theoretical data referenced in this work are those of Hirschfelder-Linnett (10a). The fit may be different if the more recent H_2 triplet data of Kolos and Wolniewicz (10b) are employed.
10. (a) J. O. Hirschfelder and J. W. Linnett, J. Chem. Phys. 18, 130 (1950); (b) W. Kolos and L. Wolniewicz, J. Chem. Phys. 43, 2429 (1965).
11. Preceding proposition.
12. C. Eckart, Phys. Rev. 35, 1303 (1930).

13. H. S. Johnston, Gas Phase Reaction Rate Theory, Ronald Press, New York, 1966, p. 195.

14. R. A. Marcus, J. Chem. Phys. 46, 959 (1967).

15. The one-dimensionality is imposed by the fact that BEBO gives the potential only along the reaction path. Even with this restricted dimensionality, it would be possible, as Truhlar (16) suggests, to obtain the exact (numerical, finite difference) solution to the tunneling through the BEBO barrier, rather than relying on analytic formulae for tunneling through a dubious Eckart fit to the reaction path. Such an alteration would encumber the simple method with the inversion of large matrices making it an exercise for the computer rather than the "back-of-an-envelope" calculation it is in its present form.

16. D. G. Truhlar, private communication.

17. R. E. Weston, J. Chem. Phys. 31, 892 (1959).

18. H. Eyring, J. Walter, and G. E. Kimball, Quantum Chemistry, John Wiley and Sons, Inc., New York, 1944, p. 306. The quantity under discussion is called κ_{nk} in this reference.

19. R. A. Marcus, J. Chem. Phys. 41, 610 (1964).

Proposition C. Volatile Substrates for Ultra-Thin Films

> It is proposed that free, ultra-thin films may be obtained by vacuum deposition on substrates which may be removed by sublimation. The uses of such films are reviewed.

It has been proposed (1) that volatile substrate techniques be developed to allow separation of vacuum deposited thin films by cryogenic pumping. This would yield a minimum of damage to the films during the separation process and allow one to produce ultra-thin films free of substrate effects at temperatures well below annealing or even most Debye temperatures. The technique suggested (1) was (a) condensation of Ne gas on a helium-cooled window followed by (b) slow vapor phase condensation of the film material from a well-baffled oven source (2) and finally (c) separation of the film-substrate from the window and sublimation of the neon substrate by cryogenic pumping.

The prime motivation for the production of free, cold, ultra-thin films is the hope of obtaining information on their intrinsic (non-thermal) stresses. In the words of R. W. Hoffman (3), "a satisfactory theory for the origin of intrinsic stresses has yet to be formulated." There are, however, almost as many models for intrinsic stress in thin films as there are investigators in the field. The notion that a significant temperature differential between the film and substrate leads to tensile stresses during growth (4) has largely been put aside due to the findings of Pashley et al. (5) indicating that even the surface exposed to the hot source is likely to be at substrate temperatures. Intrinsic stresses are likely to arise (3) from phase changes when amorphous

film crystallize, surface contamination (especially by oxidizing substances (6)), interfacial dislocations, and the migration of vacancies, but the role of surface tension is not expected to be significant in films over 200 Å thick (3).

Since the geometric surfaces increase much more slowly than the volume of the film, as it grows, the surface effects might be expected to disappear in thick films. However, the actual surface of a film is rarely its geometric surface. It would only be so for perfect films, which have never been found. Instead, from gas adsorption studies, it has been discovered (3,7) that the surface grows linearly with accumulated mass, indicating a very porous structure. Tensile strength (per unit area) is found to be independent (7) of film thickness beyond about 100-200 Å, where the nucleated islands of film material begin to bridge together. All this suggests that the bulk of the film is very similar in its mechanical properties to its "surface." In order to test this idea, it would be of value to compare the known properties of free, thick (several thousands of Å's) films with those of ultra-thin (several hundreds of Å's) films in the absence of what may be a large substrate perturbation. The volatile substrate proposed here and earlier (1) would afford the opportunity for such a comparison. Physical stripping techniques presently employed for separating film and substrate would rupture the ultra-thin films we are considering, as they are little more than two-dimensional filigree at thicknesses less than 1000 Å. Sublimation of the substrate would provide the most gentle separation possible.

Sublimation would not require exposure of the film to the

atmosphere or to elevated temperatures. Thus it would be possible to study uncontaminated free films in the amorphous states they exhibit before coalition of the crystallites takes place. Or one could observe this coalition (as when annealing the film) without the hindrance the substrate offers to surface mobility. Also the influence of the substrate on the bonded surface could be examined under conditions where the separation mechanism is not expected to distort the interface.

The proposal is not without its hazards. For example, most contemporary substrates are vacuum cleaved crystals or highly polished glass or quartz. It is unlikely that solid Ne would have a structure amenable to cleaving, nor is it imagined that it would take a polish. Thus the surface of vacuum deposited neon is likely to be very rough on an atomic scale. Extensive experimentation may be necessary to get a workably smooth neon surface for film deposition. Perhaps very slow growth in ultra-high vacuum would provide a satisfactory substrate surface.

REFERENCES

1. C. Parr, Ph.D. Candidacy exam, Caltech, March 12, 1965, Proposition III.
2. W. Buckel, in Structure and Properties of Thin Films (C. A. Neugebauer, ed.), John Wiley and Sons, New York, 1959.
3. R. W. Hoffman, in Physics of Thin Films (G. Hass and R. E. Thun, eds.) Vol. 3, Academic Press, New York, 1966.
4. H. Wilman, Proc. Phys. Soc. B68, 474 (1955).
5. D. W. Pashley, M. J. Stowell, M. H. Jacobs, and T. J. Law, Phil. Mag. 10, 127 (1964).
6. A. E. Hill, Brit. J. Appl. Phys. 18, 13 (1967).
7. C. A. Neugebauer, in Physics of Thin Films (G. Hass and R. E. Thun, eds.), Vol. 2, Academic Press, New York, 1964.

Proposition D. One-Dimensional Decomposition

> It is proposed that the time-dependent Schroedinger equation be solved for unbound minimum wave packets in the square well potential. The analytic nature of the corresponding classical trajectory swarms makes comparison of quantal and classical results especially simple.

The quantum mechanical concept of Heisenberg's uncertainty principle has no classical mechanical analogue. Thus in a constant potential the average position of the wave packet evolves in time as does the position of a classical particle. However, the width of the wave packet grows in time (1a). The position and momentum of the corresponding classical particle have zero uncertainties for all time. The obvious disparity may be removed by considering a swarm of classical trajectories with a (continuous) distribution in phase space matching that of the quantal wave packet. I.e., the initial classical distribution in the (one-dimensional) space co-ordinate is

$$f(x, t = 0) = \psi_0^*(x)\, \psi_0(x) \qquad \text{(D-1)}$$

while the initial distribution in the momentum co-ordinate

$$g(p, t = 0) = \phi_0^*(p)\, \phi_0(p) \qquad \text{(D-2)}$$

where $\psi_0(x)$ and $\phi_0(p)$ are the co-ordinate and momentum representation of the wave packet at time zero. If the wave packet is the "minimum wave packet," with the Gaussian form (1b,2)

$$\psi_0(x) = \frac{1}{(\pi\sigma^2)^{\frac{1}{4}}} \exp\{-[x - \langle x\rangle_0]^2/2\sigma^2 + i\langle p\rangle_0 x\} \qquad \text{(D-3)}$$

then

$$f(x, t=0) = \frac{1}{(\pi\sigma^2)^{\frac{1}{2}}} \exp\{-[x - \langle x\rangle_0]^2/\sigma^2\} \qquad \text{(D-4)}$$

and

$$g(p, t=0) = \frac{1}{(\pi\eta^2)^{\frac{1}{2}}} \exp\{-[p - \langle p\rangle_0]^2/\eta^2\} \ . \qquad \text{(D-5)}$$

Here $\eta = \hbar/\sigma$, the rms deviation of the momentum.

Since we are dealing with a free particle $\langle p\rangle$ and η remain constant in time for both quantum and classical mechanics. Thus for all the trajectories in the swarm associated with a single momentum, p, their distribution changes in time by translating (without change of shape) by pt/m, hence

$$f(x,p,t) = \frac{1}{(\pi\sigma^2)^{\frac{1}{2}}} \exp\{-[x - (\langle x\rangle_0 + \frac{pt}{m})]^2/\sigma^2\} \ . \qquad \text{(D-6)}$$

The distribution of the entire swarm is found by weighting (D-6) by the proposition of the swarm trajectories with momenta p to p + dp, i.e., by $g_0(p)dp$, and integrating over all values of p. Thus

$$f(x,t) = \int_{-\infty}^{\infty} g_0(p)\, f(x,p,t)dp \ , \qquad \text{(D-7)}$$

which, for the case at hand, results in

$$f(x,t) = \frac{1}{(\pi\xi^2)^{\frac{1}{2}}} \exp\{-[x - (\langle x\rangle_0 + \frac{\langle p\rangle_0 t}{m})]^2/\xi^2\} \qquad \text{(D-8)}$$

where $\xi^2 = \sigma^2 + \eta^2 t^2/m^2$. It may be shown (1c) that ξ^2 has the same time dependence in quantum mechanics as well. Thus, the quantal and swarm-averaged classical co-ordinate and momentum distributions for the free minimum wave packet are identical for all time. Such results encourage the hope that suitably averaged classical trajectories may be used to follow atoms and molecules through bimolecular exchange and unimolecular decomposition reactions.

Chemical reactions do not take place in uniform potential fields. Quantum interference effects for non-constant potentials eventually destroy the agreement (3) between quantal and swarm-averaged classical probability distributions. What is the time scale for such divergence? Recent calculations (4) of the evolution of wave packets in the bound energy regions of some one- and two-dimensional anharmonic potentials show serious deviations between the two distributions after a few vibration cycles. Bimolecular exchanges occur in the strongly bound regions of the potential surface, but, for unstable intermediates, the collisions are direct and the products (or reactants) separate in times on the order of a single characteristic vibration period. Because of their brevity, bimolecular collisions may be quasi-classical. Their quantum dynamics may be adequately represented by the swarm-averaged or "classical mechanics with an uncertainty relation" (4) approach.

Unimolecular decomposition is characterized by relatively long molecular lifetimes. The deviation of the quantal from the swarm-average results are likely to be more serious in this case. However, the energies of interest in unimolecular decomposition lie in the continuum for at least one molecular mode. Thus it would be very useful to see how adequate

the swarm-average distributions are when applied to energies near the dissociation limit. Beyond this limit lies the domain of metastable states. There are also effective potential (centrifugal) barriers to contend with. Both increase the lifetime of dissociative modes.

Frey and Thiele (2) have dealt with the probability of decay of metastable wave functions behind one-dimensional square barriers of the form:

$$V(x) \begin{cases} \infty \text{ for } x < 0 \\ 0 \text{ for } 0 < x < a \text{ and } x > b \\ V_b \text{ for } a < x < b \end{cases}$$

Their equations are sufficiently general to handle dissociation wells inside the barrier as well. They demonstrated that a minimum wave packet distribution loses its Gaussian shape on the first collision with the inner (infinite) potential wall. This is in contrast to the swarm-averaged classical distribution, which recovers its Gaussian shape after the first few collisions (5). However, for a barrier described only as "so thin that almost total penetration occurs on the first encounter" (2), the probability of remaining behind the barrier

$$P_2(t) = \int_0^a \psi^*(x,t)\, \psi(x,t)\, dx, \qquad \text{(D-9)}$$

the solid line in Figure 1, very much resembles its classical counterpart

$$P_2(t) = \int_0^a f(x,t)\, dx\ , \qquad \text{(D-10)}$$

given by the double dashed line in the same figure (6). Clearly, the comparison is questionable. Since the height of the barrier was not specified in the paper (2), it was assumed to be zero, and the entire range for p was used in equation (D-7). If this figure represents barrier tunneling, then $\langle p \rangle \leq (2mV_b)^{\frac{1}{2}}$, where V_b is the barrier height. Since all trajectories with $p < (2mV_b)^{\frac{1}{2}}$ reflect, the integral in (D-7) should only be taken over the range $(2mV_b)^{\frac{1}{2}}$ to ∞. Nevertheless, for such a thin barrier, its neglect in the classical case leads to near agreement with the quantal result. Had the barrier vanished in the quantal case, the agreement would, doubtless, have been better still, and this is for a wave packet which has struck the inner wall, destroying the Gaussian form. Perhaps, maintainence of the shape of the quantal distribution is not a necessary condition for swarm-averaged classical behavior. This could easily be tested with equation (D-8) and further application of the formulae in Ref. 2.

It is proposed that the time-dependent wave packets of Ref. 2 be investigated at energies above the barrier and with realistically deep wells behind the barrier, i.e., for

$$V(x) \begin{cases} \infty & \text{for } x < 0 \\ -D & \text{for } 0 < x < a \\ +V_b & \text{for } a < x < b \\ 0 & \text{for } x > b \end{cases} \qquad \text{(D-11)}$$

At any $\langle p \rangle > (2mV_b)^{\frac{1}{2}}$, the effect of reflection above the barrier will be seen in the quantal/swarm-average comparison. The effects of the metastable states should be amplified when $\langle p \rangle = E_o$, where E_o is some quasi-

FIG. 1. Probability of remaining behind a permeable barrier as a function of time. T is the (classical) period of motion behind the barrier. The probabilities are calculated by exact quantum mechanical metastable state expansion (—), and swarm-averaged classical mechanics without the barrier (— - —). The first comes from Ref. 2. The second from equation (D-8) of this paper. The minimum wave-packet parameters are $\langle x \rangle_o = 0.625$ a, $\langle p \rangle_o = -20\,\hbar/a$ and $\sigma = 0.2$ a.

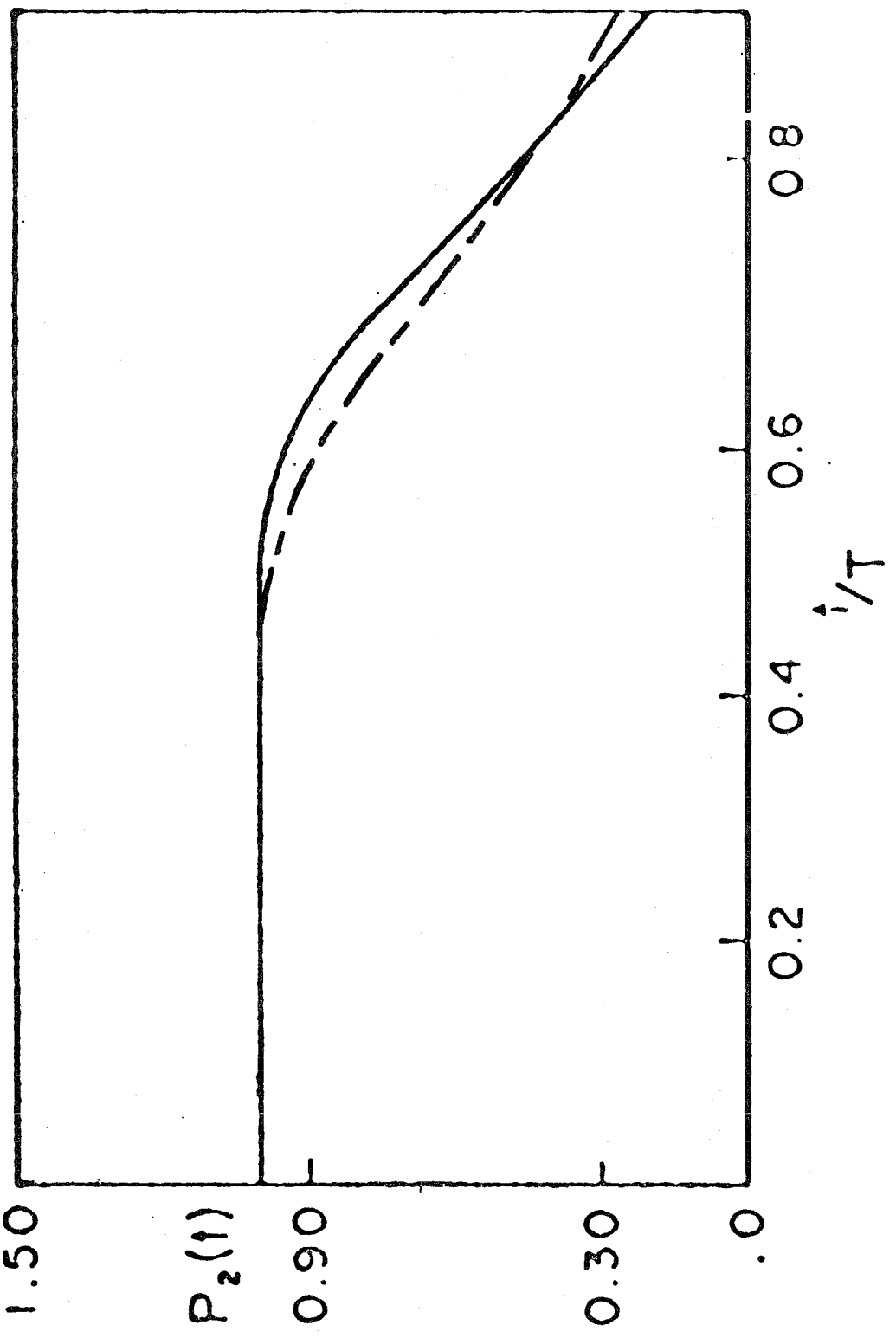
1.50
$P_2(t)$
0.90
0.30
.0
0.2
0.4
0.6
0.8
1/T

stationary level. The effect of the spacing of these levels will be important, for in chemically realistic potentials the spacing is thought (7) to be smaller than the half-widths of the quasi-stationary states. The inclusion of the non-zero dissociation energy, D, will probably have little effect, but will necessitate (2) a solution for the bound states of the potential (D-11).

The wave function for that potential is discontinuous in 2nd derivative over three boundaries. It may be obtained as follows, for $E < 0$:

$$\psi_I(x) = A_1 \sin k_1 x \quad \text{for} \quad 0 < x < a$$
$$\psi_{II}(x) = A_2 e^{-k_2 x} + B_2 e^{k_2 x} \quad \text{for} \quad a < x < b \qquad \text{(D-12)}$$

and

$$\psi_{III}(x) = A_3 e^{-k_3 x} \quad \text{for} \quad x > b.$$

The wave numbers, k, are

$$k_1 = (-2mE)^{\frac{1}{2}}/\hbar$$
$$k_2 = [2m\,(V_b - E)]^{\frac{1}{2}}/\hbar \qquad \text{(D-13)}$$
$$k_3 = [2m(D - E)]^{\frac{1}{2}}/\hbar \quad .$$

The continuity conditions on the first and second derivatives of $\psi(x)$ lead to

$$
\begin{aligned}
(\sin k_1 a)\, A_1 \;-\; (e^{-k_2 a})\, A_2 \;-\; (e^{-k_2 a})\, B_2 \;&=\; 0 \\
(k_1 \cos k_1 a)\, A_1 \;+\; (k_2 e^{-k_2 a})\, A_2 \;-\; (k_2 e^{-k_2 a})\, B_2 \;&=\; 0 \\
(e^{-k_2 b})\, A_2 \;+\; (e^{-k_2 b})\, B_2 \;-\; (e^{-k_3 b})\, A_3 \;&=\; 0 \\
-(k_2 e^{-k_2 b})\, A_2 \;+\; (k_2 e^{-k_2 b})\, B_2 \;+\; (k_3 e^{-k_3 b})\, A_3 \;&=\; 0
\end{aligned}
\qquad \text{(D-14)}
$$

which has non-trivial solutions only when the determinant is zero. The latter condition leads to the quantization formula

$$
(k_2 + k_3)(k_1 + k_2 \operatorname{tg} k_1 a) e^{2k_2(b-a)} \;=\; (k_3 - k_2)(k_1 - k_2 \operatorname{tg} k_1 a), \qquad \text{(D-15)}
$$

which, by equations (D-13), is a transcendental equation in E_n, the bound state energy levels, i.e., quantization of the k_i. The equations (D-14) lead to A_2, B_2, and A_3 in terms of A_1, which is fixed by the normalization condition,

$$
\int_o^a \psi_I^* \psi_I dx \;+\; \int_a^b \psi_{II}^* \psi_{II} dx \;+\; \int_b^\infty \psi_{III}^* \psi_{III} dx \;=\; 1 \,. \qquad \text{(D-16)}
$$

The quasi-stationary levels are given in Ref. 2 for $D = 0$. They will have to be solved again for two more cases, viz., $0 < E < V_h$ and $E > V_h$, with a non-zero D.

It is hoped that comparisons of the quantal and swarm-averaged classical results at these energies will enable some definitive statements to be made about the validity of the use of classical trajectories in chemical dynamics.

REFERENCES

1. (a) A. Messiah, Quantum Mechanics, John Wiley and Sons, Inc., New York, 1966, Vol. I, p. 221; (b) p. 327; (c) pp. 218-222.
2. R. B. Frey and E. Thiele, J. Chem. Phys. 48, 3240 (1968).
3. The exception to this statement, at least as far as the motion of the center of the packet is concerned, involves potentials which are quadratic in the co-ordinate. The harmonic oscillator is one example. See D. I. Blokhintsev, Principles of Quantum Mechanics, Allyn and Bacon, Inc., Boston, Mass., 1964, footnote p. 124.
4. See P. F. Endres and D. J. Wilson, J. Chem. Phys. 46, 425 (1967) and references therein.
5. This is evident since the classical trajectory has a constant velocity, $\pm$ p/m, over the length of the square well. After some time elapses, the natural spread in the distribution increases beyond the length of the well and the "folding" of the ends of the classical distribution into the well gives a non-Gaussian shape.
6. The figure (without the doubled dashed line) was taken from Ref. 2. The abscissa scale mark for 0.8 is in error. In its present position it should read 0.825. T is the period of the classical trajectory with momentum $\langle p \rangle$, i.e., $T = am/\langle p \rangle$, where a is the length of the well behind the barrier.
7. F. H. Mies and M. Krauss, J. Chem. Phys. 45, 4455 (1966).

Proposition E. High Temperature Wall Poison for H and X Atoms

It is proposed the potassium metaborate (KBO_2) be investigated as a wall poison to recombination of hydrogen and halogen atoms. The utility of such a poison is described.

Recently, flow systems have been developed for more-or-less direct measurements of radical reaction kinetics (1,2,3). Molecule A_2 is dissociated upstream by microwave discharge (1) or hot filament (2,3). Molecule BC is bled into the reaction tube and analysis is made downstream for the amount of AB, AC, B, C, or attenuation of A resulting from A + BC reactions. The detection of the molecules is usually by gas chromatography (2,3). The atoms are measured by ESR (1) or wire calorimetry (2). When A's are oxygen or nitrogen atoms, it is found (1a) that clean quartz tubing suffices, as O and N radical recombination rates on such a surface are relatively low. However, when A is a hydrogen or halogen atom, the wall of the reaction tube must be "poisoned," coated to changed its surface reactivity, otherwise few H or X atoms are detected downstream of their source.

Surface poisons for H atom are discussed in Ref. 4. Such poisons include boric acid, H_3BO_3 (1b), and teflon (3). Some materials which poison Cl or Br atom recombination are listed in Ref. 5. The latter paper includes boric acid but finds teflon ineffective. Of these wall coatings, boric acid $\stackrel{\Delta}{\rightarrow} B_2O_3$ seems most attractive, for it can be used in H atom reactions (1b) at temperatures up to about 720°K, where it melts and is flushed out of the reaction tube. In Cl atom reactions, however, the glassy boric oxide is stripped off the walls at temperatures

above 460°K (1c). All other known, chemically inert, poisons soften at temperatures below the melting point of B_2O_3. Thus high temperature radical reaction studies by these flow techniques require a tougher poison.

It is proposed that potassium metaborate (KBO_2) be used as a surface poison in these experiments. It is readily dissolved in hot water, making application to the tube surface simple. (The hot solution is allowed to stand in the reaction tube for an hour say, after which the tube is baked out to drive off the water.) The poisoning properties of KBO_2 should be similar to those of B_2O_3, but the melting point of the metaborate is 1220°K or 500°K in excess of that of the glassy boric oxide. This higher melting point enables one to extend the range of the H atom studies.

The greater cohesion implied by the higher melting point of the metaborate may also lead to higher resistivity to halogen attack for the metaborate over the oxide. There is very little literature on the reactivity of metaborates. The trigonal B_2O_3 resists attack by all halogens and halogen acids except fluorine. Tetrahedral borates are generally observed to be less reactive than trigonal ones (6). The bonding in KBO_2 is still a matter of speculation. X-ray studies find evidence of trigonal boron, while NMR results suggest tetrahedral co-ordination. In either case, the metaborate should be no less inert than the glassy oxide. Since the B—Cl bond energy is some 60 kcal/mole below the B—O bond energy of 164 kcal/mole, the chlorine replacement reaction is seen to be highly endothermic (6). Nevertheless, the report that Cl_2 streams erode boric acid surfaces (1c) at temperatures 300°K below the melting point of B_2O_3, while H_2 streams do not, implies some chemical effect. There may be an opening of the B_2O_3 structure at temperatures so near the melting

point. This would facilitate Cl penetration of and attack upon the oxide. If metaborate poisons remain on the walls to within 300°K of their melting points, the Cl atom experiments should become feasible up to 900°K.

In that event, the predictions of activated complex theory (ACT) and classical trajectory calculations for the H + DBr abstraction and exchange reactions could be tested in a region where they differ. It has been shown (7) that a Sato surface for HDBr, which fits experimental activation energies and room temperature abstraction fractions,

$$AF = k_a/(k_a + k_e) \qquad \text{(E-1)}$$

where

$$H + DBr \xrightarrow{k_a} HD + Br \qquad \text{(E-2)}$$

and

$$H + DBr \xrightarrow{k_e} HBr + D \ , \qquad \text{(E-3)}$$

yields ACT and trajectory calculated AF's which have very similar temperature dependences up to about 700°K. In the range $800 \leq T \leq 900$°K, the trajectory AF's are some 30-50% higher than the ACT ones. This difference is larger than the accuracies claimed for the flow methods. For example, ESR detection (1) yields absolute rate constants for A + BC → AB + C type reactions to within 10%. It is readily seen that when the abstraction fraction (equation E-1) is about 0.2 (the ACT value for 900°K), a 10% uncertainty in the rate constants, k_e and k_a, leads to a 17% error limit (95% confidence) in the experimental AF. Thus the experimental AF at temperatures approaching 900°K could be used to comment on the theoretical predictions of Ref. 7.

This is but one small example of the utility of high temperature poisons. The reactions of H atoms hold even greater theoretical interest, and with the aid of potassium metaborate, they may be observed up to the 1220°K melting point in these flow experiments.

REFERENCES

1. (a) A. A. Westenberg and N. de Haas, J. Chem. Phys. 40, 3087 (1964); (b) ibid., 47, 1393 (1967); (c) ibid., 48, 4405 (1968).
2. B. A. Ridley, W. R. Schulz, and D. J. LeRoy, J. Chem. Phys. 44, 3344 (1966).
3. D. R. Davis, private communication.
4. B. A. Thrush, Prog. Reaction Kinetics 3, 63, (1965).
5. E. A. Ogryzlo, Can. J. Chem. 39, 2556 (1961).
6. E. L. Muetterties, The Chemistry of Boron and Its Compounds, John Wiley and Sons, Inc., New York, 1967.
7. Part III, Section 4.3., this thesis.